Topics in Numerical Relativity

by

Gray Reid

B.Sc., Acadia University, 2012

A THESIS SUBMITTED IN PARTIAL FULFILLMENT OF
THE REQUIREMENTS FOR THE DEGREE OF

DOCTOR OF PHILOSOPHY

in

THE FACULTY OF SCIENCE

(Physics and Astronomy)

THE UNIVERSITY OF BRITISH COLUMBIA

(Vancouver)

September 2023

The following individuals certify that they have read, and recommend to the Faculty of Graduate and Postdoctoral Studies for acceptance, the thesis entitled:

Topics in Numerical Relativity

submitted by **Gray Reid** in partial fulfillment of the requirements of the degree of **Doctor of Philosophy** in **Physics and Astronomy**

Examining Committee:

Matthew Choptuik, Professor, Physics and Astronomy, UBC
Supervisor

TBD
University Examiner

TBD
University Examiner

Additional Supervisory Committee Members:

Aaron Boley, Associate Professor, Physics and Astronomy, UBC
Supervisory Committee Member

Jeremy Heyl, Professor, Physics and Astronomy, UBC
Supervisory Committee Member

Scott Oser, Professor, Physics and Astronomy, UBC
Supervisory Committee Member

Kristin Schleich, Associate Professor, Physics and Astronomy, UBC
Supervisory Committee Member

William Unruh, Professor, Physics and Astronomy, UBC
Supervisory Committee Member

Abstract

In this thesis we present a series of studies in numerical relativity investigating stability, hyperbolicity and critical phenomena. The first part of our work is dedicated to the study of d-stars, hypothetical objects consisting of a boson star and global monopole minimally or nonminimally coupled to the general relativistic gravitational field. The space of solutions for these systems is large and, for a wide range of coupling parameters, exhibits ground state solutions with asymptotic shells of bosonic matter. After demonstrating the existence of these stationary solutions, we turn our attention to their stability through a combination of linear perturbation theory and dynamical simulation. In doing so, we demonstrate that the novel solutions we have found, as well as the highly compact solutions investigated by previous authors, appear to be generically unstable to radial perturbations. As such, we find that d-stars are poor candidates for astrophysically relevant black hole mimickers.

Generalizing from the stability of solutions to the stability of methods, we introduce a novel formulation of numerical relativity which we refer to as *reference metric covariant and conformal Z4* (RCCZ4). Like its Z4 namesake, RCCZ4 promotes the 3+1 Hamiltonian and momentum constraints to dynamical degrees of freedom. Unlike Z4 however, RCCZ4 accomplishes this by coupling the constraints to an external reference metric completely independently of the physical metric. Although we have only investigated RCCZ4 in the case of time independent Lorenzian reference metrics, the method may generalize to user specifiable reference metrics which could potentially confer additional beneficial properties. Even in this simple case, however, the performance of RCCZ4 is comparable to leading hyperbolic formulations.

The final part of our thesis works towards developing superior understanding of strong field gravity through the investigation of gravitational collapse. We consider the system consisting of the electromagnetic and general relativistic gravitational fields and investigate the threshold of black hole formation in axisymmetry. Previous studies of this system have reported family dependent scaling phenomena as criticality is approached. Although we find good agreement with previous investigations of dipole-type initial data, our investigations of quadrupole-type initial data point towards universal scaling as opposed to family dependent scaling.

Lay Summary

General relativity (GR), describes how mass and energy interact with the fabric of space and time. While the equations governing GR are incredibly powerful, they are often far too complicated to solve analytically for scenarios of interest. By studying GR in a numerical lab, we are able to investigate extreme conditions and test GR's predictions both against observations and in comparison with other theories of gravity.

Our research focuses on three key topics within numerical relativity. We start by examining boson d-stars, theoretical objects that our simulations reveal to be poor candidates for black hole mimickers. Next, we introduce a novel computational approach for GR simulations. This new technique not only performs well against established methods but also leaves room for future improvements. Lastly, we study the threshold of black hole formation from electromagnetic waves, or light, offering new viewpoints that contrast with earlier research.

Preface

The research in this thesis was conducted by Gray Reid, under the guidance of research supervisor Matthew Choptuik who played a central role in directing the research focus and provided significant editorial contributions to our published works. Additional input, in the form of discussions, suggestions, and proofreading, was provided by other members of the Choptuik research group, peer reviewers, and faculty at the University of British Columbia. Chapters 1 and 2 provide background to the topics considered in the thesis and do not constitute original work. Each of Chapters 3–6 forms the basis of a separate publication as follows:

- Chapter 3 and Appendix A have been published in Physical Review D [Gray D. Reid and Matthew W. Choptuik, Nonminimally coupled topological-defect boson stars: Static solutions. Phys. Rev. D 93, 044022, 2016]. I was the lead investigator, responsible for all coding, investigation and analysis as well as the primary manuscript composition. Matthew Choptuik was responsible for the conception of the study, directing its scope and made significant contributions to editing the manuscript.

- Chapter 4 and Appendix B have been accepted for publication in Physical Review D [109]. I was the lead investigator, responsible for all coding, investigation and analysis as well as the primary manuscript composition. Matthew Choptuik was responsible for the conception of the study, directing its scope and made significant contributions to editing the manuscript.

- Chapter 5 and a version of Appendix E have been submitted for publication in Physical Review D [108] and are presently under review. I was the lead investigator, responsible for all major areas of concept formation, coding, investigation and analysis as well as the primary manuscript composition. Matthew Choptuik provided guidance, helped to direct scope and made significant contributions to editing the manuscript.

- Chapter 6 has been accepted for publication in Physical Review D [110]. I was the lead investigator, responsible for all coding, investigation and analysis as well as the primary manuscript composition. Matthew Choptuik was responsible for the conception of the study, directing its scope and made significant contributions to editing the manuscript. Our investigation makes use of data generously provided by Maria F. Perez Mendoza and Thomas W Baumgarte [17, 20, 85].

Table of Contents

Abstract . . . iii

Lay Summary . . . iv

Preface . . . v

Table of Contents . . . vi

List of Tables . . . x

List of Figures . . . xii

Acknowledgements . . . xxv

Dedication . . . xxvi

1 Introduction . . . 1
- 1.1 A Brief History of General Relativity . . . 1
- 1.2 Numerical Relativity . . . 3
- 1.3 Conventions and Notation . . . 3
- 1.4 The ADM Decomposition . . . 4
- 1.5 A Brief History of BSSN-Type Formulations . . . 6
- 1.6 Boson Stars and Topological Defects . . . 9
- 1.7 Critical Collapse in General Relativity . . . 10
- 1.8 Plan of the Thesis . . . 12

2 Overview of Numerical Methods . . . 14
- 2.1 Finite Difference Approximations . . . 14
- 2.2 Stability of Hyperbolic Schemes . . . 16
- 2.3 Dissipation . . . 19
- 2.4 Convergence Testing . . . 21
- 2.5 Independent Residual Convergence Tests . . . 23
- 2.6 Elliptic Equations . . . 25
- 2.7 Relaxation Methods for Elliptic PDEs . . . 25
- 2.8 Multigrid for Elliptic PDEs . . . 26
- 2.9 Adaptive Mesh Refinement . . . 28

3 Non-Minimally Coupled Topological-Defect Boson Stars: Static Solutions . . . 30
- 3.1 Introduction . . . 30
- 3.2 Static Equations . . . 33
- 3.3 Methodology . . . 37

3.3.1 Solution Families and Branches . . . 37
3.3.2 Solution Procedure . . . 38
3.3.3 Convergence of Numerical Solutions . . . 39
3.4 Results . . . 40
3.4.1 Branching Behavior of Minimal Boson D-Stars . . . 45
3.4.2 Branching Behavior of Non-Minimal Boson D-Stars . . . 49
3.4.3 Critical Scaling of Asymptotic Shells . . . 53
3.4.4 Derivation of Scaling Law . . . 54
3.5 Summary . . . 56
3.6 Acknowledgements . . . 56

4 Non-Minimally Coupled Topological-Defect Boson Stars: Stability of Solutions 57
4.1 Background . . . 57
4.2 Review of Stationary D-Stars . . . 58
4.3 Overview . . . 61
4.4 Matter Model . . . 61
4.4.1 Boundary Conditions . . . 63
4.4.2 Conserved and Diagnostic Quantities . . . 64
4.5 Dynamical Simulation . . . 65
4.5.1 Initial Data . . . 65
4.5.2 Evolution Scheme . . . 65
4.5.3 Convergence . . . 66
4.5.4 Extraction of Growth Modes . . . 68
4.6 Linear Perturbation Theory . . . 69
4.6.1 Solution Procedure . . . 69
4.6.2 Convergence . . . 71
4.7 Results . . . 71
4.7.1 Dynamical Simulations . . . 72
4.7.2 Linear Perturbation Theory . . . 78
4.7.3 Comparison of Methods . . . 83
4.8 Summary . . . 85
4.9 Acknowledgements . . . 85

5 RCCZ4: A Reference Metric Approach to Z4 . . . 86
5.1 Introduction . . . 86
5.2 Derivation of RCCZ4 . . . 88
5.3 FCCZ4 and GBSSN Equations of Motion . . . 91
5.4 Comparison of GBSSN, FCCZ4 and RCCZ4 . . . 92
5.4.1 Convergence and Independent Residual Tests . . . 93
5.4.2 Evolution of Black Hole Spacetimes . . . 94
5.4.3 Critical Collapse . . . 102
5.5 Hyperbolicity of RCCZ4 . . . 105
5.6 Summary and Conclusions . . . 109
5.7 Acknowledgements . . . 110

6 Universality in the Critical Collapse of the Einstein-Maxwell System 111
6.1 Introduction 111
6.2 Background 114
6.3 Initial Data 118
6.4 Numerics and Validation 120
6.4.1 Choice of Gauge 121
6.4.2 Classification of Spacetimes 122
6.4.3 GBSSN Considerations 122
6.4.4 Convergence 123
6.5 Results 126
6.5.1 Massless Scalar Field 126
6.5.2 Einstein-Maxwell System 129
6.5.3 Direct Comparison to Previous Work. 134
6.6 Summary and Conclusions 136
6.7 Acknowledgements 137

Bibliography 138

Appendices

A Multiple Precision Shooting Method 146
A.1 Summary 146
A.2 Shooting Method for BVPs 146
A.3 Multiple Precision Shooting Method 147
A.4 Generalization to Arbitrary Shooting Problems 149

B Linear Perturbation Equations for Minimally Coupled d-Stars 150
B.1 Equations of Motion 150
B.2 Linear Perturbation Theory Equations 151

C Derivation of the GBSSN Formulation 155
C.1 Conventions 155
C.2 Derivation Overview 157
C.3 Hamiltonian and Momentum Constraints 158
C.4 Evolution of the Conformal Metric 159
C.5 Evolution of Extrinsic Curverature Trace 159
C.6 Evolution of Trace Free Extrinsic Curvature 160
C.7 Covariant Decomposition of the Ricci Tensor 160
C.8 Conformal Covariant Ricci Tensor 162
C.9 Evolution of Contracted Christoffel Quantities 163

D Derivation of the FCCZ4 Formulation 165
D.1 Derivation Overview 165
D.2 Spatial projection 167
D.3 Temporal Projection 167
D.4 Mixed Projection 168
D.5 FCCZ4 Form of the Equations 168
D.5.1 Evolution of Extrinsic Curvature Trace 169

D.5.2 Evolution of Trace Free Extrinsic Curvature . . . 169
D.5.3 Evolution of Theta . . . 170
D.5.4 Evolution of Lambda . . . 170

E Derivation of the RCCZ4 Formulation . . . 171
E.1 3+1 Form of RZ4 . . . 171
E.1.1 Spatial projection . . . 171
E.1.2 Temporal Projection . . . 172
E.1.3 Mixed Projection . . . 173
E.2 Derivation of RCCZ4 . . . 173
E.2.1 Evolution of the Extrinsic Curvature Trace . . . 174
E.2.2 Evolution of the Trace-Free Extrinsic Curvature . . . 174
E.2.3 Evolution of Theta . . . 175
E.2.4 Evolution of Lambda . . . 175
E.2.5 Simplifying Substitution . . . 175

F Hyperbolicity of FCCZ4 and GBSSN . . . 177
F.1 Hyperbolicity of the Nonlinear Wave Equation . . . 177
F.2 Hyperbolicity of FCCZ4 . . . 179
F.3 Hyperbolicity of GBSSN . . . 180

G Derivation of the Embedded Covariant and Conformal Maxwell Equations . . . 183
G.1 Maxwell Equations in Curved Space . . . 183
G.2 Embedded Maxwell Equations . . . 183
G.3 Evolution Equations for Constraint Advecting Quantities . . . 184
G.4 Evolution equations for E and B . . . 185
G.5 Conformal Form of Evolution Equations . . . 186
G.6 Heuristic Proof of Damping Properties . . . 186

H Achieving Smoothness at AMR Boundaries . . . 188
H.1 AMR in Brief . . . 188
H.2 Introduction and Conventions . . . 189
H.3 Spatial Derivatives and Discontinuities . . . 190
H.4 The Issue With Temporal Boundary Interpolation . . . 191
H.5 Getting Around Temporal Boundary Interpolation . . . 192
H.6 Determination of Parameters . . . 195
H.7 Implementation . . . 197
H.8 Smooth AMR for the 2D Wave Equation . . . 198

List of Tables

3.1 Parameters for families of solutions. Each family consists of a continuum of solutions differentiated by the central amplitude of the boson star. 41

4.1 Families of solutions and their associated parameters. Each family consists of a continuum of solutions labelled by the central amplitude of the boson star. In particular, family h corresponds to a family in the high compactness regime as defined in [83]. Due to their relatively simple and illustrative modal structure, families p_1 and p_2 are the only ones we explore with perturbation theory. 59

5.1 Parameters for the meshes in fixed mesh refinement convergence simulations. The fixed mesh refinement simulations use a total of 7 refinement levels as labeled in the first column. The extent of each mesh is displayed in columns 2 and 3 ($r_{\rm min}$ and $r_{\rm max}$). The grid spacings for the lowest resolution simulation are shown in the fourth column (h_r^0). Each of the final three columns (h_r^1, h_r^2 and h_r^3) give grid spacings for progressively higher resolution simulations. As an example, the $6^{\rm th}$ refinement level (Level 6) has a spatial extent of $r = (0, 64)$. For the most resolved simulation (h_r^3), the grid spacing on that level is 2^{-5}. 98

6.1 Families of initial data for the massless scalar field. The form of the initial data is scale invariant with respect to λ and we adopt $\lambda = 1$, $\rho_0 = 0$ for all simulations. We refer to family $W_{l=0}$ as monopole type initial data and family $W_{l=1}$ as dipole type. The final column gives the approximate value of the critical parameter $p^\star$ for each family. 119

6.2 Families of initial data for the Einstein-Maxwell system. The form of the initial data is scale invariant with respect to λ and we refer to family $E_{l=1}$ as the electric dipole type, $M_{l=1}$ as the magnetic dipole type and $M_{l=2}$ as the magnetic quadrupole type. $\tilde{B}^i$ is determined from A^ϕ via (6.69)–(6.71). All of our investigations adopt $\lambda = 1$ and $\rho_0 = 0$. We note that although $\tilde{E}^i$ and A^i are pure multipoles, the initial spacetime is far from flat and, in fact, the evolution is initially in the strong-field regime. 120

6.3 Families of initial data specified in [85]. Here, we have expressed the initial data in standard tensor notation, rather than in an orthonormal basis as in [85], so that p is a dimensionless strength parameter. 120

6.4 Parameters for magnetic dipole (family $M_{l=1}$) convergence tests. These simulations are well within the nonlinear regime with the critical point given by $p^\star \approx 0.377$. Similar convergence tests were performed for all families listed in Tables 6.1–6.3. . . 123

6.5 Estimated scaling exponents for axisymmetric scalar field collapse. The results summarized here agree with previous investigations to within the estimated error of our calculations. Although Δ_3 is far less precisely determined than Δ_1, it can be found in the absence of knowledge concerning a privileged inertial observer. 128

6.6 Summary of computed scaling exponents in critical collapse of the EM field for the families presented in Tables 6.2 and 6.3. The analysis of E_{quad} is presented in Section 6.5.3. Here, the two separate rows for $M_{l=2}$ and E_{quad} denote fits to the distinct behavioral regions of the quadrupole solutions; the first row is for p fairly distant from $p^\star$ while the second is for $p \to p^\star$. Results in bold indicate that the measurements were made using the world line of an accelerated observer and are unlikely to be accurate. 131

List of Figures

1.1 Coordinates (x^i) on the hypersurfaces Σ_t and Σ_{t+dt}. The shift, β^i, links the points $(t+dt, x^i - \beta^i dt)$ and $(t+dt, x^i)$ while the normal vector, n^μ, is oriented along the line linking (t, x^i) and $(t+dt, x^i - \beta^i dt)$. The proper time experienced by observers whose world line is tangent to n^μ is αdt. 5

2.1 Finite difference stencil for the first order in time, second order in space discretization of the wave equation (2.10)–(2.11). The value of the fields at the point $(n+1, j)$ is determined by the stencil shown in blue. 15

2.2 Magnitude of the eigenvalues, (2.30), for the first order in time, second order in space explicit finite difference scheme (2.10)–(2.11). Squared eigenvalues are plotted for λ and c as given in the legend. For all θ and λ, $\mu\mu^* > 1$ and the scheme is unconditionally unstable. 18

2.3 Finite difference stencil for the Crank-Nicholson discretization of the wave equation. The value of the fields at the point $(n+1, j)$ is determined by the stencil shown in blue. 19

2.4 Magnitude of the squared eigenvalues, (2.42), for the first order in time, second order in space finite difference scheme (2.10)–(2.11) with added dissipation. Eigenvalues are plotted for λ and ϵ given as in the legend. For λ, c and ϵ satisfying (2.43) and (2.44), the eigenvalues lie within the unit circle and the scheme is stable. 20

2.5 An AMR grid consisting of 4 levels (displayed in black, blue, purple and red) with a 2:1 refinement ratio. In this example, the grids would be allocated using local truncation error estimates. The grid functions on each grid are evolved separately, but the boundaries of a refinement region are set via interpolation from the coarser parent grid. When time levels are aligned, the fine grid solution is injected onto the coarse level grid as described in [24, 101, 102] 29

3.1 Asymptotic mass, M_∞, and maximum compactness, C_{max}, as a function of boson star central amplitude, $\psi(0)$, for ground state boson stars with no quartic self interaction potential (so called mini-boson stars). Stars located to the left of the first turning point are stable against small perturbation while stars located to the right are unstable [75]. Using our terminology, the set of mini-boson stars is a family consisting of a single branch, since the mass is everywhere C^1. 37

3.2 Asymptotic mass, M_∞, as a function of boson star central amplitude, $\psi(0)$, for a hypothetical family of solutions with three branches. The branches of the family are separated by vertical lines, the positions of which correspond to values of $\psi(0)$ where $dM_\infty/d\psi(0)$ is undefined. 38

3.3 Convergence of independent residuals for a solution near the limit of our code's ability to resolve solutions. This limit occurs when features are present at very large distances from the origin. Here we plot the scaled residuals of the metric function a evaluated on grids of 8192, 4096 and 2048 points using a second order finite difference scheme for the IR evaluator. With the scaling given in the figure, overlap of curves implies second order convergence. As described in the subsequent sections, the large spikes near the middle and right of the graph are caused by the presence of shells of matter far from the origin. However, even in the vicinity of these shells convergence is sufficiently precise that it is difficult to distinguish the separate scaled residuals. . 40
3.4 Radial component of the metric, $a(r)$, as a function of areal radius, r, for representative solutions from families b, d and e. Here the meaning of the global monopole's solid deficit angle is obvious: rather than approaching flat space as $r \to \infty$, we approach a space-time which is the four dimensional analog of a cone. 41
3.5 lapse, $\alpha(r)$, as a function of areal radius, r, for the same solutions plotted in Fig. 3.4. When the energy contribution of the global monopole is strong, observers at infinity see time at the centre of symmetry as flowing faster rather than slower as is the case for ordinary compact stars. 42
3.6 Global monopole field, $\phi(r)$, as a function of areal radius, r, for the previously plotted solutions. Relative to the boson star profile (Fig. 3.7), where the effect of coupling to the monopole is clear, for the majority of the parameter space the global monopole field is not significantly distorted by the presence of the boson star. In the presence of large non-minimal couplings, however, the field can become significantly distorted near the origin, which contributes to the compactness of the stars [83]. 42
3.7 Boson star field, $\psi(r)$, as a function of areal radius, r, for the previously plotted solutions. Here, we can see that the solutions from families d and e are not monotonically decreasing, instead exhibiting successive shells of matter. Excluding the central peak, the solutions from families d and e consist of seven and three shells respectively. Between shells, ψ may reach extremely small values. For these simulations, family d reached a minima far below our ability to confidently resolve the solutions before the final peak. 43
3.8 Mass function, $M(r)$, as a function of areal radius, r, for the previously plotted solutions. It can be seen from inspection that the majority of the bosonic mass is contained within the matter shells rather than near the origin. In the minimally coupled case, the mass contributions from the monopole and boson star are roughly equal and opposite, while in the non-minimal case the global monopole may contribute a positive effective mass [83, 92]. 43
3.9 Charge, $N(r)$, as a function of areal radius, r, for the previously plotted solutions. When the number of shells is relatively small and well separated, each matter shell is seen to contribute roughly the same quantity of bosonic matter. 44
3.10 Progression of boson star profile, ψ, about a critical central amplitude for family d as a function of central amplitude, $\psi(0)$. Approaching the critical central amplitude ($\psi_i^c \approx 1.255843 \cdot 10^{-4}$) from below (yellow), there are no shells far from the origin. After crossing the critical central amplitude (blue), there is a shell of bosonic matter located far from the origin. As the central amplitude is further increased (red), the asymptotic shell migrates inwards. 45

3.11 Progression of global monopole field, ϕ, about a critical central amplitude ($\psi_i^c \approx 1.255843 \cdot 10^{-4}$) for family d for the same solutions shown in Fig. 3.10. The global monopole field is not significantly affected by the presence of the asymptotic shells and exhibits no significant changes near the critical point. 46
3.12 Asymptotic mass and compactness as a function of central amplitude for family c. Unlike the other families, family c does not exhibit critical central amplitudes and consists of only a single branch. This is likely due to the size of the global monopole self interaction ($\lambda_{\rm GM} = 1.00$) which greatly reduces the length scale of the monopole (in the case of the minimally coupled monopole, the transformation $\lambda_{GM} \to \kappa^2 \lambda_{GM}, r \to r/\kappa, t \to t/\kappa$ generates a new solution from an existing one). As such, the space-time achieves its asymptotic solid angle deficit on a length scale small compared to the size of the boson star. 47
3.13 Asymptotic mass and maximum compactness as a function of central amplitude for family d. The bottom plot shows an expanded view of the top one, highlighting the structure. Note the turning point showcased in the subplot and marked with the vertical dashed line. This corresponds to a matter shell that was originally progressing inwards (as a function of boson star central amplitude), progressed to some minimal distance from the origin (corresponding to the turning point) and then reversed direction and progressed outwards. 47
3.14 Progression of mass function, $M(x)$ about a critical central amplitude ($\psi_i^c \approx 1.255843 \cdot 10^{-4}$) for solutions from family d as a function of central amplitude. Here we have plotted the same solutions shown in Fig. 3.10. As one progresses across the critical point, a new shell of matter appears far from the origin (blue dashed line) and then moves inward (red dot-dashed line). Note that the inner and asymptotic shells contain approximately the same amount of bosonic matter and that as we cross the critical central amplitude, the asymptotic mass changes discontinuously. 48
3.15 Progression of criticality function, $\delta(x)$, about a critical central amplitude ($\psi_i^c \approx 1.255843 \cdot 10^{-4}$) for solutions from family d as a function of central amplitude. As before, we have plotted the same solutions shown in Figs. 3.10 and 3.11, however we have plotted versus x to more clearly showcase the turning points of the criticality function. Note that as we cross the critical central amplitude, $\delta(x)$ never dips below 0 asymptotically. 48
3.16 Asymptotic mass as a function of central amplitude for family e. The subplot shows an expanded view of the upper plot highlighting the structure. The non-minimal global monopole coupling appears to smooth out the transitions for at least a subsection of the parameter space. However, note the discontinuity between the final and penultimate branches of the uppermost subplot, which is not an artifact of the resolution of the plot. At the critical central amplitude, the mass approaches ≈ 1.5 on the left and ≈ -1.3997 on the right. The locations of local maxima resulting from the appearance of shells at finite radius are not highlighted to avoid cluttering. . . . 49
3.17 Asymptotic mass as a function of central amplitude for family f with a minimally coupled global monopole and non-minimally coupled boson star. The subplot shows expanded views of the uppermost plot, highlighting structure which is insufficiently resolved in the first plot. Unlike Figs. 3.16 and 3.18, there is no smoothing between the solution branches. 50

3.18 Asymptotic mass as a function of central amplitude for family g. As with family e, the branches exhibit significant smoothing. Correspondingly, the smoothing behavior appears to be an effect of the non-minimal global monopole coupling rather than non-minimal boson star coupling. 50
3.19 Progression of boson star profile, ψ, about a critical central amplitude for family e as a function of central amplitude. Approaching the critical central amplitude ($\psi_i^c \approx 4.04229 \cdot 10^{-2}$) from below (yellow), there are no shells far from the origin. As the critical central amplitude is crossed (blue), a matter shell appears some finite distance from the origin. As the central amplitude is further increased (red), the shell increases in mass and begins to migrate inwards. In contrast to the behavior of the minimally coupled case (Fig. 3.10), the shells of matter appear/disappear at some finite distance from the origin. Note that when a version of this figure appeared in [107], there was an error where the y-axis was labeled "$\psi(r)\cdot r$" rather than "$\psi(r)$" corresponding to an earlier version which did not use a logarithmic scale. 51
3.20 Progression of mass function, $M(x)$, about a critical central amplitude ($\psi_i^c \approx 4.04229 \cdot 10^{-2}$) for family e as a function of central amplitude. Here we have plotted the same solutions shown in Fig. 3.19. In contrast to the apparent behavior of the minimally coupled case where the critical points can be determined by eye, in the non-minimally coupled case the shells of matter disappear at some finite distance from the origin and the asymptotic mass is continuous across the critical central amplitude. In general, when the shells of matter appear/vanish at a finite distance from the origin, the criticality function is of limited use in determining the value of the critical central amplitudes. 52
3.21 Areal radius of outermost shell (r_s) as a function of $|\psi(0) - \psi_i^c|$ for selected branches of family d. Within a given family, the areal radius of the outermost shell follows the scaling law Eqn. (3.59) with very similar exponents, $p \approx 1$. It is possible that the variations in the computed exponents, relative to $p = 1$, would disappear in the limit $r_s \to \infty$, $|\psi(0) - \psi_i^c| \to 0$, with the metric functions approaching their asymptotic values. However, our code is incapable of exploring this regime. 53
3.22 Areal radius of outermost shell (r_s) as a function of $|\psi(0) - \psi_i^c|$ for selected branches of families a, b and d. Given the variation in the parameters, the scaling exponent p is remarkably consistent across families ($p \approx 1$). As in the case of a single family (see Fig. 3.21), it is possible that these small variations would disappear in the asymptotic limit. 54
3.23 Areal radius of outermost shell (r_s) as a function of $|\psi(0) - \psi_i^c|$ for selected branches of families e and f. Here we plot the penultimate branch of family e as it is the only one which exhibits a mass gap (see Fig. 3.16). It is observed that both the minimally coupled and non-minimally coupled cases exhibit approximately the same scaling exponent, $p \approx 1$. 54

4.1 Asymptotic mass as a function of central amplitude for a hypothetical family consisting of three branches. The first branch consists of a single region while each of the subsequent branches consist of two regions, the extent of which are delimited by their mass turning points. Solid vertical lines denote the extent of branches while regions within a branch are separated with vertical dashed lines. 60

4.2 Asymptotic mass as a function of central amplitude for family d. The lower panel shows an expanded view of the upper plot highlighting the central structure. As demonstrated in [107], the apparent discontinuities are genuine. These discontinuities correspond to shells of bosonic matter of finite mass and particle number appearing or disappearing at spatial infinity. 60
4.3 Convergence of the l_2-norm of independent residuals for the trace of the Einstein field equations ($T + R = 0$) in the case of a very strongly perturbed d-star. The residuals of the higher resolution simulations are scaled by 16 and 256, respectively such that overlap of the curves implies second order convergence. This figure encompasses approximately 50 light-crossing times or 20 periods of the central boson star oscillation, $\tau_{\rm BS}$. 67
4.4 Convergence of charge conservation for strong field data where the residuals of the higher resolution simulations have been scaled such that overlap of the curves implies second order convergence. The oscillation period of the unperturbed central boson star is denoted $\tau_{\rm BS}$. 67
4.5 Convergence of mass conservation for strong field data where the residuals of the higher resolution simulations have been scaled such that overlap of the curves implies second order convergence. 68
4.6 Convergence of independent residuals for $\delta\lambda$ from family p_1 for a stable mode corresponding to $\psi(0) = 0.030$ and $\beta^2 \approx 3.21 \cdot 10^{-6}$. Here we plot the scaled residuals of the metric function evaluated on grids of 2049, 1025 and 513 points using a second order finite difference scheme for the independent residual evaluator. With the scaling given in the figure, overlap of the curves implies second order convergence. . 71
4.7 Combined asymptotic mass and maximum compactness plot for the family of mini-boson stars (minimally coupled boson stars in the absence of a global monopole). The region of stability is denoted in gray. Dashed lines show turning points of the mass. 73
4.8 Combined asymptotic mass and maximum compactness plot for family c ($\Delta^2 = 0.36$, $\lambda_G = 1.000$, $\xi_B = 0$, $\xi_G = 0$). The region of stability is denoted in gray. Dashed lines show turning points of the mass. 73
4.9 Combined asymptotic mass and maximum compactness plot for family d ($\Delta^2 = 0.81$, $\lambda_G = 0.010$, $\xi_B = 0$, $\xi_G = 0$). No region of stability is found. Dashed vertical lines show turning points of the mass while solid vertical lines denote boundaries of solution branches. Here and in the next two plots the bottom panel shows a zoomed-in view of a portion of the data in the top panel. 74
4.10 Combined asymptotic mass and maximum compactness plot for family e ($\Delta^2 = 0.25$, $\lambda_G = 0.001$, $\xi_B = 3$, $\xi_G = 3$). The region of stability is shown in gray. Dashed vertical lines show turning points of the mass while solid vertical lines denote boundaries of solution branches. 74
4.11 Combined asymptotic mass and maximum compactness plot for family f ($\Delta^2 = 0.49$, $\lambda_G = 0.010$, $\xi_B = 5$, $\xi_G = 0$). The region of stability is shown in gray. Dashed vertical lines show turning points of the mass while solid vertical lines denote boundaries of solution branches. 75
4.12 Combined asymptotic mass and maximum compactness plot for family g ($\Delta^2 = 0.09$, $\lambda_G = 0.010$, $\xi_B = 0$, $\xi_G = 5$). No region of stability is found. Dashed vertical lines show turning points of the mass while solid vertical lines denote boundaries of solution branches. 75

4.13 Combined asymptotic mass and maximum compactness plot for family h ($\Delta^2 = 0.08$, $\lambda_G = 0.10$, $\xi_B = -4$, $\xi_G = 5$). No region of stability is found. Dashed vertical lines show turning points of the mass. 76
4.14 Combined asymptotic mass and maximum compactness plot for family p_1 ($\Delta^2 = 0.09$, $\lambda_G = 0.04$, $\xi_B = 0$, $\xi_G = 0$). The region of stability is shown in gray. Dashed vertical lines show turning points of the mass while solid vertical lines denote boundaries of solution branches. 76
4.15 Combined asymptotic mass and maximum compactness plot for family p_2 ($\Delta^2 = 0.25$, $\lambda_G = 0.04$, $\xi_B = 0$, $\xi_G = 0$). The region of stability is shown in gray. Dashed vertical lines show turning points of the mass while solid vertical lines denote boundaries of solution branches. 77
4.16 Eigenvalues for the family of mini-boson stars. The modal structure shown here contrasts with behaviour presented in Figs. 4.17–4.19 for minimally coupled d-stars. Note that at each turning point of the mass (vertical black dashed lines), a stable mode transitions to unstable. Here, and in subsequent plots, eigenvalues, β^2, are shown as functions of $\sinh(\chi\beta^2)$ to better display the overall modal structure: the magnitude of β^2 varies greatly so χ is chosen on a plot-by-plot basis to more clearly show the overall behaviour of the eigenvalues. 78
4.17 Eigenvalues of family p_1 as a function of the boson star central amplitude, $\psi(0)$. Note the apparent discontinuities in the eigenvalues near branch transitions. In these regions, the eigenvalues become near-degenerate and our solutions are no longer convergent. Our observations, however, are consistent with the stable eigenvalues approaching $\beta^2 = 0$ at the branch transitions. Note also that there are an infinite number of stable modes in each region; here we have plotted only the first three. . . 79
4.18 A more detailed view of the central region of Fig. 4.17 for family p_1. Interestingly, the central branch is composed of four regions (rather than two), with the first and last corresponding to shells very far from the origin. Unfortunately, the eigenvalue degeneracy prevents us from investigating these regions in detail, but it is regardless evident that the unstable modes persist through these regions (with the potential exception of the very last region where we were unable to resolve any perturbations). 79
4.19 Eigenvalues of family p_2 as a function of the boson star central amplitude, $\psi(0)$. The additional two branch transitions have split the second branch of family p_1 into three distinct regions (see Fig. 4.17). Note that the region after the final branch transition is qualitatively very similar to that of mini-boson stars as shown in Fig. 4.16. As for family p_1, it can be seen that the central branches exhibit turning points in the mass corresponding to shells very far from the origin. 80
4.20 Expanded view of Fig. 4.19 showcasing details that were poorly resolved in the original plot. Our simulation data is consistent with the eigenvalues of the poorly resolved modes approaching 0. As for family p_1, it can be seen that the central branches exhibit turning points in the mass corresponding to shells very far from the origin. Unfortunately, the extreme length scales in these solutions, coupled with the eigenvalue degeneracy of the stable modes, prevents us from examining these regions in more detail. 80
4.21 Idealized plot of eigenvalues highlighting the underlying structure of family p_1. Here we plot stable modes in black, unstable modes in blue and modes which undergo a stability transition within a region in orange. Note in particular how in a family "close" to developing an additional branch transition, the eigenvalues "near" where the transition would develop become increasingly degenerate. 82

4.22 Idealized plot of eigenvalues in the case of a degenerate branch transition. The transitioning mode has been split into a stable and unstable branch. As before, we plot stable modes in black, unstable modes in blue and modes which undergo a stability transition within a region in orange. 83
4.23 Idealized plot of eigenvalues highlighting the underlying structure of family p_2. As Δ^2 is increased further relative to p_1, the degeneracy of Fig. 4.22 is resolved, and we gain a new branch of stable and unstable modes corresponding to the new shell of matter. 83
4.24 Mass and mode structure for family p_1. The asymptotic mass and eigenvalues measured via perturbation theory are shown in black and red as in Fig. 4.17. Eigenvalues measured directly from dynamical simulation are shown as blue diamonds. In the second branch, the blue diamonds indicating the existence of an oscillatory mode with $\beta^2 > 0$ do not correspond to any perturbative mode that we were able to identify. 84

5.1 l_2 norms of the Hamiltonian and momentum constraint violations for the GBSSN formulation. Simulations are shown for fixed resolutions (dashed lines) of 1025, 2049 and 4097 points. Results from an AMR simulation with a relative local error tolerance of 10^{-4} are shown as the solid colored lines. The AMR simulations are well within the convergent regime. 94
5.2 l_2 norms of the Hamiltonian and momentum constraint violations for the FCCZ4 formulation. Simulations are shown for fixed resolutions (dashed lines) of 1025, 2049 and 4097 points. Results from an AMR simulation with a relative local error tolerance of 10^{-4} are shown as the solid colored lines. The AMR simulations are observed to be well within the convergent regime. 95
5.3 l_2 norms of the Hamiltonian and momentum constraint violations for the RCCZ4 formulation. Simulations are shown for fixed resolutions (dashed lines) of 1025, 2049 and 4097 points. Results from an AMR simulation with a relative local error tolerance of 10^{-4} are shown as the solid colored lines. The AMR simulations are well within the convergent regime. 95
5.4 l_2 norm of the Hamiltonian constraint violation for the case of strong field initial data for each of GBSSN, FCCZ4 and RCCZ4. The difference between RCCZ4 and FCCZ4 is largely due to a more pronounced outgoing pulse of constraint violation (which leaves nearly flat space in its wake) while the large static constraint violation of GBSSN is concentrated at the origin and leaves behind a metric that does not appear to be a valid solution to the Einstein-scalar equations. 96
5.5 l_2 norm of the momentum constraint violation for the case of strong field initial data for each of GBSSN, FCCZ4 and RCCZ4. Not surprisingly, the performance of the three methods is largely equivalent as they are all designed to advect away the momentum constraint violation. 96
5.6 l_2 norm of $\bar{Z}_r = g_a(\tilde{\Lambda}^r - \tilde{\Delta}^r)/2$ for the case of strong field initial data for each of GBSSN, FCCZ4 and RCCZ4. As in the case of the Hamiltonian constraint, the GBSSN errors are concentrated at the origin where the curvature takes on its largest values. This error remains essentially static save for the mitigating factor of dissipation. At this resolution, FCCZ4 preserves the constraint about 100 times better than GBSSN while RCCZ4 improves upon this by a further factor of ~ 3 or so at late times. 97

5.7 l_2 norm of the independent residual evaluator for K_b. At late times, as the solution should be approaching flat space, RCCZ4 has better performance than either FCCZ4 or GBSSN. 97
5.8 Evolution of α and β^r from $t = 0$ to $t = 64M = 256$. The initial puncture type initial data quickly evolves towards trumpet type data with α going as r as opposed to r^2 at the puncture. 99
5.9 Evolution of X and Θ_{Hor} from $t = 0$ to $t = 64M = 256$. The initial puncture type initial data quickly evolves towards trumpet type initial data with X going as r as opposed to r^2 at the puncture. As can be seen in the graph of Θ_{Hor}, the coordinate location of the apparent horizon (where $\Theta_{\text{Hor}} = 0$) increases slowly with coordinate time. 99
5.10 l_2 norms of the Hamiltonian and momentum constraint violations for the GBSSN formulation. Each successive line denotes a factor of 2 grid refinement. The solid line denotes the most refined simulation. 100
5.11 l_2 norms of the Hamiltonian and momentum constraint violations for the FCCZ4 formulation. The errors in the momentum constraint appear to be dominated by artifacts that arise at the mesh refinement boundaries. Our GBSSN and RCCZ4 simulations used identical parameters and neither experienced the same sort of issues arising at the mesh refinement boundaries. Rather than attempting to find more optimal parameters which could resolve these issues at the cost of preventing direct comparison with GBSSN and RCCZ4, the simulation is left as-is and we note that it would almost certainly be possible to find better parameters for FCCZ4 which would mitigate these issues. 100
5.12 l_2 norms of the Hamiltonian and momentum constraint violations for the RCCZ4 formulation. Each successive line denotes a factor of 2 grid refinement. The solid line denotes the most refined simulation. 101
5.13 l_2 norms of the Hamiltonian constraint and momentum constraint violation for the $h_r = h_r^3$ run of each of the RCCZ4, FCCZ4 and GBSSN formulations. Here we can observe key differences in the constraint violating behaviours of each formulation. As the GBSSN simulation does not couple the Hamiltonian constraint to a propagating degree of freedom, errors within the horizon and at refinement boundaries are unable to propagate. Due to the fact that the black hole is not moving and the simulation quickly approaches a nearly stationary state, this lack of time dependence is advantageous. As shown in Section 5.4.1, the opposite is true when the simulation is highly dynamic. In those cases, both RCCZ4 and FCCZ4 provide orders of magnitude better constraint conservation. 101
5.14 Lapse, α, at the accumulation point as a function of $-\ln(\tau^\star - \tau)$ with $\tau^\star$ an approximate accumulation time which is different for each set of simulations. Each of GBSSN, FCCZ4 and RCCZ4 are well suited to performing the critical evolutions. The observed discrepancies in α are primarily due to our output of data with insufficient frequency to resolve the peaks adequately. As expected, we are able to resolve approximately 3 echos at a relative search tolerance of 10^{-12}. 102
5.15 Scalar field, ψ, at the accumulation point as a function of $-\ln(\tau^\star - \tau)$. The discrete self similarity (DSS) is evident. Tuning the amplitude of our initial data to the threshold of black hole formation with a relative tolerance of $\sim 10^{-12}$ allows us to resolve approximately three echos. 103

5.16 Cumulative maximal values of R, $\bar{Z}_r$, the Hamiltonian constraint and momentum constraint violations for critical collapse of the scalar field in the GBSSN formulation. For clarity, we have not shown the behaviour of the Hamiltonian constraint post-dispersal, where it is dominated by a large non propagating remnant similar to that seen in Fig. 5.1. 103
5.17 Cumulative maximal values of R, $\bar{Z}_r$, the Hamiltonian constraint and momentum constraint violations for critical collapse of the scalar field in the FCCZ4 formulation. For subcritical simulations close to criticality, the post dispersal constraint violating remnant is much smaller than that of GBSSN but is still too large to continue the simulation for long periods of time. 104
5.18 Cumulative maximal values of R, $\bar{Z}_r$, the Hamiltonian constraint and momentum constraint violations for critical collapse of the scalar field in the RCCZ4 formulation. For subcritical simulations close to criticality, the post dispersal constraint violating remnant is much smaller than that of GBSSN but is still too large to continue the simulation for long periods of time. Close to criticality, the constraint violations grow noticeably faster than either GBSSN or FCCZ4 (while still providing adequate resolution to investigate criticality). 104

6.1 Convergence of l_2 norms of Ψ_B and Hamiltonian constraint violations for strong field initial data given by Table 6.4. The plotted norms of the residuals for each run are evaluated by interpolating the results to a uniform grid which has sufficient resolution to resolve the details of the simulation. This enables us to directly compare the convergence properties at the various resolutions. Each of the dashed lines represents a successive refinement (by a factor of 2) of the initial data while the solid line represents an AMR run with a relative error tolerance of $5{\cdot}10^{-5}$. The grid parameters for the various unigrid runs are given in Table 6.4. 124
6.2 As Fig. 6.1 but for the convergence of the momentum constraints. Each of the dashed lines represents a successive refinement of the initial data while the solid line represents an AMR run with a relative error tolerance of $5 \cdot 10^{-5}$. 125
6.3 Magnitude of the 3D Ricci scalar, R, evaluated at $(0, 0)$ and the l_∞ norms of the Hamiltonian and momentum constraint violations for the AMR runs shown in Figs. 6.1 and 6.2. Post-dispersal, the solution becomes dominated by a non dispersing Hamiltonian constraint violation. Our critical search AMR simulations maintain constraint violations to about 1 part in 500 relative to the magnitude of the relevant fields throughout collapse. 125
6.4 Lapse, α, and value of the scalar field, μ, as a function of $-\ln(\tau^\star - \tau)$ at the center of collapse (in this case the origin). Here, family $W_{l=0}$ data is used and both marginally subcritical (solid line) and supercritical (dashed line) solutions with $|p^\star - p|/p^\star \approx 1 \cdot 10^{-15}$ are shown. Since the scalar field quickly approaches the critical solution with an associated strong-field scale that significantly decreases with each echo, we are able to accurately determine $\tau^\star$ to $\approx 1 \cdot 10^{-6}$. Direct measurement of Δ from μ gives $\Delta_1 = 3.43(3)$, $\Delta_2 = 3.5(4)$ and $\Delta_3 = 3.6(4)$. 127
6.5 Lapse, α, and value of the scalar field, μ, as a function of $-\ln(\tau^\star - \tau)$ at the center of collapse (in this case $z \approx 0.594$). In this case family $W_{l=1}$ data is used and the marginally subcritical (solid line) and supercritical (dashed line) solutions have been determined to an overall accuracy of $|p^\star - p|/p^\star \approx 1 \cdot 10^{-14}$. Here, $\tau^\star$ is computed to $\approx 1 \cdot 10^{-5}$. Direct measurement of Δ from μ gives $\Delta_1 = 3.44(4)$, $\Delta_2 = 3.4(3)$ and $\Delta_3 = 3.2(4)$ 127

6.6 Inverse Lyapunov exponent, γ, determined via the scaling of the energy density ρ_E. Plotted here are the maximum values of ρ_E obtained in each subcritical run as a function of $|p^\star - p|/p^\star$. The energy density has dimensions M^{-2} and therefore scales according to $|p^\star - p|^{-2\gamma}$. Superior accuracy would be obtained by fitting to the maximum value of the 4D Ricci scalar or another invariant quantity. The lines represent an averaged fit to the underlying data. 128

6.7 Inverse Lyapunov exponent, γ, determined via the scaling of the 3D Ricci scalar R. Plotted here are the maximum values of R obtained in each subcritical run as a function of $|p^\star - p|/p^\star$. The Ricci scalar density has dimensions of M^{-2} and therefore scales according to $|p^\star - p|^{-2\gamma}$. As in Fig. 6.6, the lines represent an averaged fit to the underlying data. 129

6.8 Lapse, α, and invariant scalar, $|F_{\mu\nu}F^{\mu\nu}|$, at the center of collapse for family $M_{l=1}$ as a function of $-\ln(\tau^\star - \tau)$ for marginally subcritical (solid line) and supercritical (dashed line) solutions with $|p^\star - p|/p^\star \approx 1 \cdot 10^{-13}$. Unlike the case of the scalar field, the strong-field scale of the critical solution only slowly decreases (i.e. Δ is small compared to the scalar case) and $\tau^\star$ can only be determined to a relative tolerance of about 10^{-4}. Direct measurement of Δ from $F_{\mu\nu}F^{\mu\nu}$ gives $\Delta_1 = 0.64(2)$ via statistical analysis, $\Delta_2 = 0.63(3)$ via Fourier analysis and $\Delta_3 = 0.59(6)$ from (6.80). 130

6.9 Lapse, α, and invariant scalar, $|F_{\mu\nu}F^{\mu\nu}|$, at the center of collapse for family $E_{l=1}$ as a function of $-\ln(\tau^\star - \tau)$ for marginally subcritical (solid line) and supercritical (dashed line) solutions with $|p^\star - p|/p^\star \approx 1 \cdot 10^{-9}$. As with family $M_{l=1}$, the strong-field scale of the critical solution slowly decreases and $\tau^\star$ can only be determined to a relative tolerance of about 10^{-3}. Direct measurement of Δ from $F_{\mu\nu}F^{\mu\nu}$ gives $\Delta_1 = 0.65(3)$ via statistical analysis, $\Delta_2 = 0.65(4)$ via Fourier analysis, and $\Delta_3 = 0.67(8)$ from (6.80). 131

6.10 Lapse, α, and invariant scalar, $|F_{\mu\nu}F^{\mu\nu}|$, at the center of collapse for family $M_{l=2}$ as a function of $-\ln(\tau^\star - \tau)$ with $|p^\star - p|/p^\star \approx 5 \cdot 10^{-13}$. We use the proper time of a gauge dependent accelerated observer located at $z \approx 0.440$ as our independent variable, τ, making the interpretation of length and time scales potentially problematic. It appears that the critical solution is divided into two separate regions (transition region shown in gray) with differing Δ and γ. A naive measurement of Δ under the assumption that our observer is approximately inertial gives $\Delta_1 = 0.30(2)$ and $\Delta_2 = 0.31(3)$ for the first region and $\Delta_1 = 0.56(3)$, $\Delta_2 = 0.63(6)$ for the second region. Application of (6.80) (which is valid irrespective of the status of the observer) gives $\Delta_3 = 0.19(4)$ for the first region and $\Delta_3 = 0.64(9)$ for the second The values of Δ_2 and Δ_3 measured in the second region as $p \to p^\star$ appear to be consistent with those found for families $E_{l=1}$ and $M_{l=1}$. 132

6.11 Inverse Lyapunov exponent, γ, determined via the scaling of the invariant scalar $|F_{\mu\nu}F^{\mu\nu}|$ which should scale as $|p^\star - p|^{-2\gamma}$. Plotted here are the maximum values of the invariant obtained in each subcritical run as a function of $|p^\star - p|/p^\star$. The lines shown are averaged fits of the underlying data and the quoted values of γ are the slopes of those fits. As described in the text, fits to two distinct regions of family $M_{l=2}$ have been made. 133

6.12 Minimum value of α on each spatial slice for family $E_{\rm quad}$ vs the proper time at the origin, τ_0. The data plotted here represents the subcritical simulations closest to criticality for both our investigation (solid black line) and that of Mendoza and Baumgarte [17, 85] (dashed red line). The lower plot highlights the difference in behaviour at late times. Note that we have scaled τ_0 for the data of Mendoza and Baumgarte by a factor of ≈ 1.003 to better align the early minima and maxima of α_0 with our own data. This degree of rescaling should be understood within the context of our simulations being only second order accurate and is performed to eliminate the dominant source of variation in our results far from the critical point. The simulations begin to differ markedly at $\tau \approx 18$, earlier than would be expected based on the relative precision of our searches. 134

6.13 Lapse, α, and invariant scalar, $|F_{\mu\nu}F^{\mu\nu}|$, at the center of collapse for family $E_{\rm quad}$ as a function of $-\ln(\tau^\star - \tau)$ for marginally subcritical (solid black line) and supercritical (dashed black line) solutions with $|p^\star - p|/p^\star \approx 4 \cdot 10^{-15}$. Here, the black lines show the extremal values obtained on a spatial slice while the colored lines show the values at the center of collapse as determined by the coordinate location with largest value of $|F_{\mu\nu}F^{\mu\nu}|$ in the subcritical simulation closest to criticality. 135

6.14 γ determined via the scaling of the invariant scalar $|F_{\mu\nu}F^{\mu\nu}|$ which should scale as $|p^\star - p|^{-2\gamma}$. Plotted here are the maximum values of $|F_{\mu\nu}F^{\mu\nu}|$ obtained in each subcritical run as a function of $|p^\star - p|/p^\star$. It is apparent that although both quadrupole solutions exhibit scaling with similar γ close to criticality the initial behaviour is highly family dependent. 136

A.1 Profile of the boson star profile for a solution from family b (See Table 3.1). It can be seen that the double precision shooting method ($\epsilon \approx 10^{-16}$) does not localize ω sufficiently to integrate the solution to the asymptotic regime. Here we compare the true solution (black) to the bounding solutions generated via the shooting method and observe that the integration with double precision fails before all relevant features are resolved. 148

H.1 An AMR grid consisting of 4 levels (displayed in black, blue, purple and red) with a 2:1 refinement ratio. In this example, the grids would be allocated using local truncation error estimates. The grid functions on each grid are evolved separately, but the boundaries of a refinement region are set via interpolation from the coarser parent grid. When time levels are aligned, the fine grid solution is injected onto the coarse level grid as described in [24, 101, 102] 189

H.2 The first five blending functions with $x = i/(N_{\rm b} - 1)$ where i is the number of grid points from the edge of a region and $N_{\rm b}$ is the width of the blending region. The function $b_1(x)$ is designed to smoothly interpolate between 0 and 1 over the course of $N_{\rm b}$ grid points. Each successive $b_i(x)$ is derived by requiring that an additional set of derivatives vanishes at the endpoints. E.g. the first derivatives of $b_2(x)$ vanish at $x = 0, 1$ while the first and second derivatives of $b_3(x)$ vanish at $x = 0, 1$. These polynomials are identical to those derived in [88] 193

H.3 The effect of applying the second order accurate centered first and second derivative stencils to b_0 for $N_{\rm b} = 8, 16, 32$. As resolution increases, the relative error increases dramatically going as $1/N_{\rm b}$ for first derivatives and $1/N_{\rm b}^2$ for second derivatives. This effect can cause significant numerical error to develop at grid boundaries contributing to spurious regridding. 194

H.4 The effect of applying the second order accurate centered first and second derivative stencils to b_1 for $N_{\rm b} = 8, 16, 32$. As resolution increases, $D_x b_1(x)$ converges while $D_x x b_1(x)$ diverges as $1/N_{\rm b}$. 194
H.5 The effect of applying the second order accurate centered first and second derivative stencils to b_2 for $N_{\rm b} = 8, 16, 32$. As resolution increases, both $D_x b_1(x)$ and $D_x b_2(x)$ converge. 195
H.6 l_2 norm of the error between the true solution, π, and the computed solutions, π^h, restricted to uniform grids. As AMR with $2^{\rm nd}$ or $3^{\rm rd}$ order boundary interpolation develops regridding pathologies for $\epsilon_0 = 1 \cdot 10^{-5}$, these simulations were performed using the b_2 regridding procedure to give a "best case" comparison. The smooth AMR technique seems relatively independent of blending function with the b_0 step function surprisingly outperforming both b_1 and b_2. When we examine the evolution in detail, we see that at the initial time, the b_0 simulation creates larger regridding regions thereby reducing the error. Compare with Fig. H.7 which examines the higher derivative residuals. 199
H.7 l_2 norm of the error between $\partial_{xxxx}\pi$ and $\partial_{xxxx}\pi^h$ restricted to uniform grids. Although the presence of the smoothing functions had a minor negative impact on the overall accuracy of the simulation (see Fig. H.6), here we can see its utility. When boundaries are not smoothed, regridding can lead to the formation of high frequency modes (spikes in the above graph) which may then propagate causing additional spurious regridding. In the b_2 and b_1 simulations, regridding is smooth at the level of the fourth derivative, however we see that $N_{\rm b} = 16$ is evidently insufficient to derive any improvements from b_2 over b_1. In the case of the wave equation simulation, the boundary errors in the b_0 simulation damp out and are transient. In more complex simulations with frequent regridding and many length scales, those same sorts of errors may become significant and lead to spurious regridding. 200
H.8 Second derivative, $\partial_{xx}\pi$ evaluated at $t = 6$ for AMR with blending function b_2 (represented as $\pi^h_{b_2}$) and a high accuracy unigrid simulation (represented as π). Here we have zoomed in on the region $x = [-1, 1]$, $y = [1, 3]$ to better compare with Fig. H.9 which plots the corresponding solution for AMR using second and third order boundary interpolation in time. Note that we are plotting $\mathrm{arcsinh}(\pi^{\rm h}_{\rm xx})$ rather than π^h_{xx} and that the AMR simulation appears smooth and essentially indistinguishable from the high-order unigrid solution. 201
H.9 Second derivative, $\partial_{xx}\pi$ evaluated at $t = 6$ for AMR with second order boundary interpolation (represented as $\pi^h_{o=2}$) and AMR with third order boundary interpolation (represented as $\pi^h_{o=3}$). Here we have zoomed in on the region $x = [-1, 1]$, $y = [1, 3]$ to better highlight propagating high frequency modes which can be seen as narrow striations (compare with Fig. H.8). At an error tolerance of $1 \cdot 10^{-5}$, AMR with second and third order boundary interpolation in time regrids pathologically rendering direct comparisons meaningless. As such, this simulation was performed using the regridding script of the b_2 smooth AMR run. Note that we are plotting $\mathrm{arcsinh}(\psi^{\rm h}_{\rm xx})$ rather than ψ^h_{xx} to better highlight the propagating high frequency modes. 201

H.10 Fourth derivative, $\partial_{xxxx}\pi$ evaluated at $t = 6$ for AMR with blending function b_2 (represented as $\pi^h_{b_2}$) and a high accuracy unigrid simulation (represented as π). Here we have zoomed in on the region $x = [-1, 1]$, $y = [1, 3]$ to better compare with Fig. H.11 which plots the corresponding solution for AMR using second and third order boundary interpolation in time. Note that we are plotting $\mathrm{arcsinh}(\pi^{\mathrm{h}}_{\mathrm{xxxx}})$ rather than π^h_{xxxx} and although there are clearly departures from the high accuracy unigrid solution, given the overall scale, they are fairly minimal. 202

H.11 Fourth derivative, $\partial_{xxxx}\pi$ evaluated at $t = 6$ for AMR with second order boundary interpolation (represented as $\pi^h_{o=2}$) and AMR with third order boundary interpolation (represented as $\pi^h_{o=3}$). Here we have zoomed in on the region $x = [-1, 1]$, $y = [1, 3]$ to better highlight propagating high frequency modes which can be seen to completely dominate the solution (compare with Fig. H.10). 202

Acknowledgements

This research was made possible through the support of the University of British Columbia (UBC) and the Natural Sciences and Engineering Research Council of Canada (NSERC).

Dedication

I would like to thank my family for their love and support, my primary supervisor Matthew Choptuik for his guidance and bottomless patience and my wonderful partner Hao Wang for being there for me and making it all worthwhile.

I would also like to thank my supervisory committee consisting of Jeremy Heyl, Bill Unruh, Kristin Schleich, Scott Oser and Aaron Boley. Thank you for your insight and aid throughout the years. Bill, out of every class I have ever taken in my academic career, your course on general relativity provided the most insights into the structure of reality and remains my all-time favorite.

Chapter 1

Introduction

In this introductory chapter, we provide background information as well as reference material relevant to subsequent chapters in the main body of the thesis. In Sec. 1.1, we present a concise overview of the history of general relativity (GR). Building on this foundation, Sec. 1.2 delves into a review of numerical relativity, highlighting its key successes. Sec. 1.3 introduces the conventions adopted throughout the thesis. The basis of the 3+1 decomposition of general relativity is detailed in Sec. 1.4 where we discuss the Arnowitt, Deser, and Misner (ADM) formulation of general relativity.

Section 1.5, builds upon Sec. 1.4 and further discusses the development of numerical relativity with an emphasis on hyperbolic formulations. It introduces key concepts which serve to motivate the investigations into our novel formulation of numerical relativity that is discussed in detail in Chapter 5.

In Secs. 1.6 and 1.7 we shift gears and discuss boson stars and general relativistic critical collapse respectively. These sections provide background information relevant to our investigations of boson d-stars in Chapters 3–4 and the critical collapse of the Einstein-Maxwell system in Chapter 6. Finally, in Sec. 1.8, we provide a structured outline of the entire thesis, summarizing the content and objectives of each subsequent chapter and appendix.

1.1 A Brief History of General Relativity

Albert Einstein's theory of general relativity, first proposed in 1915, dramatically transformed our understanding of gravity, replacing the Newtonian conception with a fundamentally new paradigm. In Newton's model, gravity acted instantaneously across vast distances which was at odds with the speed-of-light limit and locality posed by Einstein's earlier special theory of relativity (SR) [127, 129].

Prior to the development of GR, a significant struggle of Newtonian gravitational physics was its inability to convincingly account for some experimental observations and theoretical inconsistencies. Physicists around the turn of the 20^{th} century hypothesized a medium called the *ether*, permeating all of space to transmit light waves, akin to how waves propagate in air or water. But experiments, notably the Michelson-Morley experiment, found no evidence for such a medium [129].

The problems posed by the concepts of ether and action at a distance were largely resolved by Einstein's SR, which postulated that the laws of physics remain the same for all observers in inertial frames of reference, and that the speed of light in a vacuum is the same for all observers regardless of their relative motion or the motion of light sources. However, SR pertained only to inertial frames, leaving the question of gravity to be addressed.

Thus emerged GR, a theory that coherently incorporated gravity into a relativistic framework, offering a better understanding of the universe's observed phenomena. In stark contrast to Newtonian physics, where space and time are independent entities, GR combined these seemingly unrelated concepts into a single interconnected framework known as spacetime [127]. GR described gravity not as a force transmitted across space but as a manifestation of the curvature of four-dimensional spacetime [127]. In short, the distribution of energy and matter warps spacetime, and

this curvature, in turn, guides the trajectories of particles and light.

This understanding was notably demonstrated in explaining Mercury's perihelion precession, a subtle shift in its orbit over time [129]. Further evidence for GR came from the observation of light bending around massive objects, or gravitational lensing, which was first observed during the 1919 solar eclipse experiment, led by Arthur Eddington [129]. The observation of starlight bending around the Sun matched GR's predictions, bringing Einstein's theory into the scientific mainstream.

The confirmation of GR's predictions ushered in a paradigm shift in physics on par with the development of quantum theory. From the inexplicable precession of Mercury's orbit to gravitational time dilation, GR succeeded where Newtonian physics had fallen short. Yet GR hasn't been without its quandaries. Over the years, physicists have identified certain limitations and theoretical puzzles that GR alone cannot fully resolve.

A major challenge lies in reconciling GR with the principles of quantum mechanics, which governs the universe at the smallest scales. This incongruity gives rise to several conundrums, perhaps the most notable being the black hole information paradox [106]. Quantum mechanics upholds that information cannot be destroyed, only decohered and moved throughout a system. GR, however, predicts that information absorbed by a black hole will vanish irretrievably, creating a glaring contradiction [106].

Moreover, GR's theoretical implications, like the existence of black holes and their singularities, have provoked significant debates. For instance, the prediction of *naked singularities*, points of infinite density not obscured by an event horizon, has been a topic of intense discussion [58]. Naked singularities represent a breakdown of the known laws of physics, and their existence raises deep questions about the nature of spacetime, cosmic censorship, and the extent of our current theoretical framework's validity.

To mediate this divide, a host of theories have been proposed. String theory, for example, postulates that the most elementary constituents of the universe are not zero-dimensional point-like particles but rather one-dimensional entities: strings. Each string vibrates at a distinct frequency, which corresponds to a specific particle type, providing a framework that naturally incorporates gravity and offers a glimpse at a potential unification of GR and quantum mechanics [133]. Conversely, theories such as loop quantum gravity seek to quantize spacetime itself [114], suggesting it is constructed of discrete, interconnected loops rather than as a smooth continuum, as proposed by GR. This discrete structure could potentially harmonize the spacetime concept of GR with the inherent quantization found in quantum mechanics.

Even outside of the realm of quantum mechanics, GR faces significant challenges. Conspicuously, it does not provide a direct explanation for phenomena such as dark matter and dark energy, entities that account for approximately 95% of the mass-energy content of the universe [129]. These puzzles underscore the need for a more profound understanding of GR, including potential modifications to the theory or the development of entirely new frameworks for the gravitational interaction.

Despite its limitations, GR's legacy is undeniable. It has shaped the scientific narrative of the 20^{th} century and continues to be the dominant gravitational theory for ongoing research in cosmology, astrophysics, and high-energy physics. It is the cornerstone for our understanding of the universe's large-scale structure and dynamics, ranging from the behavior of galaxies and black holes to the evolution of the universe itself.

1.2 Numerical Relativity

In studying the Einstein equations, researchers have discovered solutions which correspond to, among other things, black holes, collapsing matter, and cosmologies. However, a purely analytic approach reaches its limits due to the inherent complexity of GR. The non-linear nature of the Einstein field equations ensures that for the vast majority of physical scenarios closed form solutions are impossible to find. It is here that numerical relativity (NR)—computer solution of the Einstein and related field equations—becomes an essential tool, effectively acting as a *numerical laboratory* for probing the rich phenomenology of our gravitational theories [5, 45, 54].

To date, one of the most important application of NR has been in its use in facilitating the understanding of black hole mergers [5, 54]. The dynamics of two black holes spiraling inward due to gravitational wave emission, culminating in a merger, is beyond the grasp of analytic solutions. With numerical simulations, however, we can precisely predict the resulting gravitational waveforms. This has been crucial for the observations made by gravitational wave detectors such as LIGO and Virgo, providing not just evidence for the existence of gravitational waves, but also offering rigorous tests for GR itself.

Simultaneously, the scope of NR extends beyond two-body dynamics. It grants insights into multi-black hole interactions, black hole formation from stellar collapse and the intricate behavior of matter and gravity at the threshold of black hole formation [5, 45, 54]. On the front of alternative gravitational theories, NR's utility is evident. While GR remains relatively unchallenged, it may not be the conclusive theory of gravity in the classical regime. Numerous alternative propositions suggest deviations from GR, especially in the strong field regime or on cosmological scales [129]. As it is easiest to probe these regimes in a numerical laboratory, NR becomes the tool of choice to derive predictions from these theories, setting the stage for observational comparisons and possibly uncovering new aspects of the gravitational interaction.

1.3 Conventions and Notation

Here, we briefly review the notational conventions used throughout this thesis. With the exceptions of Chapters 3 and 4, we adopt units where Newton's constant, G, and the speed of light, c, are set to 1. In Chapters 3 and 4 we expand upon the work of Marunovic and Murkovic [83] and make use of their notation with $c = 1$ and $G = 1/8\pi$. We adopt the spacetime metric signature commonly used in NR, $(-+++)$, and use Einstein's summation convention wherein repeated indices are summed over. Greek indices (α, β, γ, δ, ...) are used to index 4 dimensional quantities while Latin indices (i, j, k, l, ...) are used to index purely 3 dimensional tensors.

The four dimensional covariant derivative with respect to the metric, $g_{\mu\nu}$, is denoted ∇ while D denotes the covariant derivative with respect to the induced 3-metric, γ_{ij}, on spatial hypersurfaces in a 3+1 decomposition. The symbols $\widetilde{D}$ and $\mathring{D}$ are used to denote covariant differentiation with respect to a conformal metric, $\widetilde{\gamma}_{ij}$, and flat metric, $\mathring{\gamma}_{ij}$, respectively.

We use curved parentheses enclosing the indices of a tensor to denote symmetrization of those indices

$$M_{(\mu\nu)} = \frac{1}{2!}\left(M_{\mu\nu} + M_{\nu\mu}\right), \tag{1.1}$$

while square parentheses denote antisymmetrization

$$M_{[\mu\nu]} = \frac{1}{2!}\left(M_{\mu\nu} - M_{\nu\mu}\right). \tag{1.2}$$

The symbol TF is used to denote the trace-free part of a tensor:

$$M_{ij}^{\mathrm{TF}} = M_{ij} - \frac{1}{3}\gamma_{ij}M^{i}{}_{i}. \tag{1.3}$$

1.4 The ADM Decomposition

The Einstein field equations are the governing equations of GR:

$$G_{\mu\nu} = 8\pi T_{\mu\nu}. \tag{1.4}$$

Here, $T_{\mu\nu}$ is the stress-energy tensor of the matter which is coupled to the gravitational field, and the Einstein tensor, $G_{\mu\nu}$, may be expressed in terms of the Ricci tensor, $R_{\mu\nu}$, as

$$G_{\mu\nu} = R_{\mu\nu} - \frac{1}{2}g_{\mu\nu}R. \tag{1.5}$$

In four dimensions, Eqn. (1.4) constitutes a set of ten coupled second order partial differential equations (PDEs) for the metric fields, $g_{\mu\nu}$. However, in order to efficiently solve these equations, we must cast them in the form of a Cauchy problem such that we may specify some consistent initial data at an instant in time and subsequently evolve the equations forward in a unique manner.

In doing so, we perform the 3+1 decomposition of Arnowitt, Deser, and Misner (ADM) [87] following [58] and [5]. We imagine foliating four dimensional spacetime into three dimensional spacelike hypersurfaces, Σ_t, which are the level sets of some scalar function t (see Fig. 1.1). The geometry of the region of spacetime between any two nearby hypersurfaces is determined by the induced 3-metric, γ_{ij},

$$ds^2 = \gamma_{ij}dx^i dx^j, \tag{1.6}$$

the lapse, α, which measures the rate at which proper time advances for an observer moving with world line tangent to Σ_t relative to the global time,

$$d\tau = \alpha(t, x^i)dt, \tag{1.7}$$

and the shift vector, β^i, which measures the relative velocity between observers moving normal to Σ_t versus those moving along lines of constant spatial coordinates. The foliation of spacetime is non-unique and for any spacetime the lapse, α, and shift, β^i, are freely specifiable. Specification of these *gauge functions* is equivalent to the choice of coordinates, (t, x^i).

In terms of the functions, α, β^i and γ_{ij}, the 4D spacetime metric takes the form

$$ds^2 = \left(-\alpha^2 + \beta_i\beta^i\right)dt^2 + 2\beta_i dx^i dt + \gamma_{ij}dx^i, dx^j, \tag{1.8}$$

which may be represented in terms of the matrices:

$$g_{\mu\nu} = \begin{pmatrix} -\alpha^2 + \beta_k\beta^k & \beta_i \\ \beta_j & \gamma_{ij} \end{pmatrix}, \tag{1.9}$$

$$g^{\mu\nu} = \begin{pmatrix} -1/\alpha^2 & \beta^i/\alpha^2 \\ \beta^j/\alpha^2 & \gamma^{ij} - \beta^i\beta^j/\alpha^2 \end{pmatrix}. \tag{1.10}$$

Here, γ^{ij} is the inverse of γ_{ij} and $\beta_i = \gamma_{ij}\beta^j$.

The unit normal vector to the hypersurfaces, Σ_t, is denoted n^μ and is given by

$$n^\mu = \left(\frac{1}{\alpha}, -\frac{\beta^i}{\alpha}\right). \tag{1.11}$$

With it, we can define the 3-metric induced on the hypersurface Σ_t as

$$\gamma_{\mu\nu} = g_{\mu\nu} + n_\mu n_\nu, \tag{1.12}$$

the spatial components of which are given by γ_{ij} as previously described. Raising an index on this quantity, we find the projection operator, $\gamma^\mu{}_\nu$:

$$\gamma^\mu{}_\nu = \delta^\mu{}_\nu + n^\mu n_\nu, \tag{1.13}$$

which, when applied to each index of a 4D tensor, produces a purely spatial tensor defined on Σ_t. Explicitly, if $N_{\mu\nu}$ is a generic 4D tensor, then $\gamma^\mu{}_\alpha \gamma^\nu{}_\beta N_{\mu\nu}$ has no projection along the unit normal n^γ

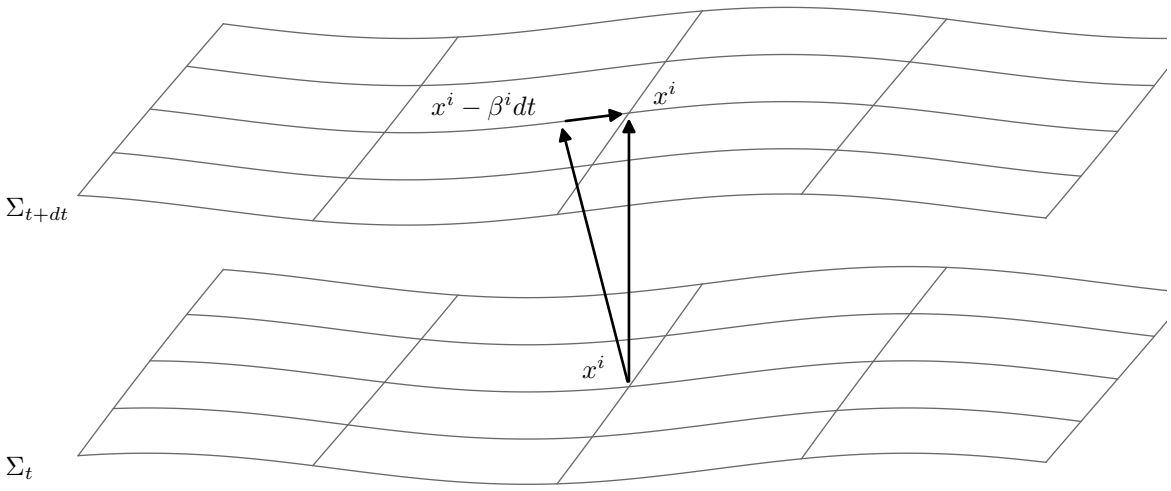

Figure 1.1: Coordinates (x^i) on the hypersurfaces Σ_t and Σ_{t+dt}. The shift, β^i, links the points $(t + dt, x^i - \beta^i dt)$ and $(t + dt, x^i)$ while the normal vector, n^μ, is oriented along the line linking (t, x^i) and $(t + dt, x^i - \beta^i dt)$. The proper time experienced by observers whose world line is tangent to n^μ is αdt.

Projecting the covariant derivative of the normal vector, $\nabla_\mu n_\nu$, onto Σ_t, we find $K_{\mu\nu}$:

$$K_{\mu\nu} = \gamma^\alpha{}_\mu \gamma^\beta{}_\nu \nabla_\alpha n_\beta. \tag{1.14}$$

This quantity is called the extrinsic curvature of the spacetime and it encodes information concerning how the hypersurfaces are embedded in the spacetime. Rewritten in terms of the Lie derivative of the spatial metric along the normal direction, we find

$$K_{\mu\nu} = -\frac{1}{2}\mathcal{L}_n \gamma_{\mu\nu}. \tag{1.15}$$

Alternatively, defining $m^\mu = \partial_t - \beta^\mu$, and noting that $K_{\mu\nu}$ is a purely spatial quantity, this expression can be rearranged to yield an evolution equation for the components of the 3-metric:

$$\mathcal{L}_m \gamma_{ij} = -2\alpha K_{ij}. \tag{1.16}$$

Now that we have an evolution equation for γ_{ij}, all that is needed to complete the 3+1 decomposition is an evolution equation for K_{ij}. This equation can be found by projecting (1.4) onto and orthogonal to the spatial hypersurfaces. Focusing on the stress-energy tensor, we define the energy density, ρ, momentum density, j^μ, and stress tensor, $S_{\mu\nu}$, as,

$$\rho = n^\mu n^\nu T_{\mu\nu}, \tag{1.17}$$

$$j^\alpha = -\gamma^{\alpha\beta} n^\delta T_{\beta\delta}, \tag{1.18}$$

$$S_{\mu\nu} = \gamma^\alpha{}_\mu \gamma^\beta{}_\nu T_{\alpha\beta}. \tag{1.19}$$

The relationship between the four dimensional Riemann tensor, $R_{\alpha\beta\gamma\delta}$, the intrinsic three dimensional Riemann tensor of the hypersurface, ${}^{(3)}R_{\alpha\beta\gamma\delta}$, and the extrinsic curvature tensor, $K_{\mu\nu}$ is found though application of the Gauss equation,

$$\gamma^\mu{}_\alpha \gamma^\nu{}_\beta \gamma^\gamma{}_\rho \gamma^\sigma{}_\delta R^\rho{}_{\sigma\mu\nu} = {}^{(3)}R^\gamma{}_{\delta\alpha\beta} + K^\gamma{}_\alpha K_{\delta\beta} - K^\gamma{}_\beta K_{\alpha\delta}, \tag{1.20}$$

Codazzi equation,

$$\gamma^\gamma{}_\rho n^\sigma \gamma^\mu{}_\alpha \gamma^\nu{}_\beta R^\rho{}_{\sigma\mu\nu} = D_\beta K^\gamma{}_\alpha - D_\alpha K^\gamma{}_\beta, \tag{1.21}$$

and Ricci equation,

$$\gamma_{\alpha\mu} n^\rho \gamma^\nu{}_\beta n^\sigma R^\mu{}_{\rho\nu\sigma} = \frac{1}{\alpha}\mathcal{L}_m K_{\alpha\beta} + \frac{1}{\alpha} D_\alpha D_\beta \alpha + K_{\alpha\mu} K^\mu{}_\beta. \tag{1.22}$$

Using these relations, and restricting to spatial indices, we arrive at the evolution equation for K_{ij}

$$\mathcal{L}_m K_{ij} = -D_i D_j \alpha + \alpha\left(R_{ij} + K K_{ij} - 2K_{ik}K^k{}_j\right) + 4\pi\alpha\left(\gamma_{ij}\left(S-\rho\right) - 2S_{ij}\right), \tag{1.23}$$

where R_{ij} is the 3D Ricci tensor on Σ_t, $K = \gamma^{ij}K_{ij}$ and $S = \gamma^{ij}S_{ij}$. In addition to the evolution equation for K_{ij}, we find the Hamiltonian and momentum constraints:

$$H = \frac{1}{2}\left(R + K^2 - K_{ij}K^{ij}\right) - 8\pi\rho = 0, \tag{1.24}$$

$$M^i = D_j K^{ij} - \gamma^{ij} D_j K - 8\pi j^i = 0. \tag{1.25}$$

These elliptic equations are constraints on γ_{ij} and K_{ij} that must hold both at the initial time and on every subsequent spacelike hypersurface. We direct interested readers to [5, 54, 87] for a much more in-depth review of the 3+1 approach.

1.5 A Brief History of BSSN-Type Formulations

The development of the ADM formalism in the 1950's and 1960's by Arnowitt, Deser, and Misner [14] gave relativists a set of tools for investigating general relativity as an initial value problem. Around the same time, other rapid advances in the theoretical understanding of general relativity were occurring. The work of Flock and Pirani on gravitational waves set the groundwork for later

numerical simulations [50, 98], while the work of Kerr, Penrose and others lead to much deeper understanding of the role that black holes and singularities played in GR [61, 67, 97].

During this time, computational methods, such as finite difference approximations (FDAs), were developed for calculating approximate solutions to ODEs and PDEs on computers (see Chapter 2). Although computers were still in an era of relative infancy, researchers began attempts to solve the ADM equations for simple matter configurations.

The 1970's brought about the realization that mergers of compact objects such as black holes and neutron stars would be primary sources of gravitational waves. This came coupled with the understanding that perturbative techniques were insufficient to fully resolve the mergers in an analytic manner; numerical simulations of binary mergers would be needed to accurately extract gravitational waveforms and permit comparisons with experiment. At the same time, the problem of setting initial conditions in GR was investigated: building on the work Choquet-Bruhat in the 1950's [51, 52], York's research in the 1970's [131] would set the stage for much of the subsequent work on the initial value problem.

Work continued steadily throughout the 1980's, but it was the 1990's that was a truly transformative decade for the field of numerical relativity. Gauges were found which would later become critical to evolving so-called puncture initial data [13], huge strides were made on the initial value formulation [33], high performance computing came to the fore, methods to find apparent horizons (enabling accurate excision of the interior of black holes) were developed, simulations of neutron star binaries were performed successfully and techniques to accurately extract gravitational waveforms were created. Despite these successes, it was becoming clear that some of the most widely used techniques were not well suited to long-term stable simulations in full 3D. The issue, as it came to be realized, was with the ADM formalism itself.

Importantly, a system of time dependent PDEs is said to be strongly hyperbolic if it admits a well-posed initial value formulation. Strong hyperbolicity implies that, for any given initial data, there exists a unique solution and that the growth rate of this solution remains bounded by an exponential function of time, independent of the initial data [5, 89, 90]. In terms of the principal symbol of the differential system (a matrix constructed from the coefficients of the highest-order derivatives which dominate in the short wavelength regime), this implies that strongly hyperbolic systems of equations have real eigenvalues and a complete set of eigenvectors [5, 89, 90]. Weakly hyperbolic systems, on the other hand, are those which have real eigenvalues but do not possess a complete set of eigenvectors. Such systems admit solutions but have issues related to illposedness when boundary conditions or constraints are enforced. In particular, numerical solutions of weakly hyperbolic systems are likely to be unstable.

The core of the issue with earlier investigations into numerical relativity was that the ADM formalism itself is not strongly hyperbolic [5]. And so, starting around the 1990's, research began into finding alternative formulations of the 3+1 decomposition which possessed the desired stability properties. Among the most popular class of NR formalisms which were created as a result were those of the Baumgarte, Shapiro, Shibata and Nakamura (BSSN) family of formulations developed quasi-empirically through the 1990's and 2000's [5, 23, 41, 120].

BSSN was partially inspired by York's conformal approach to the task of generating initial data and was originally formulated in Cartesian coordinates. Rather than evolve γ_{ij} and K_{ij} directly, BSSN introduced the dynamical quantities $\hat{\gamma}_{ij}$, χ, K and $\hat{A}_{ij}$ defined in terms of the ADM variables [5] as:

$$\chi = \frac{1}{12} \ln(\gamma), \tag{1.26}$$

$$\hat{\gamma}_{ij} = e^{-4\chi}\gamma_{ij}, \tag{1.27}$$

$$K = \gamma^{ij}K_{ij}, \tag{1.28}$$

$$\hat{A}_{ij} = e^{-4\chi}\left(K_{ij} - \frac{1}{3}\gamma_{ij}K\right). \tag{1.29}$$

Here, χ is a conformal factor which is used to factor out the overall scale dependence of the 3-metric, $\hat{\gamma}_{ij}$ is a conformal metric with unit determinant, K is the trace of the extrinsic curvature and $\hat{A}_{ij}$ is the conformal trace-free extrinsic curvature. In addition, the BSSN formulation promoted the contracted Christoffel symbols $\hat{\Gamma}^i = \hat{\Gamma}^i{}_{jk}\hat{\gamma}^{jk}$ (also known as conformal connection functions) to dynamical degrees of freedom rather than considering them as functions of $\hat{\gamma}_{ij}$ [5]. In BSSN, the Ricci tensor is decomposed into two parts as

$$R_{ij} = \hat{R}_{ij} + R^{\chi}_{ij}, \tag{1.30}$$

where $\hat{R}_{ij}$ is the Ricci tensor of the conformal metric and is calculated using the aforementioned conformal connection functions rather than entirely in terms of $\hat{\gamma}_{ij}$. After adding a multiple of the momentum constraint to the evolution equation for $\hat{\Gamma}^i$ and substituting the Hamiltonian constraint into the evolution equation for K, we are left with the standard Cartesian BSSN equations [5]:

$$\partial_t\chi = -\frac{1}{6}\left(\alpha K - \partial_m\beta^m\right) + \beta^m\partial_m\chi, \tag{1.31}$$

$$\mathcal{L}_m\hat{\gamma}_{ij} = -2\alpha\hat{A}_{ij}, \tag{1.32}$$

$$\mathcal{L}_m K = -D^2\alpha + \alpha\left(\hat{A}_{ij}\hat{A}^{ij} + \frac{1}{3}K^2\right) + 4\pi\alpha\left(\rho + S\right), \tag{1.33}$$

$$\mathcal{L}_m\hat{A}_{ij} = e^{-4\chi}\left[-D_iD_j\alpha + \alpha R_{ij} - 8\pi\alpha S_{ij}\right]^{\mathrm{TF}} + \alpha\left(K\hat{A}_{ij} - 2\hat{A}_{ik}\hat{A}^k{}_j\right), \tag{1.34}$$

$$\begin{aligned}\partial_t\hat{\Gamma}^i = {}& \hat{\gamma}^{ij}\partial_j\partial_k\beta^i + \frac{1}{3}\hat{\gamma}^{ij}\partial_j\partial_k\beta^k - 2\hat{A}^{ij}\partial_j\alpha - \alpha\left(2-\xi\right)\partial_j\hat{A}^{ij} + \alpha\xi\left(\Gamma^i{}_{jk}\hat{A}^{jk} + 6\hat{A}^{ij}\partial_j\chi\right. \\ & \left. - \frac{2}{3}\hat{\gamma}^{ij}\partial_j K - 8\pi\hat{j}^i\right) + \beta^j\partial_j\hat{\Gamma}^i - \hat{\Gamma}^j\partial_j\beta^i + \frac{2}{3}\hat{\Gamma}^i\partial_j\beta^j.\end{aligned} \tag{1.35}$$

Here, ξ is a free parameter representing the multiple of the momentum constraint that is added to the evolution equation for $\hat{\Gamma}^i$.

Together with a 1+log lapse (or related lapse choices from the Bona-Masso family [5, 30]) and Gamma driver shift conditions [5], the BSSN system would go on to be used in some of the first stable evolutions of binary black hole mergers [5, 30, 54]. It was, however, not the first evolutionary formulation to be used for this purpose. Indeed, Pretorius's 2005 work using the generalized harmonic formulation represented the first binary black hole merger simulations [103–105].

Throughout the early and mid 2000's, a number of formalisms quite similar to BSSN were created. The formulation due to Nagy Ortiz and Reula (NOR), for example, forewent the conformal and trace-free decomposition but similarly promoted the contracted Christoffel symbols to dynamical degrees of freedom [5, 9, 90]. At about the same time Bona, Ledvinka, Palenzuela and Zacek [26] developed the Z4 formulation which embedded general relativity inside a larger system given by

$$G_{\mu\nu} + 2\nabla_{(\mu}Z_{\nu)} - g_{\mu\nu}\nabla_\sigma Z^\sigma = 8\pi T_{\mu\nu}, \tag{1.36}$$

where Z^μ is a vector field that must ultimately vanish for Einstein's theory to be recovered. Using a decomposition similar to that of ADM, the Hamiltonian and momentum constraints were thereby

replaced with evolution equations for $Z_i = \gamma^\mu{}_i Z_\mu$ and $\Theta = -n^\mu Z_\mu$, resulting in the Z4 equivalent of the ADM equations [26]:

$$\mathcal{L}_m \gamma_{ij} = -2\alpha K_{ij}, \tag{1.37}$$

$$\begin{aligned}\mathcal{L}_m K_{ij} = &-D_i D_j \alpha + \alpha \left(R_{ij} + 2D_{(i} Z_{j)} - 2K_{ik} K^k{}_j + (K - 2\Theta) K_{ij} \right) \\ &+ 4\pi\alpha \left(\gamma_{ij} (S - \rho) - 2S_{ij} \right),\end{aligned} \tag{1.38}$$

$$\mathcal{L}_m \Theta = \frac{\alpha}{2} \left(R + K^2 - K_{ij} K^{ij} - 16\pi\rho - 2\Theta K + 2D_i Z^i - 2Z^i D_i \ln \alpha \right), \tag{1.39}$$

$$\mathcal{L}_m Z_i = \alpha \left(D_j K^j{}_i - D_i K - 8\pi j_i + D_i \Theta - 2Z_j K^j{}_i - \Theta D_i \ln \alpha \right). \tag{1.40}$$

Unlike the ADM equations, however, the Z4 formulation proved to be strongly hyperbolic.

In the late 2000's, the BSSN formulation was adapted into a fully covariant form by Brown [37] resulting in the GBSSN system. Subsequently Sanchis-Gual et al. developed a fully covariant and conformal version of Z4 (FCCZ4) using the GBSSN variables [116]. These formulations have proven to be extremely successful at evolving complicated and highly dynamical spacetimes in a variety of symmetries and have since seen great success in simulating black hole mergers, critical collapse and other highly dynamical systems [3, 9, 85].

During the course of their development and study, it became evident that BSSN and Z4 were fundamentally interrelated systems: the promotion of the contracted Christoffel symbols to independent degrees of freedom and subsequent addition of the momentum constraint, resulted in what was effectively an evolution equation for $\hat{\Gamma}^i + 2\hat{\gamma}^{ij} Z_j$ [5, 47, 108, 116]. As such, it is not unreasonable to consider BSSN derived formulations to be partial implementations of Z4 in which the Hamiltonian constraint is assumed to hold.

Our work in Chapter 5 as well as the derivations in Appendices C–E serve to expand upon these concepts. In particular, we demonstrate that Z4 is not a uniquely suitable embedding for GR and that it is possible to significantly generalize the formulation. This exploration is fueled both by our curiosity and by a deliberate approach to advance techniques in numerical relativity. By examining the relatively uncomplicated extension outlined in Chapter 5, we aspire to uncover insights that are crucial for developing methods with superior constraint-preserving attributes, exceeding those of BSSN or Z4 derived formulations.

1.6 Boson Stars and Topological Defects

Starting in the 1950's, John Wheeler attempted to model stable solitonic, particle-like configurations of electromagnetic fields held together via the gravitational interaction of general relativity, creating something akin to gravitational atoms [80, 128]. Although these objects, known as geons, proved to be unstable, further work by Kaup [66] and Ruffini and Bonazzola [115], lead to the discovery of the massive solitons today known as boson stars [80]. Whereas ordinary celestial bodies like stars and planets are held up against gravitational collapse by thermal, degeneracy, or mechanical pressure, boson stars are supported against gravitational collapse by the intrinsically dispersive nature of their constituent fields. Unlike their geon progenitors, studies have demonstrated that boson stars are stable to perturbations provided that the central density of the star is sufficiently small [53, 73, 73, 75, 80, 86], making them well suited to studies in numerical relativity.

Over the intervening years, boson stars and their descendants have been invoked for a large variety of processes and models including black hole mimickers [15, 83], models of neutron stars [83, 94, 96, 122, 132], binary systems [94], sources of dark matter [86, 92, 113, 118, 124] and sources of gravitational waves [86, 94]. Though boson stars are not known to exist in nature, the simplicity of

their matter model makes them a valuable tool for qualitative analysis and for providing a simple first step and test bed for more complex matter models [80, 94].

Without a self-interaction term in the potential, the mass of boson stars scale as $\frac{1}{2}m_p^2/m$ (where m_p is the Planck mass and m is the boson mass). For reasonable particle masses, this results in stars with masses far below the usual Chandrasekhar limit for fluid stars of m_p^3/m^2 [12, 46, 80]. Thus, these so-called mini-boson stars are useful primarily as a test bed with their more specialized cousins (having, for example, additional terms in the potential) being adopted as models for various astrophysical situations [80]. By adding a fourth order term to the potential, for example, one can achieve maximum masses which scale as m_p/m, permitting much larger masses and allowing boson stars to be used as crude models of neutron stars.

The interplay between pressure and gravity—which results in stable compact objects in the case of boson and fluid stars—is not the only way to generate stable structures in a gravitational context. When symmetries are broken such that various different vacuum states are connected, objects known as topological defects are created. Unlike boson stars, topological defects exhibit topological stability. In the case of global topological defects this stability is due to a global symmetry-breaking phase transition [16, 119, 126]. Examples of this type of object include textures, domain walls, strings, and the structures we are interested in, global monopoles.

Like other topological defects, monopoles are expected to form generically when underlying field symmetries are broken through early-universe phase transitions mediated by expansion and cooling [126]. In the case of the monopole, the simplest class of defect consists of a scalar field triplet with a global $O(3)$ symmetry which is spontaneously broken to $U(1)$ on a non-contractible 2-surface. If the broken symmetry is a local gauge symmetry, the resulting monopole is charged and will be shielded by a long range force (for example electromagnetism in the case of a $U(1)$ symmetry) and have finite energy and extent. Conversely, if the field exhibits a global symmetry, we find that the resulting energy is linearly divergent in radius [16, 93, 119, 126].

Although this divergence may seem somewhat problematic, there are two important caveats. First, the energy divergence cuts off upon encountering another monopole or antimonopole. Second, in the context of general relativity, the energy divergence has the simple effect of producing a solid angle deficit spacetime along with a small effective negative mass core, rather than more exotic features [16, 93, 107, 119]. As shown by Barriola et al. [16], we would expect global monopoles and anti-monopoles to annihilate extremely efficiently due to the fact that the interaction strength between them is independent of distance. As such, if they exist, we would expect the Hubble volume to contain only ≈ 1 global monopole at the present time.

Our work in Chapters 3 and 4 expands on the work of Marunovic and Murkovic [83] concerning non-minimal d-stars, composite structures consisting of a boson star and a global monopole, both of which can be non-minimally coupled to the general relativistic field. In Chapter 3 we investigate the existence of and properties of families of unusual ground state solutions while in Chapter 4 we consider the stability of these solutions via dynamical simulation and perturbation theory.

1.7 Critical Collapse in General Relativity

For almost all types of initial data in a general relativistic context, we can imagine adjusting some parameter p which controls the strength of the coupling to gravity. If we choose this parameter so that the gravitational interaction becomes stronger as p is increased, then we should expect that for p greater than some critical threshold, $p^\star$, a black hole will form. Roughly speaking, there are two possibilities: as $p \to p^\star$ from above, the mass, M, of the resulting black hole must either approach some finite value, $M \to M_0$, or it must become infinitesimal, $M \to 0$.

In the case where $M \to M_0$, we have a direct connection with first order phase transitions in statistical mechanics and these systems are said to exhibit type I critical behaviour in analogy [32, 58]. In type I critical behaviour, as $p \to p^\star$, M changes discontinuously, taking on the same role as the order parameter in a first order phase transition. As p is tuned to $p^\star$, we approach a transient critical solution which may either be stationary or periodic in time depending on the matter model under consideration. The amount of time, t_p, that the system is well approximated by the critical solution before either collapsing or dispersing to form some remnant is given by [58]

$$t_p = -\frac{1}{\lambda_0} \ln |p - p^\star| + c_t, \tag{1.41}$$

where c_t is some constant and λ_0 is the growth rate of an unstable perturbation about the critical solution. This type of critical behaviour occurs when a mass or length scale in the equations governing the system becomes dynamically relevant and it is for this reason that the mass approaches a finite value.

Conversely, systems for which $M \to 0$ in the critical limit show no preferential length scale and this form of critical behaviour is therefore limited to systems with massless or highly relativistic matter fields. In this case, there is a connection with second order (continuous) phase transitions and these systems are said to exhibit type II critical behaviour in analogy [32, 58]. Our interest in this thesis is exclusively with type II critical solutions and the rest of the discussion in this section deals only with that type.

Depending on the specific matter content of the system under consideration, the critical solution may be either continuously self similar (CSS) or discretely self similar (DSS). For a CSS spacetime in coordinates adapted to the symmetry, the metric coefficients take the form [58]:

$$g_{\mu\nu}\left(\tau, x^i\right) = e^{-2\tau} \widetilde{g}_{\mu\nu}\left(x^i\right), \tag{1.42}$$

where τ is the negative logarithm of a spacetime scale and x^i are generalized dimensionless angles about the critical point. For DSS spacetimes in adapted coordinates, we have instead [58]:

$$g_{\mu\nu}\left(\tau, x^i\right) = e^{-2\tau} \widetilde{g}_{\mu\nu}\left(\tau, x^i\right), \tag{1.43}$$

$$\widetilde{g}_{\mu\nu}\left(\tau, x^i\right) = \widetilde{g}_{\mu\nu}\left(\tau + \Delta, x^i\right), \tag{1.44}$$

where $\widetilde{g}_{\mu\nu}$ is function of τ and x^i which is periodic in τ with period Δ. Therefore, in the vicinity of $p^\star$, a DSS critical solution exhibits periodic scale invariance in length and time. In almost all cases which have been studied in spherical symmetry, the critical solutions which have been found (for both types of self-similarity) are universal, by which we mean that they do not depend on the specifics of the initial data families that are used to generate them [55, 58, 70, 81]. The echoing period, Δ, when it exists, is similarly universal.

For systems with a CSS critical solution, invariant dimensionful quantities, such as the mass of the resulting black hole in the supercritical regime, scale according to

$$\ln\left(M\right) = \gamma \ln |p - p^\star| + c_{\mathrm{M}}, \tag{1.45}$$

where γ is a universal exponent and c_M is some family-dependent constant. When the critical solution is DSS, a universal periodic function, f_M, with period Δ is superimposed on this basic power law [58]:

$$\ln\left(M\right) = \gamma \ln |p - p^\star| + f_{\mathrm{M}}\left(\gamma \ln |p - p^\star|\right) + c_{\mathrm{M}}. \tag{1.46}$$

Other dimensionful quantities scale in a corresponding manner. For example, if we were to look at the maximum energy density, $\rho_{\max}$, encountered during a given subcritical simulation (performed in coordinates adapted to the self similarity) we would have

$$\ln(\rho_{\max}) = -2\gamma \ln|p - p^\star| + f_\rho(\gamma \ln|p - p^\star|) + c_\rho, \tag{1.47}$$

where f_ρ is another universal periodic function and c_ρ is another family-dependent constant. Although type II critical solutions are generically unstable, they tend to be minimally so: they typically have a single unstable mode in perturbation theory and, in the above scaling laws, γ turns out to be the inverse of the Lyapunov exponent of this unstable mode [32, 58].

A notable consequence of studying critical collapse is the potential to achieve exceptionally large space-time curvatures outside of a black hole through purely gravitational processes. An infinite fine-tuning of the family parameter leads to the formation of a naked singularity in the critical limit [32, 58]. Such singularities, devoid of an event horizon, are of great interest in GR: they are at the core of the issue of cosmic censorship and they may provide information relevant to the study of quantum gravity.

The prototypical example of type II critical behaviour in gravitational collapse came from the work of Choptuik on the critical collapse of the scalar field in spherical symmetry [43]. Since this original research, many other models have been thoroughly investigated in the pursuit of better understanding general relativity in the strong-field regime. Going beyond spherical symmetry, among the most important studies are those of the critical collapse of vacuum gravitational waves, which could reveal information concerning the existence of naked singularities in a purely gravitational context.

The original studies of axisymmetric gravitational collapse were performed by Abrahams and Evans [1, 2] but replication (or otherwise) of their early results has proven challenging. It has only been in the past few years that work in this context has seen significant progress [68, 74]. In particular, advances in formalisms and in the choices of gauge has enabled groups to expand upon the original work. In general, investigations into the collapse of non-spherically symmetric systems have yielded far more complicated pictures than their spherically symmetric counterparts, with family-dependent scaling and splitting of the critical solution into distinct loci of collapse appearing in a number of models [1, 2, 20, 44, 58, 74, 85].

1.8 Plan of the Thesis

Chapter 2 deals with the numerical techniques relevant to the ensuing chapters. These include: finite difference approximations, stability analysis, numerical dissipation, convergence testing, independent residual evaluation, relaxation methods for elliptic PDEs, the multigrid technique, and adaptive mesh refinement. It is intended to serve only as a very brief primer or refresher for these concepts. Curious readers should look towards references such as [24, 34, 42, 77, 99, 123] for more detailed information concerning numerical methods for solving PDEs.

Our work on boson d-stars, a variation of the well studied boson star systems first investigated by Kaup [66] and Ruffini and Bonazzola [115], is presented in Chapters 3 and 4. In Chapter 3 we study the ground-state static solutions to this system and demonstrate that the solution space is much richer than previous studies had suggested. This solution space contains a number of unusual features including scaling relations analogous to phase transitions as well as unusual shells of matter in the ground state solutions.

In Chapter 4, we look at the stability of boson d-stars in spherical symmetry. This is done through a combination of dynamical simulations and perturbation theory wherein the explicit

modal structure of a number of solution families is investigated. Combining these two approaches, we attempt to achieve a more complete picture of the conditions under which boson d-stars are stable.

Chapter 5 is focused on our development and subsequent investigation of an alternative formulation of numerical relativity which we refer to as reference metric covariant conformal Z4 (RCCZ4). This formulation is similar to the fully covariant conformal Z4 (FCCZ4) of Sanchis-Gual et al. [116] but approaches the subject from a very different perspective. We demonstrate that Z4 type formulations may be given additional degrees of freedom which could potentially be used to obtain superior constraint-preserving properties. Chapter 5 introduces the formulation and presents the results of a number of tests which demonstrate that RCCZ4 performs similarly to FCCZ4 and the generalized BSSN (GBSSN) formulation of Brown [37]. Sec 5.5 expands upon this and gives an explicit proof of the fact that RCCZ4 is strongly hyperbolic in the high frequency regime.

Finally, in Chapter 6 we investigate critical phenomena in the Einstein-Maxwell system. That is, we investigate the threshold of black hole formation for the system consisting of the electromagnetic field coupled to the general relativistic gravitational field. We perform detailed numerical simulations of four families of initial data including one previously studied by Mendoza and Baumgarte [20, 85]. In contrast to the previous studies, we find evidence for universality and approximate discrete self-similarity near the threshold of black hole formation for all families of initial data.

Various appendices provide background material for the material in the main chapters of the thesis. Appendices A and B provide background for Chapters 3 and 4 while Appendices C–E provide derivations of the GBSSN, FCCZ4 and RCCZ4 formulations of general relativity relevant to Chapters 5–6. A derivation of our formulation of the Maxwell equations (relevant to Chapter 6) is given in Appendix G. Finally, Appendix H provides a detailed overview of a scheme designed to improve the performance of AMR in the vicinity of grid boundaries which turns out to be nearly identical to the treatment of AMR boundaries performed by Mongwane in [88].

Chapter 2

Overview of Numerical Methods

This chapter provides a brief overview of numerical techniques and is not intended to provide comprehensive instruction. It is intended to serve as a quick reference to those not overly familiar with numerical methods when reading the subsequent sections of this thesis. Curious readers should consult references such as [24, 34, 42, 77, 99, 123] for more detailed information concerning numerical methods for solving PDEs.

2.1 Finite Difference Approximations

At a very basic level, our task in numerical relativity is to find solutions to systems of partial differential equations (PDEs) on a computer. To that end, we turn to finite difference approximations (FDAs), a class of numerical techniques for approximately solving differential equations by replacing those equations with algebraic expressions defined at a finite number of discrete points. In doing so, we discretize the domain of the problem both in space and time (when applicable) and approximate differential operators acting upon continuous fields with algebraic difference operators acting upon discretized versions of those fields.

Consider some continuous function $f(t)$ and its value at the points $t_0 + nh_t$ where n is some integer and h_t some small timestep. We can perform a Taylor series expansions in t about the point $t = t_0$ to find

$$f(t_0 + h_t) = f(t_0) + h_t f'(t_0) + \frac{h_t^2}{2} f''(t_0) + O(h_t^3), \tag{2.1}$$

$$f(t_0 - h_t) = f(t_0) - h_t f'(t_0) + \frac{h_t^2}{2} f''(t_0) + O(h_t^3), \tag{2.2}$$

where h_t is chosen such that higher order terms in these expressions quickly become negligible and the notation $O(h_t^m)$ represents terms of order h_t^m or higher. Solving for the derivatives $f'(t_0)$ and $f''(t_0)$, we find the centred second order finite difference approximations to the first and second derivatives:

$$f'(t_0) = \frac{1}{2h_t} \left(f(t_0 + h_t) - f(t_0 - h_t) \right) + O(h_t^2), \tag{2.3}$$

$$f''(t_0) = \frac{1}{h_t^2} \left(f(t_0 + h_t) - f(t_0) + f(t_0 - h_t) \right) + O(h_t^2). \tag{2.4}$$

Consider now a simple one dimensional, non-dispersive, hyperbolic wave equation in which solutions propagate with speed c

$$\partial_{tt} u = c^2 \partial_{xx} u \,. \tag{2.5}$$

We can represent this as two coupled PDEs which are first order in time

$$\partial_t v = c^2 \partial_{xx} u, \tag{2.6}$$

$$\partial_t u = v, \tag{2.7}$$

and discretize the system on a uniform grid in x and t such that the values of x and t on the grid are given by

$$x_j = j \cdot h_x, \tag{2.8}$$
$$t^n = n \cdot h_t. \tag{2.9}$$

Here, j and n are integers which index grid positions and h_x and h_t are the grid spacings along x and t respectively. There are an infinite number of ways to discretize this equation, but we consider among the simplest: a first order in time and second order in space method where the value of the fields at the point (t^{n+1}, x_j) depends only upon the points shown in the finite difference stencil depicted in Fig. 2.1:

$$\frac{1}{h_t}\left(v_j^{n+1} - v_j^n\right) = \frac{c^2}{h_x^2}\left(u_{j-1}^n - 2u_j^n + u_{j+1}^n\right) + O(h_t, h_x^2), \tag{2.10}$$
$$\frac{1}{h_t}\left(u_j^{n+1} - u_j^n\right) = v_j^n + O(h_t). \tag{2.11}$$

Equations 2.10 and 2.11 may then be rearranged to find v_j^{n+1} and u_j^{n+1} at the advanced time:

$$v_j^{n+1} = v_j^n + \frac{c^2 h_t}{h_x^2}\left(u_{j-1}^n - 2u_j^n + u_{j+1}^n\right) + O(h_t^2, h_x^2 h_t), \tag{2.12}$$
$$u_j^{n+1} = u_j^n + h_t v_j^n + O(h_t^2). \tag{2.13}$$

We thus have an explicit evolution scheme for u_j^{n+1} and v_j^{n+1}, the values of the fields at the advanced time, in terms of the values of the fields at the current time.

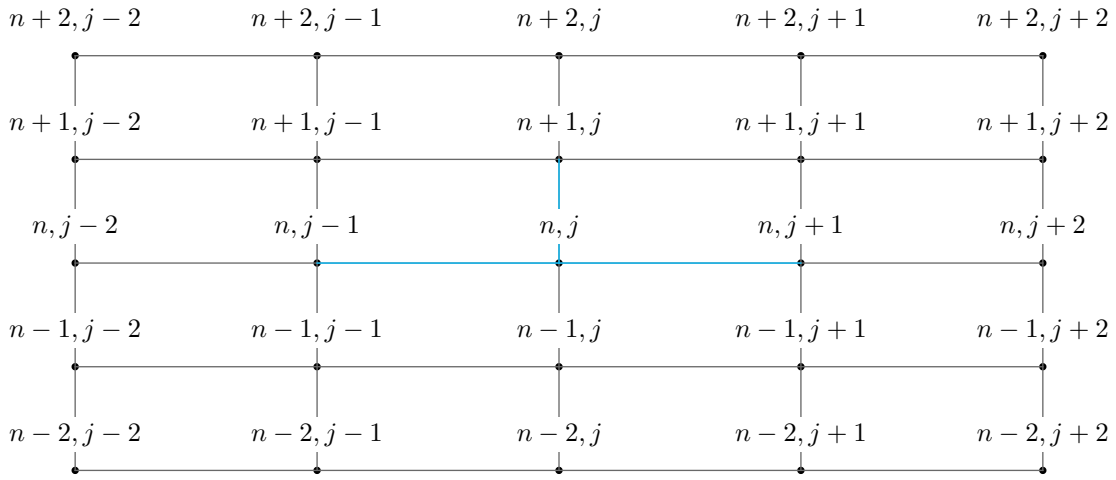

Figure 2.1: Finite difference stencil for the first order in time, second order in space discretization of the wave equation (2.10)–(2.11). The value of the fields at the point $(n+1, j)$ is determined by the stencil shown in blue.

If we wish to evolve this system for some period of time, τ, we must take $N_t = \tau/h_t$ steps and

we anticipate the cumulative error in v (denoted ϵ_v) and u (denoted ϵ_u) to scale as,

$$\epsilon_v \sim \frac{\tau}{h_t} O(h_t^2, h_x^2 h_t) \sim O(h_t, h_x^2), \tag{2.14}$$

$$\epsilon_u \sim \frac{\tau}{h_t} O(h_t^2) \sim O(h_t). \tag{2.15}$$

As such, we say that the method is first order accurate in time and second order accurate in space. If $h_t \propto h_x$, the dominant error term in these expressions scales as $O(h_t)$ and the method is considered to be first order accurate overall.

2.2 Stability of Hyperbolic Schemes

Having a method to evolve hyperbolic FDAs is an excellent start. Unfortunately, if we were to implement the explicit first order scheme for the wave equation (2.10)–(2.11), we would find it to be unstable, with smooth initial data quickly becoming swamped by high frequency modes. What is needed is some means of quantifying the stability properties of the system and determining for which values of h_t and h_x, if any, the system is stable. To this end, we look towards Von-Neumann (or Fourier) stability analysis. We note that, particularly for more complex equations than the simple example considered here, a Von Neumann analysis generally provides necessary, but not sufficient, conditions for stability.

In the case of linear PDEs, we can represent the solutions to our FDAs as a vector, $\mathbf{u}$, the entries of which are the values of the various fields on our underlying grid. At times $t = t^n$ and $t = t^{n+1}$, we will write the value of our fields as the vectors $\mathbf{u}^n$ and $\mathbf{u}^{n+1}$ respectively. In this scheme, a linear finite difference operator can be represented as a matrix, $\mathbf{G}$, and the equation for a simple two time-level scheme may be written

$$\mathbf{G}_1 \mathbf{u}^{n+1} = \mathbf{G}_0 \mathbf{u}^n, \tag{2.16}$$

or

$$\mathbf{u}^{n+1} = \mathbf{G}_1^{-1} \mathbf{G}_0 \mathbf{u}^n = \mathbf{G}\mathbf{u}^n. \tag{2.17}$$

Taking advantage of the fact that our difference operators are linear, we will consider u to be a sum of Fourier modes

$$u(x) = \frac{1}{\sqrt{2\pi}} \int_{-\infty}^{\infty} e^{ik_x \cdot x} \tilde{u}(k) dk, \tag{2.18}$$

and examine the action of our difference operators on modes of a single frequency. In doing so, we define the Fourier transformed grid function,

$$\tilde{u}(k) = \frac{1}{\sqrt{2\pi}} \int_{-\infty}^{\infty} e^{-ik_x \cdot x} u(x) dx, \tag{2.19}$$

and consider the Fourier domain equivalent of (2.17)

$$\tilde{\mathbf{u}}^{n+1} = \tilde{\mathbf{G}} \tilde{\mathbf{u}}^n, \tag{2.20}$$

where $\tilde{\mathbf{G}} = \tilde{\mathbf{G}}_1^{-1} \tilde{\mathbf{G}}_0$ is a function of $\theta = k_x h_x$. Due to the Nyquist sampling theorem, the maximum wavenumber that can be represented on a grid of spacing h_x is $k_x = \pm(2\pi)/\lambda = \pm\pi/h_x$ and we find that the domain of θ is therefore $[-\pi, \pi]$.

The stability properties of the system are then encoded in the eigenvalues of $\tilde{\mathbf{G}}$ which determine the growth rate of a given mode and which we denote $\mu(\theta)$. If the eigenvalues satisfy $\mu\mu^* \leq 1$ for all θ, then it is evident that the scheme has no growing modes and will be Von Neumann stable.

As an example, consider the action of the difference operator D^2 in the Fourier domain:

$$\begin{aligned} D^2u(x) &= u(x+h_x) - 2u(x) + u(x-h_x), \\ &= \int_{-\infty}^{\infty} \left(e^{ik_xh_x} - 2 + e^{-ik_xh_x}\right) e^{ik_x\cdot x}\tilde{u}(k_x)dk_x, \\ &= \int_{-\infty}^{\infty} \left(e^{i\theta} - 2 + e^{-i\theta}\right) e^{ik_x\cdot x}\tilde{u}(k_x)dk_x, \\ &= \int_{-\infty}^{\infty} 2(\cos(\theta)-1) e^{ik_x\cdot x}\tilde{u}(k_x)dk_x. \end{aligned} \tag{2.21}$$

We therefore find that the Fourier representation is simply

$$\tilde{D}^2 = 2(\cos(\theta) - 1). \tag{2.22}$$

Now, consider the case of our first order explicit wave equation (2.10)–(2.11) with $\mathbf{u}$ expressed as

$$\mathbf{u}^{\mathrm{T}} = \left[u_0, u_1, \cdots, u_n, v_0, v_1, \cdots, v_n\right], \tag{2.23}$$

$$\mathbf{u} = \begin{bmatrix} \vec{u} \\ \vec{v} \end{bmatrix}, \tag{2.24}$$

and with position space operators given by:

$$\mathbf{G}_1 = \begin{bmatrix} \frac{1}{h_t} & 0 \\ 0 & \frac{1}{h_t} \end{bmatrix}, \tag{2.25}$$

$$\mathbf{G}_0 = \begin{bmatrix} \frac{1}{h_t} & \frac{c^2}{h_x^2}D^2 \\ 1 & \frac{1}{h_t} \end{bmatrix}. \tag{2.26}$$

We have just shown that in the Fourier domain, $\tilde{D}^2 = 2(\cos(\theta) - 1)$, and we therefore find

$$\tilde{\mathbf{G}} = \begin{bmatrix} 1 & \frac{2c^2h_t}{h_x^2}(\cos(\theta)-1) \\ h_t & 1 \end{bmatrix}. \tag{2.27}$$

Substituting $h_t = \lambda h_x$, where λ is the Courant factor (which represents the ratio of the distance information travels in one timestep to the spatial step size),

$$\tilde{\mathbf{G}} = \begin{bmatrix} 1 & \frac{2c^2\lambda}{h_x}(\cos(\theta)-1) \\ \lambda h_x & 1 \end{bmatrix}, \tag{2.28}$$

we find the eigenvalues

$$\mu = 1 \pm c\lambda\sqrt{2\cos(\theta) - 2}, \tag{2.29}$$

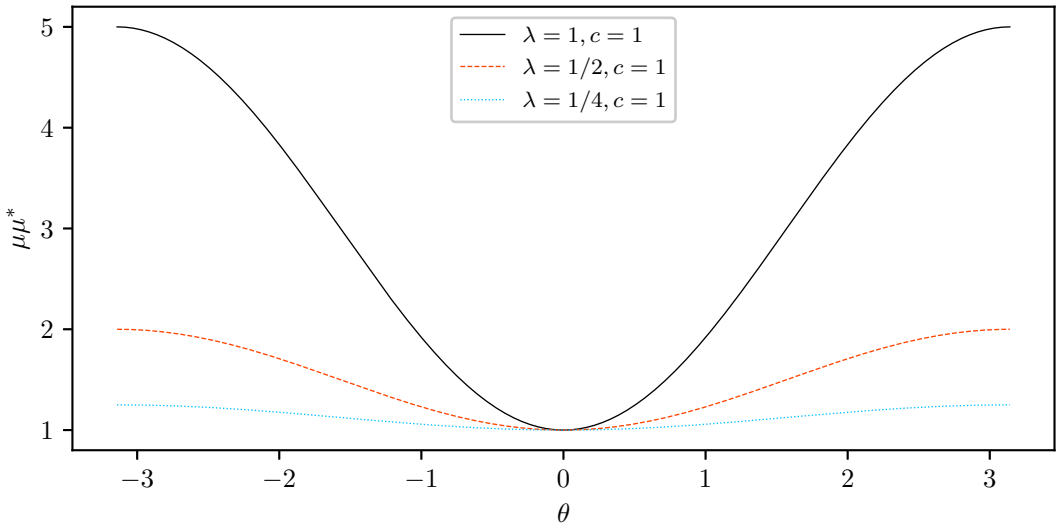

Figure 2.2: Magnitude of the eigenvalues, (2.30), for the first order in time, second order in space explicit finite difference scheme (2.10)–(2.11). Squared eigenvalues are plotted for λ and c as given in the legend. For all θ and λ, $\mu\mu^* > 1$ and the scheme is unconditionally unstable.

each with squared magnitude

$$\mu\mu^* = 1 + 2\left(1 - \cos\left(\theta\right)\right)\lambda^2 c^2. \tag{2.30}$$

Since the magnitude of these eigenvalues is always greater than 1 (see Fig. 2.2), we conclude that our explicit discretization of the wave equation is unconditionally unstable.

Working towards finding a scheme with better stability properties, we consider an alternate discretization of the wave equation known as the Crank-Nicholson method. This method is second order accurate in time and space and has the finite difference stencil shown in Fig. 2.3:

$$\frac{1}{h_t}\left(v_j^{n+1} - v_j^n\right) = \frac{c^2}{2h_x^2}\left(u_{j-1}^n - 2u_j^n + u_{j+1}^n\right) + \frac{c^2}{2h_x^2}\left(u_{j-1}^{n+1} - 2u_j^{n+1} + u_{j+1}^{n+1}\right) + O(h_t^2, h_x^2), \tag{2.31}$$

$$\frac{1}{h_t}\left(u_j^{n+1} - u_j^n\right) = \frac{1}{2}\left(v_j^{n+1} + v_j^n\right) + O(h_t^2). \tag{2.32}$$

In matrix form this becomes:

$$\mathbf{G}_1 = \begin{bmatrix} \frac{1}{h_t} & -\frac{c^2}{2h_x^2}D^2 \\ -\frac{1}{2} & \frac{1}{h_t} \end{bmatrix}, \tag{2.33}$$

$$\mathbf{G}_0 = \begin{bmatrix} \frac{1}{h_t} & \frac{c^2}{2h_x^2}D^2 \\ \frac{1}{2} & \frac{1}{h_t} \end{bmatrix}, \tag{2.34}$$

with Fourier representation

$$\tilde{\mathbf{G}} = \begin{bmatrix} \frac{-\tilde{D}^2c^2\lambda^2-4}{\tilde{D}^2c^2\lambda^2-4} & \frac{-4\lambda c^2\tilde{D}^2}{h_x\left(\tilde{D}^2c^2\lambda^2-4\right)} \\ \frac{-4\lambda h_x}{\tilde{D}^2c^2\lambda^2-4} & \frac{-\tilde{D}^2c^2\lambda^2-4}{\tilde{D}^2c^2\lambda^2-4} \end{bmatrix}, \tag{2.35}$$

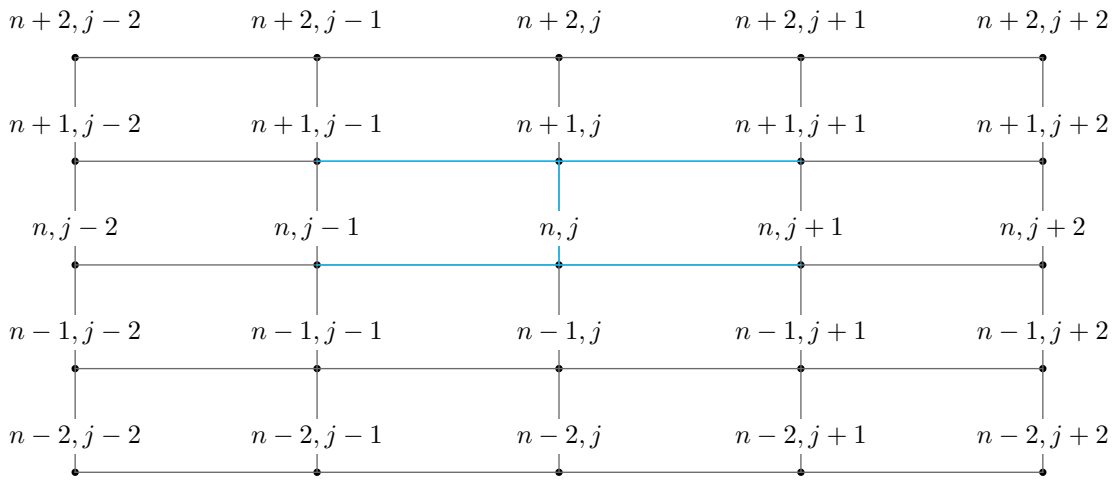

Figure 2.3: Finite difference stencil for the Crank-Nicholson discretization of the wave equation. The value of the fields at the point $(n+1, j)$ is determined by the stencil shown in blue.

and eigenvalues

$$\mu = \frac{2 - (1 - \cos(\theta))\lambda^2 c^2 \pm 2ic\lambda\sqrt{2 - 2\cos(\theta)}}{2 - (\cos(\theta) - 1)\lambda^2 c^2}, \tag{2.36}$$

each with squared magnitude

$$\mu\mu^* = 1. \tag{2.37}$$

As such, we find that the Crank-Nicolson scheme applied to the wave equation is unconditionally stable. It should be noted however that this scheme still requires $h_t \lesssim h_x$ for accuracy although it is not required for Von Neumann stability.

2.3 Dissipation

In the previously examined case of the explicit first order scheme for the wave equation, we saw that the solution was unconditionally unstable. Plotting (2.30) as in Fig. 2.2, we see that the high frequency modes (which are worst resolved on the scale of the grid) are the most highly unstable; arguably, there is little harm in attenuating these components. In fact, when treating boundaries and non-linearities, attenuating high frequency modes is frequently advantageous. We can damp these components in a manner that does not effect the convergence rate of the method by adding in higher order differencing terms multiplied by a relevant factor of the grid spacing. For the scheme (2.10)–(2.11) if we add a multiple, ϵ, of the differencing operator D^2 at the current time

$$\mathbf{G}_1 = \begin{bmatrix} \frac{1}{h_t} & 0 \\ 0 & \frac{1}{h_t} \end{bmatrix}, \tag{2.38}$$

$$\mathbf{G}_0 = \begin{bmatrix} \frac{1}{h_t} & \frac{c^2}{h_x^2} D^2 \\ 1 & \frac{1}{h_t} \end{bmatrix} + \begin{bmatrix} \epsilon \frac{D^2}{4} & 0 \\ 0 & \epsilon \frac{D^2}{4} \end{bmatrix}, \tag{2.39}$$

we find the Fourier representation,

$$\tilde{\mathbf{G}} = \begin{bmatrix} 1 + \frac{\epsilon \tilde{D}^2}{4} & \frac{\lambda c^2 \tilde{D}^2}{h_x} \\ \lambda h_x & 1 + \frac{\epsilon \tilde{D}}{4} \end{bmatrix}. \tag{2.40}$$

Analysis of $\tilde{\mathbf{G}}$ reveals that this revised version has eigenvalues

$$\mu = 1 \pm c\lambda\sqrt{2\cos(\theta) - 2} + \frac{\epsilon}{4}\left(2\cos(\theta) - 2\right), \tag{2.41}$$

each with squared magnitude

$$\mu\mu^* = -c^2\lambda^2\left(2\cos(\theta) - 2\right) + \frac{\left(2 + \epsilon\left(\cos(\theta) - 1\right)\right)^2}{4}. \tag{2.42}$$

In this case, we can see that if we enforce

$$1 - \sqrt{1 - 4c^2\lambda^2} \leq \epsilon \leq 1 + \sqrt{1 - 4c^2\lambda^2} \tag{2.43}$$

and

$$\lambda < \frac{1}{2c}, \tag{2.44}$$

the magnitudes of the highest frequency eigenvalues will be less than 1 and the scheme is therefore Von Neumann stable. This restriction on the Courant factor, λ, is known as the Courant-Friedrichs-Lewy (CFL) condition. It typically arises for explicit schemes and gives the maximum possible timestep that can be taken for a given spatial step. Fig. 2.4 shows the behaviour of the eigenvalue moduli for a few values of λ and ϵ. Note that as ϵ is made large, we start to attenuate modes which are fairly well resolved on the scale of the grid.

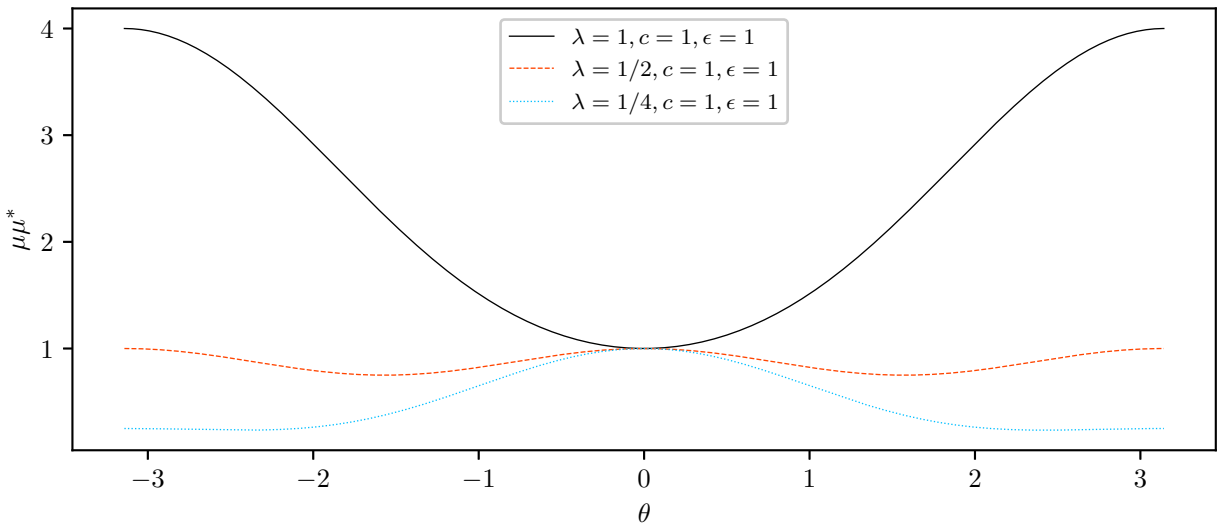

Figure 2.4: Magnitude of the squared eigenvalues, (2.42), for the first order in time, second order in space finite difference scheme (2.10)–(2.11) with added dissipation. Eigenvalues are plotted for λ and ϵ given as in the legend. For λ, c and ϵ satisfying (2.43) and (2.44), the eigenvalues lie within the unit circle and the scheme is stable.

The generalization of this technique is known as Kriess-Oliger dissipation [72] and is usually performed with 4^{th} or 6^{th} order differencing operators. The dissipation is often applied before or after the evolution step (rather than being incorporated directly as a part of the step) and can be thought of as a low pass filter which damps those high frequency modes which are not well resolved on the scale of the grid.

Performing a Von Neumann stability analysis for more complicated finite difference schemes involving non-linearities and non-constant coefficients is much more involved, requires more assumptions to be made, and is frequently impractical. It is often sufficient to analyse simple model PDEs with the chosen differencing scheme and verify that the solutions are well behaved before generalizing the scheme to more complicated systems. Once this is done, it is possible to validate the stability and accuracy of solutions through the use of convergence tests and independent residual evaluators as discussed in the next sections.

2.4 Convergence Testing

Once we have developed a stable means of solving our initial value problem, it is *crucial* to ensure that our solutions are converging at the expected rate. Issues which prevent this convergence may take the form of simple mistakes when converting symbolic expressions to FDAs (this sort of error can be mitigated in part through the use of tools like RNPL [130] and FD [3] which help automate the construction of FDAs), but they may also represent genuine problems with the finite difference schemes being used.

Consider a partial differential equation,

$$\mathbf{D}(u) - f = 0, \tag{2.45}$$

with f some source functions and $\mathbf{D}$ some potentially non-linear differential operator which acts upon the fields u. We derive an FDA operating on a grid of uniform spacing h_t, h_x, h_y, $\cdots$ with all spacings satisfying $h_i \sim h$:

$$\mathbf{D}^h(u^h) - f^h = 0, \tag{2.46}$$

and apply this FDA to the continuum solution, u, to find the truncation error, τ^h:

$$\tau^h = \mathbf{D}^h(u) - f^h. \tag{2.47}$$

In what follows, we broadly follow [42] and consider the simple advection equation

$$\partial_t u - \partial_x u = 0, \tag{2.48}$$

and the FDA:

$$\mathbf{D}^h_x(u^n_j) = \frac{1}{2h_x}\left(u^n_{j+1} - u^n_{j-1}\right), \tag{2.49}$$

$$\mathbf{D}^h_t(u^n_j) = \frac{1}{2h_t}\left(u^{n+1}_j - u^{n-1}_j\right), \tag{2.50}$$

$$\mathbf{D}^h(u^h) = \mathbf{D}^h_t(u^h) - \mathbf{D}^h_x(u^h). \tag{2.51}$$

Expressed in terms of the continuum differential operators, we therefore have:

$$\mathbf{D}^h_x = \partial_x + \frac{1}{6}h_x^2\partial_{xxx} + O(h_x^4), \tag{2.52}$$

$$\mathbf{D}^h_t = \partial_t + \frac{1}{6}h_t^2\partial_{ttt} + O(h_t^4), \tag{2.53}$$

and (2.47) may be written in terms of (2.51) as

$$\begin{aligned}\tau^h &= \mathbf{D}^h(u) - f^h, \\ &= \mathbf{D}_t^h(u) - \mathbf{D}_x^h(u), \\ &= \left(\partial_t + \frac{1}{6}h_t^2\partial_{ttt} + O(h_t^4)\right)u - \left(\partial_x + \frac{1}{6}h_x^2\partial_{xxx} + O(h_x^4)\right)u, \\ &= (\partial_t u - \partial_x u) + \frac{h_x^2}{6}\left(\lambda^2\partial_{ttt}u - \partial_{xxx}u\right) + O(h_x^4), \\ &= \frac{h^2}{6}\left(\lambda^2\partial_{ttt}u - \partial_{xxx}u\right) + O(h^4),\end{aligned} \tag{2.54}$$

where we have substituted $h_t = \lambda h_x = h$. According to the Richardson ansatz [112], the solution to *any* FDA which uses a uniform mesh structure (with scale parameter h) will have the expansion

$$u^h = u + h\epsilon_1 + h^2\epsilon_2 + h^3\epsilon_3 + \cdots \tag{2.55}$$

where the functions ϵ_i are (continuum) error functions which are independent of h. Substituting (2.55) into (2.51) we find:

$$\begin{aligned}\mathbf{D}^h(u^h) &= \mathbf{D}_t^h(u^h) - \mathbf{D}_x^h(u^h), \\ &= (\partial_t - \partial_x)\left(u + h\epsilon_1 + h^2\epsilon_2 + \cdots\right) + \frac{h^2}{6}\left(\lambda^2\partial_{ttt} - \partial_{xxx}\right)\left(u + h\epsilon_1 + h^2\epsilon_2 + \cdots\right) + O(h^4).\end{aligned} \tag{2.56}$$

Demanding that these terms vanish order by order in h, we find (to order h^2) the equations:

$$(\partial_t - \partial_x)\, u = 0, \tag{2.57}$$

$$h\,(\partial_t - \partial_x)\,\epsilon_1 = 0, \tag{2.58}$$

$$h^2\,(\partial_t - \partial_x)\,\epsilon_2 = -\frac{h^2}{6}\left(\lambda^2\partial_{ttt} - \partial_{xxx}\right)u. \tag{2.59}$$

Here, (2.57), is simply a statement of the consistency of the difference approximation; that as $h \to 0$, we approach the continuum solution. More interesting are the expressions (2.58) and (2.59) for the truncation error terms of order $O(h)$ and $O(h^2)$ respectively. At order $O(h)$, we find that the solution to ϵ_1 is simply:

$$\epsilon_1(t, x) = \epsilon_1(t_0, x + (t - t_0)), \tag{2.60}$$

where $\epsilon_1(t_0, x)$ is the value of ϵ_1 at the initial time. We find therefore that if $\epsilon_1(t_0, x) = 0$ (i.e. we initialize the FDA with the exact solution so that $u^h(t_0, x) = u(t_0, x)$), it remains 0 throughout the evolution and we therefore have no error term of order h. At order $O(h^2)$, if $u = u(t + x)$ and $\epsilon_2(t_0, x) = 0$, we have

$$\epsilon_2(t, x) = -\frac{t\left(\lambda^2 - 1\right)u'''(t + x)}{6}, \tag{2.61}$$

and we find that the error grows linearly in time. The key observation then, is that, for an arbitrary PDE (including nonlinear ones, and systems), if we have have an FDA operating on a uniform grid which has accuracy $O(h^p)$ its solution will have a Richardson expansion of the form

$$u^h = u + h^p\epsilon_p + h^{p+1}\epsilon_{p+1} + \cdots \tag{2.62}$$

where the quantities ϵ_i are smooth functions *independent of* h which represent the degree to which u^h differs from u. Computing u^{2h} and u^{4h}, we find

$$u^{2h} = u + (2h)^p \epsilon_n + (2h)^{p+1} \epsilon_{p+1} + \cdots , \tag{2.63}$$

$$u^{4h} = u + (4h)^p \epsilon_n + (4h)^{p+1} \epsilon_{p+1} + \cdots , \tag{2.64}$$

and if we take the differences

$$u^{4h} - u^{2h} = \left((4h)^p - (2h)^p\right) \epsilon_p + \cdots , \tag{2.65}$$

$$u^{2h} - u^{h} = \left((2h)^p - (h)^p\right) \epsilon_p + \cdots , \tag{2.66}$$

we can find the convergence factor, $Q(t)$:

$$Q(t) = \frac{||u^{4h} - u^{2h}||_x}{||u^{2h} - u^h||_x} \approx \frac{||(4h)^p - (2h)^p||_x}{||(2h)^p - (h)^p||_x}, \tag{2.67}$$

where $||\cdot||_x$ is some suitable discrete spatial norm (such as the l_2 norm) evaluated at grid points common to all solutions. In the convergent limit where $h \to 0$, we find

$$\lim_{h \to 0} Q(t) = 2^p. \tag{2.68}$$

Therefore, if h is sufficiently small and our solutions are in the convergent regime, we can verify the order of our FDA by calculating $Q(t)$ for a sequence of solutions of mesh spacing h, $2h$, $4h$, etc. This sort of test serves also to determine what grid spacing is required for accuracy and how long a solution can be trusted: if a solution leaves the convergent regime after some period of time, τ, we should be extremely skeptical of any results extracted from times $t > \tau$.

2.5 Independent Residual Convergence Tests

Once we have established that our numerical procedure is converging, it is important to ensure that it is converging to the continuum solution. To do so, all of our codes employ the sort of independent residual (IR) convergence tests described below.

With reference to (2.46), we can derive an alternative finite difference approximation to our continuum expression. Denoting this alternative FDA by $\tilde{\mathbf{D}}^h$, we assume the following expansions for $\tilde{\mathbf{D}}^h$ and $\mathbf{D}^h$:

$$\mathbf{D}^h = \mathbf{D} + h^p \mathbf{D}_p + \cdots , \tag{2.69}$$

$$\tilde{\mathbf{D}}^h = \mathbf{D} + h^m \tilde{\mathbf{D}}_m + \cdots , \tag{2.70}$$

Let u^h be the solution to $\mathbf{D}^h(u^h) - f^h = 0$ with Richardson expansion given by

$$u^h = u + h^p \epsilon_p + h^{p+1} \epsilon_{p+1} + \cdots . \tag{2.71}$$

We can apply $\tilde{\mathbf{D}}^h$ to u^h to find:

$$\begin{aligned} \tilde{\mathbf{D}}^h(u^h) &= \left(\mathbf{D} + h^m \tilde{\mathbf{D}}_m + \cdots\right) \left(u + h^p \epsilon_p + h^{p+1} \epsilon_{p+1} + \cdots\right), \\ &= \mathbf{D} \left(u + h^p \epsilon_p + \cdots\right) + h^m \tilde{\mathbf{D}}_m \left(u + h^p \epsilon_p + \cdots\right) + \cdots . \end{aligned} \tag{2.72}$$

Now, provided that $\mathbf{D}$ and $\tilde{\mathbf{D}}_m$ are linear (if they are not, we can simply perform a series expansion about $h = 0$), this may be written:

$$\begin{aligned}\tilde{\mathbf{D}}^h(u^h) &= \mathbf{D}(u) + h^p\mathbf{D}(\epsilon_p) + h^m\tilde{\mathbf{D}}_m(u) + \cdots, \\ &= \mathbf{D}(u) + O(h^{\min(p,m)}),\end{aligned} \tag{2.73}$$

and we therefore find the following relationship between our two FDAs:

$$\begin{aligned}\tilde{\mathbf{D}}^h(u^h) - \mathbf{D}^h(u^h) &= \mathbf{D}(u) - \mathbf{D}^h(u^h) + O(h^{\min(p,m)}), \\ &= \mathbf{D}(u) - f^h + O(h^{\min(p,m)}), \\ &= O(h^{\min(p,m)}).\end{aligned} \tag{2.74}$$

Making use of this relation, we see that the action of $\tilde{\mathbf{D}}^h$ when applied to u^h yields a residual given by

$$\tilde{\epsilon}^h = \tilde{\mathbf{D}}^h(u^h) - f^h \propto O\left(h^{\min(m,p)}\right). \tag{2.75}$$

If we calculate the convergence factor for this residual then, provided that both $\mathbf{D}^h$ and $\tilde{\mathbf{D}}^h$ are properly implemented, we should find $Q(t) = \min(2^p, 2^m)$. Typically, an error in the implementation of $\mathbf{D}^h$ or $\tilde{\mathbf{D}}^h$ will result in the independent residual being $O(1)$, but this is not always the case.

As a concrete example, consider the case where $\mathbf{D}^h$ is intended to have accuracy $O(h^4)$ but an error is made in the derivation such that it is instead $O(h^1)$ (this sort of error happens relatively frequently when a mistake is made implementing explicit integration schemes). If we correctly derive $\tilde{\mathbf{D}}^h$, such that it is order $O(h^6)$, upon computing the convergence factor for $\tilde{\epsilon}^h$, we would expect to find $\min(2^4, 2^6) = 16$. Instead we would find $\min(2^1, 2^6) = 2$ and would know that an error had been made in deriving either $\mathbf{D}^h$ or $\tilde{\mathbf{D}}^h$.

There is, of course, the issue that we could make similar sorts of mistakes when deriving $\tilde{\mathbf{D}}^h$ and $\mathbf{D}^h$ such that the errors precisely canceled each other out. It is for this reason that it is best to use different schemes implemented using different stencils completely independently from one another. Unfortunately, independent residual convergence tests do not help in the slightest if the equations we have derived are themselves incorrect. It is for this reason that in addition to convergence testing and independent residual convergence testing, it best practice to:

- Derive equations via provably correct symbolic algebra from manifestly correct field equations.
- Generate IRs via symbolic algebra from provably correct equations.
- Monitor the preservation of any constraints.
- Verify that conserved quantities, if they exist, are preserved to the anticipated level of accuracy.
- Perform convergence testing based on analytic solutions for the system under consideration provided that such solutions exist.

2.6 Elliptic Equations

Although the work presented in Chapters 5–6 is based on hyperbolic formulations of general relativity (see Sec. 1.5 and Appendices C–E), we must, in general, solve elliptic PDEs at the initial time to find initial data which satisfies the Hamiltonian and momentum constraints. Despite only being calculated for a single time-slice, these solutions are sufficiently computationally intensive that it can be well worth optimizing them.

While hyperbolic PDEs may be formulated as initial boundary value problems, elliptic PDEs are boundary value problems. This means that the solution at any given point depends on the boundary conditions and the bulk coupling across the entire domain, implying a global nature to the solutions.

Due to this global property, changes at the boundaries or in the coupled (generally time dependent) fields in the bulk, produce instantaneous changes in the solution across the entire domain. For this reason, evolutionary-type schemes, in which we attempt to solve an elliptic PDE by marching in some direction fail; the solution must be computed globally (exceptions exist in the case of shooting methods, see Appendix A).

Also largely due to this global property, many numerical techniques for solving FDAs of elliptic PDEs are inefficient, with solution time scaling considerably worse than $O(N)$ where N is the number of grid points. Contrast this with hyperbolic FDAs for which, due to the local nature of the solutions, we can generally compute a solution for any given time slice in $O(N)$ operations.

2.7 Relaxation Methods for Elliptic PDEs

If we have some elliptic differential equation,

$$\mathbf{D}(u) - f = 0, \tag{2.76}$$

with $\mathbf{D}$ some elliptic differential operator, u a vector of fields and f a vector of source functions, we can formulate an FDA

$$\mathbf{D}^h(u^h) - f^h = 0, \tag{2.77}$$

and define the residual

$$\tilde{r}^h = \mathbf{D}^h(\tilde{u}^h) - f^h = \mathbf{F}^h(\tilde{u}^h), \tag{2.78}$$

where $\tilde{u}^h$ is an approximation of u^h. In the case that $\mathbf{D}^h$ is a linear operator, we can in principle solve for u^h directly. In most situations however, $\mathbf{D}^h$ is a sparse banded matrix and solving it directly is both inefficient and inaccurate: for a 2D Laplace equation on a grid of size (N_x, N_y), for example, a naive implementation of $\mathbf{D}^h$ has $N_x^2 N_y^2$ entries making direct calculation difficult and prone to serious roundoff errors.

Instead of solving (2.77) in a single step, we aim to gradually drive the residual (2.78) to 0. In what follows, we denote the value of $\tilde{u}^h$ and $\tilde{r}^h$ at the n^{th} iteration on the i^{th} grid point as $\tilde{u}_i^{(n)}$ and $\tilde{r}_i^{(n)}$ respectively. Note that we are not restricting to a one dimensional grid, i simply represents some position in a grid of arbitrary dimension. Appealing to Newton's method, we find an improved approximation, $\tilde{u}^{(n+1)}$:

$$\tilde{u}_i^{(n+1)} = \tilde{u}_i^{(n+1)} - \tilde{r}_i^{(n+1)} \left[\frac{\partial \left[\mathbf{F}^h(u^h)\right]_i}{\partial u_i^h} \Big|_{u_i = \tilde{u}_i^{(n)}} \right]^{-1}. \tag{2.79}$$

If these updates to $\tilde{u}^h$ are applied immediately such that the calculations make use of previously updated points within a single pass (e.g. the calculation of $\tilde{u}_{i+1}^{(n+1)}$ makes use of $\tilde{u}_i^{(n+1)}$), the technique is known as the Gauss-Seidel method. If, on the other hand, the values for $\tilde{u}^{(n+1)}$ are computed entirely terms of $\tilde{u}^{(n)}$, we have the Jacobi method.

Although simple, solvers based on the Jacobi or Gauss-Siedel methods are very inefficient and for a d dimensional grid of N total grid points scale as $O(N^{(d+2)/d})$.

2.8 Multigrid for Elliptic PDEs

The elliptic solvers previously described have the extremely unfavorable property of scaling super-linearly with the number of grid points. As such, it can be fairly cheap to compute a low resolution solution, but higher resolution solutions may require a large amount of compute time. We could, however, imagine speeding the solution process up by first computing a low resolution solution and then using that as an initial guess for a higher resolution solution. We could repeat this process, scaling from a level 0 grid ($l = 0$) all the way to a level m grid ($l = m$) with factor of 2 refinements at each level.

This process does indeed speed convergence, but it is not optimal. However, using a process known as multigrid [34], we can solve elliptic FDAs efficiently in $O(N)$ time. For the remainder of this section we provide an overview of the multigrid method, following the derivation in [42] relatively closely.

Consider our solution, u^h, as a function of a current estimate, $\tilde{u}^h$, and some correction, v^h:

$$u^h = \tilde{u}^h + v^h. \tag{2.80}$$

With this substitution, our FDA may be written as

$$\mathbf{D}^h(u^h) = \mathbf{D}^h(\tilde{u}^h + v^h) = f^h, \tag{2.81}$$

and it is evident that the residual, $\tilde{r}^h$, is given by

$$\tilde{r}^h = \mathbf{D}^h(\tilde{u}^h) - \mathbf{D}^h(\tilde{u}^h + v^h). \tag{2.82}$$

If $\tilde{r}^h$ is not smooth, we rely on the fact that standard relaxation techniques (such as the Gauss-Seidel method) are very efficient smoothers and perform a few relaxation sweeps until $\tilde{r}^h$ is smooth. If $\tilde{r}^h$ is smooth, we may sensibly pose a coarse grid version of (2.82)

$$\mathbf{D}^{2h}(\mathbf{I}_h^{2h}\tilde{u}^h + \mathbf{I}_h^{2h}v^h) - \mathbf{D}^{2h}(\mathbf{I}_h^{2h}\tilde{u}^h) = -\mathbf{I}_h^{2h}\tilde{r}^h, \tag{2.83}$$

where $\mathbf{I}_h^{2h}$ is a restriction operator which takes values from a fine grid with spacing h to a coarse grid with spacing $2h$. If we take $u^{2h} = \mathbf{I}_h^{2h}\tilde{u}^h + \mathbf{I}_h^{2h}v^h$, this may be rewritten as an equation for u^{2h} on the coarse grid:

$$\mathbf{D}^{2h}(u^{2h}) = \mathbf{D}^{2h}(\mathbf{I}_h^{2h}\tilde{u}^h) - \mathbf{I}_h^{2h}\tilde{r}^h. \tag{2.84}$$

Upon solving this expression, we can update $\tilde{u}^h$ as

$$\tilde{u}^h \to \tilde{u}^h + \mathbf{I}_{2h}^h(u^{2h} - \mathbf{I}_h^{2h}\tilde{u}^h), \tag{2.85}$$

where $\mathbf{I}_{2h}^h$ is a prolongation operator from the coarse grid to the fine grid and $\mathbf{I}_{2h}^h\mathbf{I}_h^{2h}$ will not, in general, be the identity operator.

Now consider the quantity τ^h defined as the truncation error for the continuum solution u,

$$\tau^h = \mathbf{D}^h(u) - f^h, \tag{2.86}$$

which is equivalent to

$$\tau^h = \mathbf{D}^h(u) - \mathbf{D}^h(u^h). \tag{2.87}$$

We cannot compute τ^h exactly, but we can consider, by analogy, a quantity τ_h^{2h}

$$\tau_h^{2h} = \mathbf{D}^{2h}(\mathbf{I}_h^{2h}u^h) - \mathbf{I}_h^{2h}\mathbf{D}^h(u^h) \tag{2.88}$$

which is called the relative local truncation error. We can rewrite this last expression as

$$\mathbf{D}^{2h}(\mathbf{I}_h^{2h}u^h) = \mathbf{I}_h^{2h}\mathbf{D}^h(u^h) + \tau_h^{2h}, \tag{2.89}$$

and if we identify $\mathbf{I}_h^{2h}u^h$ with the coarse grid unknown, u^{2h}, and use $\mathbf{D}^h(u^h) = f^h$, this becomes

$$\mathbf{D}^{2h}(u^{2h}) = f^{2h} + \tau_h^{2h}. \tag{2.90}$$

As such, τ_h^{2h} may be thought of as a correction term to the coarse grid equations which makes the solution of the coarse grid equations coincide with the fine grid solution. Even though we cannot compute τ_h^{2h} explicitly, given an approximate solution to the fine grid equations, $\tilde{u}^h$, we can define an approximation to τ_h^{2h}:

$$\tilde{\tau}_h^{2h} = \mathbf{D}^{2h}(\mathbf{I}_h^{2h}\tilde{u}^h) - \mathbf{I}_h^{2h}\mathbf{D}^h(\tilde{u}^h). \tag{2.91}$$

Substituting this for τ_h^{2h} in (2.90), we find

$$\begin{aligned} \mathbf{D}^{2h}(u^{2h}) &= f^{2h} + \tau^{2h}, \\ &= f^{2h} + \mathbf{D}^{2h}(\mathbf{I}_h^{2h}\tilde{u}^h) - \mathbf{I}_h^{2h}\mathbf{D}^h(\tilde{u}^h), \\ &= \mathbf{D}^{2h}(\mathbf{I}_h^{2h}\tilde{u}^h) - \mathbf{I}_h^{2h}\left(\mathbf{D}^h(\tilde{u}^h) - f^h\right), \\ &= \mathbf{D}^{2h}(\mathbf{I}_h^{2h}\tilde{u}^h) - \mathbf{I}_h^{2h}\tilde{r}^h, \end{aligned} \tag{2.92}$$

which is precisely (2.84), the equation for computing u^{2h} for use with the coarse-grid correction process. The multigrid method thus consists of the steps depicted in Algorithm 1. In practice, the method efficiently solves many elliptic PDEs. It is common for each fine-to-coarse-to-fine cycle (a so-called V-cycle) to result in approximately an order of magnitude reduction in error. Further details can be found in [34].

Algorithm 1 V-cycle

set $m = l$
while $m \neq 0$ **do**
    apply smoothing relaxations to u^m
    compute $\tilde{u}^{m-1}$, f^{m-1} and $\tilde{\tau}_m^{m-1}$ on the next finest grid
    set $m = m - 1$
end while
solve coarse grid problem to find u^0
while $m \neq l$ **do**
    set $m = m + 1$
    apply coarse grid correction to u^m
    apply smoothing relaxations to u^m
end while

2.9 Adaptive Mesh Refinement

Up until this point we have considered only grids with uniform mesh spacing across the entirety of the computational domain. When solving hyperbolic partial differential equations on such grids, inefficiencies arise if the solution spans a broad range of relevant length scales. To capture fine details, we require high resolution, while smoother regions can be adequately represented with much coarser grids. Given that the computational demand scales roughly linearly with the grid point count, a uniformly high-resolution grid becomes computationally burdensome. We could consider the use of non-uniform grids as a remedy, however a significant drawback emerges: due to the CFL condition (Sec. 2.2–2.3), the entire grid must evolve with a time step constrained by the smallest grid spacing, leading to computational inefficiencies.

These issues are circumvented by the adaptive mesh refinement (AMR) technique. In this approach, the computational domain is represented as a dynamic hierarchy of meshes, with each level of the hierarchy having increasing resolution and its own distinct time step. As we evolve our numerical simulations, refined meshes are strategically introduced where necessary and subsequently discarded when the additional resolution is no longer needed. This dynamic adaptation ensures both computational efficiency and, importantly, solution accuracy where it is most crucial.

The Berger-Oliger approach to AMR, introduced in the 1980's [24] is one of the pioneering, and still most prevalent, approaches to adaptive mesh refinement. At the heart of this method is the idea of using a hierarchy of nested uniform grids to allocate additional resolution (which may be contrasted with other, grid free, approaches to achieve adaptive resolution). In the Berger-Oliger scheme, the computational domain is initially covered by a coarse grid and as the simulation progresses and additional resolution is required, child grids are introduced in regions of interest as depicted in Fig. 2.5.

The location of these child grids is typically determined based on features of the solution being computed. These features may be identified through the calculation of gradients, thresholds in one or more diagnostic quantities or, as in our simulations, estimates of local truncation error. (Sec 2.4) When new child grids are created at any level, initial data is determined by transfer of values from regions which overlap extant grids at that level, as well as by interpolation from the parent grid, as necessary.

In order to ensure accuracy, fine grids are typically evolved using smaller time steps than the coarse grids and the boundaries of the fine grids are set using interpolation from the coarser parent grids. Conversely, when parent and child time levels are aligned, the values computed on the child

grid are passed back to the parent grid using a restriction operation. For hyperbolic PDEs, the temporal and spatial refinement factors are typically set equal.

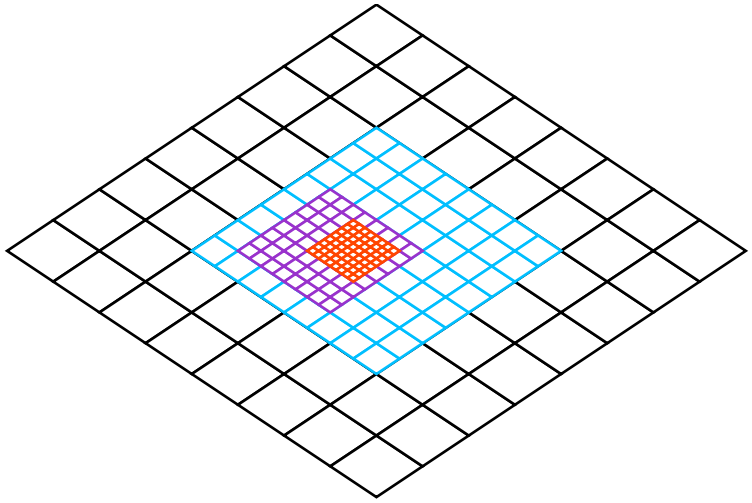

Figure 2.5: An AMR grid consisting of 4 levels (displayed in black, blue, purple and red) with a 2:1 refinement ratio. In this example, the grids would be allocated using local truncation error estimates. The grid functions on each grid are evolved separately, but the boundaries of a refinement region are set via interpolation from the coarser parent grid. When time levels are aligned, the fine grid solution is injected onto the coarse level grid as described in [24, 101, 102]

Our codes employ the variant of the Berger-Oliger AMR technique as implemented in PAMR [102] and AMRD [101]. Additional information concerning the Berger-Oliger AMR technique can be found in [24, 101, 102]. Aspects of this are expanded upon in Appendix H which gives an overview and derivation of our improved smooth AMR technique.

Chapter 3

Non-Minimally Coupled Topological-Defect Boson Stars: Static Solutions

This chapter closely follows work completed in our 2016 paper, Non-Minimally Coupled Topological-Defect Boson Stars: Static Solutions [107]. In it, we consider spherically symmetric static composite structures consisting of a boson star and a global monopole, minimally or non-minimally coupled to the general relativistic gravitational field. In the non-minimally coupled case, Marunovic and Murkovic [83] have shown that these objects, so-called boson d-stars, can be sufficiently gravitationally compact so as to potentially mimic black holes. Here, we present the results of an extensive numerical parameter space survey which reveals additional new and unexpected phenomenology in the model. In particular, focusing on families of boson d-stars which are parameterized by the central amplitude of the boson field, we find configurations for both the minimally and non-minimally coupled cases that contain one or more shells of bosonic matter located far from the origin. In parameter space, each shell spontaneously appears as one tunes through some critical central amplitude of the boson field. In some cases the shells apparently materialize at spatial infinity: in these instances their areal radii are observed to obey a universal scaling law in the vicinity of the critical amplitude. We derive this law from the equations of motion and the asymptotic behavior of the fields.

3.1 Introduction

The first attempts to construct solitonic solutions in the context of general relativity were made by John Wheeler in 1955 [128] with his investigation of massless scalar fields minimally coupled to gravity. Although the field configurations he discovered were found to be unstable, subsequent developments by Kaup [66] and Ruffini & Bonazzola [115] lead to the discovery of the stable solitons now known as boson stars.

In its simplest form, a boson star is a self-gravitating configuration of a complex massive scalar field, Ψ, governed by the Lagrangian

$$S_{\mathrm{BS}} = \int dx^4 \sqrt{-g} \left[-\frac{1}{2} \left(\nabla_\mu \Psi^* \right) \left(\nabla^\mu \Psi \right) - \frac{m^2}{2} \Psi \Psi^* \right], \tag{3.1}$$

with a spherically symmetric, time-harmonic ansatz for the scalar field

$$\Psi(\mathbf{x}) = \psi(r) e^{i\omega t}. \tag{3.2}$$

Here, the radial amplitude function $\psi(r)$ is real valued, m is the scalar field's mass parameter, and ω is the angular frequency eigenvalue of the boson star. The boson stars comprise a one-parameter family that can be conveniently labelled by the central value, $\psi(0)$, of the amplitude function.

Stability studies have shown that boson stars are stable against all perturbations if the central amplitude of the star is sufficiently small [75, 86], yet, without self-interaction, boson stars have maximum masses far below the Chandrasekhar limit for normal fermionic matter. Correspondingly, these so-called mini-boson stars are unsuitable for use as simplified models of gravitationally compact astrophysical objects such as white dwarfs and neutron stars. When a quartic self interaction potential is added, it is found that for reasonable scalar boson masses, the maximum gravitational mass is comparable to the Chandrasekhar limit [46].

Motivated by their simplicity and stability, boson stars have been studied extensively as dark matter candidates [48, 113, 124], simplified models for compact objects such as neutron stars [80, 94, 96] and alternatives to black holes [15, 83, 122, 132]. Additionally, they have been considered in models where they are non-minimally coupled to gravity [83, 125] and in conformal and scalar-tensor extensions to gravity [35]. For overviews of boson stars and results pertaining to them, we refer the reader to the reviews by Liebling & Palenzuela [80] and Schunck & Mielke [117].

In this paper we investigate the boson d-star (topological-defect star) system, previously studied by Xin-zhou Li [78, 79] and Marunovic & Murkovic [83], which consists of a boson star and global monopole non-minimally coupled to gravity via the Ricci scalar. Unlike boson stars, which may be considered gravitationally bound clumps of Klein-Gordon matter, global monopoles are topological defects formed via spontaneous symmetry breaking and can exist in the absence of gravity [126]. The simplest realization of such a global monopole is through a scalar field theory consisting of a triplet of scalar fields with a global $\mathcal{O}(3)$ symmetry which is spontaneously broken to $\mathcal{U}(1)$ [16]. These simple global monopoles may be constructed by starting from the Lagrangian

$$S_{\mathrm{GM}} = \int dx^4 \sqrt{-g} \left[-\frac{\Delta^2}{2} \left(\nabla_\mu \phi^a\right) \left(\nabla^\mu \phi^a\right) - \frac{\lambda_{\mathrm{GM}}}{4} \Delta^4 \left(\phi^a \phi^a - 1\right)^2 \right], \tag{3.3}$$

where $\phi^a, a = 1, 2, 3$ denotes a triplet of real scalar fields and the parameters Δ and λ_{GM} set the scale for the interaction potential. Examining the interaction potential, it can be seen that the potential energy of the configuration is minimized at $\phi^a \phi^a = \sum_i \phi^i \phi^i = 1$ and that the action is invariant under a global $\mathcal{O}(3)$ symmetry within the inner space of the fields.

Assuming the field transitions to a directionally dependent vacuum state as $r \to \infty$, where r is the areal radius, one takes the hedgehog ansatz for the fields,

$$\phi^a = \phi(r) \frac{x^a}{r}, \tag{3.4}$$

and finds global monopole solutions by solving a second order boundary value equation for $\phi(r)$ [16].

Analysis of these solutions reveals that the energy density of the configuration goes as r^{-2} so that the total energy of the solutions is linearly divergent in r [16]. When minimally coupled to gravity, the linearly divergent global monopole energy produces an effect analogous to a solid angle deficit and a negative central mass described by the following asymptotic metric [16, 119]:

$$ds^2 = -\nu dt^2 + \nu^{-1} dr^2 + r^2 d\theta^2 + r^2 \sin^2(\theta) d\phi^2, \tag{3.5}$$

where

$$\nu = \left(1 - \Delta^2 - \frac{2M}{r}\right). \tag{3.6}$$

Here Δ^2 is the solid angle deficit, where Δ is the parameter appearing in the Lagrangian (3.3).

In terms of astrophysical motivation, global monopoles at first appear to be attractive models of galactic dark matter halos. The fact that the energy density of the solutions varies as r^{-2}

seems to be precisely what is called for from observations of galactic rotation curves. Moreover, with reasonable assumptions, the mass of the solution within the neighborhood of a typical 10^{11} solar-mass host galaxy [91] is about ten times that of the luminous matter.

However, closer inspection reveals that the negative effective mass of minimally coupled global monopoles produces repulsive gravitational effects and they correspondingly do not support bound orbits [60, 91]. Additionally, due to the fact that the monopole does not couple directly to any matter sources, the scale of the solutions is essentially independent of the galactic matter content, which is in conflict with the observation that, for a wide range of masses, galaxies consist of about ten times as much dark matter as luminous matter [91]. Finally, Vilkin and Shellard [126] have shown that global monopoles and anti-monopoles annihilate very efficiently due to their long range interaction, indicating that there would have to be a large overabundance of global monopoles in relation to anti-monopoles for them to be remotely realistic candidates for galactic dark matter.

Although these problems are substantial, Nucamendi, Salgado & Sudarsky, demonstrated that they may be partially ameliorated by non-minimally coupling the monopole field to gravity [91, 92]. With this modification, global monopoles exhibit attractive gravity and the non-minimal coupling permits coupling to other matter sources more directly. More recently, Marunovic & Murkovic studied non-minimally coupled boson d-stars[1] and demonstrated that these objects can be far more compact than minimally coupled boson stars and nearly as compact as maximally compact fluid stars [83]. This observation then invites the question of whether boson d-stars are viable as black hole mimickers. Although the gravitational compactness of these objects is interesting, it is not the focus of our investigation. Rather, in this paper we extend the work of [83], finding new numerical solutions to the spherically symmetric boson d-star model in both the minimally coupled and non-minimally coupled cases. Unlike boson stars, whose asymptotic mass is a smooth function of the boson star central amplitude, the families we have discovered exhibit a series of discrete boson star central amplitudes, across which the asymptotic mass of the configuration changes non-smoothly, and sometimes discontinuously, due to the appearance of shells of bosonic matter far from the origin. As this is superficially analogous to a first order phase transition in statistical mechanics, we borrow terminology from that field and refer to these transitional solutions as critical solutions corresponding to a critical central amplitude, ψ_i^c. Here the superscript c on ψ_i^c denotes "critical", while the subscript i serves as an integer label of the shells, ordered by central amplitude of the boson field.

We demonstrate that the areal radii of these asymptotic shells, r_s, appear to obey a universal scaling law $r_s \propto |\psi(0) - \psi_i^c|^{-p}$, with $p \approx 1$ independent of the interaction potentials. To our knowledge, neither the shell-like configurations themselves, nor the scaling behavior of their radial locations has been previously reported.

The plan of the remainder of this chapter is as follows: in Section 3.2 we derive the governing equations for the static system consisting of a boson star and global monopole, non-minimally coupled to gravity. In Section 3.3 we describe the methodology adopted to find static solutions and introduce terminology used to present the results of the study. Specifically, Section 3.3.1 introduces terminology used to describe the unusual features of our solutions, Section 3.3.2 describes our solution procedure and outlines the numerical techniques employed, while Section 3.3.3 demonstrates the convergence of the solutions.

In Section 3.4 we present the results and analysis of our parameter space survey. The behavior of the minimally coupled solutions is described in Section 3.4.1 while the corresponding behavior of the non-minimally coupled solutions is presented in Section 3.4.2. Section 3.4.3 describes the scaling

[1] Minimal boson d-stars had been previously studied by Xin-zhou Li [78, 79] but using an interaction potential which ensured the radii of the monopole and boson star were effectively equal.

behavior observed in the vicinity of the critical central amplitudes while Section 3.4.4 presents a derivation of the observed scaling law. We make some brief concluding remarks in Section 3.5.

Finally, in the appendices, we present a brief review of the shooting method (Appendix A) and provide a description of our modified shooting technique which, for certain models, permits integration to arbitrary distances (Appendix A.3).

3.2 Static Equations

Starting from a dimensionless Einstein-Hilbert action ($c = 1, G = 1/8\pi$) and following the prescription of Marunovic & Murkovic [83],

$$S_{\rm EH} = \int dx^4\sqrt{-g}\left(\frac{R}{2} + \mathcal{L}_{\rm m}\right), \tag{3.7}$$

the actions for the boson star and global monopole are

$$S_{\rm BS} = \int dx^4\sqrt{-g}\left[-\frac{1}{2}\left(\nabla_u\Psi^*\right)\left(\nabla^u\Psi\right) - V_{\rm BS} + \frac{\xi_{\rm BS}}{2}R\left(\Psi^*\Psi\right)\right], \tag{3.8}$$

and

$$S_{\rm GM} = \int dx^4\sqrt{-g}\left[-\frac{\Delta^2}{2}\left(\nabla_u\phi^a\right)\left(\nabla^u\phi^a\right) - V_{\rm GM} + \frac{\xi_{\rm GM}}{2}R\Delta^2\left(\phi^a\phi^a\right)\right], \tag{3.9}$$

respectively.

Here Ψ is the complex scalar field of the bosonic matter, ϕ^a is a triplet of scalar fields, Δ is the solid angle deficit parameter, $V_{\rm BS}$ and $V_{\rm GM}$ are the self interaction potentials for the boson field and monopole fields respectively, R is the Ricci scalar, and $\xi_{\rm BS}$ and $\xi_{\rm GM}$ are the non-minimal coupling constants.

The stress-energy tensors associated with these actions are,

$$\begin{aligned} T^{\rm BS}_{\mu\nu} = {} & \frac{1}{2}\left(\nabla_\mu\Psi^*\right)\left(\nabla_\nu\Psi\right) + \frac{1}{2}\left(\nabla_\nu\Psi^*\right)\left(\nabla_\mu\Psi\right) - \frac{1}{2}g_{\mu\nu}\left(\left(\nabla_\alpha\Psi\right)\left(\nabla^\alpha\Psi^*\right) + 2V_{\rm BS}\right) \\ & - \xi_{\rm BS}\left(G_{\mu\nu} + g_{\mu\nu}\nabla_\alpha\nabla^\alpha - \nabla_\mu\nabla_\nu\right)\left(\Psi\Psi^*\right), \end{aligned} \tag{3.10}$$

$$\begin{aligned} T^{\rm GM}_{\mu\nu} = {} & \frac{\Delta^2}{2}\left(\nabla_\mu\phi^a\right)\left(\nabla_\nu\phi^a\right) + \frac{\Delta^2}{2}\left(\nabla_\nu\phi^a\right)\left(\nabla_\mu\phi^a\right) - \frac{1}{2}g_{\mu\nu}\left(\Delta^2\left(\nabla_\alpha\phi^a\right)\left(\nabla^\alpha\phi^a\right) + 2V_{\rm GM}\right) \\ & - \xi_{\rm GM}\Delta^2\left(G_{\mu\nu} + g_{\mu\nu}\nabla_\alpha\nabla^\alpha - \nabla_\mu\nabla_\nu\right)\left(\phi^a\phi^a\right). \end{aligned} \tag{3.11}$$

Here $G_{\mu\nu}$ is the Einstein tensor and we have used the result that the variation of an arbitrary function of the Ricci scalar, $f(R)$, is

$$\frac{\delta f(R)}{\delta g^{\mu\nu}} = \frac{\partial f(R)}{\partial R}R_{\mu\nu} - \frac{1}{2}f(R)g_{\mu\nu} + \left(g_{\mu\nu}\nabla_\alpha\nabla^\alpha - \nabla_\mu\nabla_\nu\right)\frac{\partial f(R)}{\partial R}. \tag{3.12}$$

We take quartic potentials for the fields [83],

$$V_{\rm GM} = \frac{\lambda_{\rm GM}}{4}\Delta^4(\phi^a\phi^a - 1)^2, \tag{3.13}$$

$$V_{\rm BS} = \frac{m^2}{2}\left(\Psi^*\Psi\right) + \frac{\lambda_{\rm BS}}{4}\left(\Psi^*\Psi\right)^2, \tag{3.14}$$

$$\tag{3.15}$$

where $\lambda_{\rm GM}$ and $\lambda_{\rm BS}$ are additional parameters. We now impose spherical symmetry and time independence of the geometry, and work in polar-areal (Schwarzschild-like) coordinates, (t, r, θ, ϕ), in which the line element takes the form

$$ds^2 = -\alpha(r)^2 dt^2 + a(r)^2 dr^2 + r^2 d\Omega^2, \tag{3.16}$$

where $d\Omega^2$ is the line-element of the unit two sphere.

Taking the hedgehog ansatz for the monopole, $\phi^a = \phi(r)x^a/r$, and assuming harmonic time dependence for the boson star, $\Psi = \psi(r)e^{i\omega t}$, the total potential, V, defined by

$$V \equiv V_{\rm GM} + V_{\rm BS}, \tag{3.17}$$

becomes

$$V = \frac{\lambda_{\rm GM}}{4}\Delta^4(\phi^2-1)^2 + \frac{m^2}{2}\psi^2 + \frac{\lambda_{\rm BS}}{4}\psi^4. \tag{3.18}$$

We then derive the following equations for the stationary field configurations by varying the actions with respect to the matter fields, ψ and ϕ:

$$\partial_r^2\psi = \left(\xi_{\rm BS}\psi T - \frac{\psi\omega^2}{\alpha^2} + \partial_\psi V\right)a^2 - \frac{2\partial_r\psi}{r} - \frac{(\partial_r\alpha)(\partial_r\psi)}{\alpha} + \frac{(\partial_r a)(\partial_r\psi)}{a}, \tag{3.19}$$

$$\partial_r^2\phi = \left(\xi_{\rm GM}\phi T + \frac{2\phi}{r^2} + \frac{\partial_\phi V}{\Delta^2}\right)a^2 - \frac{2\partial_r\phi}{r} - \frac{(\partial_r\alpha)(\partial_r\phi)}{\alpha} + \frac{(\partial_r a)(\partial_r\phi)}{a}. \tag{3.20}$$

Here $T = -R = T^\mu_\mu$ is the trace of the stress energy tensor and $\partial_\psi V$ and $\partial_\phi V$ are given by

$$\partial_\psi V = m^2\psi + \lambda_{\rm BS}\psi^3, \tag{3.21}$$

$$\partial_\phi V = \lambda_{\rm GM}\Delta^4\left(\phi^2-1\right)\phi. \tag{3.22}$$

Equations for the metric components follow directly from the Einstein equations. After rearranging, we have:

$$\begin{aligned}\partial_r\alpha = \frac{-1}{4\left(r+\zeta r^2\left(\xi_{\rm BS}\psi\left(\partial_r\psi\right)+\xi_{\rm GM}\Delta^2\phi\left(\partial_r\phi\right)\right)\right)}\Bigg[\Bigg[\Bigg(\left(2\Delta^2\phi^2+2Vr^2\right)\alpha - r^2\psi^2\frac{\omega^2}{\alpha^2}\alpha\Bigg)a^2 \\ + \left(-r^2\left(\partial_r\psi\right)^2 + 8\xi_{\rm BS}\psi\left(\partial_r\psi\right)r - r^2\Delta^2\left(\partial_r\phi\right) \quad + 8\xi_{\rm GM}\Delta^2\phi\left(\partial_r\phi\right)r\right)\alpha\Bigg]\zeta \\ - 2\alpha a^2 + 2\alpha\Bigg],\end{aligned} \tag{3.23}$$

$$\begin{aligned}\partial_r a = \Bigg[\Bigg(\Bigg(\xi_{\rm GM}^2\Delta^2\phi^2 T + \xi_{\rm BS}^2\psi^2 T + \frac{1}{2}V + \frac{\omega^2}{\alpha^2}\psi^2 \quad \left(\frac{1}{4}-\xi_{\rm BS}\right)\Bigg)a^3 + \Bigg(\frac{\Delta^2}{4}\left(\partial_r\phi\right)^2 \\ + \xi_{\rm GM}\Delta^2\left(\partial_r\phi\right)^2 + +\frac{1}{4}\left(\partial_r\psi\right)^2 + \xi_{\rm BS}\left(\partial_r\psi\right)^2 - \frac{\xi_{\rm BS}\psi\left(\partial_r\alpha\right)\left(\partial_r\psi\right)}{\alpha} \\ - \frac{\xi_{\rm GM}\Delta^2\phi\left(\partial_r\alpha\right)\left(\partial_r\phi\right)}{\alpha}\Bigg)a\Bigg)r + \frac{\left(\Delta^2\phi^2+4\xi_{\rm GM}\Delta^2\phi^2\right)a^3}{2r}\Bigg]\zeta + \frac{a-a^3}{2r} \\ + a^3 r\zeta\left(\xi_{\rm GM}\phi\partial_\phi V + \xi_{\rm BS}\psi\partial_\psi V\right),\end{aligned} \tag{3.24}$$

where

$$T = \frac{-\zeta}{a^2 r^2 \left(1 + 6\zeta\xi_{\rm BS}^2\psi^2 + 6\zeta\xi_{\rm GM}^2\Delta^2\phi^2\right)} \Big[\Delta^2 \left(2\phi^2 \ +12\xi_{\rm GM}\phi^2\right) a^2 + \Delta^2 \left((\partial_r\phi)^2 r^2 + 6\xi_{\rm GM} r^2 (\partial_r\phi)^2\right) + \left(-6\xi_{\rm BS} r^2\psi^2\frac{\omega^2}{\alpha^2} + 4Vr^2 - \psi^2 r^2\frac{\omega^2}{\alpha^2}\right) a^2 + \left(r^2 (\partial_r\psi)^2 + 6\xi_{\rm BS} r^2 (\partial_r\psi)^2\right)\Big] - \frac{6\zeta\xi_{\rm GM}\phi\partial_\phi V + 6\zeta\xi_{\rm BS}\psi\partial_\psi V}{1 + 6\zeta\xi_{\rm BS}^2\psi^2 + 6\zeta\xi_{\rm GM}^2\Delta^2\phi^2}, \tag{3.25}$$

and we have defined ζ as,

$$\zeta \equiv \frac{1}{1 + \xi_{\rm BS}\psi^2 + \xi_{\rm GM}\Delta^2\phi^2}\,. \tag{3.26}$$

Note that if we have functions a, α, ψ, ϕ and eigenvalue ω which satisfy Eqns. (3.19–3.24), then $\omega \to \tau\omega$, $\alpha \to \tau\alpha$, $a \to a$, $\psi \to \psi$, $\phi \to \phi$, where $\tau \in \mathbb{R}^+$, yields another, physically identical solution, corresponding to a rescaling of the polar time coordinate, t.

In the much simpler minimally coupled case, Eqns. (3.19–3.24) reduce to:

$$\partial_r^2\psi = \left(-\frac{\psi\omega^2}{\alpha^2} + \partial_\psi V\right) a^2 - \frac{2\partial_r\psi}{r} - \frac{(\partial_r\alpha)(\partial_r\psi)}{\alpha} + \frac{(\partial_r a)(\partial_r\psi)}{a}, \tag{3.27}$$

$$\partial_r^2\phi = \left(\frac{2\phi}{r^2} + \frac{\partial_\phi V}{\Delta^2}\right) a^2 - \frac{2\partial_r\phi}{r} - \frac{(\partial_r\alpha)(\partial_r\phi)}{\alpha} + \frac{(\partial_r a)(\partial_r\phi)}{a}, \tag{3.28}$$

$$\partial_r\alpha = \left(\left(-\frac{V\alpha}{2} + \frac{1}{4}\frac{\psi^2\omega^2}{\alpha^2}\alpha\right) a^2 + \frac{\alpha}{4}\left(\Delta^2 (\partial_r\phi)^2 + (\partial_r\psi)^2\right)\right) r + \frac{\left(1 - \Delta^2\phi^2\right)\alpha a^2 - \alpha}{2r}, \tag{3.29}$$

$$\partial_r a = -\frac{a^3}{2r} + \frac{a}{2r} + \left(\frac{\psi^2\omega^2}{4\alpha^2} + \frac{V}{2} + \frac{\Delta^2\phi^2}{2r^2}\right) a^3 r + \frac{ar}{4}\left((\partial_r\psi)^2 + \Delta^2(\partial_r\phi)^2\right). \tag{3.30}$$

Since the boson star action is invariant under the transformation $\psi \to \psi e^{-i\theta}$, $\theta \in \mathbb{R}$, we can define a conserved current, J_μ, associated with the transformation,

$$J_\mu = \frac{i}{16\pi}\left(\Psi^*\nabla_\mu\Psi - \Psi\nabla_\mu\Psi^*\right), \tag{3.31}$$

$$J_t = -\frac{\omega\psi^2}{8\pi}, \tag{3.32}$$

and with it a conserved charge, N,

$$N = \int J_\mu n^\mu \sqrt{\gamma} dx^3 = \int \frac{ar^2}{2\alpha}\omega\psi^2 dr, \tag{3.33}$$

where γ is the determinant of the metric induced on the $t =$ const. spacelike hypersurfaces and n^μ is the vector field normal to those surfaces.

Regularity of the metric at the origin requires,

$$\partial_r\psi\,|_{r=0} = 0, \tag{3.34}$$

$$\phi\,|_{r=0} = 0, \tag{3.35}$$

$$\partial_r a\,|_{r=0} = 0, \tag{3.36}$$

$$a\,|_{r=0} = 1, \tag{3.37}$$

$$\partial_r\alpha\,|_{r=0} = 0. \tag{3.38}$$

We note that Eqn. (3.38) is not linearly independent of the other boundary conditions, but is a consequence of the regularity of a at the origin.

Unlike the boson star profile, ψ, the global monopole field, ϕ, is not free to take on arbitrary values at the origin. Recall that ϕ is the magnitude of the ϕ^a's and that, at every point, ϕ^a is analogous to an outward pointing vector field. As such, to maintain a regularly spherically symmetric solution, we must have $\phi = 0$ at the centre of symmetry.

In the limit that $r \to \infty$, the boson star profile approaches zero exponentially while the global monopole transitions to its vacuum state: $\psi \to 0$, $\phi \to 1 + \sum_i c_i r^{-i}$. Assuming series expansions in $1/r$, the metric equations can be integrated, yielding the following regularity conditions as r approaches infinity [83, 92]:

$$\psi = 0, \tag{3.39}$$

$$\phi = 1 - \frac{1}{\lambda_{\rm GM}\Delta^2 r^2\left(1+\xi_{\rm GM}\Delta^2\right)}, \tag{3.40}$$

$$a = \left(1 - \frac{\Delta^2}{1+\xi_{\rm GM}\Delta^2} - \frac{2M}{r}\right)^{-1/2}, \tag{3.41}$$

$$\alpha = \left(1 - \frac{\Delta^2}{1+\xi_{\rm GM}\Delta^2} - \frac{2M}{r}\right)^{1/2}. \tag{3.42}$$

The asymptotic expansion Eqn. (3.41) motivates the definition of the mass function, $M(r)$, as

$$M(r) = \frac{r}{2}\left(1 - \frac{\Delta^2}{1+\xi_{\rm GM}\Delta^2} - a^{-2}\right), \tag{3.43}$$

which, in the asymptotic limit, is proportional to the Arnowitt-Deser-Misner (ADM) mass in a solid angle deficit space-time [93],

$$M_\infty = \lim_{r\to\infty} M(r), \tag{3.44}$$

$$M_{\rm ADM} = M_\infty\left(1 - \frac{\Delta^2}{1+\xi_{\rm GM}\Delta^2}\right)^{-3/2}. \tag{3.45}$$

Together, Eqns. (3.34–3.42) give the following boundary conditions [83]:

$$\phi|_{r=0} = 0, \tag{3.46}$$

$$a|_{r=0} = 1, \tag{3.47}$$

$$\lim_{r\to\infty}\psi = 0, \tag{3.48}$$

$$\lim_{r\to\infty}\phi = 1 - \frac{1}{\lambda_{\rm GM}\Delta^2\left(1+\xi_{\rm GM}\Delta^2\right)}, \tag{3.49}$$

$$\lim_{r\to\infty}\alpha = \frac{1}{a}. \tag{3.50}$$

Finally, rather than numerically solving Eqns. (3.19–3.24) in r, we find it more convenient to adopt a compactified coordinate, x, defined by,

$$x = \frac{r}{r+\rho}, \tag{3.51}$$

$$r = \frac{\rho x}{1-x}, \tag{3.52}$$

$$x \in [0,1], \tag{3.53}$$

where ρ is a positive real number and is typically set between 1 and 100, such that the solution features are well resolved on a grid uniformly spaced in x.

3.3 Methodology

In the following section, we review the numerical techniques used to find solutions to Eqns. (3.19–3.24). First we introduce the terminology used to discuss the novel features of the model (Section 3.3.1) and discuss the solution procedure itself (Section 3.3.2). Finally, we test the convergence of the numerical solutions (Section 3.3.3), demonstrating that the solutions we have found are not numerical artifacts. Additional information on the shooting method may be found in Appendix A. Likewise, the details of our multiple precision shooting method can be found in Appendix A.3.

3.3.1 Solution Families and Branches

The solutions we present in Section 3.4 exhibit sufficiently complex behavior that we believe it is worthwhile to define a number of terms at the outset. Specifically, we will later make extensive use of the terms *family* and *branch* to denote specific sets of solutions.

The parameter space we consider here is six-dimensional, spanned by $\psi(0)$, Δ, $\lambda_{\rm GM}$, $\lambda_{\rm BS}$, $\xi_{\rm GM}$ and $\xi_{\rm BS}$. From this point forward, we set $m = 1$, and note that this sets the energy scale of the solutions. We define a family of solutions to be the set of all ground state solutions with common Δ, $\lambda_{\rm GM}$, $\lambda_{\rm BS}$, $\xi_{\rm GM}$ and $\xi_{\rm BS}$. As such, within a given family, solutions can be indexed by the boson star central amplitude, $\psi(0)$, which is the only free parameter of the family. As a concrete example, consider the set of all mini-boson stars (boson stars without self interaction) which may be considered a family with $\Delta = 0$, $\lambda_{\rm BS} = 0$, $\xi_{\rm GM} = 0$, $\xi_{\rm BS} = 0$ and $\lambda_{\rm GM}$ arbitrary. From this perspective, Fig. 3.1 plots the progression of asymptotic mass M_∞ for the mini-boson star family.

We define a branch of a family to be the set of all solutions in the family where the asymptotic mass, M_∞, is C^1 as a function of the central amplitude, $\psi(0)$. Using this definition, mini-boson stars are a family consisting of a single branch as shown in Fig. 3.1, while Fig. 3.2 provides a mass plot illustrating a hypothetical family with three branches.

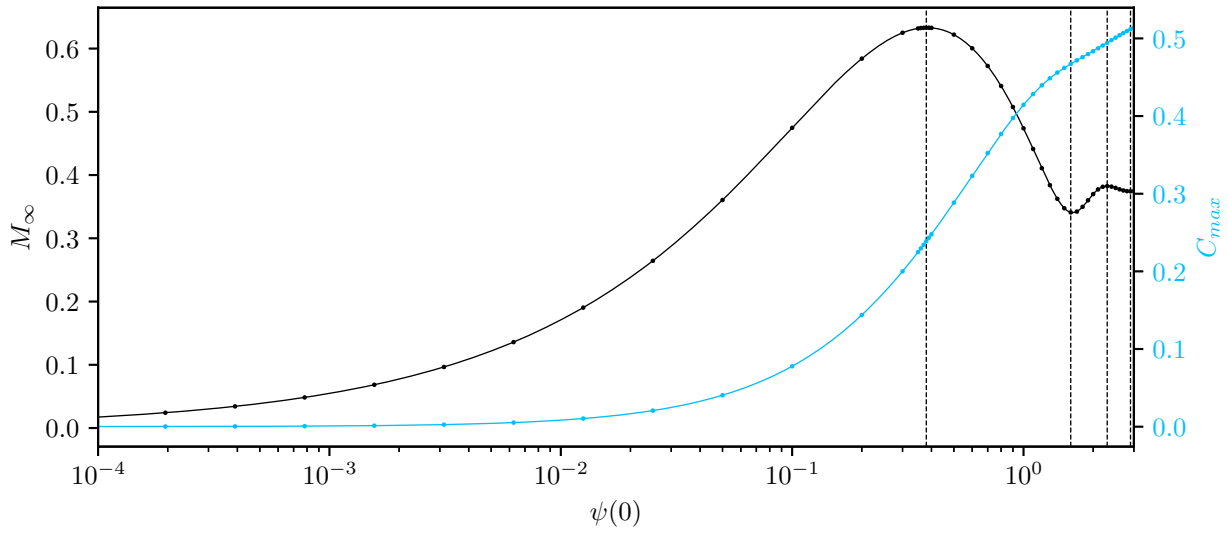

Figure 3.1: Asymptotic mass, M_∞, and maximum compactness, C_{max}, as a function of boson star central amplitude, $\psi(0)$, for ground state boson stars with no quartic self interaction potential (so called mini-boson stars). Stars located to the left of the first turning point are stable against small perturbation while stars located to the right are unstable [75]. Using our terminology, the set of mini-boson stars is a family consisting of a single branch, since the mass is everywhere C^1.

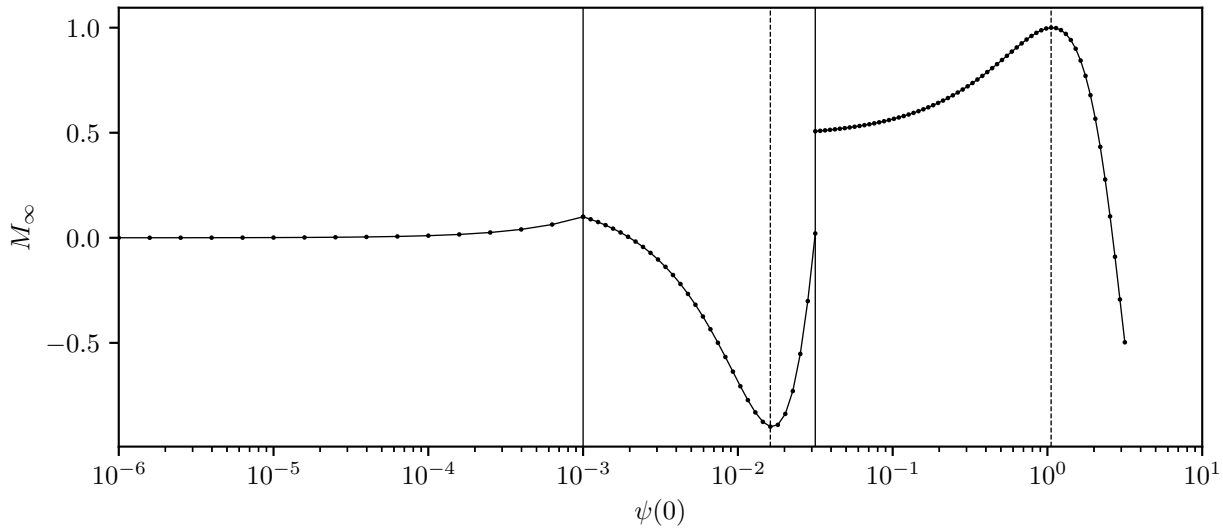

Figure 3.2: Asymptotic mass, M_∞, as a function of boson star central amplitude, $\psi(0)$, for a hypothetical family of solutions with three branches. The branches of the family are separated by vertical lines, the positions of which correspond to values of $\psi(0)$ where $dM_\infty/d\psi(0)$ is undefined.

3.3.2 Solution Procedure

The set of Eqns. (3.19–3.24) and boundary conditions (3.46–3.50) define a boundary value problem (BVP) where $\omega/\alpha(0)$ is the eigenvalue of the system. Due to the appearance of features that shall be discussed shortly, it is quite difficult to find initial guesses which will converge to the correct solutions using standard iterative BVP solvers. The primary computational challenge, therefore, is finding sufficiently accurate initial guesses whereupon we can let the BVP solver we use do its job.

To arrive at a suitable initial guess, the static equations are first integrated using an iterative shooting technique [100]. In this method, the boson star profile, $\psi(r)$, is initialized to 0 and the equations for the monopole, $\phi(r)$, and metric are integrated using a Runge-Kutta-Fehlberg solver (RK45) until the monopole field is well approximated by its asymptotic expansion, Eqn. (3.49). At this point, a tail satisfying the expansion is fit to the global monopole such that ϕ and $\partial_r\phi$ are continuous across the join, and the metric equations are integrated to the end of the numerical domain.

Subsequently, the monopole field is held fixed and the boson star is solved for via shooting by varying the ω parameter. Typically this parameter is chosen such that the mass of the configuration is a minimum and the boson star is in the ground state (i.e. the boson star profile exhibits no nodes) [80]. Once complete, the boson star field is held fixed and the monopole equations are re-integrated, etc. This iterated shooting process is continued until the initial guess is sufficiently close to the true numerical solution so as to converge in the BVP solver we use. Sufficient convergence is typically achieved after 3-5 iterations, at which point the ℓ_2 norms of the residuals are typically around 10^{-5}. This process is summarized in Algorithm 2.

This shooting problem is itself particularly difficult due to the (potentially) very different characteristic length scales of the boson star and global monopole. Correspondingly, a naive application of the shooting method will not yield guesses suitable for use in a BVP solver for the vast majority of the parameter space. The interested reader is directed to Appendix A.3 for a detailed description of how we overcame this issue using a novel multiple precision shooting method.

Algorithm 2 Iterated Shooting Procedure

initialize $\phi(x)$ to 0
initialize $\psi(x)$ to 0
while not converged **do**
    hold $\psi(x)$ fixed
    shoot for $\phi(x)$
    fit tail to $\phi(x)$
    integrate metric functions to asymptotic region
    hold $\phi(x)$ fixed
    shoot for $\psi(x)$
    fit tail to $\psi(x)$
    integrate metric functions to asymptotic region
end while

Upon achieving a sufficient level of convergence, the fields are used as an initial guess for a boundary value solver built using the program TWPBVPC, which solves two point boundary value problems using a mono-implicit Runge-Kutta method [40]. To account for the fact that the static equations constitute an eigenvalue problem in ω/α, the equations and boundary conditions are supplemented by the trivial ordinary differential equation, $\partial_r \omega = 0$ [82]. Our BVP solver requires the same number of boundary conditions as equations and we have many possible choices for a boundary condition for this last equation. Of these, we adopt $\partial_r \alpha|_{r=0} = 0$ [82] which, as noted above, is satisfied automatically in the continuum as a consequence of regularity at the origin.

As detailed in Sections 3.3.1 and 3.4, the solutions we have found are characterized as belonging to specific branches of various families. Within a given branch, it is possible to use parameter continuation[2] to find additional solutions on that same branch, but we were unable to use this method to traverse between branches. Our procedure for finding solutions is thus as follows: within a given family, we identify all branches using the shooting method, and these approximate solutions are used as initial data for our BVP solver. Subsequently, we populate the various branches using parameter continuation (one continuation per branch) and the BVP solver.

3.3.3 Convergence of Numerical Solutions

Once we have constructed our solutions, it is necessary to verify that the results we have found are in fact approximate solutions of Eqns. (3.19–3.24) and not numerical artifacts. We accomplish this by performing independent residual (IR) convergence tests on the results (see Sec 2.5).

Fig. 3.3 demonstrates second order IR convergence for a typical solution from the BVP solver. When higher order schemes for the independent residuals are used on the 8192 point grid, the residuals are observed to be non-smooth fluctuations about zero with an amplitude of $\approx 10^{-12}$, indicating that our solutions are essentially exact to machine precision.

All results presented in the subsequent sections are based on solutions output on a grid of at least 8192 points with a specified error tolerance of no more that 10^{-12}. We note that TWPBVPC allocates additional grid points in the vicinity of poorly resolved features and verifies convergence through the use of high order discretizations [40]. As such, if 8192 grid points is insufficient to

[2]By using the solution output from the BVP solver as an initial guess for a problem with slightly modified parameters, it is possible to generate a solution to the modified problem if that solution does not exhibit significantly different characteristics. Unfortunately, we were unable to use this method to generate solutions on different branches as solutions on distinct branches are radically different from one another.

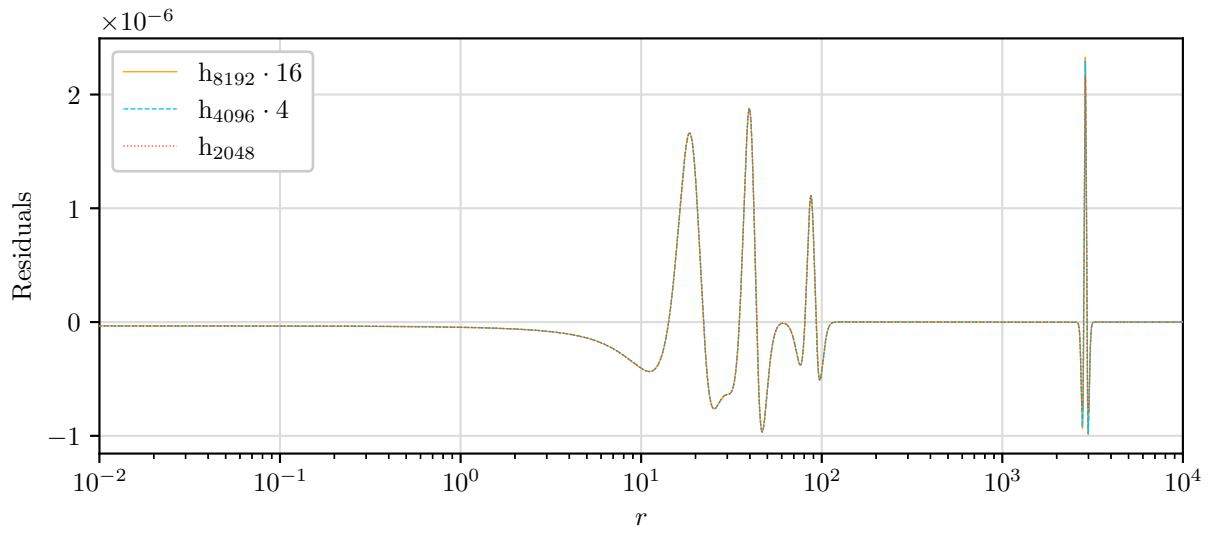

Figure 3.3: Convergence of independent residuals for a solution near the limit of our code's ability to resolve solutions. This limit occurs when features are present at very large distances from the origin. Here we plot the scaled residuals of the metric function a evaluated on grids of 8192, 4096 and 2048 points using a second order finite difference scheme for the IR evaluator. With the scaling given in the figure, overlap of curves implies second order convergence. As described in the subsequent sections, the large spikes near the middle and right of the graph are caused by the presence of shells of matter far from the origin. However, even in the vicinity of these shells convergence is sufficiently precise that it is difficult to distinguish the separate scaled residuals.

resolve a particular feature of a solution, TWPBVPC will automatically allocate additional points to ensure that the desired error tolerance is maintained. Note that in the above convergence test, these advanced features are deactivated so that each output resolution is not "polluted" by higher order approximations. As such, the true solutions are of higher fidelity than those used in our testing.

3.4 Results

Due to the large parameter space associated with these solutions (as noted above, six dimensional in $\psi(0)$, $\lambda_{\rm BS}$, $\lambda_{\rm GM}$, Δ, $\xi_{\rm BS}$ and $\xi_{\rm GM}$), it was not feasible to perform a comprehensive survey of the solution space. Instead, we focus on a number of families of solutions which appear to capture the novel behavior associated with this model.

Specifically, in subsequent sections we will deal with seven families of solutions whose fixed parameters are given in Table 3.1 and where the variable family parameter in each instance is the central amplitude, $\psi(0)$, of the boson star. For simplicity, the boson star quartic self interaction coupling constant, $\lambda_{\rm BS}$, has been set to 0, and we remind the reader that we have set $m = 1$.

To better highlight the main properties of these families and provide the reader with a representative view of some of the solution phenomenology, profiles of the metric functions, monopole field, boson star profile, mass function and Noether charge are shown in Figs. 3.4–3.9 for select solutions from families b, d and e.

It should be explicitly noted that the families presented here cannot be considered representative

Family	Δ^2	λ_{GM}	ξ_{BS}	ξ_{GM}
a	0.49	0.001	0	0
b	0.01	0.001	0	0
c	0.36	1.000	0	0
d	0.81	0.010	0	0
e	0.25	0.001	3	3
f	0.49	0.010	5	0
g	0.09	0.010	0	5

Table 3.1: Parameters for families of solutions. Each family consists of a continuum of solutions differentiated by the central amplitude of the boson star.

of the entire six dimensional parameter space. Instead, these particular values were chosen since they seemed at least representative of the phenomenology observed. Additionally, it would be remiss to treat these figures as containing all possible branches of a given family. It is entirely possible that there exist additional, disconnected branches within a given family which our methods were simply unable to find.

As is evident from these figures, the model exhibits a number of unusual properties, the most obvious of which concerns the profiles of the boson star field. For many families, these profiles are characterized by a series of matter shells which are located far from the origin and which contain the majority of the bosonic mass of the system.

Although these configurations are superficially similar to the excited states of a standard boson star, we emphasize that they represent *ground states* of the system. The excited states (which we can also find) are characterized by higher masses and nodes in the boson star profile at radii beyond the final shell, as in the case of a standard boson star [80]. In what follows, we restrict our investigation to ground state solutions.

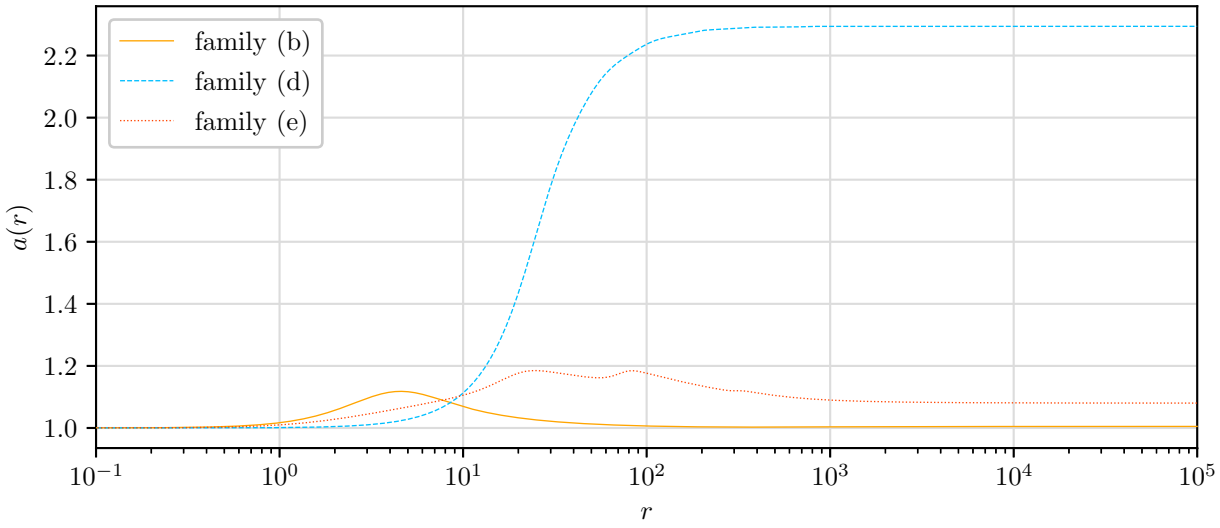

Figure 3.4: Radial component of the metric, $a(r)$, as a function of areal radius, r, for representative solutions from families b, d and e. Here the meaning of the global monopole's solid deficit angle is obvious: rather than approaching flat space as $r \to \infty$, we approach a space-time which is the four dimensional analog of a cone.

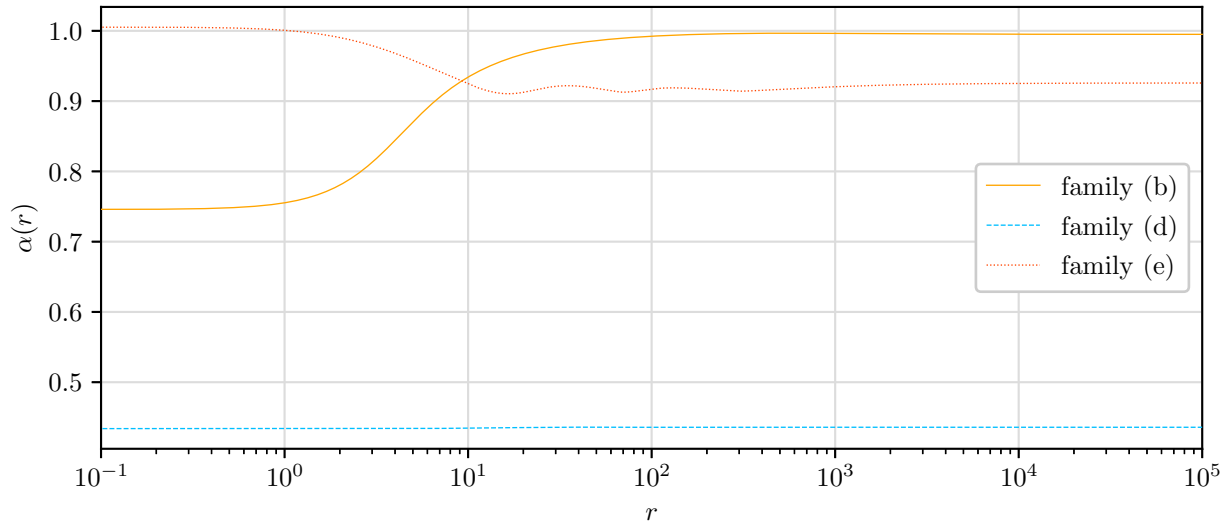

Figure 3.5: lapse, $\alpha(r)$, as a function of areal radius, r, for the same solutions plotted in Fig. 3.4. When the energy contribution of the global monopole is strong, observers at infinity see time at the centre of symmetry as flowing faster rather than slower as is the case for ordinary compact stars.

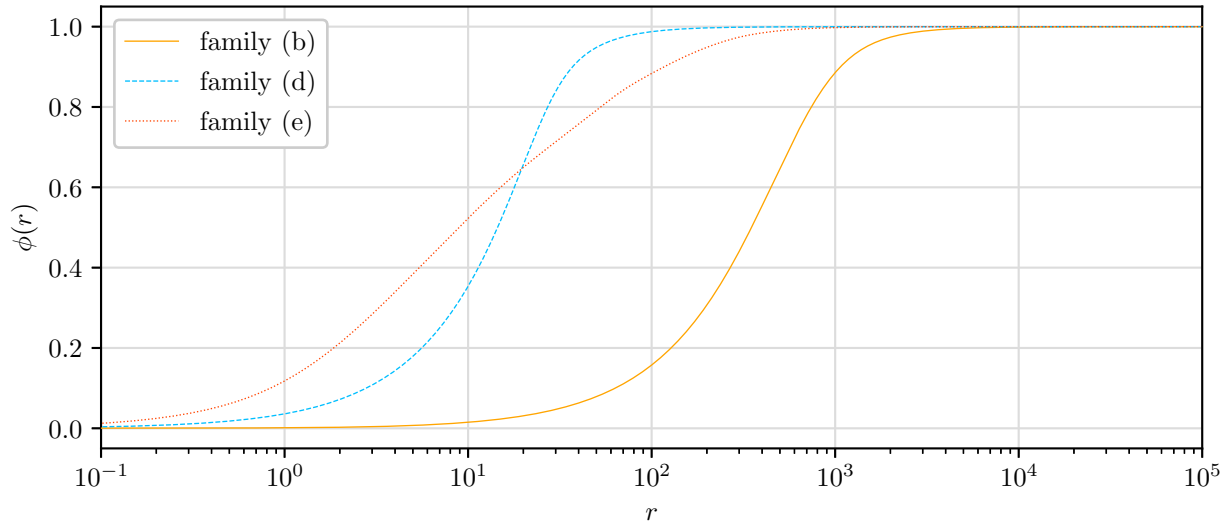

Figure 3.6: Global monopole field, $\phi(r)$, as a function of areal radius, r, for the previously plotted solutions. Relative to the boson star profile (Fig. 3.7), where the effect of coupling to the monopole is clear, for the majority of the parameter space the global monopole field is not significantly distorted by the presence of the boson star. In the presence of large non-minimal couplings, however, the field can become significantly distorted near the origin, which contributes to the compactness of the stars [83].

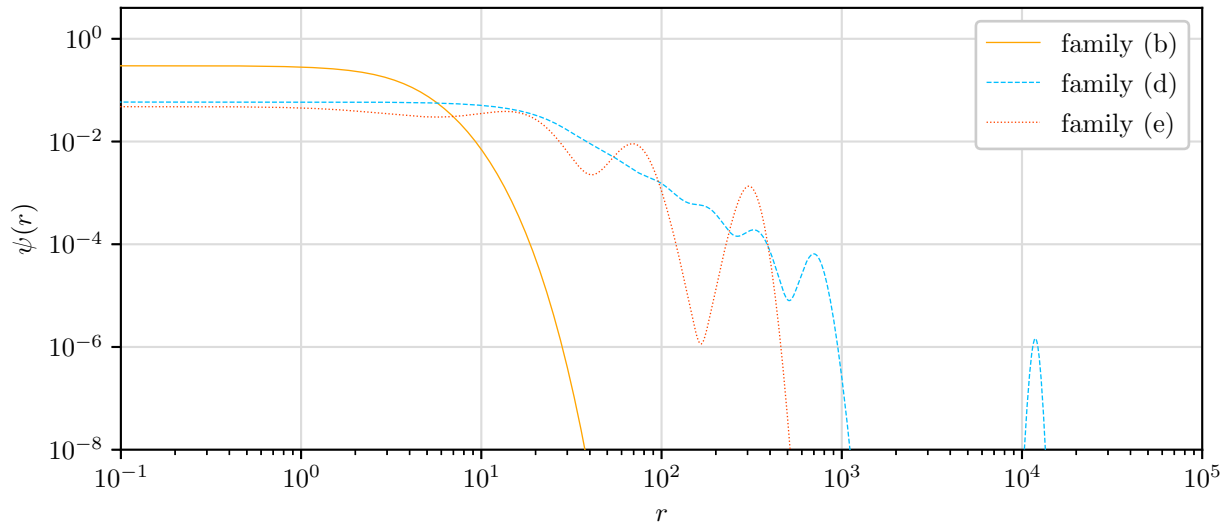

Figure 3.7: Boson star field, $\psi(r)$, as a function of areal radius, r, for the previously plotted solutions. Here, we can see that the solutions from families d and e are not monotonically decreasing, instead exhibiting successive shells of matter. Excluding the central peak, the solutions from families d and e consist of seven and three shells respectively. Between shells, ψ may reach extremely small values. For these simulations, family d reached a minima far below our ability to confidently resolve the solutions before the final peak.

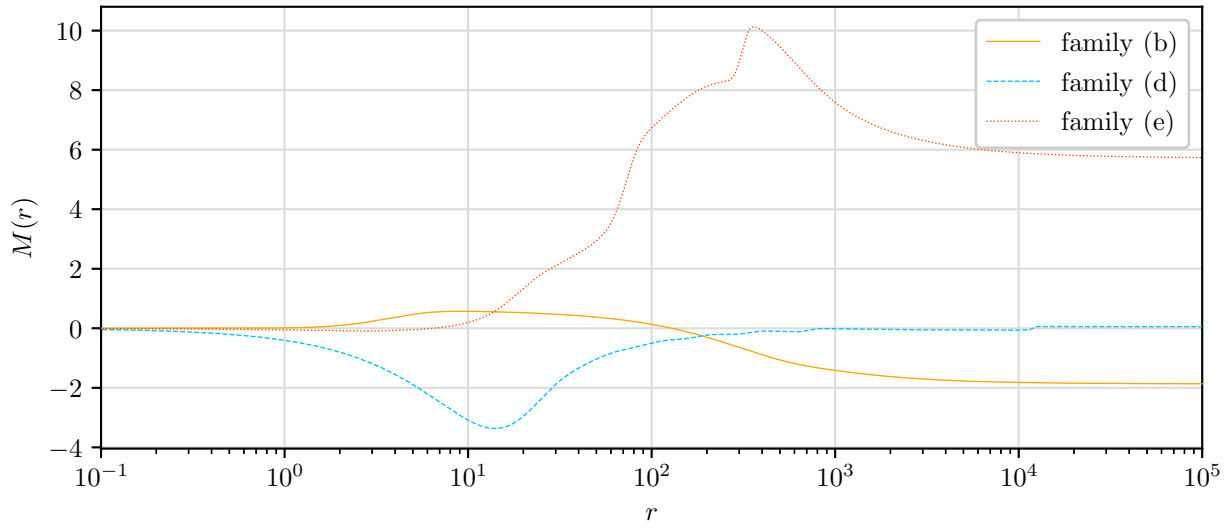

Figure 3.8: Mass function, $M(r)$, as a function of areal radius, r, for the previously plotted solutions. It can be seen from inspection that the majority of the bosonic mass is contained within the matter shells rather than near the origin. In the minimally coupled case, the mass contributions from the monopole and boson star are roughly equal and opposite, while in the non-minimal case the global monopole may contribute a positive effective mass [83, 92].

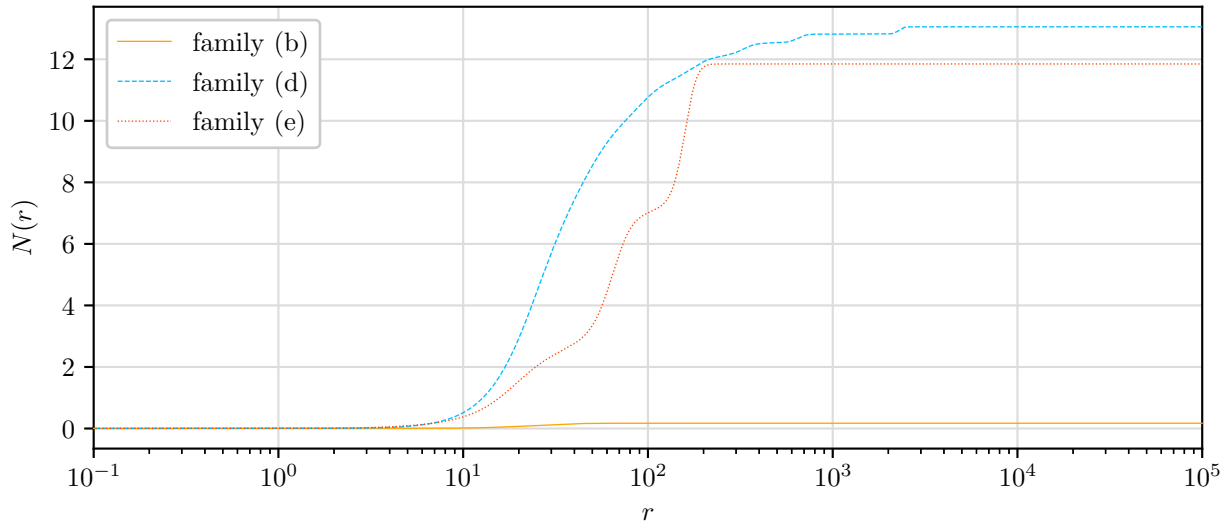

Figure 3.9: Charge, $N(r)$, as a function of areal radius, r, for the previously plotted solutions. When the number of shells is relatively small and well separated, each matter shell is seen to contribute roughly the same quantity of bosonic matter.

3.4.1 Branching Behavior of Minimal Boson D-Stars

Interestingly, the number of matter shells is not constant within a given family. Viewed as a function of the boson star central amplitude, $\psi(0)$, as one progresses through the family the matter shells will move either towards or away from the origin depending on the region of parameter space one is investigating. At discrete central amplitudes, ψ_i^c, which we will refer to as critical central amplitudes in anticipation of later results, the solution will either gain a shell far from the origin or lose the furthest shell. This behavior is shown in Figs. 3.10 and 3.11, which demonstrate the behavior of the matter fields in the vicinity of a critical central amplitude for solutions from family d. We note that in many cases the shells appear at extremely large distances: we will refer to these as *asymptotic shells* and will eventually argue that they appear at spatial infinity.

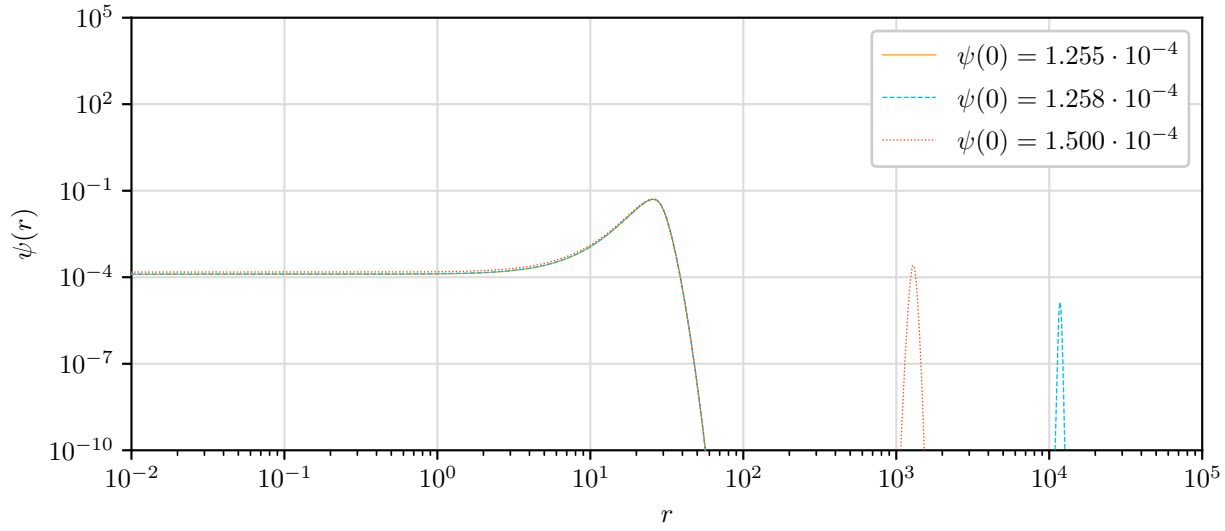

Figure 3.10: Progression of boson star profile, ψ, about a critical central amplitude for family d as a function of central amplitude, $\psi(0)$. Approaching the critical central amplitude ($\psi_i^c \approx 1.255843 \cdot 10^{-4}$) from below (yellow), there are no shells far from the origin. After crossing the critical central amplitude (blue), there is a shell of bosonic matter located far from the origin. As the central amplitude is further increased (red), the asymptotic shell migrates inwards.

Examining Fig. 3.10, one observes that the boson star field at times becomes exceedingly small in the region between successive shells. In fact, when one is sufficiently close to a critical central amplitude, it is not unusual for the boson star field in the part of the domain before the final shell to approach $\psi(r) \approx 10^{-300}$, the limit of double precision floating point numbers.[3] Correspondingly, the appearance of the shells of matter is due to the non-linear interaction of the boson star and global monopole mediated by gravity rather than a consequence of the equations describing the boson star alone.

Plotting asymptotic mass versus central amplitude, as in Figs. 3.12 and 3.13, the locations of the critical central amplitudes are clearly visible as mass gaps in the spectrum. The gaps in turn correspond to the abrupt appearance of shells of matter far from the origin.

[3]From a numerical perspective, this is not so much of a concern as it might appear. Even if the relative error of the boson field becomes large in these regions, the absolute error of the solution will remain small. What is important is that we maintain accuracy in regions of significant matter density such as the shells. Correspondingly, the exact minimum value achieved is both uncertain and unimportant.

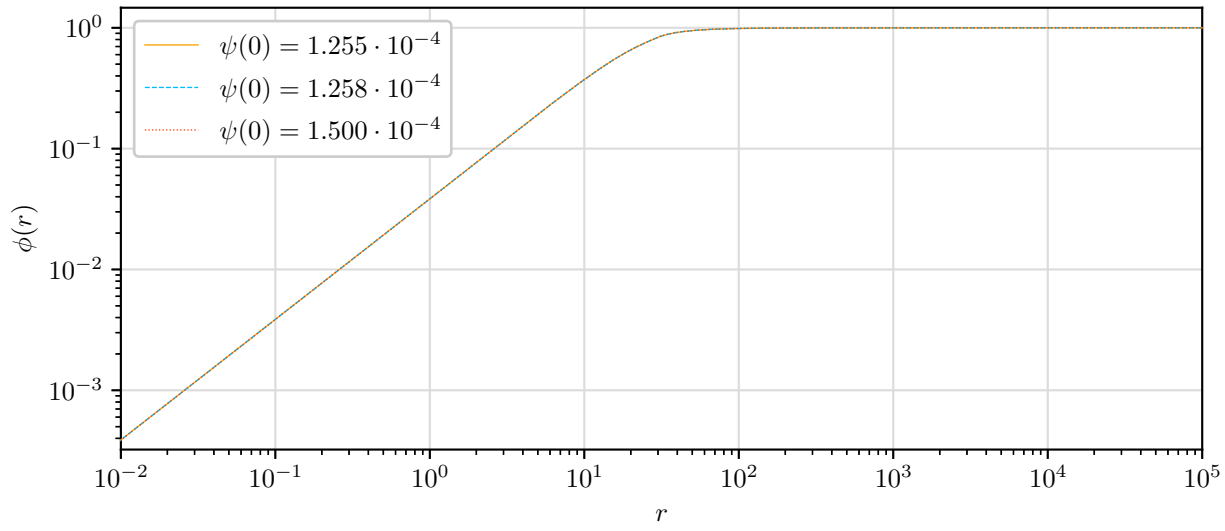

Figure 3.11: Progression of global monopole field, ϕ, about a critical central amplitude ($\psi_i^c \approx 1.255843 \cdot 10^{-4}$) for family d for the same solutions shown in Fig. 3.10. The global monopole field is not significantly affected by the presence of the asymptotic shells and exhibits no significant changes near the critical point.

We can gain some insight into the appearance (or disappearance) of a shell as follows. Assuming that the magnitude of the boson star profile goes as $|\psi| < r^{-2}$. Enforcing the boundary conditions (3.39–3.42), we find $T \propto r^{-2}$. Under these conditions, Eqn. (3.19) may be written to leading order in $1/r$ as,

$$\partial_r^2 \psi = \delta(r) \psi a^2, \tag{3.54}$$

where we define the criticality function, $\delta(r)$, as,

$$\delta(r) \equiv -\frac{\omega^2}{\alpha^2} + m^2. \tag{3.55}$$

Then, provided the following conditions hold as $r \to \infty$,

$$\delta(r) > 0, \tag{3.56}$$

$$a \to \left(1 - \frac{\Delta^2}{1 + \xi_{\mathrm{GM}} \Delta^2}\right)^{-1/2}, \tag{3.57}$$

$$\alpha \to \left(1 - \frac{\Delta^2}{1 + \xi_{\mathrm{GM}} \Delta^2}\right)^{1/2}, \tag{3.58}$$

the solutions to Eqn. (3.54) are exponentials as would be expected for the boson star by itself. If, however, $\delta(r)$ switches sign at some finite $r \gg 1$, the second derivative of the solution would become negative, forcing the appearance of a zero crossing and the nature of the solution would no longer be simple exponential growth or decay. As such, the condition $\delta(r) \to 0$ as $r \to \infty$ predicts a change in the nature of the asymptotic solution at that point, which happens to correspond to the development of a shell of matter.

The critical central amplitudes therefore correspond to the solutions which have $\delta = 0$ at infinity. An example of this is shown in Figs. 3.14 and 3.15 which plot the mass function, $M(r)$, and criticality function, $\delta(r)$, respectively, in the vicinity of a critical central amplitude.

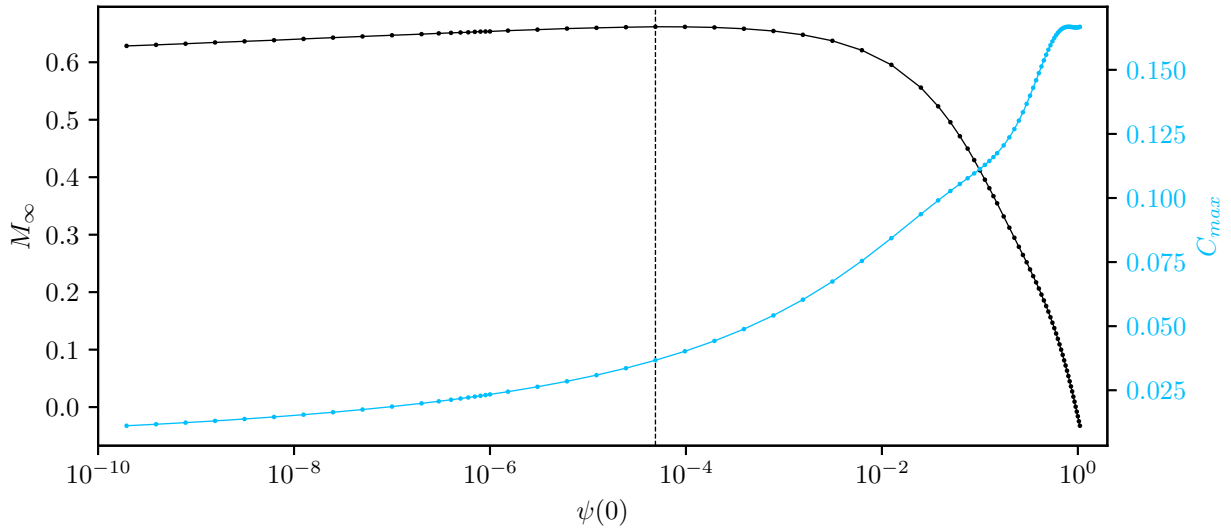

Figure 3.12: Asymptotic mass and compactness as a function of central amplitude for family c. Unlike the other families, family c does not exhibit critical central amplitudes and consists of only a single branch. This is likely due to the size of the global monopole self interaction ($\lambda_{\mathrm{GM}} = 1.00$) which greatly reduces the length scale of the monopole (in the case of the minimally coupled monopole, the transformation $\lambda_{GM} \to \kappa^2 \lambda_{GM}, r \to r/\kappa, t \to t/\kappa$ generates a new solution from an existing one). As such, the space-time achieves its asymptotic solid angle deficit on a length scale small compared to the size of the boson star.

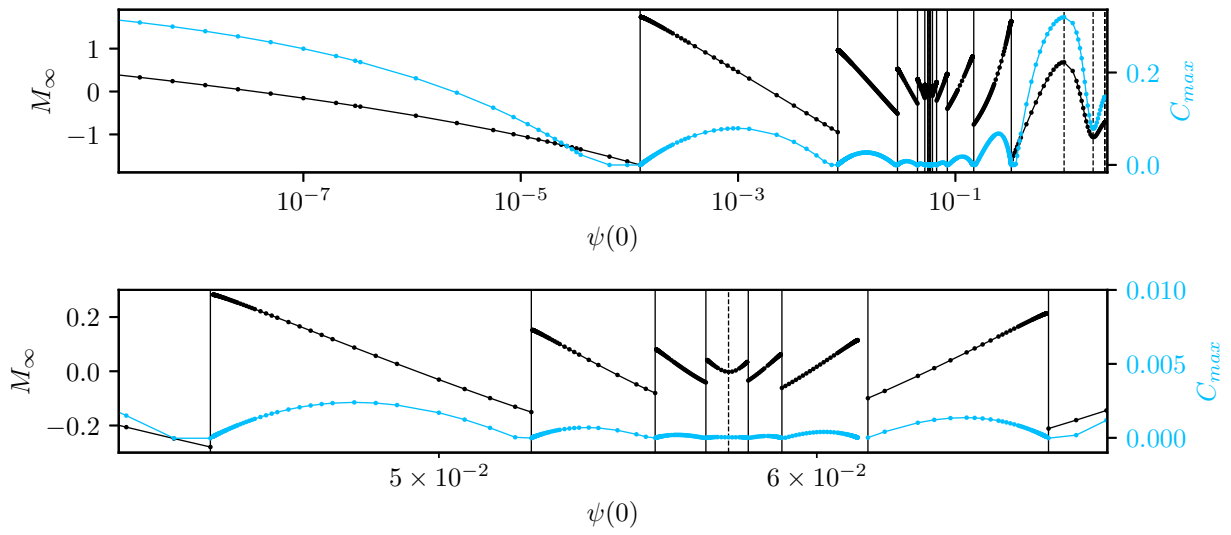

Figure 3.13: Asymptotic mass and maximum compactness as a function of central amplitude for family d. The bottom plot shows an expanded view of the top one, highlighting the structure. Note the turning point showcased in the subplot and marked with the vertical dashed line. This corresponds to a matter shell that was originally progressing inwards (as a function of boson star central amplitude), progressed to some minimal distance from the origin (corresponding to the turning point) and then reversed direction and progressed outwards.

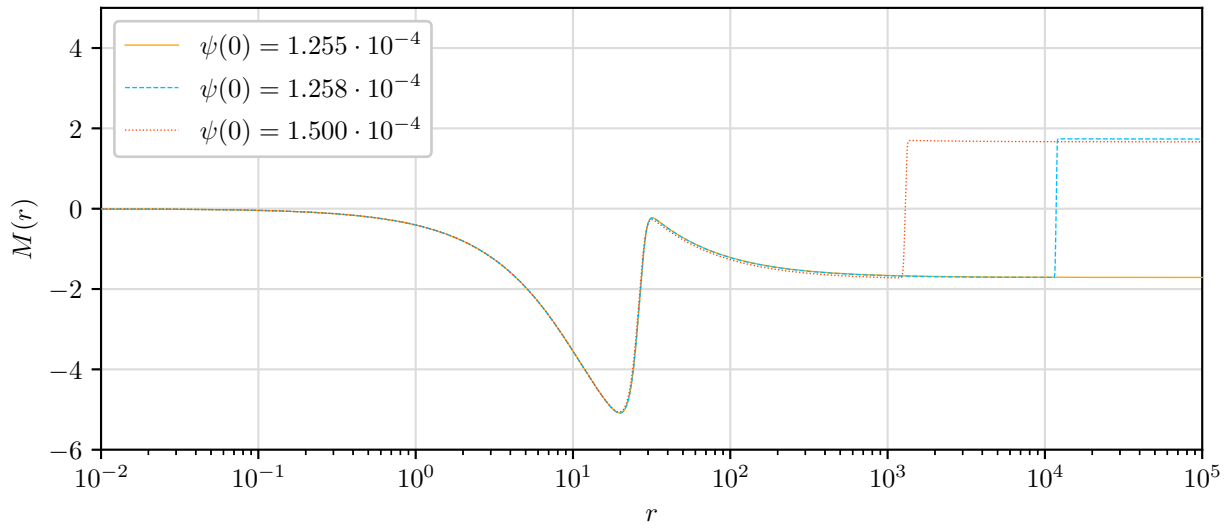

Figure 3.14: Progression of mass function, $M(x)$ about a critical central amplitude ($\psi_i^c \approx 1.255843 \cdot 10^{-4}$) for solutions from family d as a function of central amplitude. Here we have plotted the same solutions shown in Fig. 3.10. As one progresses across the critical point, a new shell of matter appears far from the origin (blue dashed line) and then moves inward (red dot-dashed line). Note that the inner and asymptotic shells contain approximately the same amount of bosonic matter and that as we cross the critical central amplitude, the asymptotic mass changes discontinuously.

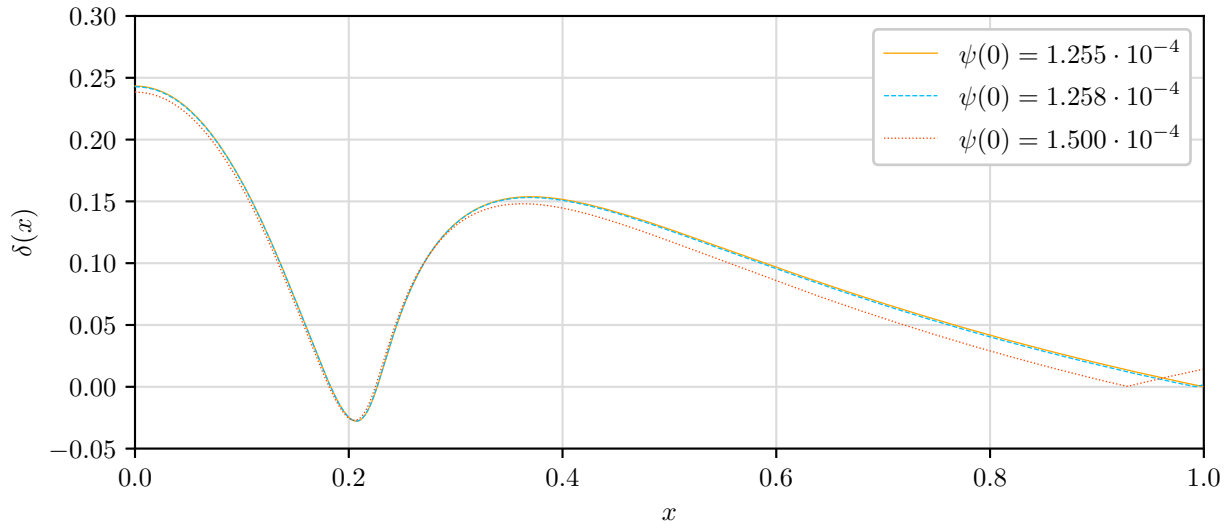

Figure 3.15: Progression of criticality function, $\delta(x)$, about a critical central amplitude ($\psi_i^c \approx 1.255843 \cdot 10^{-4}$) for solutions from family d as a function of central amplitude. As before, we have plotted the same solutions shown in Figs. 3.10 and 3.11, however we have plotted versus x to more clearly showcase the turning points of the criticality function. Note that as we cross the critical central amplitude, $\delta(x)$ never dips below 0 asymptotically.

3.4.2 Branching Behavior of Non-Minimal Boson D-Stars

Solutions with non-minimal coupling also exhibit critical central amplitudes and mass gaps, but additionally display a few crucial differences relative to the minimally coupled case. Figures 3.16–3.18 show the mass spectra for families e, f and g. From Figs. 3.16 and 3.18 it can be seen that the non-minimal coupling smooths the transitions that occur at the critical amplitudes for at least some of the parameter space. The mechanics of this smoothing mechanism are expanded upon in Figs. 3.19 and 3.20, where it is shown that as the central amplitude, $\psi(0)$, is increased, the location of the matter shell increases to some maximum radius, at which point further changes to the central amplitude result in the shell shrinking to nothing. Note, however, that this behavior is not universal for the non-minimally coupled case; there is a mass gap about the final branch of family e shown in Fig. 3.16 and family f is entirely without smoothing (Fig. 3.17). Evidence based on various solution families we have examined suggests that this smoothing behavior is a function of global monopole coupling rather than boson star coupling.

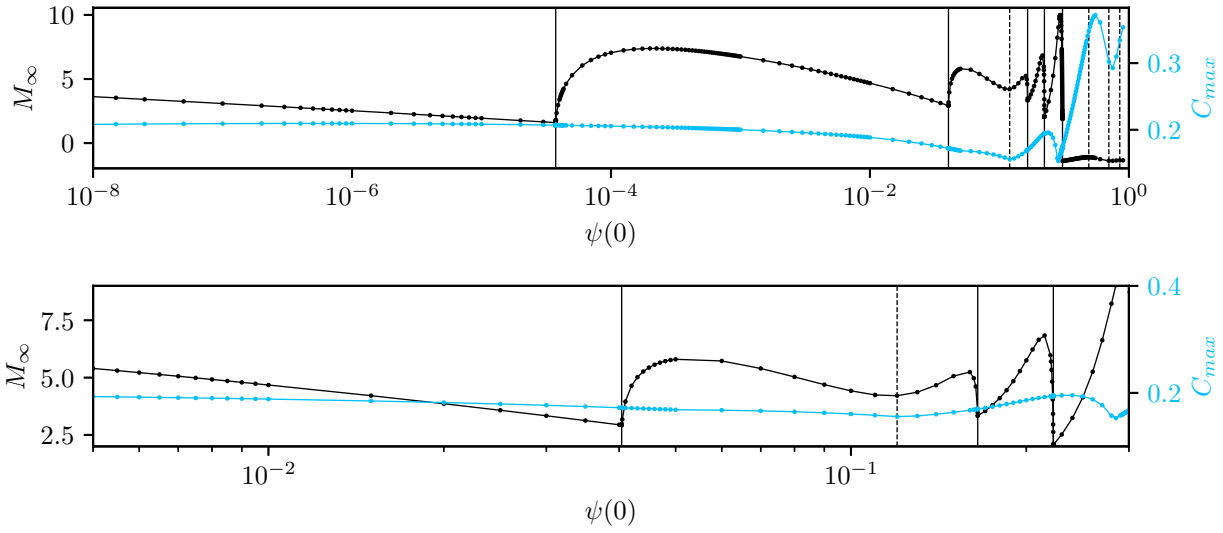

Figure 3.16: Asymptotic mass as a function of central amplitude for family e. The subplot shows an expanded view of the upper plot highlighting the structure. The non-minimal global monopole coupling appears to smooth out the transitions for at least a subsection of the parameter space. However, note the discontinuity between the final and penultimate branches of the uppermost subplot, which is not an artifact of the resolution of the plot. At the critical central amplitude, the mass approaches ≈ 1.5 on the left and ≈ -1.3997 on the right. The locations of local maxima resulting from the appearance of shells at finite radius are not highlighted to avoid cluttering.

As the asymptotic shells may appear at either some finite areal radius or at infinity in the non-minimally coupled case, the criticality function, $\delta(r)$, is of limited use in determining the value of the critical central amplitudes, ψ_i^c, when smoothing is present. When the asymptotic shell vanishes at some finite areal radius, we find the critical central amplitudes through continuation, tuning the boson star central amplitude until the final shell vanishes. In the case that the asymptotic shell vanishes at infinity, the critical central amplitudes are found via the procedure described in Section 3.4.1.

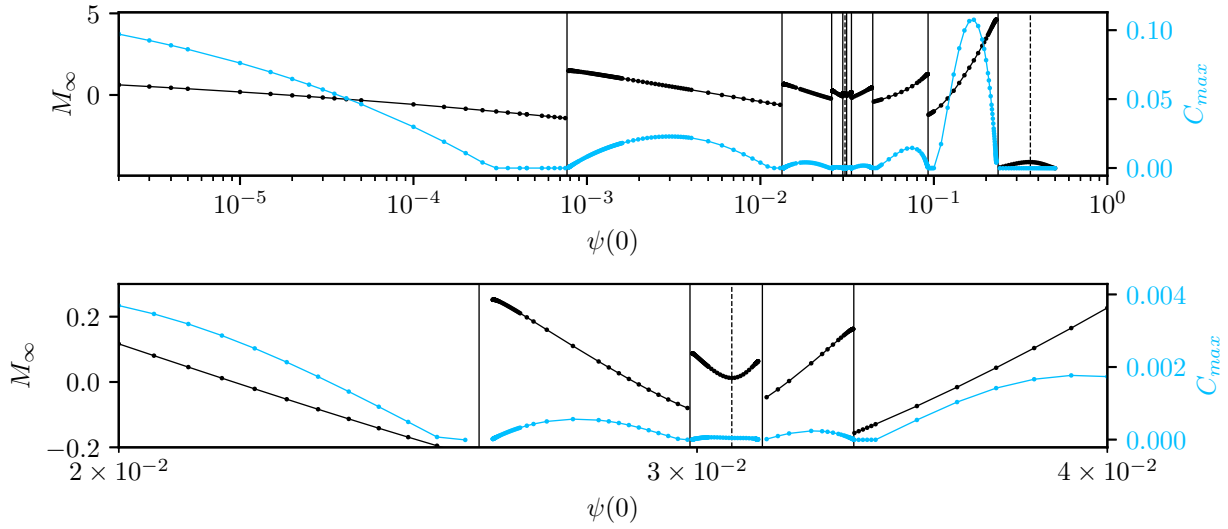

Figure 3.17: Asymptotic mass as a function of central amplitude for family f with a minimally coupled global monopole and non-minimally coupled boson star. The subplot shows expanded views of the uppermost plot, highlighting structure which is insufficiently resolved in the first plot. Unlike Figs. 3.16 and 3.18, there is no smoothing between the solution branches.

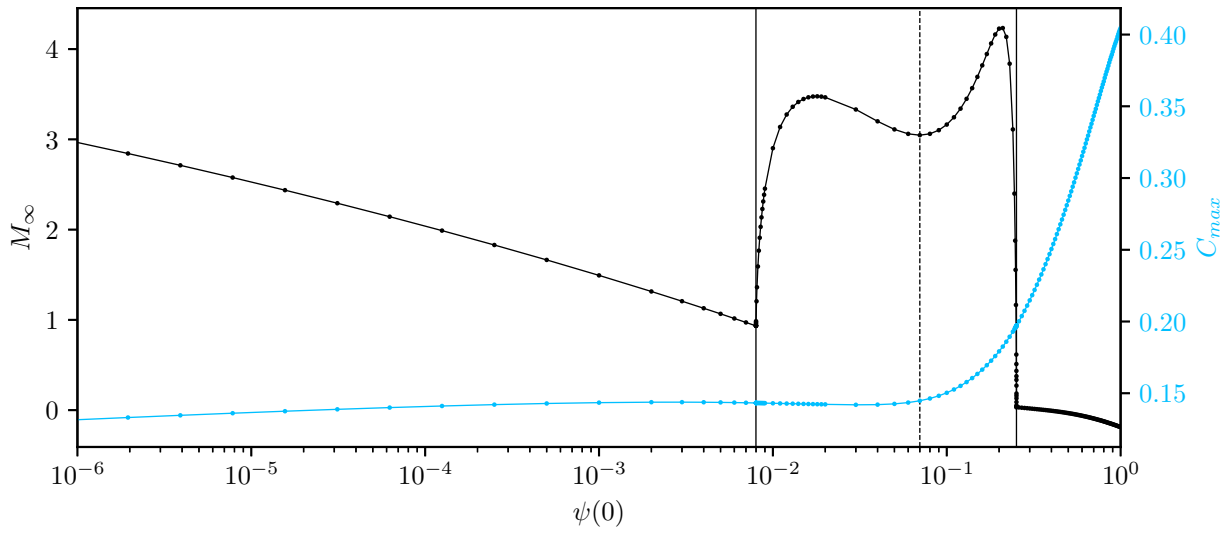

Figure 3.18: Asymptotic mass as a function of central amplitude for family g. As with family e, the branches exhibit significant smoothing. Correspondingly, the smoothing behavior appears to be an effect of the non-minimal global monopole coupling rather than non-minimal boson star coupling.

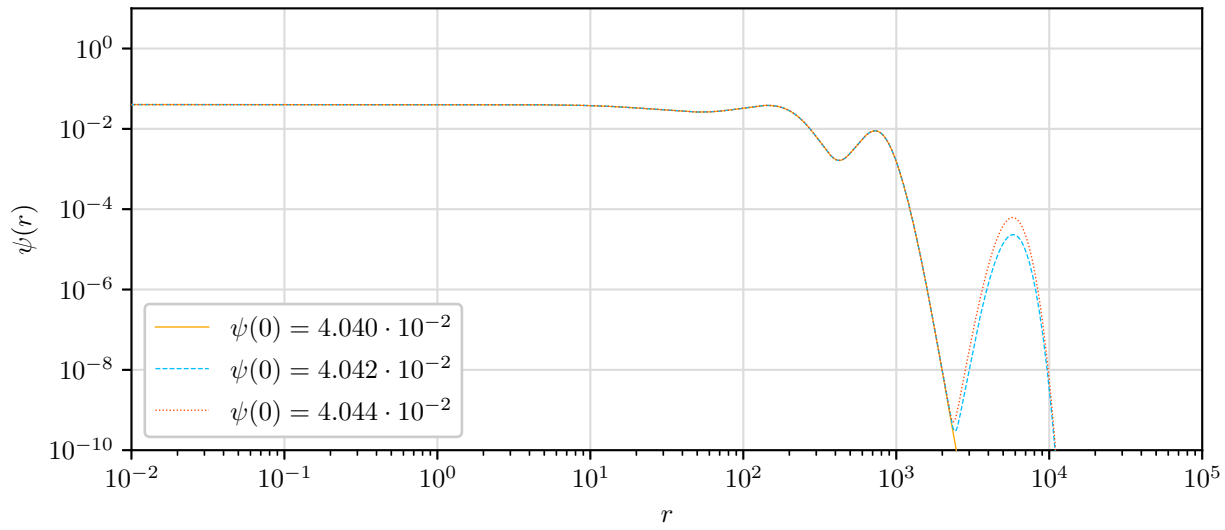

Figure 3.19: Progression of boson star profile, ψ, about a critical central amplitude for family e as a function of central amplitude. Approaching the critical central amplitude ($\psi_i^c \approx 4.04229 \cdot 10^{-2}$) from below (yellow), there are no shells far from the origin. As the critical central amplitude is crossed (blue), a matter shell appears some finite distance from the origin. As the central amplitude is further increased (red), the shell increases in mass and begins to migrate inwards. In contrast to the behavior of the minimally coupled case (Fig. 3.10), the shells of matter appear/disappear at some finite distance from the origin. Note that when a version of this figure appeared in [107], there was an error where the y-axis was labeled "$\psi(r) \cdot r$" rather than "$\psi(r)$" corresponding to an earlier version which did not use a logarithmic scale.

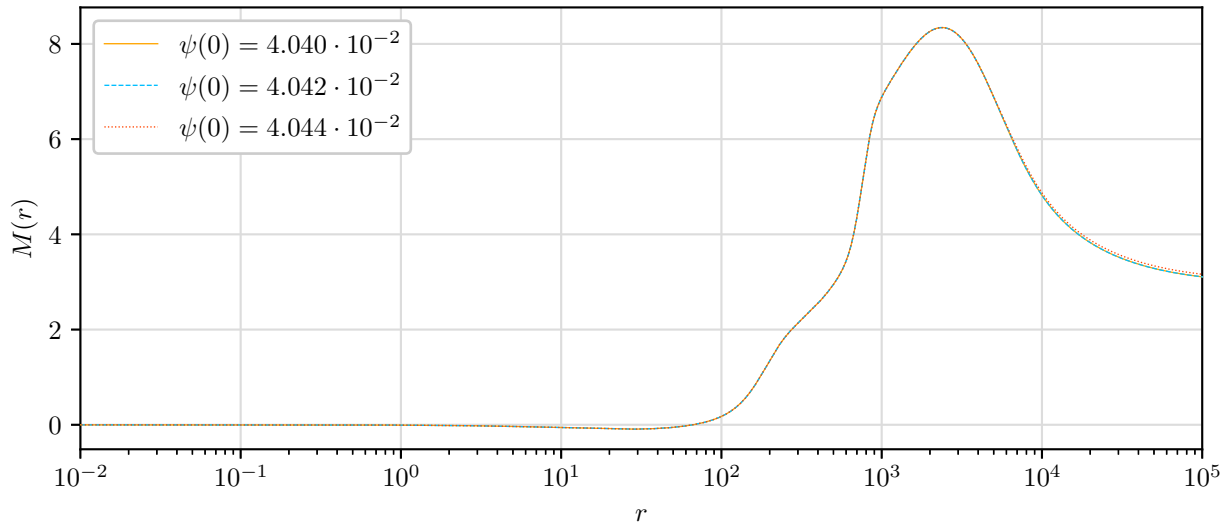

Figure 3.20: Progression of mass function, $M(x)$, about a critical central amplitude ($\psi_i^c \approx 4.04229 \cdot 10^{-2}$) for family e as a function of central amplitude. Here we have plotted the same solutions shown in Fig. 3.19. In contrast to the apparent behavior of the minimally coupled case where the critical points can be determined by eye, in the non-minimally coupled case the shells of matter disappear at some finite distance from the origin and the asymptotic mass is continuous across the critical central amplitude. In general, when the shells of matter appear/vanish at a finite distance from the origin, the criticality function is of limited use in determining the value of the critical central amplitudes.

3.4.3 Critical Scaling of Asymptotic Shells

In the non-minimally coupled case, the matter shells frequently vanish at some *finite* areal radius. Given these results, it is worth investigating in more detail whether the observed behavior of what we have identified as asymptotic shells is simply an artifact of limited resolution and/or finite precision in our numerical algorithms. The following analysis of the dependence of the location of such a shell on the family parameter strongly suggests that the phenomenology we are seeing is bona fide.

Plotting areal radius of an asymptotic shell, r_s, as a function of $|\psi(0) - \psi_i^c|$ as in Figs. 3.21 and 3.22, it is seen that r_s follows the scaling law,

$$r_s \propto |\psi(0) - \psi_i^c|^{-p}, \tag{3.59}$$

with $p \approx 1$.

This provides strong evidence that at the critical central amplitude, ψ_i^c, the shell reaches infinity. As such, a critical central amplitude appears to signal something analogous to a first order phase transition in statistical mechanics where the asymptotic mass takes the role of the energy and the mass gap is similar to latent heat. In the non-minimally coupled scenario these transitions may be partially smoothed out, as shown in Figs. 3.16 and 3.20, in which case scaling law is not obeyed.

From Fig. 3.21 it can be seen that within a given family, the areal radius of the outermost shell, r_s, appears to follow the same scaling law, indicating the presence of an underlying mechanism for the scaling that we will investigate in the next section. Moreover, Figs. 3.22 and 3.23 demonstrate that this scaling appears to be preserved across families, with variations perhaps due to the fact the shells are not entirely within the asymptotic regime. As such, there is evidence that all families, including non-minimally coupled families, follow the same universal scaling law ($p \approx 1$).

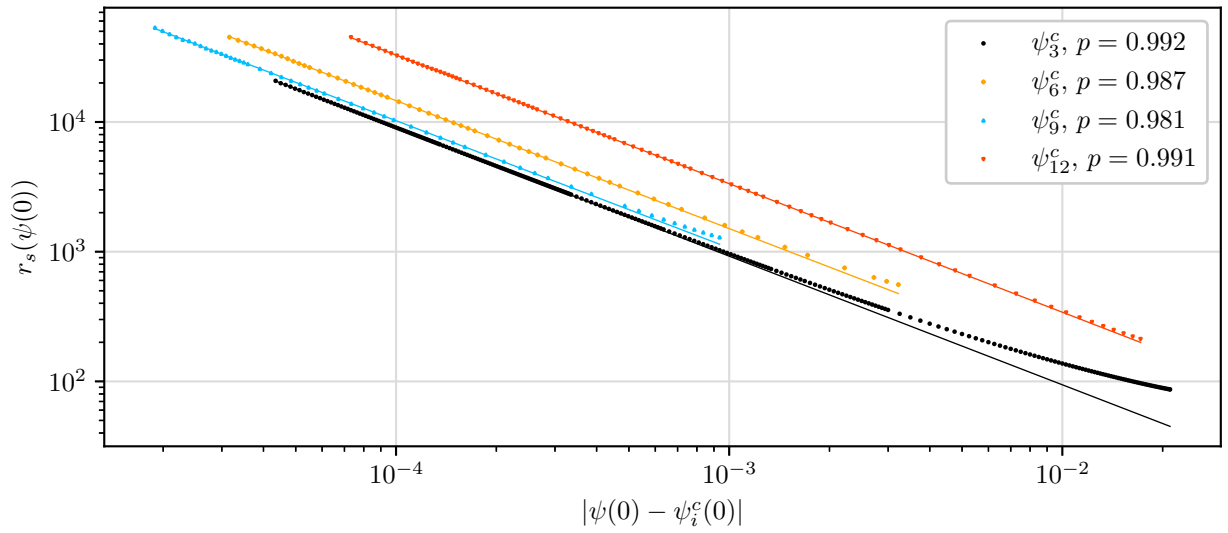

Figure 3.21: Areal radius of outermost shell (r_s) as a function of $|\psi(0) - \psi_i^c|$ for selected branches of family d. Within a given family, the areal radius of the outermost shell follows the scaling law Eqn. (3.59) with very similar exponents, $p \approx 1$. It is possible that the variations in the computed exponents, relative to $p = 1$, would disappear in the limit $r_s \to \infty$, $|\psi(0) - \psi_i^c| \to 0$, with the metric functions approaching their asymptotic values. However, our code is incapable of exploring this regime.

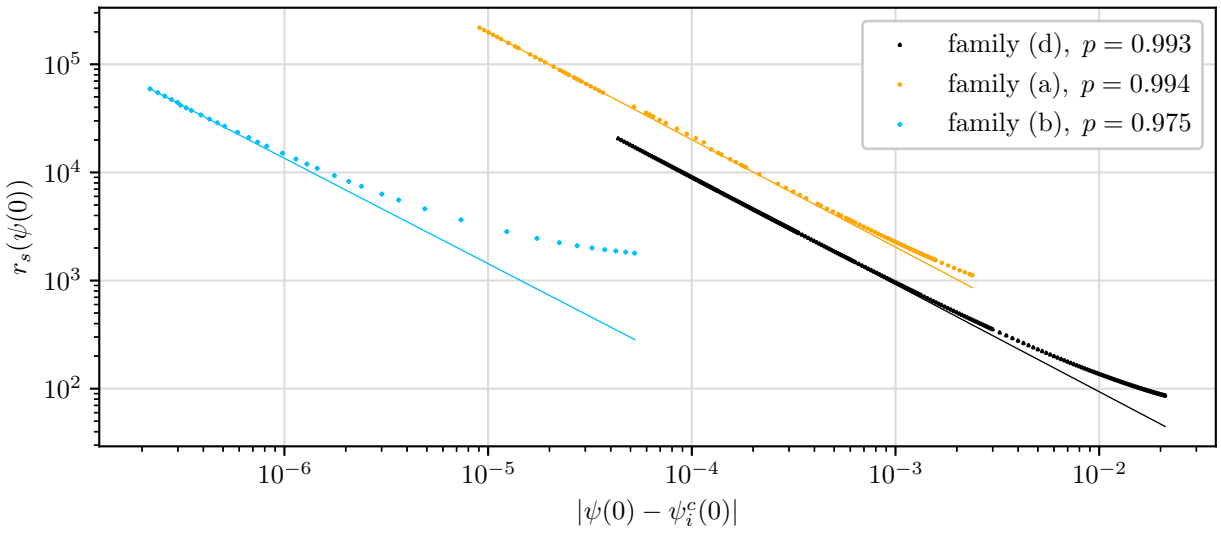

Figure 3.22: Areal radius of outermost shell (r_s) as a function of $|\psi(0) - \psi_i^c|$ for selected branches of families a, b and d. Given the variation in the parameters, the scaling exponent p is remarkably consistent across families ($p \approx 1$). As in the case of a single family (see Fig. 3.21), it is possible that these small variations would disappear in the asymptotic limit.

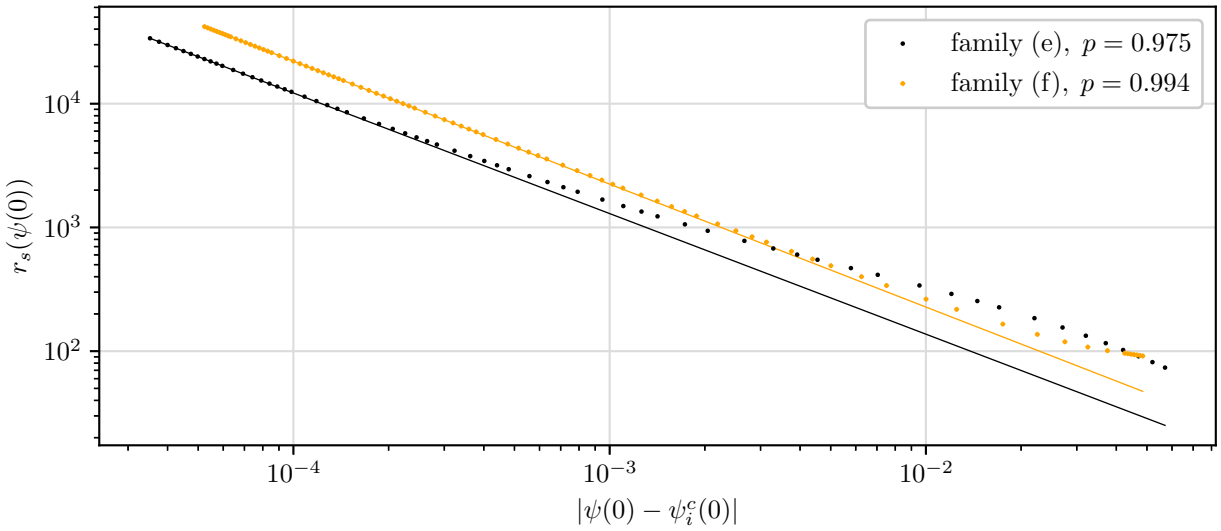

Figure 3.23: Areal radius of outermost shell (r_s) as a function of $|\psi(0) - \psi_i^c|$ for selected branches of families e and f. Here we plot the penultimate branch of family e as it is the only one which exhibits a mass gap (see Fig. 3.16). It is observed that both the minimally coupled and non-minimally coupled cases exhibit approximately the same scaling exponent, $p \approx 1$.

3.4.4 Derivation of Scaling Law

In this section we present a derivation of the apparently universal scaling law observed above. We show that the scaling relation can be derived assuming only that asymptotic shells of matter exist and that the region before the asymptotic shell is well approximated by the asymptotic expansion

of the fields given by Eqns. (3.39–3.42). In what follows, we view the solutions as simultaneous functions of r and $\psi(0)$. In particular, we consider the following functional quantities:

$$\alpha(r, \psi(0)), \tag{3.60}$$

$$\omega(\psi(0))\,. \tag{3.61}$$

As previously noted, in the case where there is a mass gap between branches, the areal radius of the asymptotic shell, r_s, corresponds to any boson star central amplitude, $\psi(0) = \psi_i^c$, where the criticality function, $\delta(0)$, is equal to 0 far from the origin. Provided we are in the asymptotic regime, we have the following condition derived from the asymptotic expansion of α as $r \to \infty$,

$$\alpha(r, \psi(0))^2 = \left(1 - \frac{\Delta^2}{1 + \xi_{\rm GM}\Delta^2} - \frac{2M(\psi(0))}{r}\right), \tag{3.62}$$

where M is the value of the mass parameter *before* the asymptotic shell. Writing the radius of the asymptotic shell as a parameterized function of $\psi(0)$,

$$r_s = r_s(\psi(0)), \tag{3.63}$$

and evaluating Eqn. (3.19) in the asymptotic regime, we have

$$\alpha(r_s, \psi(0))^2 = \frac{\omega(\psi(0))^2}{m^2} + \frac{\gamma(\psi(0))}{r_s}, \tag{3.64}$$

where $\gamma(\psi(0))$ parameterizes the $1/r$ dependence of Eqn. (3.19). Eqn. (3.64) is then the condition that the criticality function, $\delta(r)$, approximately vanishes in the vicinity of the asymptotic shell.

We expand the parameter $\gamma(\psi(0))$, mass function, $M(\psi(0))$, and eigenvalue, $\omega(\psi(0))$, as functions of the boson star central amplitude, $\psi(0)$, about the critical point, ψ_i^c,

$$\gamma(\psi(0)) = \gamma_0 + |\psi(0) - \psi_i^c| \left.\frac{\partial\gamma(\psi(0))}{\partial\psi(0)}\right|_{\psi(0)=\psi_i^c}, \tag{3.65}$$

$$M(\psi(0)) = M_0 + |\psi(0) - \psi_i^c| \left.\frac{\partial M(\psi(0))}{\partial\psi(0)}\right|_{\psi(0)=\psi_i^c}, \tag{3.66}$$

$$\omega(\psi(0)) = \omega_0 + |\psi(0) - \psi_i^c| \left.\frac{\partial\omega(\psi(0))}{\partial\psi(0)}\right|_{\psi(0)=\psi_i^c}, \tag{3.67}$$

where derivatives are evaluated on the branch with the asymptotic shell and the signs are chosen to give the observed behavior. Upon substituting Eqns. (3.62–3.67) into Eqn. (3.64) and evaluating at $r = r_s$ we find:

$$r_s = -\frac{m^2\left(\left(\frac{\partial\gamma}{\partial\psi(0)} + 2\frac{\partial M}{\partial\psi(0)}\right)|\psi(0) - \psi_i^c| + \gamma_0 + 2M_0\right)}{\omega_0^2 + 2\,|\psi(0) - \psi_i^c|\,\omega_0\frac{\partial\omega}{\partial\psi(0)} - m^2\left(1 - \frac{\Delta^2}{1+\xi_{\rm GM}\Delta^2}\right)}. \tag{3.68}$$

Noting that evaluation of Eqn. (3.62) at the critical point ($r = \infty$) gives,

$$\frac{\omega_0^2}{m^2} = 1 - \frac{\Delta^2}{1 + \xi_{\rm GM}\Delta^2}, \tag{3.69}$$

this simplifies to:

$$r_s = -\frac{\left(\frac{1}{2}\frac{\partial\gamma}{\partial\psi(0)} + \frac{\partial M}{\partial\psi(0)}\right)m^2}{\omega_0 \frac{\partial\omega}{\partial\psi(0)}} - \frac{\left(\frac{\gamma_0}{2} + M_0\right)m^2}{\omega_0 \frac{\partial\omega}{\partial\psi(0)}\,|\psi(0) - \psi_i^c|}. \tag{3.70}$$

It can be seen from inspection that in the limit $|\psi(0) - \psi_i^c| \to 0$, Eqn. (3.70) has the same functional form as the scaling law found experimentally (Eqn. (3.59)) with $p = 1$ as observed in Section 3.4.3.

3.5 Summary

Following and expanding upon the work of Marunovic & Murkovic [83], we have found new families of numerical solutions for the boson d-star system (Sections 3.1–3.2). As we were unable to find our solutions using standard BVP solvers with generic initial guesses, we developed a modification of the standard shooting method which permits integration to arbitrary distances (Appendix A.3). With initial guesses supplied by this shooting procedure, we were able to find convergent solutions using a BVP solver based on the code TWPBVPC [40] (Section 3.3.2). The correctness of these solutions was then established through the use of independent residual convergence tests (Section 3.3.3).

Analysis of these solution families (Section 3.4) reveals that the solutions possess a number of novel properties which are summarized here. Perhaps most fundamentally, in contrast to boson stars, boson d-stars cannot, in general, be deformed continuously throughout the parameter space. There exist critical central amplitudes in the parameter space for which the matter fields and metric functions exhibit finite change due to an infinitesimal change in parameters. Specifically, as one increases the central amplitude of the boson star, $\psi(0)$, while keeping all other quantities fixed, there exist a series of central amplitudes, ψ_i^c, where shells of bosonic matter either appear or disappear far from the centre of symmetry (Sections 3.4.1 and 3.4.2). To our knowledge, solutions with this behavior have not been previously observed.

These abrupt transitions in the functional form of the solutions appear similar to statistical mechanical phase transitions about a critical central amplitude. As such, these solutions may represent critical solutions in the sense that the appearance of a shell of matter far from the origin is analogous to the latent heat of a phase transition.

Of particular note is the observation that the areal radius of the centres of these asymptotic matter shells appears to follow a universal scaling law, Eqn. (3.59), with $p \approx 1$ (Section 3.4.3). This relation is observed to hold in both the minimally coupled and non-minimally coupled cases and suggests an underlying closed-form explanation which we were able to derive (Section 3.4.4).

3.6 Acknowledgements

This research was supported by the Natural Sciences and Engineering Research Council of Canada (NSERC).

Chapter 4

Non-Minimally Coupled Topological-Defect Boson Stars: Stability of Solutions

In this chapter, we build upon the foundation laid in our 2023 paper, titled "Stability of Non-Minimally Coupled Topological-Defect Boson Stars" [109]. This paper serves as a primary reference throughout our discussion, particularly as it extensively cites our earlier 2016 work, which explores families of stationary ground state solutions for the same matter model [107]. It is pertinent to note that any mention of [107] within this context can be interchangeably considered as a reference to Chapter 3.

As shown by Marunovic and Murkovic [83], non-minimal d-stars, composite structures consisting of a boson star and a global monopole non-minimally coupled to the general relativistic field, can have extremely high gravitational compactness. In a previous paper we demonstrated that these ground-state stationary solutions are sometimes additionally characterized by shells of bosonic matter located far from the center of symmetry [107]. In order to investigate the question of stability posed by Marunovic and Murkovic, we investigate the stability of several families of d-stars using both numerical simulations and linear perturbation theory. For all families investigated, we find that the most highly compact solutions, along with those solutions exhibiting shells of bosonic matter, are unstable to radial perturbations and are therefore poor candidates for astrophysically-relevant black hole mimickers or other highly compact stable objects.

4.1 Background

Attempts to create stable solitonic solutions in the context of general relativity go back to Wheeler in 1955 with the development of geons–solitonic objects comprised of various fundamental fields coupled to gravity [128]. Although Wheeler's geons proved to be unstable in general, further work by Kaup [66] and Ruffini and Bonazzola [115], lead to the discovery of the stable massive solitons today known as boson stars [80].

Over the intervening years, boson stars and their descendants have been invoked for a large variety of processes and models including black hole mimickers [15, 83], models of neutron stars [83, 94, 96, 122, 132], binary systems [94], sources of dark matter [86, 92, 113, 118, 124] and sources of gravitational waves [86, 94]. Though boson stars are not known to exist in nature, the simplicity of their matter model makes them a valuable tool for qualitative analysis and for providing a simple first step and test bed for more complex matter models [80, 94].

Studies have demonstrated that boson stars are stable to perturbations provided that the central density of the star is sufficiently small [53, 73, 73, 75, 80, 86]. However, without a self-interaction term in the potential, the mass of the star scales as $\frac{1}{2}m_p^2/m$ (where m_p is the Planck mass and m is the boson mass). For reasonable particle masses, this results in stars with masses far below the usual Chandrasekhar limit for fluid stars [12, 46, 80]. Thus, these so-called mini-boson stars are

useful primarily as a test bed with their more specialized cousins (having, for example, additional terms in the potential) being adapted to various astrophysical situations [80].

Whereas boson stars gain their stability through a conserved charge and the interplay between pressure and gravity, global monopoles are topologically stable [16, 119, 126]. Along with other topological defects such as textures, domain walls, and strings, monopoles are expected to form fairly generically when underlying field symmetries are broken through early-universe phase transitions which are mediated by expansion and cooling [126].

In the case of the monopole, the simplest class of defect consists of a scalar field triplet with a global $O(3)$ symmetry which is spontaneously broken to $U(1)$ on a non-contractible 2-surface. If the broken symmetry is local, the resulting monopole is shielded by the Maxwell field and has finite energy and extent. Conversely, if the field exhibits a global symmetry, we find that the resulting energy is linearly divergent in radius [16, 93, 119, 126].

Although this divergence may seem somewhat problematic, there are two important caveats. First, the energy divergence cuts off upon encountering another monopole or antimonopole. Second, in the context of general relativity, the energy divergence has the simple effect of producing a solid angle deficit spacetime along with a small effective negative mass core, rather than more exotic features [16, 93, 107, 119]. As shown by Barriola et al. [16], we would expect global monopoles and anti-monopoles to annihilate extremely efficiently due to the fact that the interaction strength between them is independent of distance. Although this annihilation is avoided by local monopoles, we expect a Hubble volume to contain only ≈ 1 global monopole at the present time due to the efficiency of this interaction.

Putting aside these considerations, when a global monopole and boson star are combined, the result is a novel object referred to as a topological-defect boson star or "d-star". Previously studied in [78, 79, 83, 107], it was shown that through non-minimal coupling and proper choice of interaction parameters, d-stars could be made extremely dense, thereby potentially acting as mimickers of black holes or other highly compact objects [83]. Subsequent in-depth investigation of these objects revealed novel interactions and ground state solutions [107]. When viewed as functions of the boson star central density, these ground state solutions are characterized by discontinuous changes in the global properties of the system (mass, charge, etc.). To better describe this behaviour, we borrow the terminology of statistical mechanics. In this analogy, the central density of the boson star takes the place of the temperature, the asymptotic mass takes the role of the energy and the mass gap is similar to latent heat.

The discontinuous changes in global properties are mediated by the appearance or disappearance of shells of bosonic matter at characteristic radii which can be either finite or infinite. We use the term *asymptotic shell* to refer to any shell of matter which first appears far from the coordinate origin as $\psi(0)$ is increased past some critical value and which subsequently vanishes when $\psi(0)$ is further increased past a second critical value. We refer to those families of solutions with mass gaps (when the mass is viewed as a function of the central density) as expressing a first order phase transition. Those with discontinuities in the derivative of the asymptotic mass or charge express a second order phase transition. The interested reader is directed to [107] for an in-depth review.

4.2 Review of Stationary D-Stars

We have previously solved the equations of motion assuming stationary solutions, the harmonic ansatz for the boson field and a hedgehog ansatz for the monopole fields [107]. The solutions we discovered were characterized by a series of discrete boson star central amplitudes, $\psi_i^c(0)$, about which the character of the solutions changed discontinuously in a manner analogous to a phase transition.

In what follows, we will use the same terminology and notation as our previous paper [107], which is briefly reviewed below.

The parameter space we consider here is six-dimensional, spanned by the central amplitude of the boson star, $\psi(0)$, and five coupling parameters: the solid angle defect, Δ^2, the quartic global monopole potential parameter, λ_G, the quartic boson star potential parameter, λ_B, the global monopole non-minimal coupling, ξ_G, and the boson star non-minimal coupling, ξ_B. We fix the mass of the boson star field, $m = 1$, and note that this sets the energy scale of the solutions. We define a *family* of solutions to be the set of all ground state solutions with common Δ, λ_G, λ_B, ξ_G and ξ_B. As such, within a given family, solutions can be indexed by the boson star central amplitude, $\psi(0)$, which is the only free parameter of the family (see Fig. 4.1).

Due to the large parameter space associated with these solutions, it was not feasible to perform a comprehensive parameter space survey. Instead, as in [107], we focus on a number of families of solutions which appear to capture the novel behavior associated with the model. In subsequent sections we deal with eight families of solutions whose fixed parameters are given in Table 4.1. For simplicity, the boson star quartic self interaction coupling constant, λ_B, has been set to 0 under the assumption that its primary effect will be to produce more compact objects (while having only a minor effect on the low density asymptotic shells that we find). Those families that were investigated in [107] were given identical designations.

Family	Δ^2	λ_B	λ_G	ξ_B	ξ_G
c	0.36	0	1.000	0	0
d	0.81	0	0.010	0	0
e	0.25	0	0.001	3	3
f	0.49	0	0.010	5	0
g	0.09	0	0.010	0	5
h	0.08	0	0.100	-4	5
p_1	0.09	0	0.040	0	0
p_2	0.25	0	0.040	0	0

Table 4.1: Families of solutions and their associated parameters. Each family consists of a continuum of solutions labelled by the central amplitude of the boson star. In particular, family h corresponds to a family in the high compactness regime as defined in [83]. Due to their relatively simple and illustrative modal structure, families p_1 and p_2 are the only ones we explore with perturbation theory.

We define a *branch* of a family to be the set of all solutions in the family where the asymptotic mass, M_∞, is C^1 as a function of the central amplitude, $\psi(0)$. Using this definition, Fig. 4.1 provides a mass plot illustrating a hypothetical family with three branches. We use the term *region* to refer to the set of all solutions on a given branch between extremal values of the asymptotic mass. Using our previous example, the first branch of Fig. 4.1 consists of a single region while the second and third branches each consist of two regions.

As demonstrated in Fig. 4.2, which plots the asymptotic mass, M_∞, of a family of solutions, this mass parameter is not in general a smooth function of the boson star central amplitude, $\psi(0)$, as would be expected for a fluid star. As we construct families of stationary solutions by varying the central amplitude of the boson star (keeping all other parameters fixed) we find that when the central amplitude is increased or decreased across a critical point $\psi_i^c(0)$, a shell of bosonic matter will either appear or vanish far from the center of symmetry. As shown in [107], these shells of matter may either appear suddenly at spatial infinity, or gradually at a finite radius when the boson

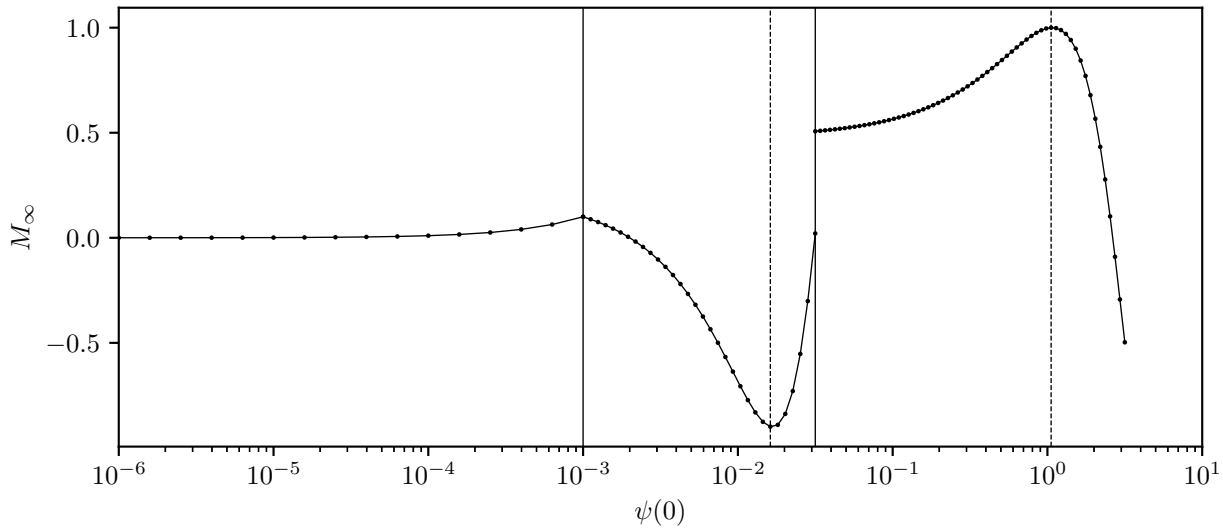

Figure 4.1: Asymptotic mass as a function of central amplitude for a hypothetical family consisting of three branches. The first branch consists of a single region while each of the subsequent branches consist of two regions, the extent of which are delimited by their mass turning points. Solid vertical lines denote the extent of branches while regions within a branch are separated with vertical dashed lines.

star is non-minimally coupled to gravity.

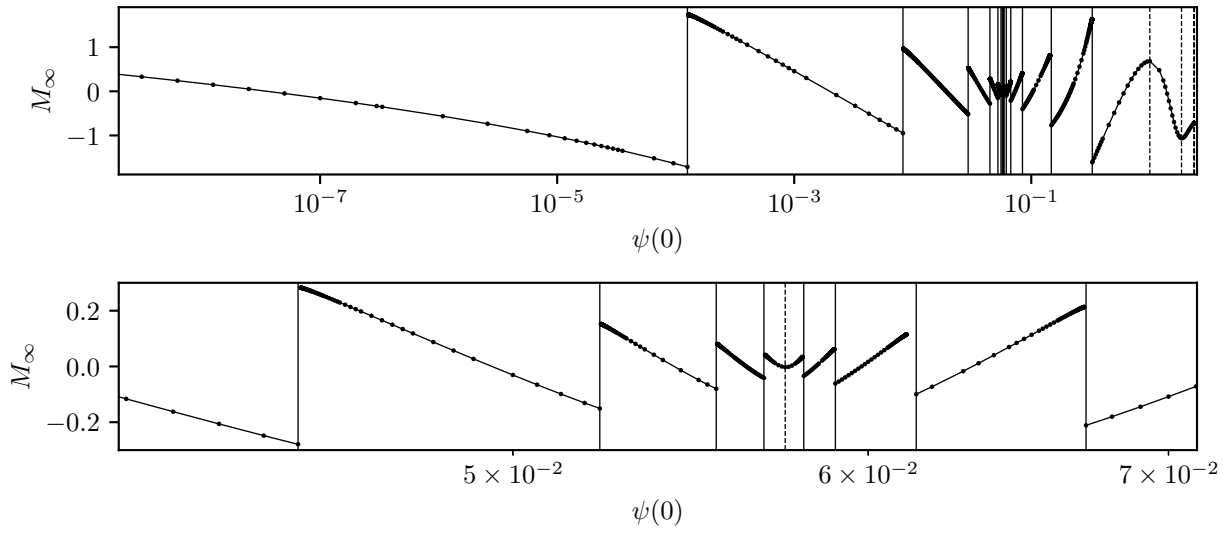

Figure 4.2: Asymptotic mass as a function of central amplitude for family d. The lower panel shows an expanded view of the upper plot highlighting the central structure. As demonstrated in [107], the apparent discontinuities are genuine. These discontinuities correspond to shells of bosonic matter of finite mass and particle number appearing or disappearing at spatial infinity.

As discussed in full detail in [107], these families of solutions have features that are in many ways analogous to critical points and phase transitions in thermodynamical systems. When shells

appear at infinity with finite mass, we have a direct analogy with first order phase transitions with $\psi(0)$ taking the role of the temperature or pressure and the mass gap being analogous to the latent heat. When the transition is gradual, as in the case of non-minimal coupling, we have a situation more analogous to second order, or continuous, phase transitions.

4.3 Overview

In analysing the stability of the boson d-star solutions, we adopt a two pronged approach. First, we consider the general non-minimally coupled case and perform dynamical simulations of a number of families which seem to be representative of the model as a whole. Specifically, from these families we choose a few solutions from each branch, perturb the solutions and follow the evolution of the system, looking for growth of excited modes. Previous studies have shown that stability transitions are confined to turning points of the asymptotic mass or charge when these quantities are viewed as functions of boson star central amplitude [53, 69, 73, 75]. We greatly simplify our investigation by considering only a small number of evolutions per region and by assuming that the observed stability for these simulations generalizes across the entire region.

Our second approach involves a detailed analysis of the mode structure of the d-star solutions via linear perturbation analysis. Due to the complexity of the resulting equations for the non-minimally coupled case, we limit ourselves to the investigation of the minimally coupled configurations. Through an exhaustive investigation of two families, we deduce a general mode structure which is in broad agreement with the results of our dynamical simulations.

4.4 Matter Model

Following the prescription of Marunovic and Murkovic [83], the dimensionless Einstein-Hilbert action ($c = 1, G = 1/8\pi$) is given by

$$S_{\mathrm{EH}} = \int dx^4 \sqrt{-g}\, \frac{R}{2} \tag{4.1}$$

while the actions for the boson star and global monopole are:

$$S_B = \int dx^4 \sqrt{-g} \left[-\frac{1}{2} \left(\nabla_u \Psi^*\right) \left(\nabla^u \Psi\right) - V_B + \frac{\xi_B}{2} R \left(\Psi^* \Psi\right) \right], \tag{4.2}$$

$$S_G = \int dx^4 \sqrt{-g} \left[-\frac{\Delta^2}{2} \left(\nabla_u \phi^a\right) \left(\nabla^u \phi^a\right) - V_G + \frac{\xi_G}{2} R \Delta^2 \left(\phi^a \phi^a\right) \right]. \tag{4.3}$$

Here, Ψ is the complex boson star field, ϕ^a are scalar field triplets comprising the monopole, V_B and V_G are the self interaction potentials for the boson field and monopole fields respectively, R is the Ricci scalar and ξ_B and ξ_G are the non-minimal coupling constants. The stress-energy tensors associated with the matter actions are:

$$\begin{aligned} T^B_{\mu\nu} = {} & \frac{1}{2} \nabla_\mu \Psi^* \nabla_\nu \Psi + \frac{1}{2} \nabla_\nu \Psi^* \nabla_\mu \Psi - \frac{1}{2} g_{\mu\nu} \left(\nabla_\alpha \Psi \nabla^\alpha \Psi^* + 2 V_B \right) \\ & - \xi_B \left(G_{\mu\nu} + g_{\mu\nu} \nabla_\alpha \nabla^\alpha - \nabla_\mu \nabla_\nu \right) \Psi \Psi^*, \end{aligned} \tag{4.4}$$

$$\begin{aligned} T^G_{\mu\nu} = {} & \frac{\Delta^2}{2} \nabla_\mu \phi^a \nabla_\nu \phi^a + \frac{\Delta^2}{2} \nabla_\nu \phi^a \nabla_\mu \phi^a - \frac{1}{2} g_{\mu\nu} \left(\Delta^2 \nabla_\alpha \phi^a \nabla^\alpha \phi^a + 2 V_G \right) \\ & - \xi_G \Delta^2 \left(G_{\mu\nu} + g_{\mu\nu} \nabla_\alpha \nabla^\alpha - \nabla_\mu \nabla_\nu \right) \phi^a \phi^a. \end{aligned} \tag{4.5}$$

We use the standard 3+1 decomposition where 4D spacetime is foliated into a sequence of spacelike hypersurfaces, Σ_t, such that each hypersurface of constant t has a 3-metric, γ_{ij}. Explicitly, the 4-metric takes the form

$$g_{\mu\nu} = \begin{pmatrix} -\alpha^2 + \beta^i\beta_i & \beta_j \\ \beta_i & \gamma_{ij} \end{pmatrix}. \tag{4.6}$$

with a time-like normal, n^ν, to the foliation, Σ_t, given by

$$n^\nu = \left(\frac{1}{\alpha}, -\frac{\beta^i}{\alpha}\right). \tag{4.7}$$

Here, α and β^i are the usual lapse and shift respectively. We impose spherical symmetry, and adopt polar-areal coordinates such that the line element becomes

$$ds^2 = -\alpha(t,r)^2dt^2 + a(t,r)^2dr^2 + r^2\left(d\theta^2 + \sin^2\theta d\phi^2\right). \tag{4.8}$$

Decomposing the boson field into a real and imaginary part and taking the hedgehog ansatz for the monopole, the matter fields and corresponding potentials are

$$\Psi = \phi_R + i\phi_I, \tag{4.9}$$
$$\phi^a = \phi_M\frac{x^a}{r}, \tag{4.10}$$
$$V_G = \frac{\lambda_G}{4}\Delta^4(\phi_M^2 - 1)^2, \tag{4.11}$$
$$V_B = \frac{m^2}{2}\left(\phi_R^2 + \phi_I^2\right) + \frac{\lambda_B}{4}\left(\phi_R^2 + \phi_I^2\right)^2. \tag{4.12}$$

Varying the actions with respect to the matter fields gives the equations of motion for the matter:

$$\nabla_\mu\nabla^\mu\phi_R = \phi_R\partial V_{\phi_R} - \xi_B R\phi_R, \tag{4.13}$$
$$\nabla_\mu\nabla^\mu\phi_I = \phi_I\partial V_{\phi_I} - \xi_B R\phi_I, \tag{4.14}$$
$$\nabla_\mu\nabla^\mu\phi_M = \frac{\phi\partial V_{\phi_M}}{\Delta} + \frac{2\phi_M}{r^2} - \xi_G R\phi_M, \tag{4.15}$$

where:

$$\partial V_{\phi_R} = m^2\phi_R + \lambda_B\left(\phi_R^2 + \phi_I^2\right)\phi_R, \tag{4.16}$$
$$\partial V_{\phi_I} = m^2\phi_I + \lambda_B\left(\phi_R^2 + \phi_I^2\right)\phi_I, \tag{4.17}$$
$$\partial V_{\phi_M} = \lambda_G\Delta^4\left(\phi_M^2 - 1\right)\phi_M. \tag{4.18}$$

We express the fields $\phi_A = (\phi_R, \phi_I, \phi_M)$ in terms of their conjugate momentum and spatial derivatives:

$$\Pi_A = \frac{a}{\alpha}\partial_t\phi_A \tag{4.19}$$
$$\Phi_A = \partial_r\phi_A \tag{4.20}$$

Evaluating tensor components and simplifying, the equations of motion for the matter fields may be expressed as

$$\partial_t \Pi_R = -(\xi_B \phi_R T + \partial_{\phi_R} V)\,\alpha a + \partial_r \left(\frac{\Phi_R \alpha}{a}\right) + \frac{2\Phi_R \alpha}{ra}, \tag{4.21}$$

$$\partial_t \Pi_I = -(\xi_B \phi_I T + \partial_{\phi_I} V)\,\alpha a + \partial_r \left(\frac{\Phi_I \alpha}{a}\right) + \frac{2\Phi_I \alpha}{ra}, \tag{4.22}$$

$$\partial_t \Pi_M = -\left(\xi_G \phi_M T + \frac{\partial_{\phi_M} V}{\Delta^2} + \frac{2\phi_M}{r^2}\right)\alpha a + \partial_r \left(\frac{\Phi_M \alpha}{a}\right) + \frac{2\Phi_M \alpha}{ar}. \tag{4.23}$$

$$\partial_t \Pi_P = \partial_r \left(\frac{\Phi_P \alpha}{a}\right) + \frac{2\Phi_P \alpha}{ra}. \tag{4.24}$$

Here, we have used the contracted Einstein equation $R = -T$, and have incorporated a massless scalar field, ϕ_P, to facilitate perturbation of the stationary solutions. The choice of polar-areal coordinates greatly simplifies the Einstein equations and after a considerable amount of manipulation we arrive at the form of the equations given in Appendix B.1.

4.4.1 Boundary Conditions

Given the hedgehog ansatz (4.10), ϕ_M is the magnitude of the global monopole fields, ϕ^a, which are analogous to an outward pointing vector field. As such, to maintain regularity we must have $\phi_M = 0$, at the center of symmetry. Further, as $r \to 0$, regularity requires ϕ_R, ϕ_I, ϕ_P, Π_R, Π_I, Π_P, a and α be even functions of r (with $a(t,0) = 1$) while ϕ_M and Π_M are odd functions of r.

In the limit that $r \to \infty$, the boson star field exponentially approaches zero while the global monopole transitions to its vacuum state ($\phi_R \to 0$, $\phi_I \to 0$, $\phi_M \to 1 + \sum_i c_i r^{-i}$). Defining $\tilde{\Delta}$ by

$$\tilde{\Delta} = \frac{\Delta^2}{1 + \xi_G \Delta^2}, \tag{4.25}$$

and assuming a series expansion in $1/r$, the metric equations can be integrated to yield the following regularity conditions as r approaches infinity [83, 92]:

$$\phi_R = \phi_I = \phi_P = 0, \tag{4.26}$$

$$\phi_M = 1 - \frac{1}{\lambda_G \Delta^2 r^2 \left(1 + \xi_G \Delta^2\right)}, \tag{4.27}$$

$$\Pi_R = \Pi_I = \Pi_P = \Pi_M = 0, \tag{4.28}$$

$$a = \left(1 - \tilde{\Delta} - \frac{2M}{r}\right)^{-1/2}, \tag{4.29}$$

$$\alpha = \left(1 - \tilde{\Delta} - \frac{2M}{r}\right)^{1/2}. \tag{4.30}$$

Here, M is a constant of integration proportional to the ADM mass of a solid angle deficit spacetime as defined in the next section.

4.4.2 Conserved and Diagnostic Quantities

The global $U(1)$ invariance of the boson star field gives rise to a conserved current,

$$J_\mu = \frac{i}{16\pi}\left(\Psi^*\nabla_\mu\Psi - \Psi\nabla_\mu\Psi^*\right), \tag{4.31}$$
$$= \frac{1}{8\pi}\left(\phi_I\nabla_\mu\phi_R - \phi_R\nabla_\mu\phi_I\right),$$

with temporal component,

$$J_t = \frac{\alpha}{8\pi a}\left(\phi_I\Pi_R - \phi_R\Pi_I\right). \tag{4.32}$$

Associated with the current is a conserved charge,

$$N = \int J_\nu n^\nu \sqrt{\gamma} dx^3, \tag{4.33}$$

with spatial gradient,

$$\partial_r N = \frac{r^2}{2}\left(\phi_I\Pi_R - \phi_R\Pi_I\right). \tag{4.34}$$

Although the energy of the spacetime is linearly divergent in r, it is possible to use the prescription of Nucamendi et al. [93] to define an ADM-like mass, $M_{\rm ADM}$, for a solid angle deficit spacetime as

$$M_{\rm ADM} = \frac{1}{16\pi\left(1-\tilde{\Delta}\right)}\int_{\partial\Sigma_t}\left(\bar{\gamma}^{ac}\bar{\gamma}^{bd} - \bar{\gamma}^{ab}\bar{\gamma}^{cd}\right)\bar{D}_b\left(\gamma_{cd}\right)dS_a. \tag{4.35}$$

Here $\bar{\gamma}_{ab}$ is a metric which is flat everywhere save a deficit solid angle, and which is induced on all constant time hypersurfaces, Σ_t. $\bar{D}_b$ is the associated connection and dS_a is the surface area element [93].

Evaluation of (4.35) using the asymptotic forms of the metric functions (4.29)–(4.30) under the coordinate changes prescribed by Nucamendi, yields

$$M_{\rm ADM} = M\left(1-\tilde{\Delta}\right)^{-3/2}, \tag{4.36}$$

where M is defined as in Eqn. (4.29). We further define a mass function as

$$M(t,r) = \frac{r}{2}\left(1 - a(t,r)^{-2} - \tilde{\Delta}\right), \tag{4.37}$$
$$M_\infty \equiv \lim_{r\to\infty} M(t,r), \tag{4.38}$$

and use it to monitor energy conservation of the system. We also use the above definition of $M(t,r)$ to define a measure of the compactness of the system. Specifically, following Marunovic and Murkovic [83], we define the compactness as

$$C(t,r) \equiv \frac{2M(t,r)}{r\left(1-\tilde{\Delta}\right)}, \tag{4.39}$$

such that $C(t,r_0)\to 1$ indicates the development of an apparent horizon at areal radius r_0. Correspondingly, we define the quantity $C_{\rm max}$ as

$$C_{\rm max} \equiv \max\left(C(t,r)\right). \tag{4.40}$$

For any given configuration of matter, then, $C_{\rm max}$ measures the maximum compactness of the configuration.

4.5 Dynamical Simulation

This section provides an overview of our evolution scheme and associated numerics. Section 4.5.1 details the initialization of the metric and matter fields, while Sec. 4.5.2 introduces the finite difference discretizations used to solve the equations of motion and describes the evolution procedure. Sec. 4.5.3 specifies the tests used to ensure convergence of our scheme. Finally, Sec. 4.5.4 describes our method of extracting stable and unstable perturbative modes from the dynamical simulations.

4.5.1 Initial Data

To initialize an evolution, the boson star fields, ϕ_R and ϕ_I, global monopole field, ϕ_M, and metric fields, a and α, are interpolated to the evolution grid from a stationary solution (computed using the methodology described in [107]) using a high order interpolation scheme. Subsequently, we add a small perturbation consisting of either a Gaussian pulse in the massless scalar field, ϕ_P, or a rescaling of the matter fields. Finally, the Hamiltonian and momentum constraints are re-integrated to account for the perturbation and the system is ready for evolution.

Specifically, when considering a case where the excited modes are observed to grow slowly compared to the light-crossing time of the star, the perturbation is set using a time-symmetric massless scalar field pulse of the form

$$\phi_P(0,r) = a_0 \exp\left(-\frac{(r-r_0)^2}{\sigma_0^2}\right), \tag{4.41}$$

where a_0, σ_0 and r_0 determine the location and intensity of the pulse at $t = 0$. A portion of this time symmetric pulse implodes inwards and excites perturbative modes in the boson d-star before dispersing to infinity.

When the growth rate of the perturbative modes are large compared to the scale of the star, this approach fails to produce good results (e.g. the perturbations evolve into the non-linear regime before the perturbing pulse is able to disperse). In this case, the truncation error induced by restricting the stationary solutions to the evolution grid (which is quite coarse compared to the one used to determine the time-independent solutions) induces growth modes over which we have very little control. These modes quickly become the dominant source of perturbation and hamper the extraction of useful information from the simulations. To overcome this, we introduce a perturbation by rescaling the matter fields as,

$$\phi_i(x) \to \phi_i\left((1+\lambda)\,x\right), \tag{4.42}$$

where λ is taken to be a small number, typically on the order of 10^{-5}, and reintegrating the Hamiltonian and polar slicing condition. Here, x, is a compactified spatial coordinate as will be discussed shortly. Although this form of perturbation works well, it is decidedly less natural than perturbing with an external matter field and we stick to the former approach whenever possible.

4.5.2 Evolution Scheme

We evolve the matter field quantities using (4.19)–(4.24) and a second order finite difference scheme with Crank-Nicholson differencing. To damp high frequency solution components we add fourth order, temporally centered, Kreiss-Oliger dissipation. Due to the global nature of the monopole field, the need to evolve the simulations for many dynamical time scales, and the fact that it helps

in implementing the $r \to \infty$ boundary conditions, we adopt compactified coordinates defined by:

$$r = \frac{\lambda x}{1-x}, \quad 0 \leq x \leq 1, \tag{4.43}$$

where λ is a positive real number that typically satisfies $1 \leq \lambda \leq 100$. Specifically, λ is chosen so that all solution features are well resolved with our choice of mesh spacing. Since x compactifies the entire domain of r, this coordinate change works in conjunction with our numeric dissipation operators to suppress wave like oscillations far from $r = 0$. This in turn permits us to forgo crafting outgoing boundary conditions for our fields and instead impose trivial boundary conditions corresponding to (4.26)–(4.30) at the $x = 1$ limit of our domain. Care must be taken, however, to ensure that the parity of functions at the origin is treated according to their behaviour in r rather than x.

As noted in Appendix B.1, it is possible to find an expression for $\partial_r a$ independent of α. As such, we may consider the equation for the metric as two initial value problems rather than a coupled boundary value problem. In practice, we find the most effective method of solving for the metric functions is to integrate $\partial_r a$ from $x = 0$ to $x = 1$, initialize $\alpha = 1/a$ at $x = 1$, and integrate $\partial_r \alpha$ back to $x = 0$.

Although our overall evolution scheme is well suited to the evolution of highly dynamical simulations, its utility for investigating nearly stationary solutions and the growth of perturbations is limited by the use of second order finite difference operators. In particular, there are significant restrictions on the period of time for which a simulation may be run before dispersion becomes the dominant factor limiting solution accuracy. The scheme was chosen for ease of implementation, but fourth order finite difference or spectral schemes would be far superior for the purpose of resolving modes with very slow growth rates.

4.5.3 Convergence

To validate the stability of the evolution scheme and to ensure that mass and charge are approximately conserved for dynamic configurations, we choose initial data consisting of a stationary solution perturbed by a large-amplitude massless scalar field pulse at the origin. The mass energy of the massless scalar field is a significant fraction of the total mass energy of the system, so the system as a whole is highly perturbed from stationarity. Specifically, the monopole is non-stationary far from the origin due to its coupling to the modified metric functions.

We demonstrate the convergence of our algorithm via the evolution of slightly sub-critical (i.e. slightly stronger initial perturbations would result in black hole formation), non-minimally coupled, initial data. In verifying the validity of our evolutionary scheme, we make use of the technique of independent residual evaluators. This involves creating alternative discretizations of the equations of motion (EOM) which are then applied to solutions computed via our evolutionary scheme. More explicitly, our evolutionary scheme solves the difference equations,

$$\tilde{D}(u^h) - f^h = 0, \tag{4.44}$$

where $\tilde{D}$ is some non-linear difference operator and u^h and f^h are our discretized fields with grid spacing h. The technique of independent residual evaluation involves finding an alternative discretization, $\tilde{D}'$, application of which to our pre-computed solution, u^h, yields,

$$\tilde{D}'(u^h) - f^h = \tilde{r}^h. \tag{4.45}$$

If $\tilde{r}^h$ is observed to converge at order $O(h^2)$, it implies that both $\tilde{D}$ and $\tilde{D}'$ match to order $O(h^2)$ and provides confidence—far beyond what can be achieved with standard convergence tests—that

we are solving the correct EOM. Figure 4.3 shows representative independent residual convergence of strong field initial data for a range of grid spacings while Figs. 4.4 and 4.5 plot conserved quantity violations for the same solutions. From these plots, it can be seen that the solution algorithm is convergent in the strong field limit.

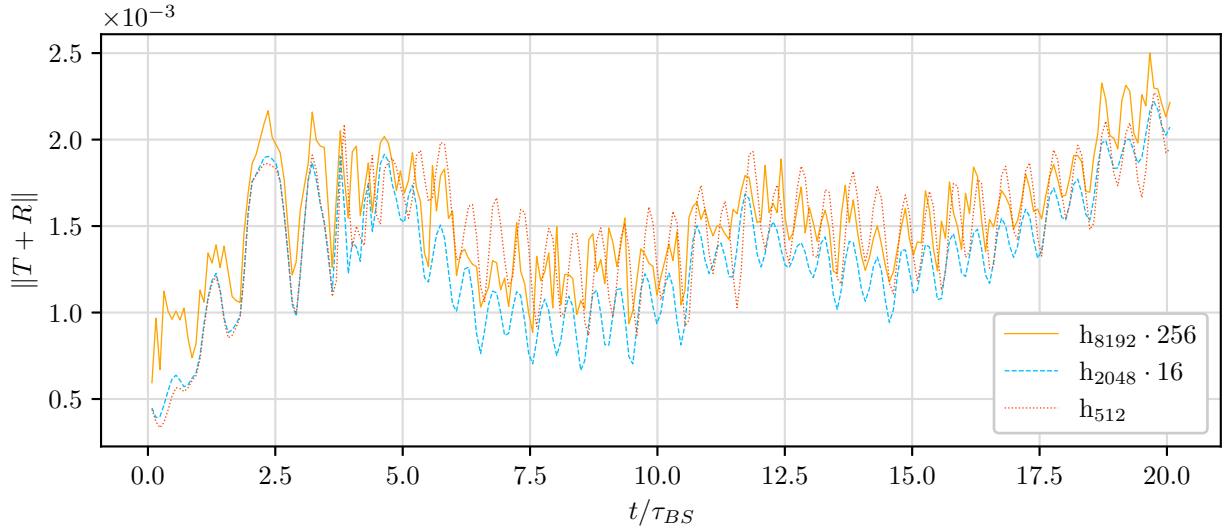

Figure 4.3: Convergence of the l_2-norm of independent residuals for the trace of the Einstein field equations ($T + R = 0$) in the case of a very strongly perturbed d-star. The residuals of the higher resolution simulations are scaled by 16 and 256, respectively such that overlap of the curves implies second order convergence. This figure encompasses approximately 50 light-crossing times or 20 periods of the central boson star oscillation, $\tau_{\rm BS}$.

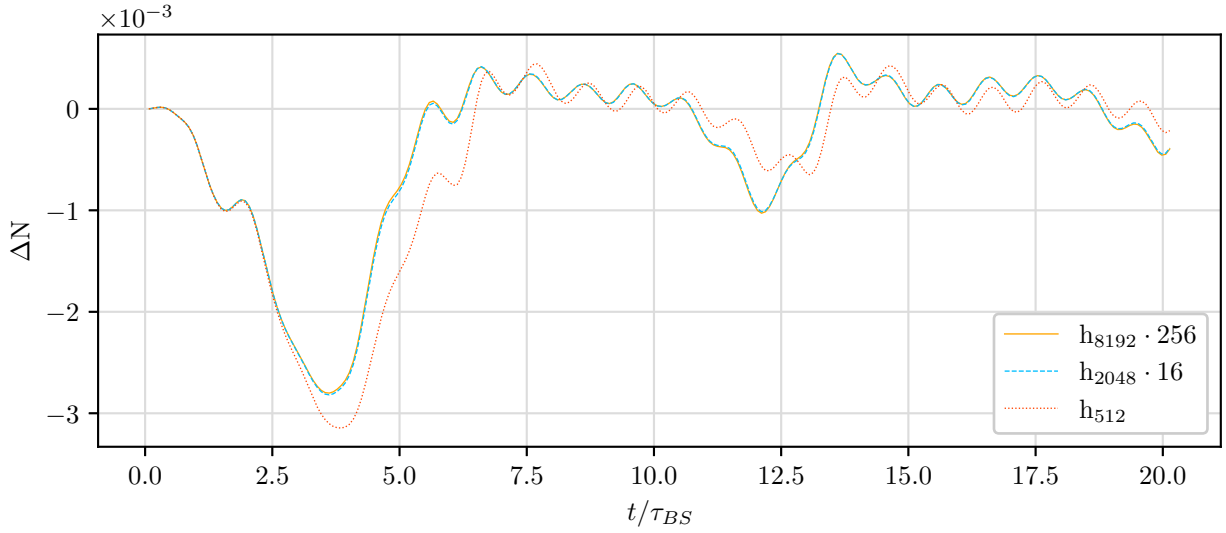

Figure 4.4: Convergence of charge conservation for strong field data where the residuals of the higher resolution simulations have been scaled such that overlap of the curves implies second order convergence. The oscillation period of the unperturbed central boson star is denoted $\tau_{\rm BS}$.

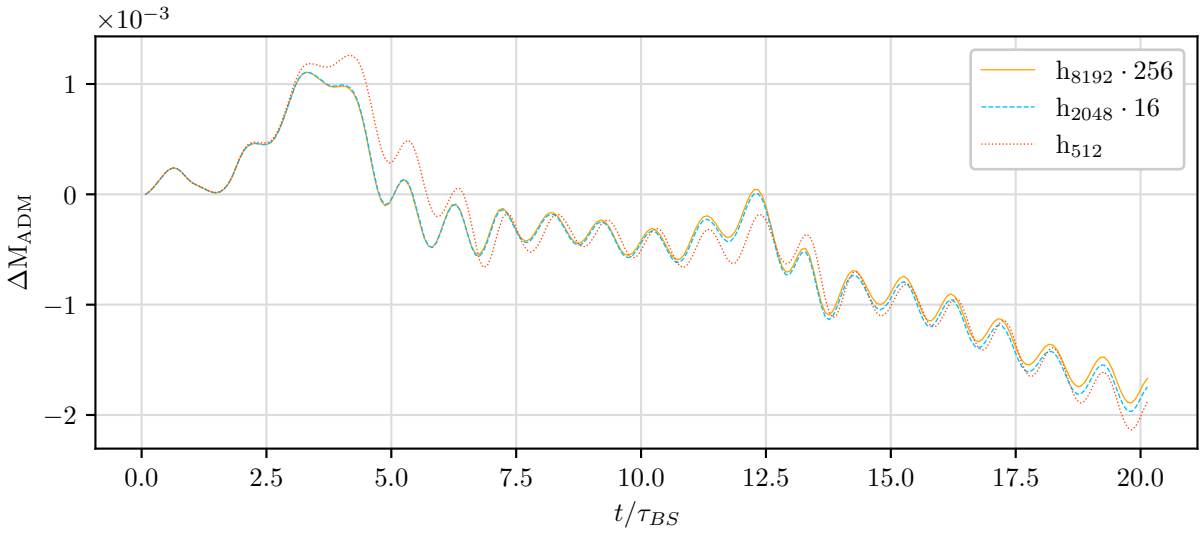

Figure 4.5: Convergence of mass conservation for strong field data where the residuals of the higher resolution simulations have been scaled such that overlap of the curves implies second order convergence.

4.5.4 Extraction of Growth Modes

The basic mechanics of a perturbation theory analysis suggest an obvious means by which the stability of a solution may be tested. By monitoring the growth rate of a quantity which would remain constant were the solution unperturbed, we can make a direct measurement of the eigenvalue of the dominant mode. In the case of instability, we expect to see exponential growth in the norm of the perturbation. In contrast, the norm of a perturbed quantity which is stable should oscillate in time. In both cases, the growth rate or period, respectively, may be determined by appropriate fits to the perturbed quantity.

A note of caution is, however, warranted: the method described above is only capable of determining a *lower* bound for the instability of the system. It is entirely possible for this method to miss unstable modes with eigenvalues much smaller than those of the excited stable modes (in which case the growth rate of the former is masked by oscillations of the latter). In an effort to counter this problem, we evolve the perturbed solutions for many dynamical timescales as given by the lowest frequency stable mode. This typically translates to hundreds of light-crossing times and thousands of boson star oscillations. Although we can never state with absolutely certainty that a solution is stable, we will nonetheless use that terminology when no growing modes are detected over such time scales.

Previous stability studies [53, 69, 73, 75] have shown that boson stars, like fluid stars, undergo stability transitions only at solutions corresponding to extrema of the asymptotic mass, M_∞, as is predicted by catastrophe theory. We therefore work under the assumption that all sets of stationary solutions in the same region (bounded by extrema of M_∞) exhibit similar stability properties. The results of Sec. 4.7.2 serve to validate this assumption for the minimally coupled case. The results presented in Sec. 4.7.1 are therefore derived from a small number of simulations chosen to be representative of each region in a given family. Typically, we perform between two and three simulations for each region.

In our analysis we make extensive use of the Noether charge as a stability diagnostic rather

than using matter fields or metric functions. Given (4.33), we see that the Noether charge is a derived quantity, tied tightly to both the metric functions and bosonic matter fields. As such, any changes to those fields are immediately reflected in the Noether charge, making it an ideal quantity for monitoring stability and for comparing the form of excited modes to those predicted by perturbation theory.

4.6 Linear Perturbation Theory

Proceeding in standard fashion, we decompose the perturbed solution, $f(t,r)$, into a stationary component and an integral over Fourier modes:

$$f(t,r) = f_0(r) + \int_{-\infty}^{\infty} \hat{f}(r,\beta) e^{i\beta t} d\beta. \tag{4.46}$$

We substitute $f(t,r) = f_0(r) + \epsilon \delta f(r) e^{i\beta t}$ into the equations of motion and expand to linear order order in ϵ. By doing so, we reduce our system of PDEs to a system of ODEs that represents the growth rate of various modes and that constitutes an eigenvalue problem in β^2. In general, this system cannot be solved for all values of β^2 while retaining conservation of our conserved quantities; for most values of β^2, the solution obtained implies that the integral of the various conserved quantities is time dependent. For those countable number of modes that do satisfy the requisite boundary conditions for the conserved quantities, those with $\beta^2 > 0$ will be stable while those with $\beta^2 < 0$ will be unstable.

Following Gleiser and Watkins [53], we transform to a set of variables ($\mu(t,r)$, $\nu(t,r)$, $\psi_R(t,r)$, $\psi_I(t,r)$, $\phi(t,r)$) defined by:

$$a = e^{\mu/2}, \tag{4.47}$$

$$\alpha = e^{\nu(t,r)/2}, \tag{4.48}$$

$$\Psi = e^{-i\omega t} \left(\psi_R + i\psi_I\right), \tag{4.49}$$

$$\phi_M = \phi. \tag{4.50}$$

The derivation and final form of the perturbation equations have been relegated to Appendix B.2 due to their significant complexity.

4.6.1 Solution Procedure

Even in the minimally coupled case, finding solutions to (B.23)–(B.28) proves to be quite challenging. Examination of the regularity conditions at the origin reveals that the appropriate degrees of freedom in the problem are given by β^2, $\delta\psi_R(r)|_{r=0}$, $\delta\psi_I(r)|_{r=0}$ and $\partial_r \delta\phi(r)|_{r=0}$. Due to the linearity of the problem, we are free to set $\delta\psi_R(r)|_{r=0} = 1$ and the equations therefore constitute an eigenvalue-boundary value problem in the remaining degrees of freedom. In general, for inexactly chosen boundary values and β^2, the matter and metric functions may only be integrated to a finite distance from the origin before the solution becomes pathological. As such, we cannot use, for example, gradient descent techniques to tune these parameters and instead turn to an iterative shooting method [107].

We expect that each successive mode of solutions to (B.23)–(B.28) will develop an additional node in each of the field variables. Correspondingly, we choose a trial value of β^2 (manually due to the difficulty encountered automating the process) and set $\delta\phi(r) = 0$. Once the fields have been initialized, we shoot on $\delta\psi_I(r)|_{r=0}$ for $\delta\psi_R$ and $\delta\psi_I$ holding $\delta\phi$ fixed until the bosonic fields

are well behaved far from the origin. We then fit a decaying tail to $\delta\psi_I$ and $\delta\psi_I$, and shoot on $\partial_r(\delta\phi)|_{r=0}$ holding the bosonic fields fixed. This shooting procedure is repeated several times until approximate convergence is achieved. Finally, we examine δN_∞ and adjust β^2, repeating the entire shooting procedure until a solution is found with $\delta N_\infty \approx 0$ to within tolerance (typically 0.05 of the maximum value of $\delta N(r)$ is sufficient). This process of determining initial data in compactified coordinates x is summarized in Algorithm 3.

Algorithm 3 Iterated Shooting Procedure

initialize background fields on the compactified grid x
initialize $\delta\phi(x)$ to 0
initialize $\delta\psi_R(x)$ and $\delta\psi_I(x)$ to 0
while $\delta N_\infty \gg 0$ **do**
  choose β^2
  while solution non-convergent **do**
    hold $\delta\phi(x)$ fixed
    shoot for $\delta\psi_R(x)$ and $\delta\psi_I(x)$
    fit tail to $\delta\psi_R(x)$ and $\delta\psi_I(x)$
    integrate $\delta\nu(x), \delta\mu(x)$ and δN to asymptotic region

    hold $\delta\psi_R(x)$ and $\delta\psi_I$ fixed
    shoot for $\delta\phi(x)$
    fit tail to $\delta\phi(x)$
    integrate $\delta\nu(x), \delta\mu(x)$ and δN to asymptotic region
  end while
end while

Upon achieving the desired tolerance, the approximate solution is used as an initial guess for a boundary value problem solver based on the collocation library TWPBVPC [84]. If the initial guess is sufficiently close to the true solution, the solver converges quickly, resulting in a solution which is accurate to within tolerance (typically 10^{-12} or better). By slowly adjusting the central amplitude, $\psi(0)$, of the stationary solution and using the previous solution to the perturbative equations as an initial guess, we can use the process of continuation to investigate the development of the mode throughout a branch of a family. [4]

As discussed in Sec. 4.5, we only perform 2 or 3 evolutions per region to assess dynamical stability. In contrast, the process of continuation gives a much more comprehensive view of the mode structure within a region. By repeating this procedure on every branch and near every extremal point of M_∞ (including discontinuities), we can achieve an accurate picture of the mode structure of the family under investigation.

Note also that, due to the presence of asymptotic shells of matter which are present in some of these solutions, traditional shooting techniques may fail to adequately resolve the perturbed boson fields. The inability of double precision shooting to provide an adequate initial guess to the TWPBVPC based solver may be resolved, to some degree, through the use of extended precision

[4] From a technical perspective, it is worth noting how the β^2 eigenvalue is incorporated in TWPBVPC. Following [82], we implemented the β^2 eigenvalue as an additional field satisfying the trivial equation $\partial_x(\beta^2(x)) = 0$.

integrators or through the use of our multi-precision shooting method [107]. Even then, we find that perturbative solutions in the presence of an asymptotic shell are quite difficult to find without the aid of continuation.

4.6.2 Convergence

As with the dynamical evolutions, we verify the convergence of our perturbative solutions via an independent residual convergence test. In this case, as in [107], care must be taken when computing these residuals due to the method by which TWPBVPC determines solutions. By default, TWPBVPC attempts to minimize solution error with a deferred error correction scheme that uses a combination of high order discretizations and allocation of additional grid points in the vicinity of poorly resolved features. Although these properties are invaluable for producing high quality solutions, they serve to increase the effective resolution and convergence order of a solution, making independent residual convergence difficult to verify. Consequently, Fig. 4.6 demonstrates the convergence of our collocation code with deferred error correction disabled.

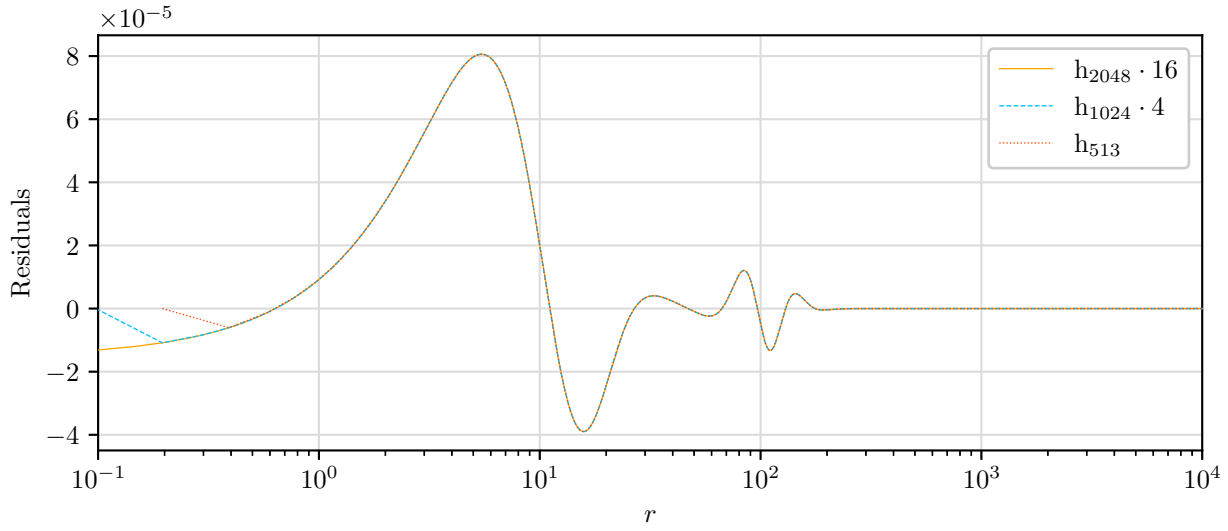

Figure 4.6: Convergence of independent residuals for $\delta\lambda$ from family p_1 for a stable mode corresponding to $\psi(0) = 0.030$ and $\beta^2 \approx 3.21 \cdot 10^{-6}$. Here we plot the scaled residuals of the metric function evaluated on grids of 2049, 1025 and 513 points using a second order finite difference scheme for the independent residual evaluator. With the scaling given in the figure, overlap of the curves implies second order convergence.

4.7 Results

Section 4.7.1 presents the results of our dynamic simulations and summarizes the regions of stability found for the families of Table 4.1. Section. 4.7.2 summarizes the results of our perturbation theory analysis for families p_1 and p_2. We derive a more complete picture of the modal structure for these families and provide important insight into the stability of other families of initial data. Finally, Sec. 4.7.3 compares the results from dynamical simulations and perturbation theory for family p_1, demonstrating the broad equivalence of the two methods.

4.7.1 Dynamical Simulations

Using slightly perturbed stationary solutions as initial data, 2 or 3 long time simulations for each region of each family in Table 4.1 were performed and the growth of perturbations in N, $\Psi\Psi^*$, Φ_M, a and α were monitored. Simulations exhibiting collapse, dispersal or non-stationary remnants were deemed unstable. Conversely, those showing oscillation about the stationary solutions with an oscillation magnitude set by the size of the initial perturbation were deemed stable. Again, we assume that the stability properties of all configurations in a given region are the same but perform a minimal validation of this assumption by performing at least 2-3 simulations per region.

In the interest of minimizing errors originating from our use of a dissipative second order code, these representative simulations were performed only near the centers of regions, fairly distant in parameter space from turning points of the mass and from branch jumps. In the case of regions with asymptotic shells, we concentrated our simulation efforts on areas where the d-stars were reasonably compact. In doing so, it was possible to uniformly excite modes and ensure that the light-crossing times for the compact objects were much less than the simulation time.

Figures 4.7–4.15 are composite plots showing both the asymptotic mass, M_∞, and maximum compactness, $C_{\max}$ as a function of boson star central amplitude for the families listed in Table 4.1. Regions highlighted in gray are stable under small radial perturbations while regions outside the gray shading are unstable. The data points plotted here are drawn from our calculations of stationary solutions, not the much more sparsely sampled dynamical simulations. As noted above, the stability of each region was determined using far fewer simulations than there are points on the graph.

Special attention should be paid to Fig. 4.7 which shows the asymptotic mass, maximum compactness and regions of stability for the case of the mini-boson star. For mini-boson stars themselves, it is the region before the first turning point in the mass that is stable [53, 73]. In all d-stars investigated, the stable region, when it exists, corresponds to the region immediately before the first turning point on the final branch (where $\psi(0)$ assumes its largest values). Since we have previously shown that this final branch has no shells of bosonic matter far from the origin [107], we find that, for all families of d-stars so far investigated, regions of stability are confined to boson-star-like branches without asymptotic shells.

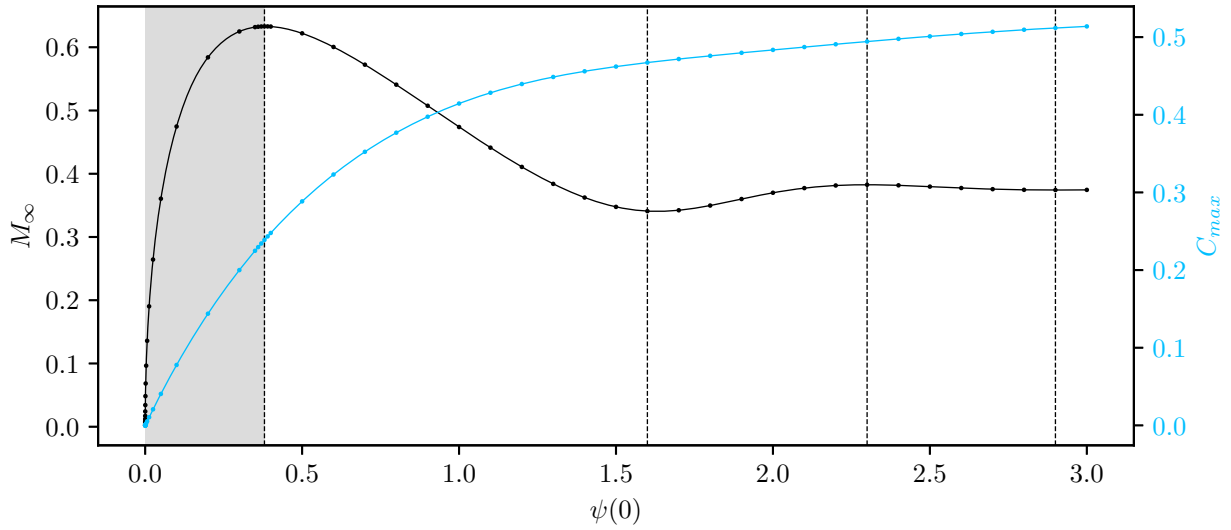

Figure 4.7: Combined asymptotic mass and maximum compactness plot for the family of mini-boson stars (minimally coupled boson stars in the absence of a global monopole). The region of stability is denoted in gray. Dashed lines show turning points of the mass.

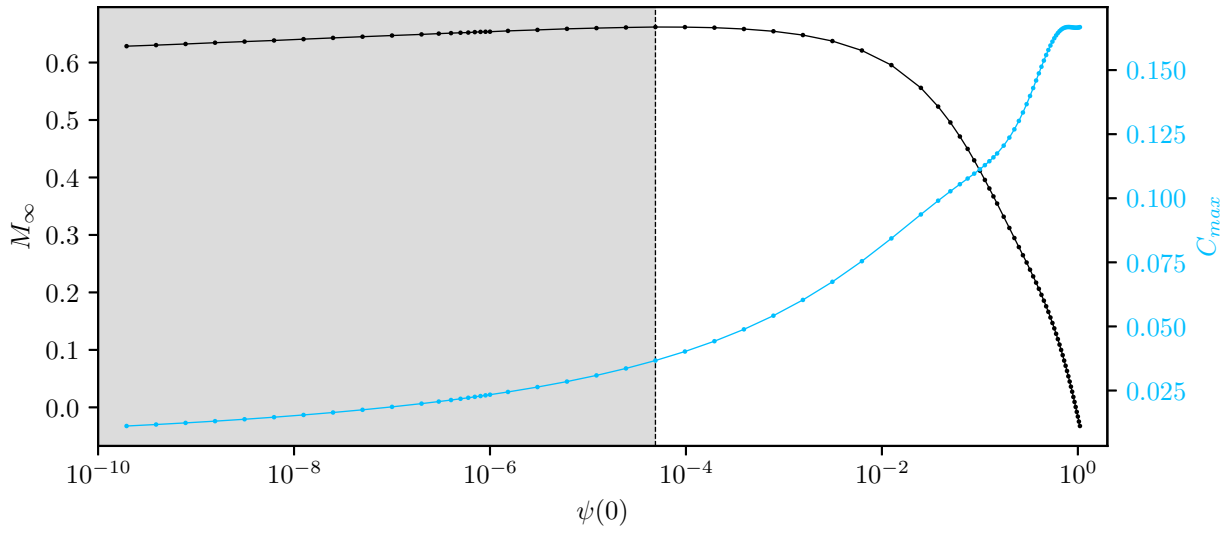

Figure 4.8: Combined asymptotic mass and maximum compactness plot for family c ($\Delta^2 = 0.36$, $\lambda_G = 1.000$, $\xi_B = 0$, $\xi_G = 0$). The region of stability is denoted in gray. Dashed lines show turning points of the mass.

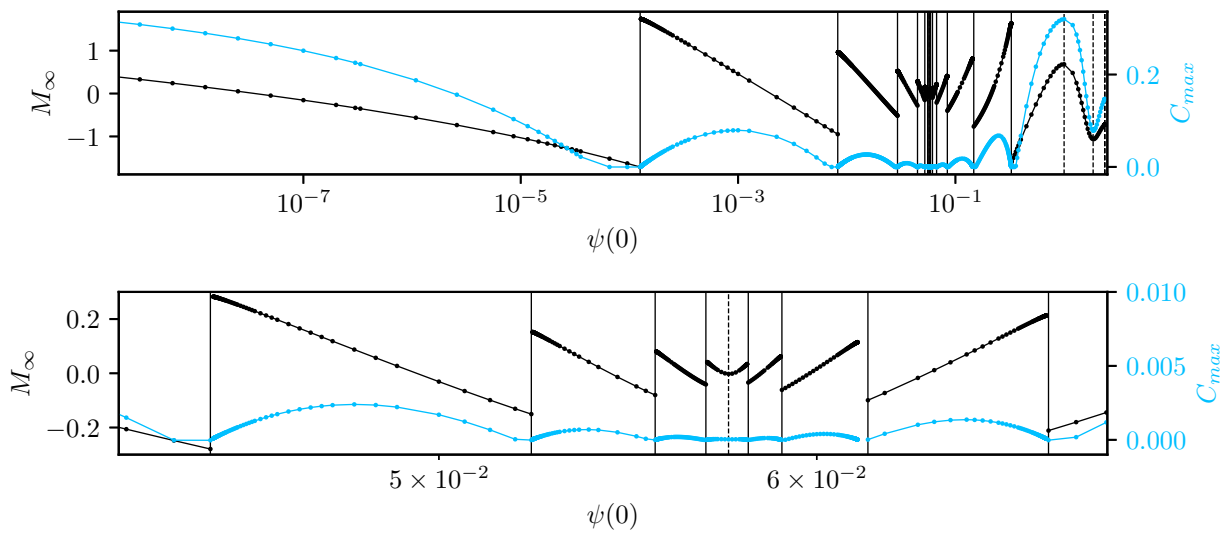

Figure 4.9: Combined asymptotic mass and maximum compactness plot for family d ($\Delta^2 = 0.81$, $\lambda_G = 0.010$, $\xi_B = 0$, $\xi_G = 0$). No region of stability is found. Dashed vertical lines show turning points of the mass while solid vertical lines denote boundaries of solution branches. Here and in the next two plots the bottom panel shows a zoomed-in view of a portion of the data in the top panel.

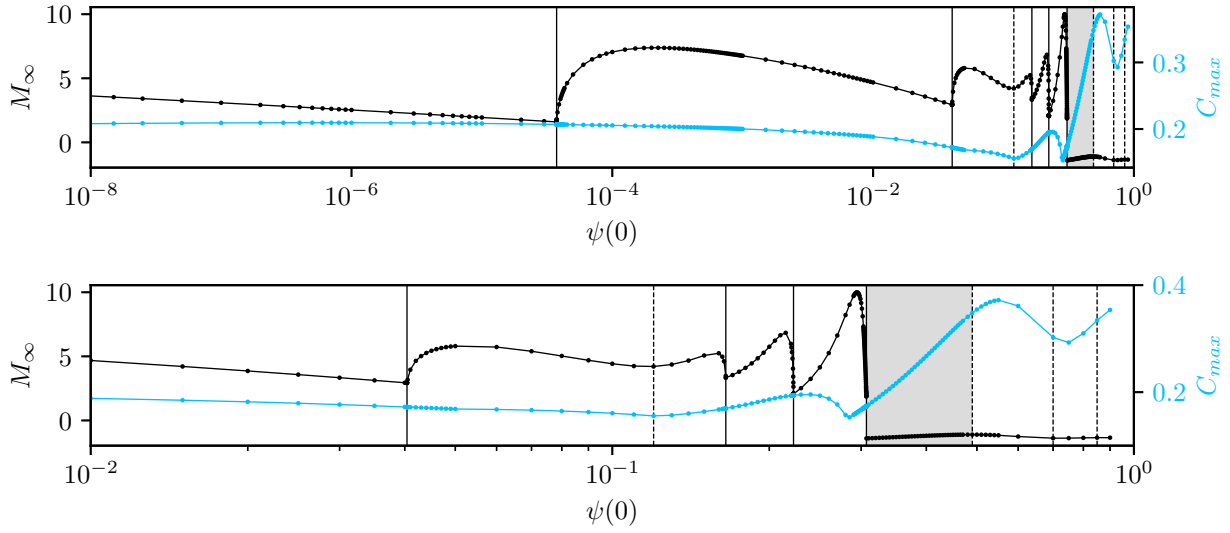

Figure 4.10: Combined asymptotic mass and maximum compactness plot for family e ($\Delta^2 = 0.25$, $\lambda_G = 0.001$, $\xi_B = 3$, $\xi_G = 3$). The region of stability is shown in gray. Dashed vertical lines show turning points of the mass while solid vertical lines denote boundaries of solution branches.

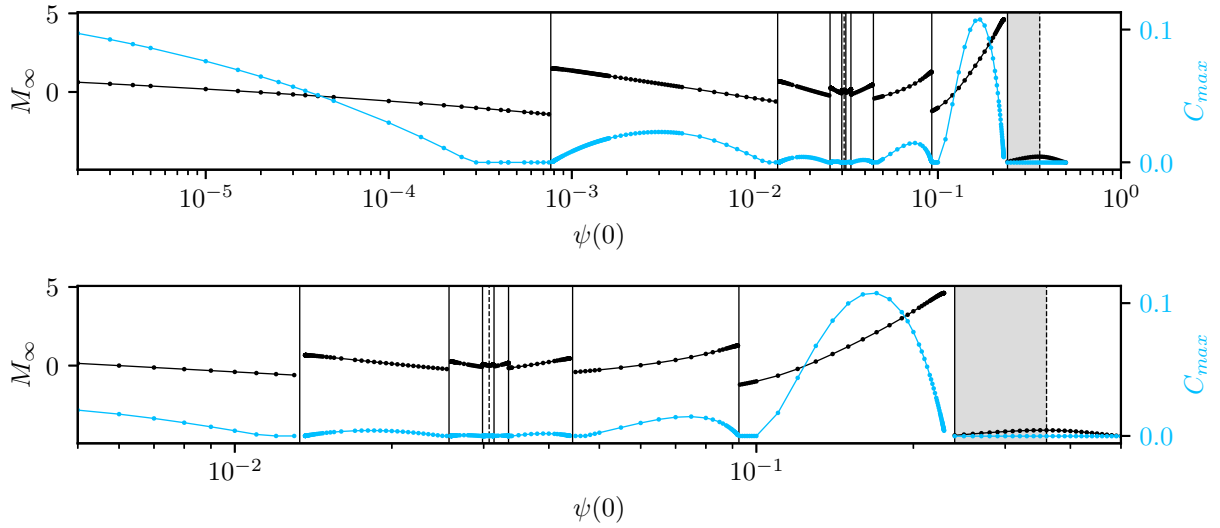

Figure 4.11: Combined asymptotic mass and maximum compactness plot for family f ($\Delta^2 = 0.49$, $\lambda_G = 0.010$, $\xi_B = 5$, $\xi_G = 0$). The region of stability is shown in gray. Dashed vertical lines show turning points of the mass while solid vertical lines denote boundaries of solution branches.

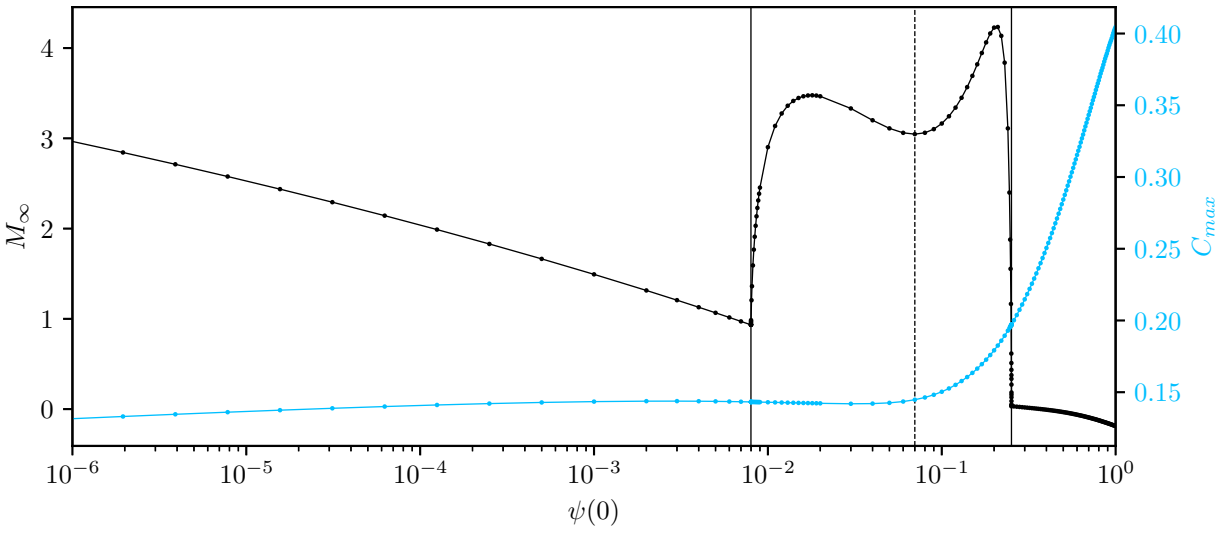

Figure 4.12: Combined asymptotic mass and maximum compactness plot for family g ($\Delta^2 = 0.09$, $\lambda_G = 0.010$, $\xi_B = 0$, $\xi_G = 5$). No region of stability is found. Dashed vertical lines show turning points of the mass while solid vertical lines denote boundaries of solution branches.

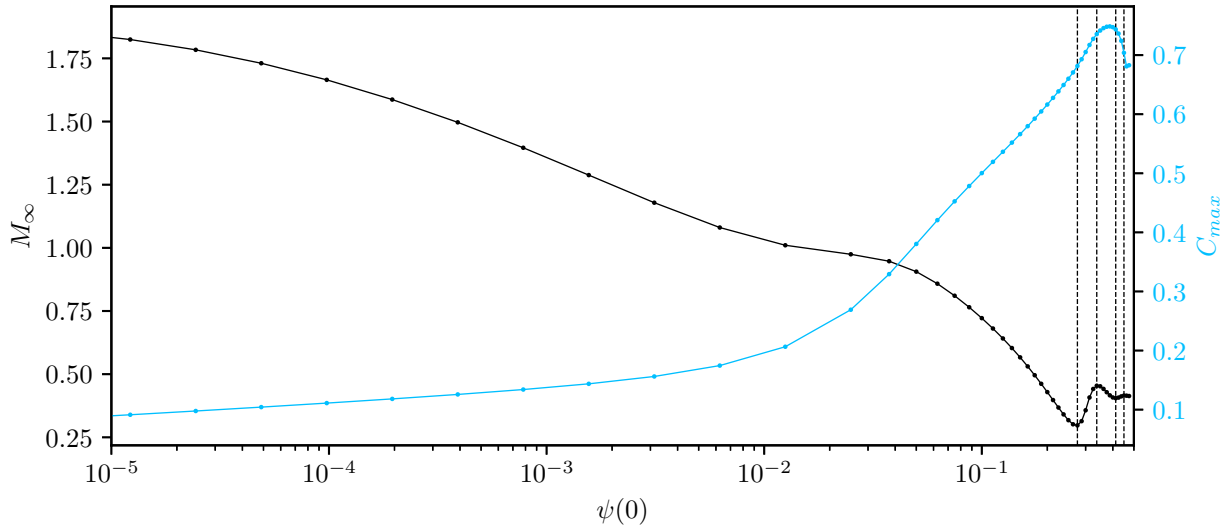

Figure 4.13: Combined asymptotic mass and maximum compactness plot for family h ($\Delta^2 = 0.08$, $\lambda_G = 0.10$, $\xi_B = -4$, $\xi_G = 5$). No region of stability is found. Dashed vertical lines show turning points of the mass.

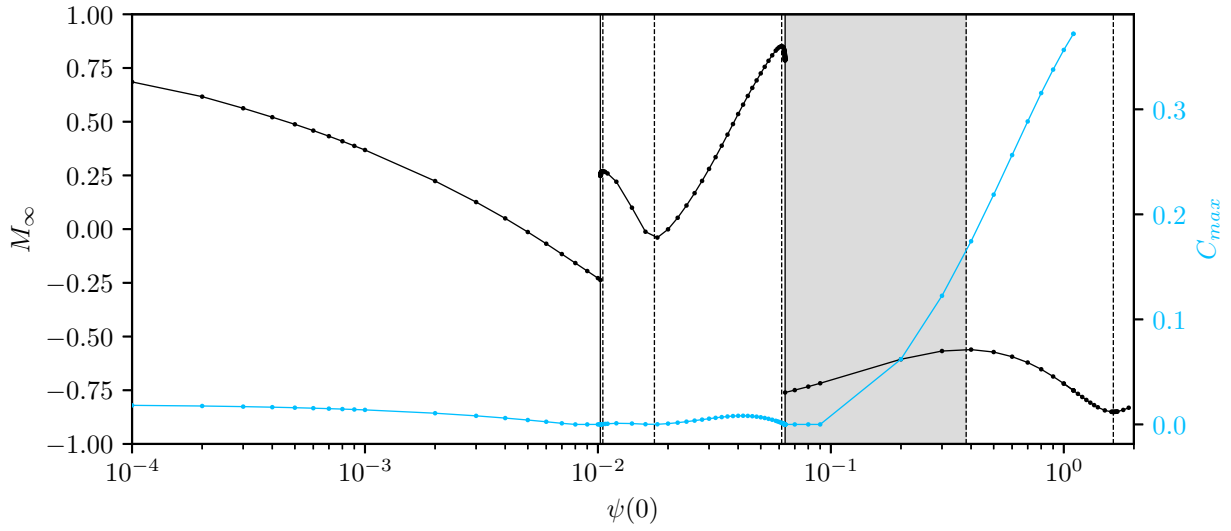

Figure 4.14: Combined asymptotic mass and maximum compactness plot for family p_1 ($\Delta^2 = 0.09$, $\lambda_G = 0.04$, $\xi_B = 0$, $\xi_G = 0$). The region of stability is shown in gray. Dashed vertical lines show turning points of the mass while solid vertical lines denote boundaries of solution branches.

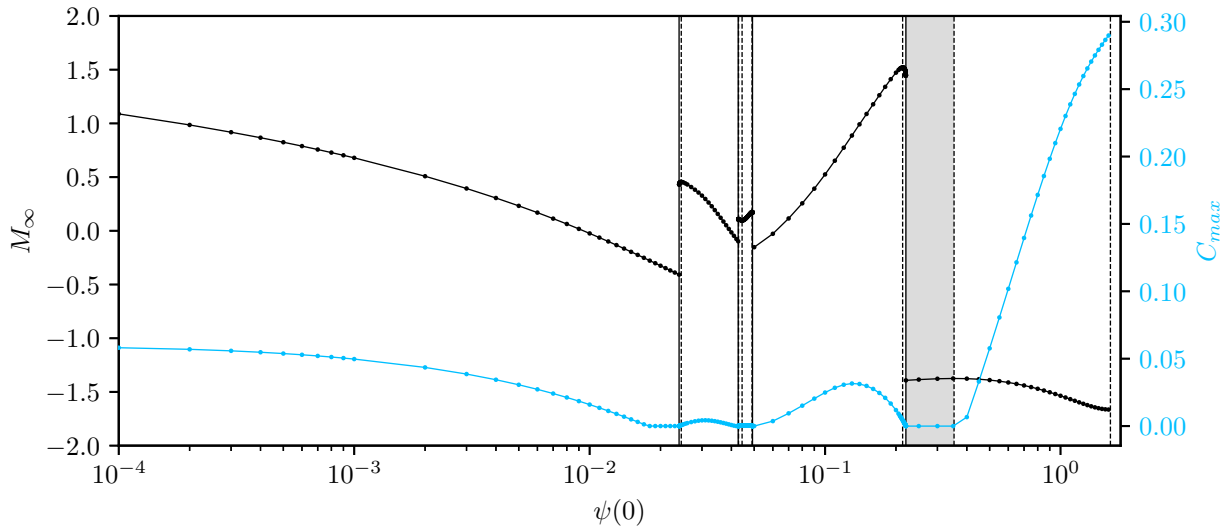

Figure 4.15: Combined asymptotic mass and maximum compactness plot for family p_2 ($\Delta^2 = 0.25$, $\lambda_G = 0.04$, $\xi_B = 0$, $\xi_G = 0$). The region of stability is shown in gray. Dashed vertical lines show turning points of the mass while solid vertical lines denote boundaries of solution branches.

4.7.2 Linear Perturbation Theory

In performing our perturbation theory analysis, we have restricted our investigation of d-stars to two minimally coupled families of solutions designated as p_1 and p_2 in Table 4.1. These families were chosen for two primary reasons. First, they have relatively simple branching structures (shown in Figs. 4.14 and 4.15) and this simplifies the perturbation analysis. Second, the two families are very close to one another in parameter space, yet have different numbers of solution branches. Correspondingly, their analysis yields clues as to how the modal structure changes as we vary parameters other than the family parameter, $\psi(0)$. For comparison purposes, we also include the results of perturbation theory applied to the case of minimally coupled mini-boson stars.

Plots displaying the modal structure for families p_1 and p_2 as well as for mini-boson stars are shown in Figs. 4.16–4.20, which plot eigenvalues, β^2, as a function of the boson star central amplitude, $\psi(0)$. Stable regions have only modes with $\beta^2 > 0$ while unstable regions have modes both with $\beta^2 > 0$ and $\beta^2 < 0$. Note that the complete spectral structures are not shown. Rather, only the first few modes (the least stable) are displayed in each case.

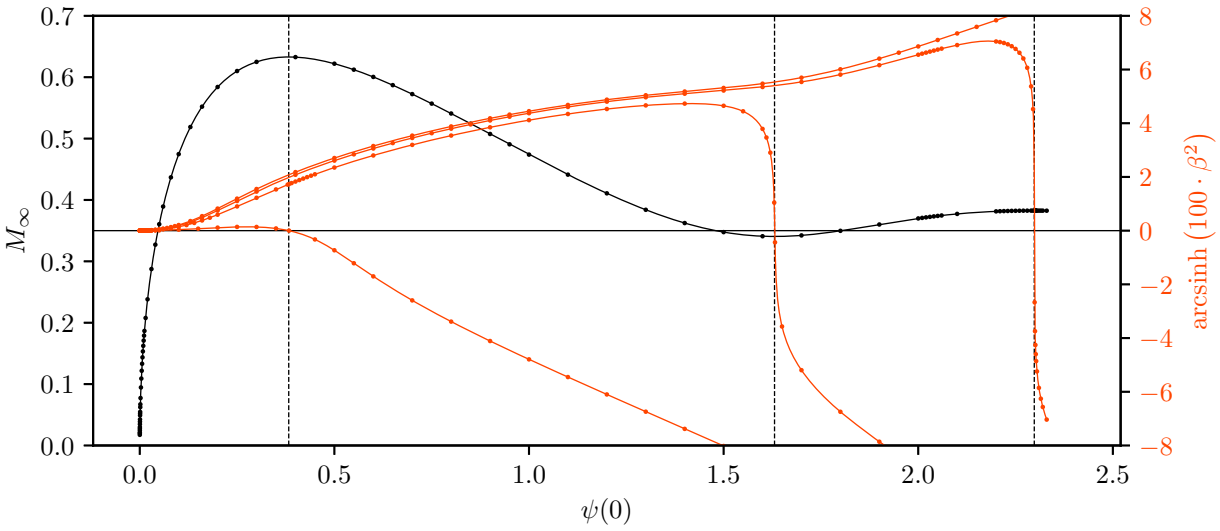

Figure 4.16: Eigenvalues for the family of mini-boson stars. The modal structure shown here contrasts with behaviour presented in Figs. 4.17–4.19 for minimally coupled d-stars. Note that at each turning point of the mass (vertical black dashed lines), a stable mode transitions to unstable. Here, and in subsequent plots, eigenvalues, β^2, are shown as functions of $\sinh(\chi\beta^2)$ to better display the overall modal structure: the magnitude of β^2 varies greatly so χ is chosen on a plot-by-plot basis to more clearly show the overall behaviour of the eigenvalues.

In Figs. 4.17–4.20 we follow the convention of the previous sections and display the locations of branch transitions (corresponding to discontinuities in the mass and Noether charge) as black vertical lines while extrema of the mass are given as black dashed vertical lines. We observe that stability transitions within a branch occur at these extremal points as predicted by catastrophe theory [69, 73].

Near the branch transitions, the eigenvalues of many modes appear to become degenerate, and neither our collocation or evolutionary codes are capable of investigating these regions in much detail. What is obvious, however, is that there is a well resolved unstable mode which persists across all but the final branch of families p_1 and p_2. The presence of this unstable mode indicates that

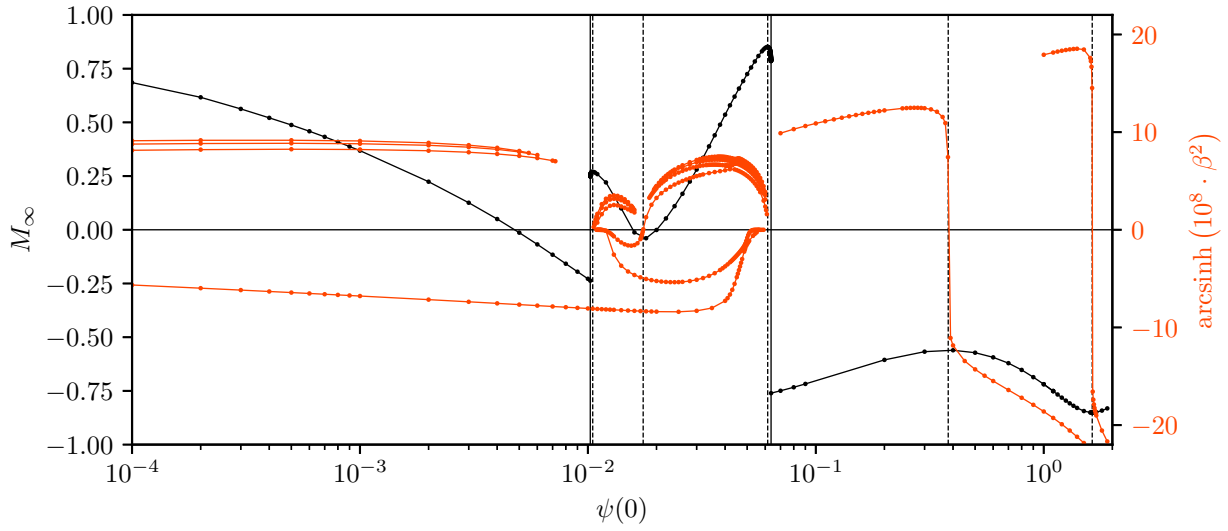

Figure 4.17: Eigenvalues of family p_1 as a function of the boson star central amplitude, $\psi(0)$. Note the apparent discontinuities in the eigenvalues near branch transitions. In these regions, the eigenvalues become near-degenerate and our solutions are no longer convergent. Our observations, however, are consistent with the stable eigenvalues approaching $\beta^2 = 0$ at the branch transitions. Note also that there are an infinite number of stable modes in each region; here we have plotted only the first three.

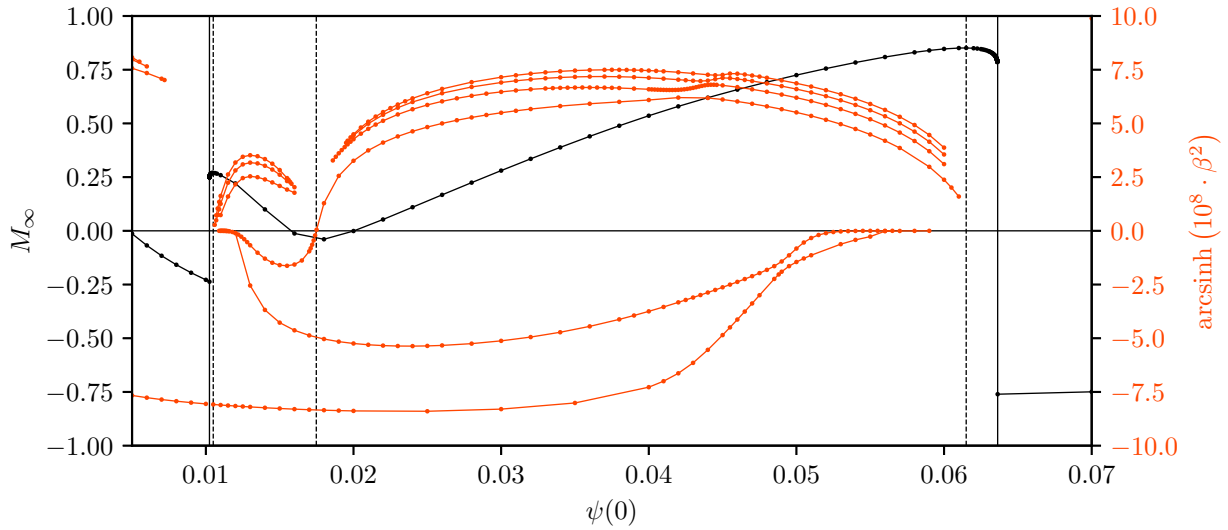

Figure 4.18: A more detailed view of the central region of Fig. 4.17 for family p_1. Interestingly, the central branch is composed of four regions (rather than two), with the first and last corresponding to shells very far from the origin. Unfortunately, the eigenvalue degeneracy prevents us from investigating these regions in detail, but it is regardless evident that the unstable modes persist through these regions (with the potential exception of the very last region where we were unable to resolve any perturbations).

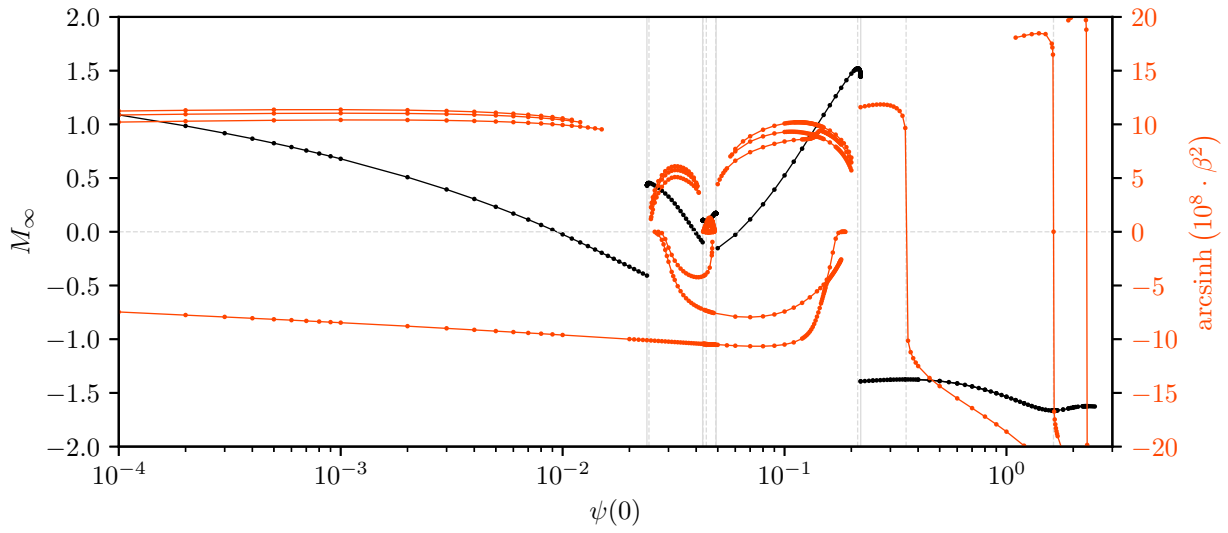

Figure 4.19: Eigenvalues of family p_2 as a function of the boson star central amplitude, $\psi(0)$. The additional two branch transitions have split the second branch of family p_1 into three distinct regions (see Fig. 4.17). Note that the region after the final branch transition is qualitatively very similar to that of mini-boson stars as shown in Fig. 4.16. As for family p_1, it can be seen that the central branches exhibit turning points in the mass corresponding to shells very far from the origin.

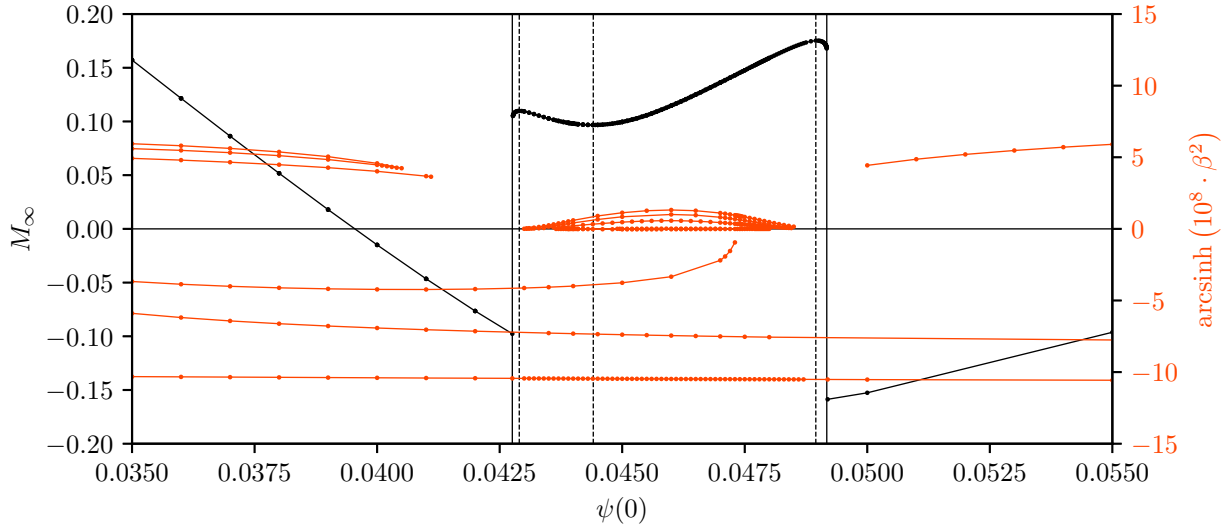

Figure 4.20: Expanded view of Fig. 4.19 showcasing details that were poorly resolved in the original plot. Our simulation data is consistent with the eigenvalues of the poorly resolved modes approaching 0. As for family p_1, it can be seen that the central branches exhibit turning points in the mass corresponding to shells very far from the origin. Unfortunately, the extreme length scales in these solutions, coupled with the eigenvalue degeneracy of the stable modes, prevents us from examining these regions in more detail.

stable solutions exist only on the final branch, in perfect agreement with our dynamical simulations.

The lack of resolution resulting from the eigenvalue degeneracies in the vicinity of the branch

transitions somewhat complicates the interpretation. We thus present a heuristic argument to build up a generic picture of the mode transitions. Recall from [107] that each branch transition before the mass turning point corresponds to the formation of a bosonic shell at infinity. This shell then migrates inward as the family parameter, $\psi(0)$, is increased. Each branch transition after the mass extrema then corresponds to the disappearance of a bosonic shell at infinity after it migrates outwards.

In the case of families p_1 and p_2, the first and final transitions can be identified with the appearance and disappearance of the first shell of matter. For family p_2, the second and third transitions can likewise be identified with the appearance and disappearance of a second shell of matter. As noted above, family p_1 is very close to developing additional branch transitions similarly to family p_2. For a marginally larger value of Δ^2, family p_1 would have a degenerate transition corresponding to a shell of matter which appears suddenly at infinity and then immediately vanishes as the family parameter, $\psi(0)$, is increased. We can, in fact, see evidence of this behaviour in Fig. 4.17 and idealized in Fig. 4.21 where the eigenvalues of the stable modes dip down towards 0 near the mass extrema.

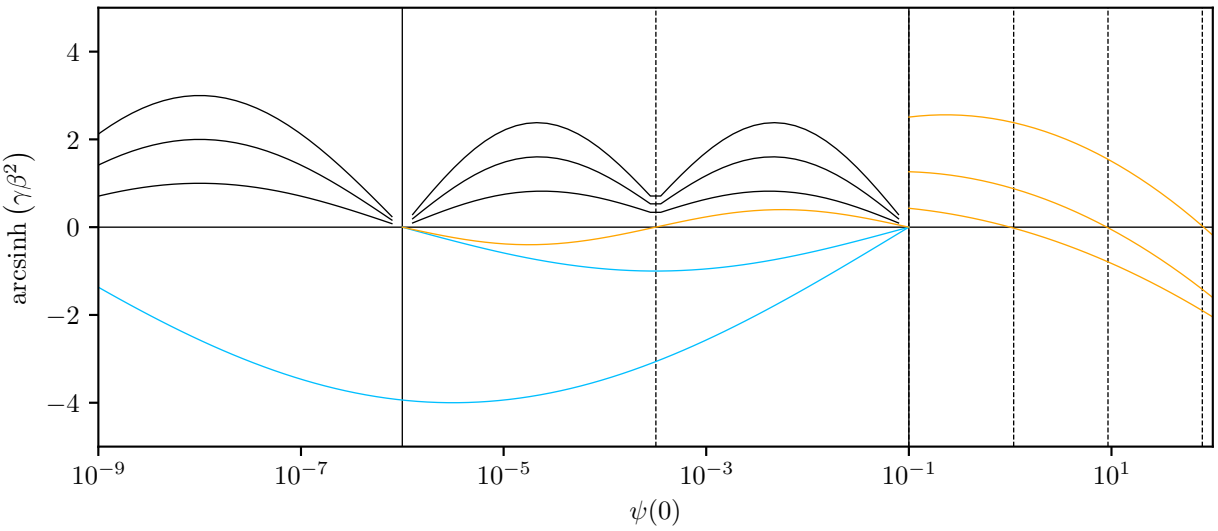

Figure 4.21: Idealized plot of eigenvalues highlighting the underlying structure of family p_1. Here we plot stable modes in black, unstable modes in blue and modes which undergo a stability transition within a region in orange. Note in particular how in a family "close" to developing an additional branch transition, the eigenvalues "near" where the transition would develop become increasingly degenerate.

This degenerate transition would split the transitioning mode into a stable and unstable region as shown in Fig. 4.22. As Δ^2 is increased further, the degeneracy is resolved, and we gain a new unstable mode corresponding to the new shell of matter as shown in Fig. 4.23. Given that there is still a mass extrema between the branch transitions, we will additionally have a new transitioning mode which changes from stable to unstable in accordance to catastrophe theory [69, 73]. The final picture is then a series of stable eigenvalues between each branch transition joined via unstable modes in the manner depicted in Fig. 4.23.

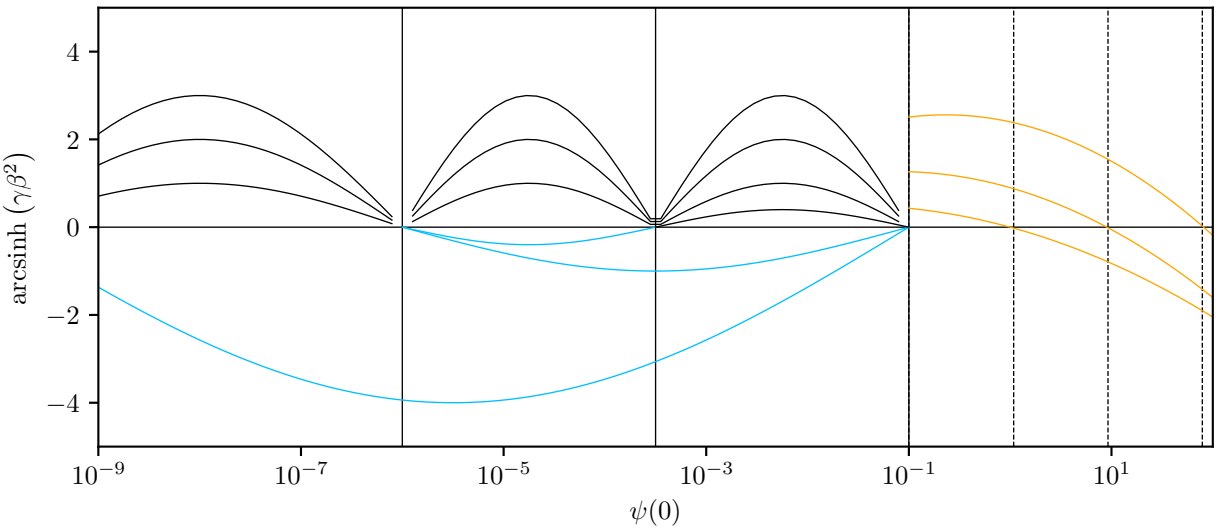

Figure 4.22: Idealized plot of eigenvalues in the case of a degenerate branch transition. The transitioning mode has been split into a stable and unstable branch. As before, we plot stable modes in black, unstable modes in blue and modes which undergo a stability transition within a region in orange.

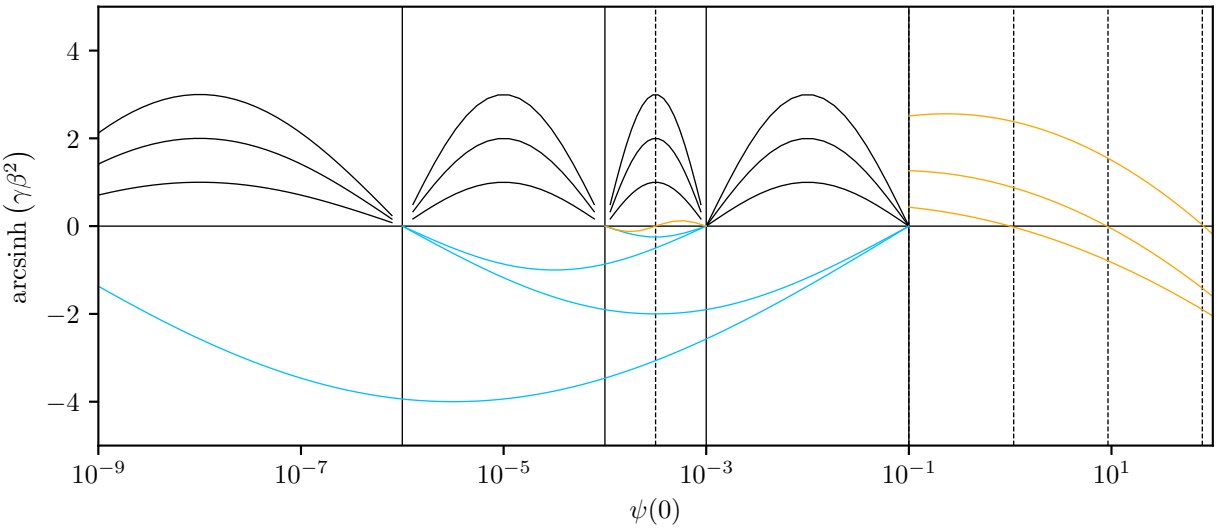

Figure 4.23: Idealized plot of eigenvalues highlighting the underlying structure of family p_2. As Δ^2 is increased further relative to p_1, the degeneracy of Fig. 4.22 is resolved, and we gain a new branch of stable and unstable modes corresponding to the new shell of matter.

4.7.3 Comparison of Methods

Using the method of Sec. 4.7.1, we extract the eigenvalues of the most unstable modes of the dynamical simulations for family p_1 and plot them against the results predicted by perturbation theory in the previous section. In Fig. 4.24, eigenvalues from individual dynamical simulations are shown as blue circles while the eigenvalues from perturbation theory are shown in red.

Examining Fig. 4.24, we can see that the perturbation theory and the dynamical simulation are in agreement for the majority of the parameter space. An interesting issue, however, arises just before the final branch. In this region, the dynamical simulations suggest the existence of a stable oscillatory mode and the absence of the unstable mode found through perturbation theory.

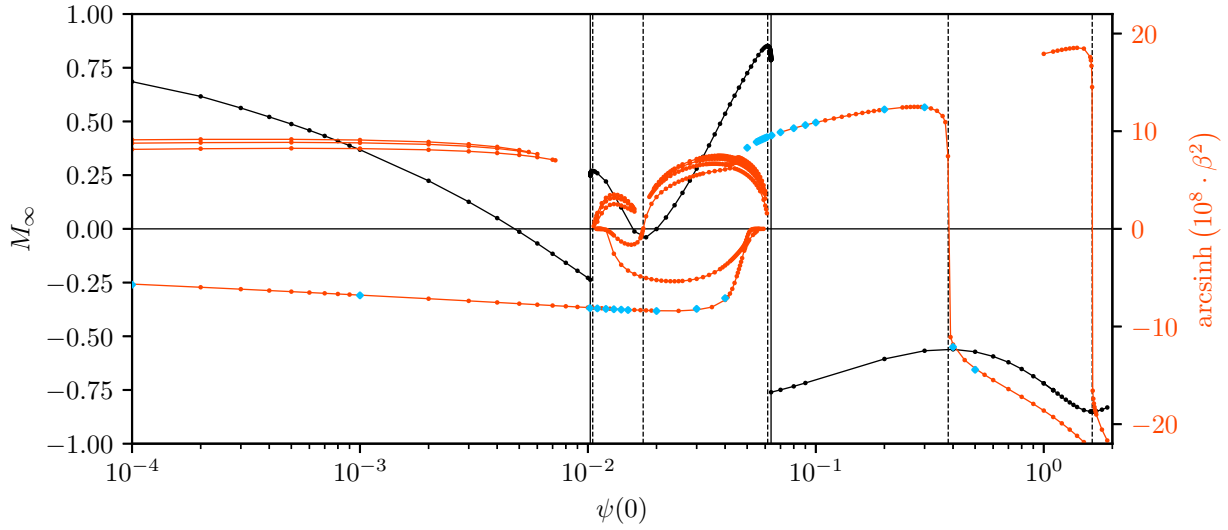

Figure 4.24: Mass and mode structure for family p_1. The asymptotic mass and eigenvalues measured via perturbation theory are shown in black and red as in Fig. 4.17. Eigenvalues measured directly from dynamical simulation are shown as blue diamonds. In the second branch, the blue diamonds indicating the existence of an oscillatory mode with $\beta^2 > 0$ do not correspond to any perturbative mode that we were able to identify.

This discrepancy is likely the result of two confounding factors. The first is that, in the region under consideration, the growth rate of the modes is extremely small ($|\beta^2| \lesssim 1 \cdot 10^{-8}$) so that the presence of an excited oscillatory mode could easily overwhelm the signal. If we were to integrate these solutions for a sufficiently long period of time, it seems likely that it would be possible to resolve the unstable eigenvalues. Unfortunately, the limited nature of our second order finite-difference based dynamical code makes maintaining temporal coherence for sufficiently long periods of time impractical. The second factor is that the oscillatory modes observed in this region are not purely oscillatory and instead decay slightly with time. As shown in Appendix B.2, however, the Hermitian character of this system requires that perturbations are either purely oscillatory or exponential in character. It seems likely that the oscillatory signals in these regions correspond to perturbations qualitatively close to those on the final branch which only nearly satisfy (B.23)–(B.23).

In addition to comparing the eigenvalues β^2, it is possible to compare the profiles of the perturbations directly. Recall that for perturbations near the stationary solutions (for a given stationary field $f(t, r)$) we have

$$f(t, r) = f_0(r) + \delta f(r) e^{-\beta t}, \tag{4.51}$$

$$\partial_t f \propto \delta f. \tag{4.52}$$

As such, we may find an approximation to the Noether charge perturbation by taking the time derivative of the Noether charge. Doing so for families p_1 and p_2, we find quite good agreement even for solutions with fairly distant bosonic shells.

4.8 Summary

We have addressed the question of boson d-star stability and suitability as black hole mimickers proposed by Marunovic and Murkovic in [83]. Through simulations of a diverse families of initial data, we have demonstrated that regions of stability, where they exist, are confined to the boson-star-like final branch of a given family in both the minimally coupled and non-minimally coupled case.

We have verified this result in the case of minimally coupled families through a fairly comprehensive mode analysis of two families of initial data (p_1 and p_2) which are close to one another in phase space. This analysis supports the results of our dynamical simulations with both perturbation theory and direct simulation being in broad agreement. The only exception to this is in regions where the magnitude of the unstable eigenvalues are small. Our evolutionary code is ill-suited to investigate these regions.

We observed how the number of branches and asymptotic shells change as the solid angle deficit, Δ^2, is changed between these two families. By analysing the differences in mode structure between families p_1 and p_2 we propose a mechanism by which the mode structure changes in response to the appearance or disappearance of an asymptotic shell of bosonic matter.

Overall, our results are consistent with the interpretation that the highly compact solutions discovered in [83] are unstable. As a result, these solutions are likely poor candidates for astrophysically relevant compact objects. Finally, we observe that the novel solutions with shells of bosonic matter far from the origin discovered in [107] are likewise unstable.

4.9 Acknowledgements

This research was supported by the Natural Sciences and Engineering Research Council of Canada (NSERC).

Chapter 5

RCCZ4: A Reference Metric Approach to Z4

The hyperbolic formulations of numerical relativity due to Baumgarte, Shapiro, Shibata & Nakamura (BSSN) and Nagy Ortiz & Reula (NOR), among others, achieve stability through the effective embedding of general relativity within the larger Z4 system. In doing so, various elliptic constraints are promoted to dynamical degrees of freedom, permitting the advection of constraint violating modes. Here we demonstrate that it is possible to achieve equivalent performance through a modification of fully covariant and conformal Z4 (FCCZ4) wherein constraint violations are coupled to a reference metric completely independently of the physical metric. We show that this approach works in the presence of black holes and holds up robustly in a variety of spherically symmetric simulations including the critical collapse of a scalar field. We then demonstrate that our formulation is strongly hyperbolic through the use of a pseudodifferential first order reduction and compare its hyperbolicity properties to those of FCCZ4 and generalized BSSN (GBSSN).

Our present approach makes use of a static Lorentzian reference metric and does not appear to provide significant advantages over FCCZ4. However, we speculate that dynamical specification of the reference metric may provide a means of exerting greater control over constraint violations than what is provided by current BSSN-type formulations.

5.1 Introduction

The formulations of numerical relativity based on the Baumgarte, Shapiro, Shibata & Nakamura (BSSN) decomposition achieve strong hyperbolicity and stability by performing a partial embedding of general relativity (GR) within the larger Z4 system [9, 63, 116]. In this paper we demonstrate that the Z4 system is not uniquely suitable for this purpose and present an alternative formulation of GR that is also well suited for numerical relativity. This formulation is based on an alternative embedding of GR and holds up well in a variety of simulations in spherical symmetry including those of black holes with puncture initial data as well as in the critical collapse of the massless scalar field. Additionally, we show that our new formulation is strongly hyperbolic and, in fact, has the same principal symbol as fully covariant and conformal Z4 (FCCZ4).

The Z4 formulation takes its name from the introduction of a four vector, Z_μ, to the Einstein equations,

$$R_{\mu\nu} + 2\nabla_{(\mu} Z_{\nu)} - 8\pi \left(T_{\mu\nu} - \frac{1}{2} g_{\mu\nu} T \right) = 0. \tag{5.1}$$

In the context of general relativity, the evolution of this system acts to advect and/or damp violations of the Hamiltonian and momentum constraints. In the limit $Z_\mu \to 0$ we recover GR [26].

If we examine formulations such as NOR [90] and generalized BSSN (GBSSN) [37] in detail, we find that they are essentially minor variations of Z4-derivable formulations in which the temporal component of Z_μ is not evolved and substitutions or additions of the Hamiltonian and momentum

constraints have been made [9–11, 47, 63, 116]. The case could also be made that the equations of motion of Z4 formalisms arise naturally while those of NOR and GBSSN come from experimentation to achieve stability and strong hyperbolicity.

In that same spirit of experimentation, we note that if we assume the Einstein equations are very nearly satisfied, such that their violation is contained in a tensor, $E_{\mu\nu}$:

$$\epsilon E_{\mu\nu} = 8\pi \left(T_{\mu\nu} - \frac{1}{2} g_{\mu\nu} T \right) - R_{\mu\nu}, \tag{5.2}$$

where $\epsilon \ll 1$, then the Z4 equations (5.1) may be written as

$$\nabla_\mu Z_\nu + \nabla_\nu Z_\mu = \epsilon E_{\mu\nu}, \tag{5.3}$$

with trace given by

$$\nabla_\mu Z^\mu = \frac{1}{2} \epsilon E_\mu{}^\mu. \tag{5.4}$$

Taking the divergence of (5.3) and using the commutator of covariant derivatives, we find

$$\begin{aligned} \Box Z^\nu &= -\nabla_\mu \nabla^\nu Z^\mu + \nabla_\mu \epsilon E^{\mu\nu}, \\ &= -\nabla^\nu \nabla_\mu Z^\mu + R^\mu{}_a{}^\nu{}_\mu Z^a + \epsilon \nabla_\mu E^{\mu\nu}, \\ &= \epsilon \left(-\frac{1}{2} \nabla^\nu E_\mu{}^\mu + \nabla_\mu E^{\mu\nu} \right) - R_\mu{}^\nu Z^\mu. \end{aligned} \tag{5.5}$$

Heuristically, Z_μ evolves according to some complicated wave equation on $g_{\mu\nu}$, which is sourced by the deviation from the Einstein equations. This is desirable since it means that Z_μ has characteristics with magnitude ~ 1 on $g_{\mu\nu}$ when ϵ is small and $g_{\mu\nu}$ is not too curved. In the presence of significant curvature, however, the picture is less clear and we note that we have completely ignored the backreaction of Z_μ on $E_{\mu\nu}$.

If we modify the Z4 formulation such that Z_μ is no longer directly coupled to the physical metric, and is instead coupled to some other metric $\mathring{g}_{\mu\nu}$ with associated connection $\mathring{\nabla}_\mu$:

$$\mathring{\nabla}_\mu Z_\nu + \mathring{\nabla}_\nu Z_\mu = 8\pi \left(T_{\mu\nu} - \frac{1}{2} g_{\mu\nu} T \right) - R_{\mu\nu}, \tag{5.6}$$

we find,

$$\mathring{\nabla}_\mu Z_\nu + \mathring{\nabla}_\nu Z_\mu = \epsilon E_{\mu\nu}, \tag{5.7}$$

with trace:

$$\mathring{\nabla}_\mu \mathring{Z}^\mu = \frac{1}{2} \epsilon \mathring{E}_\mu{}^\mu. \tag{5.8}$$

Here, variables accented with "$\circ$" have had a covariant tensorial index raised with $\mathring{g}^{\mu\nu}$. Taking the divergence of (5.7), we find:

$$\begin{aligned} \mathring{\Box} \mathring{Z}^\nu &= -\mathring{\nabla}_\mu \mathring{\nabla}^\nu \mathring{Z}^\mu + \mathring{\nabla}_\mu \epsilon \mathring{E}^{\mu\nu}, \\ &= -\mathring{\nabla}^\nu \mathring{\nabla}_\mu \mathring{Z}^\mu + \mathring{R}^\mu{}_a{}^\nu{}_\mu Z^a + \epsilon \mathring{\nabla}_\mu \mathring{E}^{\mu\nu}, \\ &= \epsilon \left(-\frac{1}{2} \mathring{\nabla}^\nu \mathring{E}_\mu{}^\mu + \mathring{\nabla}_\mu \mathring{E}^{\mu\nu} \right) - \mathring{R}_\mu{}^\nu \mathring{Z}^\mu. \end{aligned} \tag{5.9}$$

As such, if we choose $\mathring{g}_{\mu\nu}$ so that $\mathring{R}_{\mu\nu}$ vanishes, we might expect $\mathring{Z}^{\mu}$ to propagate with speed ~ 1 on $\mathring{g}_{\mu\nu}$ when ϵ is small, regardless of the curvature of $g_{\mu\nu}$. In what follows, we expand upon this idea and present a formulation of the Einstein equations based on a flat, time-invariant reference metric which yields a system which performs very similarly to the standard GBSSN [9, 37] and FCCZ4 [116] formulations. Further work with dynamical specification of the reference metric may allow for more fine-grained control over constraint damping and stability properties.

In Sec. 5.2 we give a brief derivation of our formulation; a more detailed derivation may be found in Appendices E.1 and E.2. Section 5.3 introduces the equations of motion for the GBSSN and FCCZ4 formulations of numerical relativity which we make use of in our various comparative analyses. In Sec. 5.4 we compare the performance of our formulation with FCCZ4 and GBSSN in a variety of numerical tests including strong field convergence testing, simulation of black holes and the critical collapse of the scalar field in spherical symmetry. After demonstrating that the method works in spherical symmetry, we shift gears and analyse the hyperbolicity of our approach: Sec. 5.5 sees us derive the conditions under which our method is strongly hyperbolic and examine how it compares to both GBSSN and FCCZ4. Finally, in Sec. 5.6 we present our conclusions and suggestions for future research into related formulations of numerical relativity.

5.2 Derivation of RCCZ4

We begin with the Z4 equations coupled to a reference metric as in (5.6), which we refer to as *reference metric Z4* (RZ4), with the aim of developing an ADM decomposition equivalent of the system. Once we have this initial value formulation, we perform a decomposition similar to GBSSN or FCCZ4 in terms of a conformal metric and conformal trace-free extrinsic curvature, arriving at *reference metric covariant and conformal Z4* (RCCZ4). Again, more details are provided in Appendices E.1 and E.2.

Using standard notation in which n^{μ} is the unit normal to the foliation in a 3+1 decomposition, α is the lapse, β^{i} is the shift and γ_{ij} is the induced 3-metric on the foliation, the RZ4 equations (with damping parameters κ_1 and κ_2) may be written in canonical form as:

$$R_{\mu\nu} - \frac{1}{2}g_{\mu\nu}R + 2\mathring{\nabla}_{(\mu}Z_{\nu)} - g_{\mu\nu}\mathring{\nabla}_{(\alpha}Z_{\beta)}g^{\alpha\beta} - \kappa_1\left[2n_{(\mu}Z_{\nu)} + \kappa_2 g_{\mu\nu}n_{\sigma}Z^{\sigma}\right] - 8\pi T_{\mu\nu} = 0. \tag{5.10}$$

Equivalently, the trace reversed form is:

$$R_{\mu\nu} + 2\mathring{\nabla}_{(\mu}Z_{\nu)} - 8\pi\left(T_{\mu\nu} - \frac{1}{2}g_{\mu\nu}T\right) - \kappa_1\left[2n_{(\mu}Z_{\nu)} - (1+\kappa_2)\,g_{\mu\nu}n_{\sigma}Z^{\sigma}\right] = 0. \tag{5.11}$$

Taking the trace (with respect to $g^{\mu\nu}$) of (5.11) yields:

$$R + 2\mathring{\nabla}_{(\mu}Z_{\nu)}g^{\mu\nu} + \kappa_1\,(2+4\kappa_2)\,n_{\mu}Z^{\mu} + 8\pi T = 0. \tag{5.12}$$

From here we roughly follow the ADM derivations of [5, 54] and take projections of (5.10)–(5.12) onto and orthogonal to the spatial hypersurfaces which foliate four dimensional spacetime in a standard 3+1 decomposition (see Appendix E.1).

The majority of our work has been focused on critical collapse where we expect solutions to span several decades of length scales. In such a context, choosing a preferential length scale through the introduction of dimensionful damping parameters is liable to be counterproductive. In what

follows, then, we set $\kappa_1 = \kappa_2 = 0$ in (5.10)–(5.12) yielding the simpler set of equations:

$$R_{\mu\nu} - \frac{1}{2} g_{\mu\nu} R + 2\mathring{\nabla}_{(\mu} Z_{\nu)} - g_{\mu\nu} \mathring{\nabla}_{(\alpha} Z_{\beta)} g^{\alpha\beta} - 8\pi T_{\mu\nu} = 0, \tag{5.13}$$

$$R_{\mu\nu} + 2\mathring{\nabla}_{(\mu} Z_{\nu)} - 8\pi \left(T_{\mu\nu} - \frac{1}{2} g_{\mu\nu} T \right) = 0, \tag{5.14}$$

$$R + 2\mathring{\nabla}_{(\mu} Z_{\nu)} g^{\mu\nu} + 8\pi T = 0. \tag{5.15}$$

We have considered only the simplest case where $\mathring{g}_{\mu\nu}$ is a time-invariant, curvature-free Lorentzian metric with $\mathring{g}_{tt} = -1, \mathring{g}_{tj} = 0$. With these restrictions, projection of (5.13)–(5.15) yields the ADM equivalent of the RZ4 equations:

$$\mathcal{L}_m \gamma_{ij} = -2\alpha K_{ij}, \tag{5.16}$$

$$\mathcal{L}_m K_{ij} = -D_i D_j \alpha + \alpha \left(R_{ij} + K K_{ij} - 2 K_{ik} K^k{}_j \right) + 4\pi\alpha \left([S - \rho] \gamma_{ij} - 2 S_{ij} \right) + 2\alpha \mathring{D}_{(i} \bar{Z}_{j)}, \tag{5.17}$$

$$\mathcal{L}_m \Theta = \frac{\alpha}{2} \left(R + K^2 - K_{ij} K^{ij} - 16\pi\rho \right) + \alpha \gamma^{ij} \mathring{D}_i \bar{Z}_j - \frac{\Theta}{\alpha} \mathcal{L}_m \alpha + \frac{\bar{Z}_i}{\alpha} \left(\mathcal{L}_m \beta^i - \beta^j \mathring{D}_j \beta^i \right), \tag{5.18}$$

$$\mathcal{L}_m \bar{Z}_i = \alpha \left(D_j K^j{}_i - D_i K - 8\pi j_i \right) - 2 \bar{Z}_j \mathring{D}_i \beta^j + \Theta \mathring{D}_i \alpha + \alpha \mathring{D}_i \Theta, \tag{5.19}$$

where $\mathcal{L}_m = \partial_t - \mathcal{L}_\beta$ and the quantities Θ and $\bar{Z}_i$ are defined as,

$$\Theta = -n_\mu Z^\mu, \tag{5.20}$$

$$\bar{Z}_i = \gamma^\mu{}_i Z_\mu, \tag{5.21}$$

$$\bar{Z}^i = \gamma^{ij} \bar{Z}_j. \tag{5.22}$$

Once again, we direct readers to Appendix E.1 for a more detailed derivation.

In order to cast (5.16)–(5.19) in a form better suited to evolving generic spacetimes, we perform the same covariant and conformal decomposition that we would for GBSSN and FCCZ4. We rewrite the 3-metric, γ_{ij}, and extrinsic curvature, K_{ij}, in terms of the conformal factor, χ, the conformal metric, $\widetilde{\gamma}_{ij}$, the trace of the extrinsic curvature, K, and the trace-free extrinsic curvature $\widetilde{A}_{ij}$:

$$\gamma_{ij} = e^{4\chi} \widetilde{\gamma}_{ij}, \tag{5.23}$$

$$K_{ij} = e^{4\chi} \left(\widetilde{A}_{ij} - \frac{1}{3} \widetilde{\gamma}_{ij} K \right). \tag{5.24}$$

We also define the quantities $\widetilde{\Delta}^i{}_{jk}$ and $\widetilde{\Delta}^i$ in terms of the difference between the Christoffel symbols of $\widetilde{\gamma}_{ij}$ and those of a flat background 3-metric $\mathring{\gamma}_{ij}$: the latter is chosen to coincide with the spatial portion of $\mathring{\gamma}_{\mu\nu}$:

$$\widetilde{\Gamma}^i = \widetilde{\Gamma}^i{}_{jk} \widetilde{\gamma}^{jk}, \tag{5.25}$$

$$\widetilde{\Delta}^i{}_{jk} = \widetilde{\Gamma}^i{}_{jk} - \mathring{\Gamma}^i_{jk}, \tag{5.26}$$

$$\widetilde{\Delta}^i = \widetilde{\Gamma}^i - \mathring{\Gamma}^i{}_{jk} \widetilde{\gamma}^{jk}. \tag{5.27}$$

Additionally, we define the quantity $\widetilde{\Lambda}^i$ which plays the same role as the conformal connection functions in BSSN [9] and FCCZ4 [116]:

$$\widetilde{\Lambda}^i = \widetilde{\Delta}^i + 2\widetilde{\gamma}^{ij} \bar{Z}_j, \tag{5.28}$$

$$\bar{Z}^i = \frac{1}{2} \left(\widetilde{\Lambda}^i - \widetilde{\Delta}^i \right) e^{-4\chi}. \tag{5.29}$$

Finally, adopting the Lagrangian choice for the evolution of the determinant of the conformal metric:

$$\partial_t \widetilde{\gamma} = 0, \tag{5.30}$$

and defining the quantity $\widetilde{\Theta}$ in terms of Θ, α, $\bar{Z}_i$ and β^i:

$$\widetilde{\Theta} = \alpha\Theta - \beta^i \bar{Z}_i, \tag{5.31}$$

we find the RCCZ4 equations of motion:

$$\mathcal{L}_m\chi = -\frac{1}{6}\alpha K + \frac{1}{6}\widetilde{D}_m\beta^m, \tag{5.32}$$

$$\mathcal{L}_m K = -D^2\alpha + \alpha\left(R + K^2 + 2\gamma^{ij}\mathring{D}_{(i}\bar{Z}_{j)} + 4\pi\left(S - 3\rho\right)\right), \tag{5.33}$$

$$\begin{aligned}\mathcal{L}_m\widetilde{\Theta} = {}& \frac{\alpha^2}{2}\left(R - \widetilde{A}_{ij}\widetilde{A}^{ij} + \frac{2}{3}K^2 - 16\pi\rho + 2\gamma^{ij}\mathring{D}_i\bar{Z}_j\right) - \beta^j\left(\beta^l\mathring{D}_j\bar{Z}_l + \mathring{D}_j\widetilde{\Theta}\right) \\ & - \alpha\beta^j\left(D_l\widetilde{A}^l{}_j - \frac{2}{3}\widetilde{D}_j K - 8\pi j_j\right),\end{aligned} \tag{5.34}$$

$$\mathcal{L}_m\widetilde{\gamma}_{ij} = -2\alpha\widetilde{A}_{ij} - \frac{2}{3}\widetilde{\gamma}_{ij}\widetilde{D}_m\beta^m, \tag{5.35}$$

$$\begin{aligned}\mathcal{L}_m\widetilde{A}_{ij} = {}& e^{-4\chi}\left[-D_iD_j\alpha + \alpha R_{ij} - 8\pi\alpha S_{ij} + 2\alpha\mathring{D}_{(i}\bar{Z}_{j)}\right]^{\mathrm{TF}} + \alpha\left(K\widetilde{A}_{ij} - 2\widetilde{A}_{ik}\widetilde{A}^k{}_j\right) \\ & - \frac{2}{3}\widetilde{A}_{ij}\widetilde{D}_l\beta^l,\end{aligned} \tag{5.36}$$

$$\begin{aligned}\mathcal{L}_m\widetilde{\Lambda}^i = {}& \tilde{\gamma}^{mn}\mathring{D}_m\mathring{D}_n\beta^i - 2\widetilde{A}^{im}\widetilde{D}_m\alpha + 2\alpha\widetilde{A}^{mn}\widetilde{\Delta}^i{}_{mn} + \frac{1}{3}\widetilde{D}^i\widetilde{D}_n\beta^n + \frac{2}{3}\widetilde{\Lambda}^i\widetilde{D}_n\beta^n \\ & + 4\alpha\left(\bar{Z}_j\widetilde{A}^{ij} + 3\widetilde{A}^{li}\widetilde{D}_l\chi - \frac{1}{3}\widetilde{D}^i K - 4\pi\widetilde{j}^i\right) + 2\widetilde{D}^i\widetilde{\Theta} + 2\widetilde{\gamma}^{ij}\left(\beta^l\ \mathring{D}_j\bar{Z}_l - \bar{Z}_l\mathring{D}_j\beta^l\right),\end{aligned} \tag{5.37}$$

$$\mathcal{L}_m\bar{Z}_i = \alpha\left[D_l\widetilde{A}^l{}_i - \frac{2}{3}\widetilde{D}_i K - 8\pi j_i\right] - \bar{Z}_l\mathring{D}_i\beta^l + \beta^l\mathring{D}_i\bar{Z}_l + \mathring{D}_i\widetilde{\Theta}\,. \tag{5.38}$$

Here, either $\bar{Z}_i$ or $\widetilde{\Lambda}^i$ may be viewed as the dynamical quantity associated with the momentum constraint violations and all quantities denoted by a tilde are raised and lowered with the conformal metric. "TF" denotes trace free with respect to the 3-metric γ_{ij} and the Ricci tensor may be split into scale-factor and conformal parts as

$$R_{ij} = \widetilde{R}_{ij} + R^{\chi}_{ij}, \tag{5.39}$$

with

$$\widetilde{R}_{ij} = -\frac{1}{2}\tilde{\gamma}^{mn}\mathring{D}_m\mathring{D}_n\widetilde{\gamma}_{ij} + \widetilde{\gamma}_{m(i}\mathring{D}_{j)}\widetilde{\Delta}^m + \widetilde{\Delta}^m\widetilde{\Delta}_{(ij)m} + 2\widetilde{\Delta}^{mn}{}_{(i}\widetilde{\Delta}_{j)mn} + \widetilde{\Delta}^{mn}{}_i\widetilde{\Delta}_{mnj}, \tag{5.40}$$

$$R^{\chi}_{ij} = -2\widetilde{D}_i\widetilde{D}_j\chi - 2\widetilde{\gamma}_{ij}\widetilde{D}^k\widetilde{D}_k\chi + 4\widetilde{D}_i\chi\widetilde{D}_j\chi - 4\widetilde{\gamma}_{ij}\widetilde{D}^k\chi\widetilde{D}_k\chi. \tag{5.41}$$

Note that the equations of motion for $\widetilde{\Theta}$, (5.34), and $\bar{Z}_i$, (5.38), are essentially sourced by violations of the Hamiltonian and momentum constraints respectively. In terms of the conformal decomposition these constraints then take the form

$$H = \frac{1}{2}\left(R + \frac{2}{3}K^2 - \widetilde{A}_{ij}\widetilde{A}^{ij}\right) - 8\pi\rho, \tag{5.42}$$

$$M^i = e^{-4\chi}\left(\widetilde{D}_j\widetilde{A}^{ij} - \frac{2}{3}\widetilde{\gamma}^{ij}\widetilde{D}_j K + 6\widetilde{A}^{ij}\widetilde{D}_j\chi - 8\pi\widetilde{j}^i\right). \tag{5.43}$$

5.3 FCCZ4 and GBSSN Equations of Motion

In testing the viability of RCCZ4 as a formulation for numerical relativity, we make use of the formulation of FCCZ4 due to Sanchis-Gual et al. [116] along with the formulation of GBSSN by Brown [36] as presented by Alcubierre and Mendaz [9]. In our notation, the equations of motion for FCCZ4 are:

$$\mathcal{L}_m\chi = -\frac{1}{6}\alpha K + \frac{1}{6}\widetilde{D}_m\beta^m, \tag{5.44}$$

$$\mathcal{L}_m K = -D^2\alpha + \alpha R + \alpha\left(K^2 - 2\Theta K\right) + 2\alpha D_i\bar{Z}^i + 4\pi\alpha\left(S - 3\rho\right), \tag{5.45}$$

$$\mathcal{L}_m\Theta = \frac{\alpha}{2}\left(R - \widetilde{A}_{ij}\widetilde{A}^{ij} + \frac{2}{3}K^2 - 2\Theta K + 2D_i\bar{Z}^i - 2\bar{Z}^i D_i\ln\alpha - 16\pi\rho\right), \tag{5.46}$$

$$\mathcal{L}_m\widetilde{\gamma}_{ij} = -2\alpha\widetilde{A}_{ij} - \frac{2}{3}\widetilde{\gamma}_{ij}\widetilde{D}_m\beta^m, \tag{5.47}$$

$$\begin{aligned}\mathcal{L}_m\widetilde{A}_{ij} = {} & -\frac{2}{3}\widetilde{A}_{ij}\widetilde{D}_m\beta^m + \alpha\widetilde{A}_{ij}\left(K - 2\Theta\right) + e^{-4\chi}\left[-D_iD_j\alpha + \alpha\left(R_{ij} + 2D_{(i}\bar{Z}_{j)}\right.\right. \\ & \left.\left. - 8\pi S_{ij}\right)\right]^{\mathrm{TF}} - 2\alpha\widetilde{A}_{ik}\widetilde{A}^k{}_j,\end{aligned} \tag{5.48}$$

$$\begin{aligned}\mathcal{L}_m\widetilde{\Lambda}^i = {} & \tilde{\gamma}^{mn}\mathring{D}_m\mathring{D}_n\beta^i + \frac{2}{3}\widetilde{\Lambda}^i\widetilde{D}_n\beta^n + \frac{1}{3}\widetilde{D}^i\widetilde{D}_n\beta^n - 2\widetilde{A}^{ik}\left(\widetilde{D}_k\alpha - 6\alpha\widetilde{D}_k\chi\right) + 2\alpha\widetilde{A}^{jk}\widetilde{\Delta}^i{}_{jk} \\ & - \frac{4}{3}\alpha\widetilde{D}^i K + 2\tilde{\gamma}^{ik}\left(\alpha\widetilde{D}_k\Theta - \Theta\widetilde{D}_k\alpha - \frac{2}{3}\alpha K\bar{Z}_k\right) - 16\pi\alpha\tilde{\gamma}^{ij}j_j,\end{aligned} \tag{5.49}$$

$$\mathcal{L}_m\bar{Z}_i = \alpha\left(D_j\widetilde{A}^j{}_i - \frac{2}{3}D_iK + D_i\Theta - \Theta D_i\ln\alpha - 2\bar{Z}_j\widetilde{A}^j{}_i - \frac{2}{3}\bar{Z}_iK - 8\pi j_i\right), \tag{5.50}$$

where, as with RCCZ4, either $\bar{Z}_i$ or $\widetilde{\Lambda}^i$ may be viewed as the fundamental dynamical quantity and the two are related via

$$\widetilde{\Lambda}^i = \widetilde{\Delta}^i + 2\tilde{\gamma}^{ij}\bar{Z}_j. \tag{5.51}$$

The equations of motion for GBSSN, meanwhile, are:

$$\mathcal{L}_m\chi = -\frac{1}{6}\alpha K + \frac{1}{6}\widetilde{D}_m\beta^m, \tag{5.52}$$

$$\mathcal{L}_m K = -D^2\alpha + \alpha\left(\widetilde{A}_{ij}\widetilde{A}^{ij} + \frac{1}{3}K^2\right) + 4\pi\alpha\left(\rho + S\right), \tag{5.53}$$

$$\mathcal{L}_m\widetilde{\gamma}_{ij} = -2\alpha\widetilde{A}_{ij} - \frac{2}{3}\widetilde{\gamma}_{ij}\widetilde{D}_m\beta^m, \tag{5.54}$$

$$\mathcal{L}_m\widetilde{A}_{ij} = e^{-4\chi}\left[-D_iD_j\alpha + \alpha R_{ij} - 8\pi\alpha S_{ij}\right]^{\mathrm{TF}} - \frac{2}{3}\widetilde{A}_{ij}\widetilde{D}_m\beta^m + \alpha\left(K\widetilde{A}_{ij} - 2\widetilde{A}_{ik}\widetilde{A}^k{}_j\right), \tag{5.55}$$

$$\begin{aligned}\mathcal{L}_m\widetilde{\Lambda}^i = {} & \tilde{\gamma}^{mn}\mathring{D}_m\mathring{D}_n\beta^i - 2\widetilde{A}^{im}\widetilde{D}_m\alpha + 2\alpha\left(6\widetilde{A}^{ij}\widetilde{D}_j\chi - \frac{2}{3}\tilde{\gamma}^{ij}\widetilde{D}_jK - 8\pi\tilde{j}^i\right) \\ & + \frac{1}{3}\left[\widetilde{D}^i\left(\widetilde{D}_n\beta^n\right) + 2\widetilde{\Lambda}^i\widetilde{D}_n\beta^n\right] + 2\alpha\widetilde{A}^{mn}\widetilde{\Delta}^i{}_{mn},\end{aligned} \tag{5.56}$$

where we note that we have replaced the usual variable $\widetilde{\Delta}^i$ with $\widetilde{\Lambda}^i$ for notational consistency when comparing to FCCZ4 and RCCZ4. Note that in the evaluation of GBSSN dynamical quantities $\widetilde{\Lambda}^i$ is substituted for $\widetilde{\Delta}^i$, such that (5.40) becomes

$$\widetilde{R}_{ij} = -\frac{1}{2}\tilde{\gamma}^{mn}\mathring{D}_m\mathring{D}_n\tilde{\gamma}_{ij} + \tilde{\gamma}_{m(i}\mathring{D}_{j)}\widetilde{\Lambda}^m + \widetilde{\Lambda}^m\widetilde{\Delta}_{(ij)m} + 2\widetilde{\Delta}^{mn}{}_{(i}\widetilde{\Delta}_{j)mn} + \widetilde{\Delta}^{mn}{}_i\widetilde{\Delta}_{mnj}. \tag{5.57}$$

5.4 Comparison of GBSSN, FCCZ4 and RCCZ4

This section presents the results of three strong field tests that compare RCCZ4 to FCCZ4 and GBSSN in spherical symmetry using a massless scalar field matter source. In Sec. 5.4.1 we investigate the convergence of each formalism for subcritical initial data on uniform grids. Sec. 5.4.2 then studies the relative performance of each method in simulating black hole spacetimes with puncture initial data [5, 59]. Finally, Sec. 5.4.3 investigates the performance of each formalism in the context of critical collapse, where we tune to the threshold of black hole formation using adaptive mesh refinement (AMR).

For all investigations, we work in spherical symmetry with conformal spatial metric, $\widetilde{\gamma}_{ij}$,

$$\widetilde{\gamma}_{ij} = \begin{bmatrix} g_a(t,r) & 0 & 0 \\ 0 & r^2 g_b(t,r) & 0 \\ 0 & 0 & r^2 \sin^2\theta g_b(t,r) \end{bmatrix}, \tag{5.58}$$

unit normal, n^μ, to the foliation,

$$n^\mu = \frac{1}{\alpha(t,r)} \begin{bmatrix} 1 & -r\beta_a(t,r) & 0 & 0 \end{bmatrix}, \tag{5.59}$$

trace-free extrinsic curvature, $\widetilde{A}^i{}_j$,

$$\widetilde{A}^i{}_j = \begin{bmatrix} A_a(t,r) & 0 & 0 \\ 0 & A_b(t,r) & 0 \\ 0 & 0 & A_b(t,r) \end{bmatrix}, \tag{5.60}$$

stress tensor, $S^i{}_j$,

$$S^i{}_j = \begin{bmatrix} S_a(t,r) & 0 & 0 \\ 0 & S_b(t,r) & 0 \\ 0 & 0 & S_b(t,r) \end{bmatrix}, \tag{5.61}$$

momentum density, j^i,

$$j^i = \begin{bmatrix} r j_a(t,r) & 0 & 0 \end{bmatrix}, \tag{5.62}$$

conformal connection functions $\widetilde{\Delta}^i$ and $\widetilde{\Lambda}^i$,

$$\widetilde{\Delta}^i = \begin{bmatrix} r\widetilde{\Delta}_a(t,r) & 0 & 0 \end{bmatrix}, \tag{5.63}$$

$$\widetilde{\Lambda}^i = \begin{bmatrix} r\widetilde{\Lambda}_a(t,r) & 0 & 0 \end{bmatrix}, \tag{5.64}$$

and spatial projections of Z_μ,

$$\bar{Z}_i = \begin{bmatrix} r\bar{Z}_a(t,r) & 0 & 0 \end{bmatrix}. \tag{5.65}$$

We take a massless scalar field, $\psi(t,r)$, with stress-energy tensor,

$$T_{\mu\nu} = \nabla_\mu\psi\nabla_\nu\psi - \frac{1}{2}g_{\mu\nu}\nabla_l\psi\nabla^l\psi, \tag{5.66}$$

as our matter model.

The equations of motion are found through application of the results of Secs. 5.2 and 5.3. In order to regularize the equation of motion in the vicinity of black hole punctures, we evolve the regular quantity $X = e^{-2\chi}$ in place of χ. As defined above, all of α, β_a, g_a, g_b, X, $\widetilde{A}_a$, $\widetilde{A}_b$, K, $\widetilde{\Delta}_a$, $\widetilde{\Lambda}_a$, Θ, $\bar{Z}_a$, ρ, $\widetilde{j}_a$, S, S_a and S_b are even functions of r as $r \to 0$ and the following identities hold:

$$g_a = \frac{1}{g_b^2}, \tag{5.67}$$

$$A_a = -2A_b. \tag{5.68}$$

5.4.1 Convergence and Independent Residual Tests

We validate our evolution schemes and code through the use of independent residual convergence and by monitoring the convergence of various constraints. All tests are performed for marginally subcritical initial data so that slightly stronger initial data would result in black hole formation.

Our code is implemented as a simple second order in space and time Crank-Nicolson solver using a uniform grid in r and t with fourth order Kreiss-Oliger dissipation [72] applied at the current and advanced time levels. The code is built on PAMR [102] and AMRD [101] and supports AMR in space and time using the Berger-Oliger approach [24]. Grid function values at refinement boundaries are set via third order temporal interpolation.

Our independent residual evaluators take the form of alternative discretizations of the ADM equations applied to our computed solutions. The application of an alternative discretization helps ensure that our evolution scheme is free of subtle flaws while our use of the ADM equations (as opposed to GBSSN, FCCZ4 or RCCZ4), aids in demonstrating convergence to GR rather than some other differential system.

Returning to the specific calculations performed in this subsection, the initial data is taken to be time symmetric with the massless scalar field, ψ, set according to:

$$\psi(0, r) = ae^{-(r-r_0)^2/\sigma^2}, \tag{5.69}$$

$$\partial_t \psi(0, r) = 0. \tag{5.70}$$

Specifically, for our testing we have taken $a = 0.035$, $\sigma = 2$ and $r_0 = 12$ so that, as mentioned above, we are in the subcritical regime but relatively close to the critical point of $a \approx 0.0362$. The dynamics are therefore non-linear, span several orders of magnitude, and are far from trivial. Initial data for the conformal factor, $X = e^{-2\chi}$, is determined by solving the Hamiltonian constraint on a finite grid where X is assumed to behave as $1 + a/r$ at the outer boundary. This grid is sized so that errors at the outer boundary are unable to propagate into the region of interest during the course of the convergence testing.

Our simulations are run with generalized 1+log lapses and a Lambda driver shift given by

$$\partial_t \alpha = -2\alpha K, \tag{5.71}$$

$$\partial_t \alpha = -2\alpha \left(K - 2\Theta\right), \tag{5.72}$$

$$\partial_t \alpha = -2\alpha \left(K - 2\widetilde{\Theta}\right), \tag{5.73}$$

$$\partial_{tt} \beta^i = \frac{3}{4} \partial_t \Lambda^i - 2\partial_t \beta^i, \tag{5.74}$$

where (5.71), (5.72) and (5.73) are the slicing conditions used for GBSSN, FCCZ4 and RCCZ4, respectively.

Figures 5.1–5.3 demonstrate convergence of the Hamiltonian and momentum constraints for each of GBSSN, FCCZ4 and RCCZ4. In each figure, the dashed lines show norms evaluated on a

$r = [0, 64]$ grid at fixed resolutions of 1025, 2049 and 4097 points, respectively. For each simulation, and prior to the evaluation of their norm, the constraints are interpolated to a uniform grid of fixed resolution. This enables direct comparison of the convergence rates among the simulations. In each figure, the solid color denotes an AMR simulation with a per-step error tolerance of 10^{-4} which has been interpolated to the same uniform grid used for the unigrid simulations. In these figures, a factor of 4 difference in the independent residuals or constraint maintenance between runs which differ by a factor of 2 in grid spacing indicates second order convergence. The AMR runs are observed to remain well within the convergent regime for all simulations for each of GBSSN, FCCZ4 and RCCZ4.

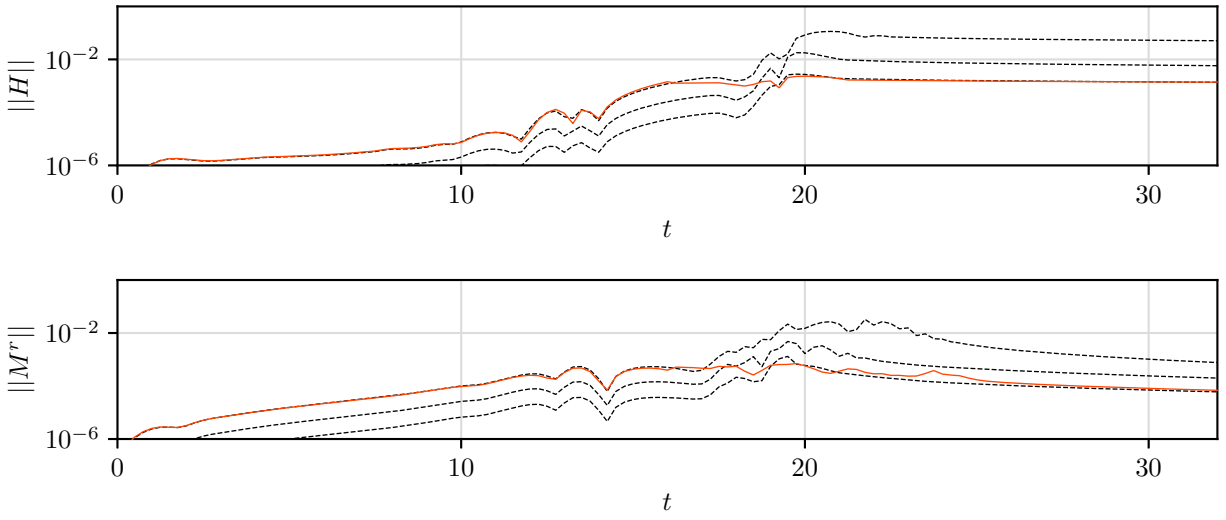

Figure 5.1: l_2 norms of the Hamiltonian and momentum constraint violations for the GBSSN formulation. Simulations are shown for fixed resolutions (dashed lines) of 1025, 2049 and 4097 points. Results from an AMR simulation with a relative local error tolerance of 10^{-4} are shown as the solid colored lines. The AMR simulations are well within the convergent regime.

Figs. 5.4–5.7 show the performance of each formalism relative to one another. The simulations are run at a resolution of 4097 grid points on a grid which extends to $r = 64$ (corresponding to the most refined unigrid run of Figs. 5.1–5.3). We choose the domain on which the norms are evaluated such that signals have not had sufficient time to propagate from the outer boundary (which is set assuming $X = 1 + a/r$ for some value a) into the domain of interest. It should be stressed that for all of the norms plotted in Figs. 5.4–5.7, the solutions are well resolved. The significant, and previously studied, improvements of the FCCZ4 method over GBSSN [47] in maintaining the Hamiltonian constraint and independent residuals is a real effect which is present even at high resolutions.

5.4.2 Evolution of Black Hole Spacetimes

In order for RCCZ4 (or a to-be-developed formalism based upon similar principles) to be competitive with GBSSN or FCCZ4 in the domain of strong field numerical simulations (which frequently involve singularities), it first needs to be capable of stably evolving black holes. Here, we show that with minor modifications to the standard 1+log and Delta driver gauges, RCCZ4 in spherical symmetry is at least as capable as FCCZ4 for the evolution of black hole space times.

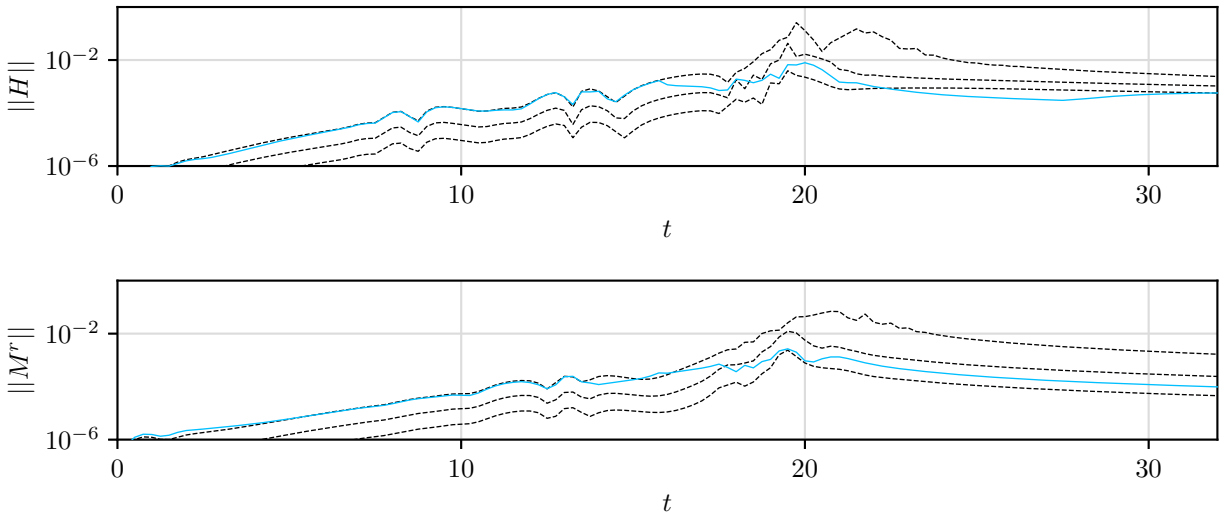

Figure 5.2: l_2 norms of the Hamiltonian and momentum constraint violations for the FCCZ4 formulation. Simulations are shown for fixed resolutions (dashed lines) of 1025, 2049 and 4097 points. Results from an AMR simulation with a relative local error tolerance of 10^{-4} are shown as the solid colored lines. The AMR simulations are observed to be well within the convergent regime.

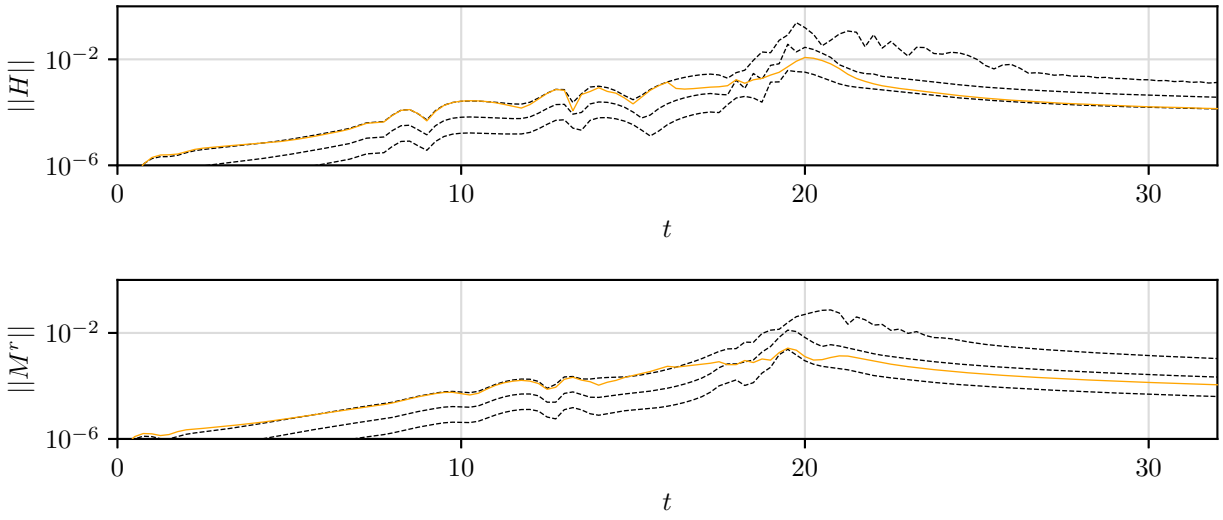

Figure 5.3: l_2 norms of the Hamiltonian and momentum constraint violations for the RCCZ4 formulation. Simulations are shown for fixed resolutions (dashed lines) of 1025, 2049 and 4097 points. Results from an AMR simulation with a relative local error tolerance of 10^{-4} are shown as the solid colored lines. The AMR simulations are well within the convergent regime.

We start with standard time symmetric, black hole puncture initial data [5, 54] given by:

$$X = \left(1 + \frac{M}{2r}\right)^{-2}, \tag{5.75}$$

$$\alpha = \left(1 + \frac{M}{2r}\right)^{-2}, \tag{5.76}$$

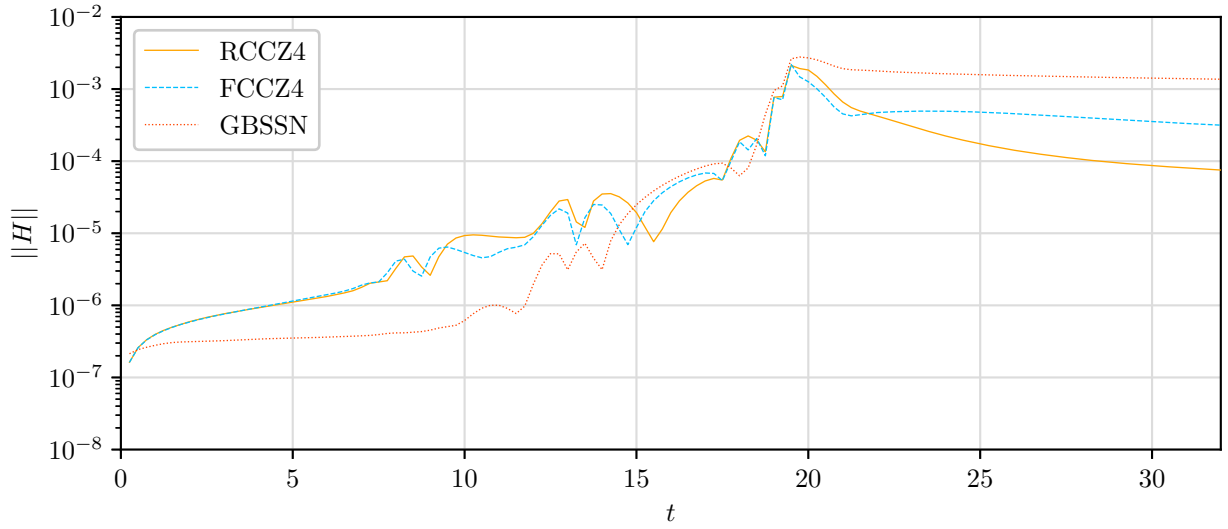

Figure 5.4: l_2 norm of the Hamiltonian constraint violation for the case of strong field initial data for each of GBSSN, FCCZ4 and RCCZ4. The difference between RCCZ4 and FCCZ4 is largely due to a more pronounced outgoing pulse of constraint violation (which leaves nearly flat space in its wake) while the large static constraint violation of GBSSN is concentrated at the origin and leaves behind a metric that does not appear to be a valid solution to the Einstein-scalar equations.

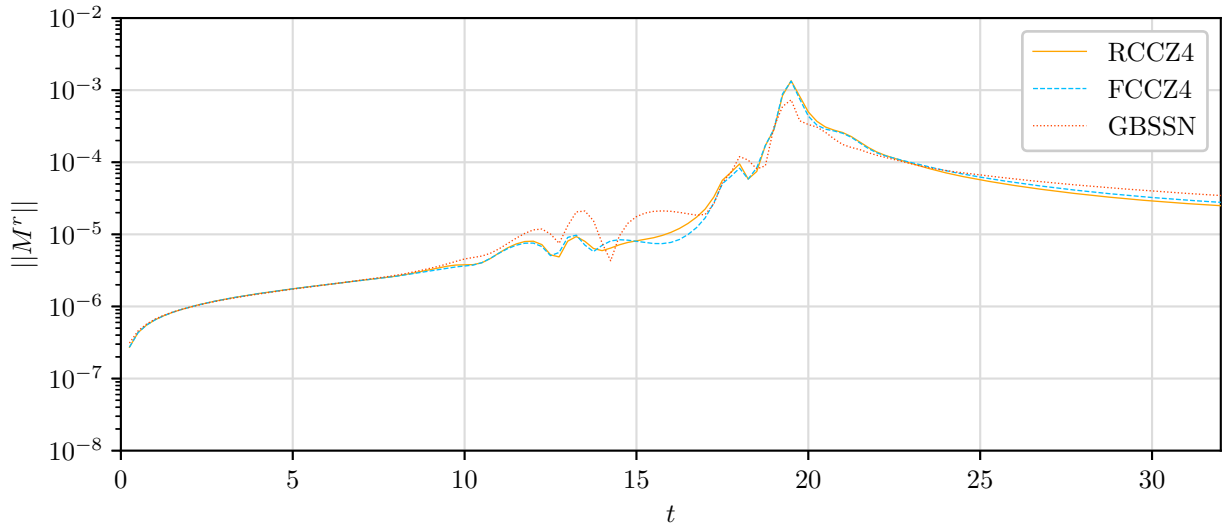

Figure 5.5: l_2 norm of the momentum constraint violation for the case of strong field initial data for each of GBSSN, FCCZ4 and RCCZ4. Not surprisingly, the performance of the three methods is largely equivalent as they are all designed to advect away the momentum constraint violation.

$$\beta_a = K = A_a = A_b = 0, \tag{5.77}$$

$$g_a = g_b = 1. \tag{5.78}$$

The simulations are performed on large grids ($r = [0, 128M]$ with $M = 4$) which are further

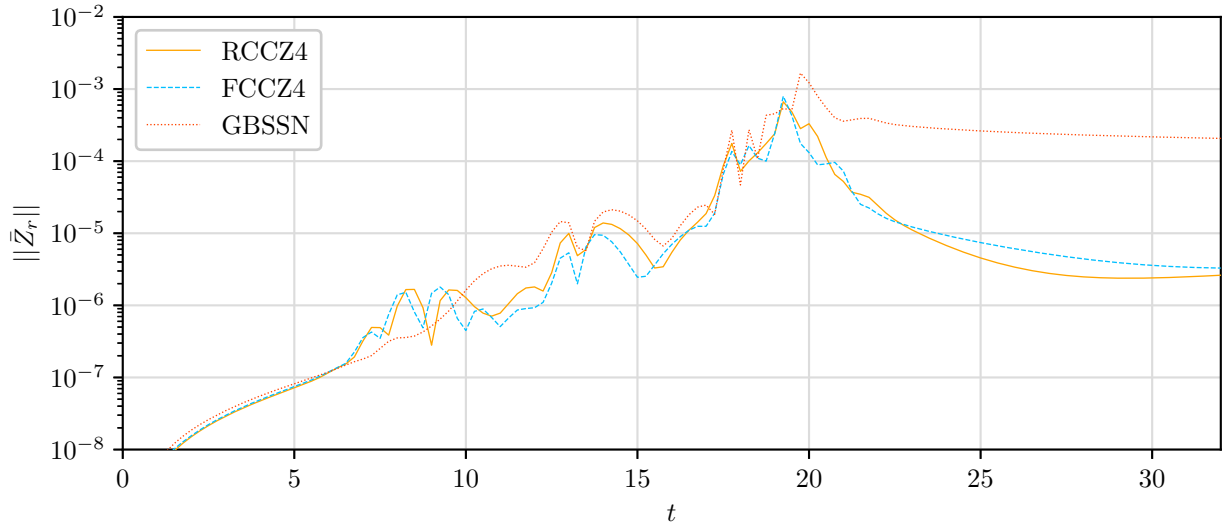

Figure 5.6: l_2 norm of $\bar{Z}_r = g_a(\tilde{\Lambda}^r - \tilde{\Delta}^r)/2$ for the case of strong field initial data for each of GBSSN, FCCZ4 and RCCZ4. As in the case of the Hamiltonian constraint, the GBSSN errors are concentrated at the origin where the curvature takes on its largest values. This error remains essentially static save for the mitigating factor of dissipation. At this resolution, FCCZ4 preserves the constraint about 100 times better than GBSSN while RCCZ4 improves upon this by a further factor of ~ 3 or so at late times.

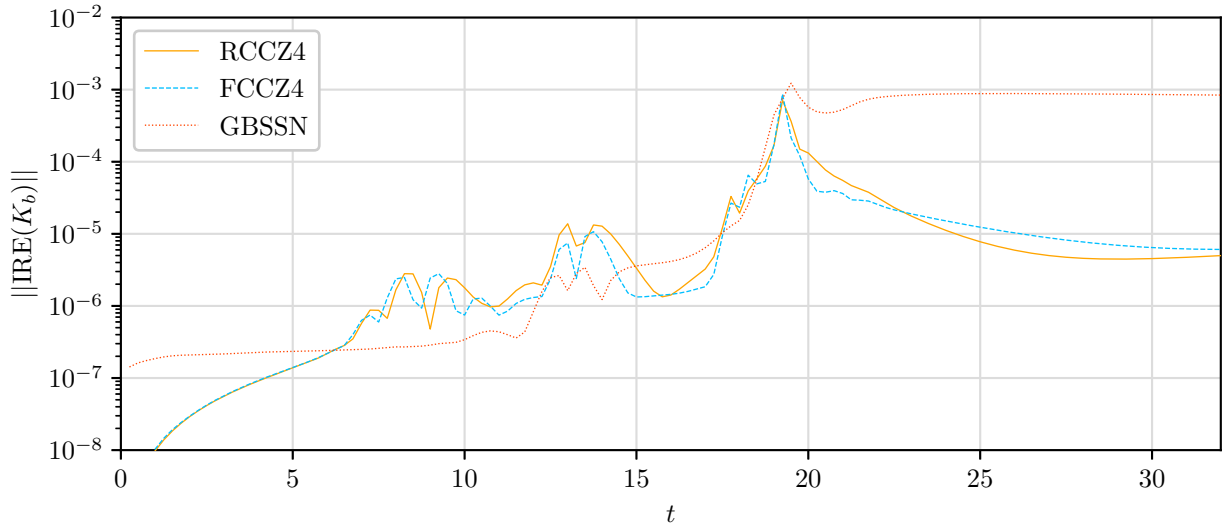

Figure 5.7: l_2 norm of the independent residual evaluator for K_b. At late times, as the solution should be approaching flat space, RCCZ4 has better performance than either FCCZ4 or GBSSN.

refined via fixed mesh refinement (FMR) [5]. The sizes of the fixed refinement regions were determined

[5]For these tests we wanted to have as little contamination from imperfectly specified boundary conditions as possible while performing long term evolutions. Correspondingly, we placed the outer boundary at $r = 128M$ and evolved until $t = 64M$. All results presented are evaluated on the portion of the spatial domain between the horizon and $r = 8M$.

by first evolving the initial data with adaptive mesh refinement. At the conclusion of this AMR run, each level of refinement had a maximum extent and that maximum extent then defined the limits of the corresponding level of refinement for the FMR calculations. In the simulations, the use of mesh refinement serves several purposes. First, it reduces the computational load for high resolution simulations. Second, it allows us to verify the compatibility of our implementation of the GBSSN, FCCZ4 and RCCZ4 formalisms with AMR. Third, by using fixed (as opposed to adaptive) mesh refinement, we eliminate complications caused by each formulation employing slightly different regridding procedures. This, in turn, facilitates the analysis of convergence properties. Table 5.1 shows the extent and refinement ratio of each grid used for the black hole simulations.

We note that the quantities $\bar{Z}_i$ and Θ are effectively error terms which serve to propagate violations of the momentum and Hamiltonian constraints and that they tend to grow in the vicinity of refinement boundaries. As such, we find that is is best to either evolve $\tilde{\Lambda}^i$ (rather than $\bar{Z}_i$) or to omit Θ and $\bar{Z}_i$ from the truncation error calculation used to determine the placement of refined regions.

Level	$r_{\min}$	$r_{\max}$	h_r^0	h_r^1	h_r^2	h_r^3
1	0	512	8	4	2	1
2	0	512	4	2	1	2^{-1}
3	0	256	2	1	2^{-1}	2^{-2}
4	0	256	1	2^{-1}	2^{-2}	2^{-3}
5	0	128	2^{-1}	2^{-2}	2^{-3}	2^{-4}
6	0	64	2^{-2}	2^{-3}	2^{-4}	2^{-5}
7	0	32	2^{-3}	2^{-4}	2^{-5}	2^{-6}

Table 5.1: Parameters for the meshes in fixed mesh refinement convergence simulations. The fixed mesh refinement simulations use a total of 7 refinement levels as labeled in the first column. The extent of each mesh is displayed in columns 2 and 3 ($r_{\min}$ and $r_{\max}$). The grid spacings for the lowest resolution simulation are shown in the fourth column (h_r^0). Each of the final three columns (h_r^1, h_r^2 and h_r^3) give grid spacings for progressively higher resolution simulations. As an example, the 6^{th} refinement level (Level 6) has a spatial extent of $r = (0, 64)$. For the most resolved simulation (h_r^3), the grid spacing on that level is 2^{-5}.

Figures 5.8–5.9 show the evolutions of α, β^r and X as well as the coordinate location of the apparent horizon ($\Theta_{\text{Hor}} = 0$). As is well known [7, 9, 36, 59, 62, 121], puncture type initial data evolves towards a trumpet like spacetime and performs a form of automatic excision in the vicinity of the puncture. In this region, the evolved and constrained quantities do not converge.

The convergence of the l_2 norms of the various constraints in the region external to the apparent horizon ($r = [r_{\text{AH}}, 8M]$) and for each formalism are shown in Figs. 5.10–5.12. The dashed lines show simulations with $h_r = h_r^0$, $h_r = h_r^1$ and $h_r = h_r^2$ while the solid color denotes the most resolved $h_r = h_r^3$ simulation. Fig. 5.13 compiles the highest resolution runs of Figs. 5.10–5.12 and permits a direct comparison of the implementations. Independent residuals behave similarly and so have not been plotted.

Examining Fig. 5.13, we see that for a stationary black hole GBSSN is favoured over either FCCZ4 or RCCZ4. For a simulation where we are concerned with computing the constraint violation external to the apparent horizon, this makes intuitive sense: the formulation which does not propagate Hamiltonian constraint violations away from punctures or grid refinement boundaries should produce superior results when the fields are nearly stationary. However, as shown in [63], for more dynamical situations we should not expect superior performance from BSSN-type simulations.

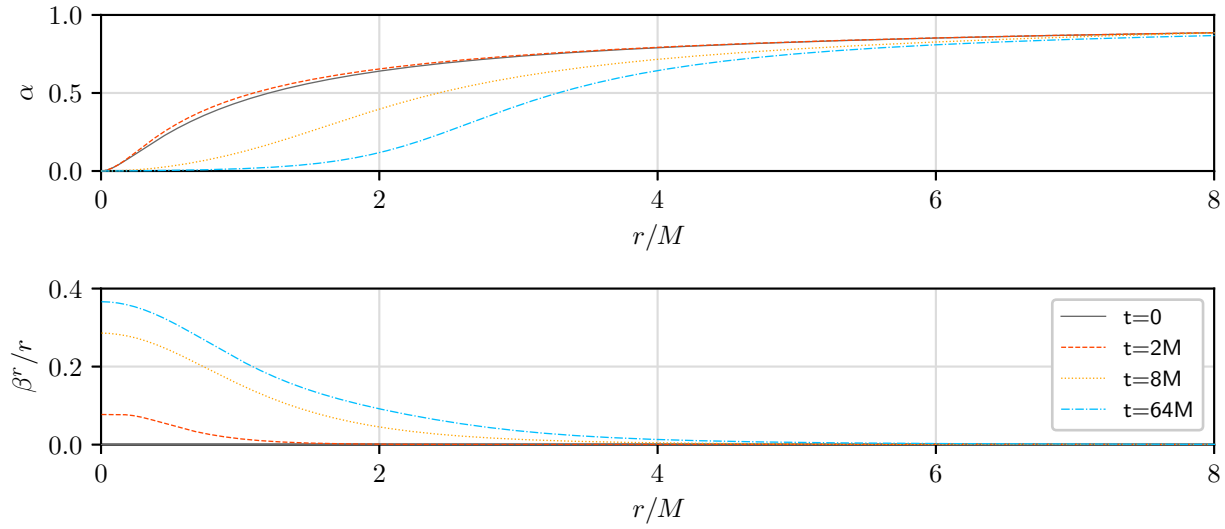

Figure 5.8: Evolution of α and β^r from $t = 0$ to $t = 64M = 256$. The initial puncture type initial data quickly evolves towards trumpet type data with α going as r as opposed to r^2 at the puncture.

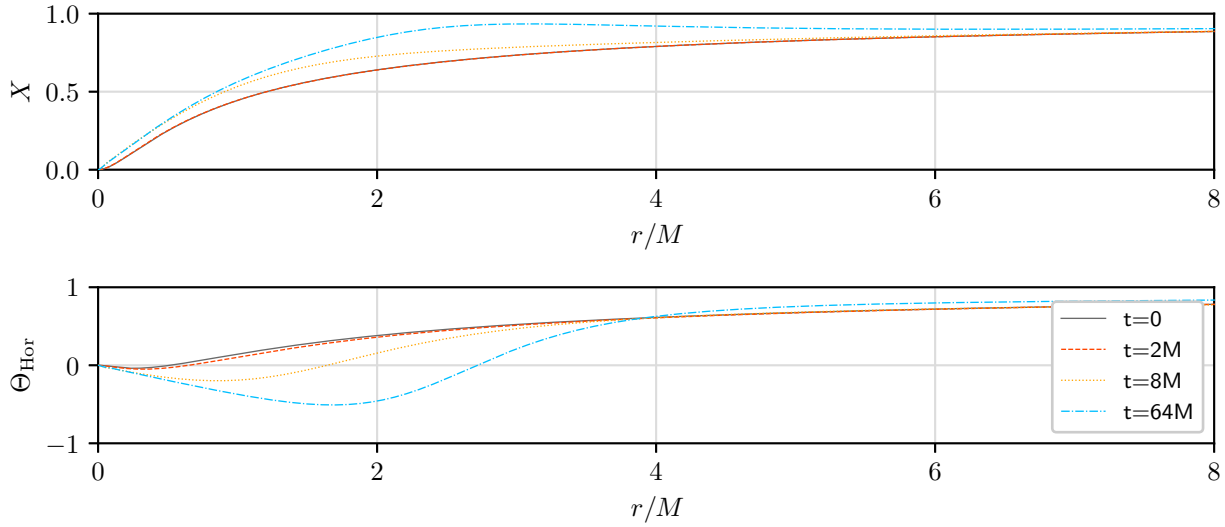

Figure 5.9: Evolution of X and Θ_{Hor} from $t = 0$ to $t = 64M = 256$. The initial puncture type initial data quickly evolves towards trumpet type initial data with X going as r as opposed to r^2 at the puncture. As can be seen in the graph of Θ_{Hor}, the coordinate location of the apparent horizon (where $\Theta_{\text{Hor}} = 0$) increases slowly with coordinate time.

As noted in Fig. 5.11, the errors in the momentum constraint (and $\bar{Z}_r$) for FCCZ4 appear to be dominated by the development of artifacts at the mesh refinement boundaries. Doubtless, these issues could be mitigated with proper attention. The relatively poor performance of FCCZ4 in comparison to GBSSN and RCCZ4 in these simulations should therefore not be seen as a shortcoming of the method, but as an issue arising from our demand that the methods be compared via runs with identical parameters. Taking this into account, we see that at early times (before the

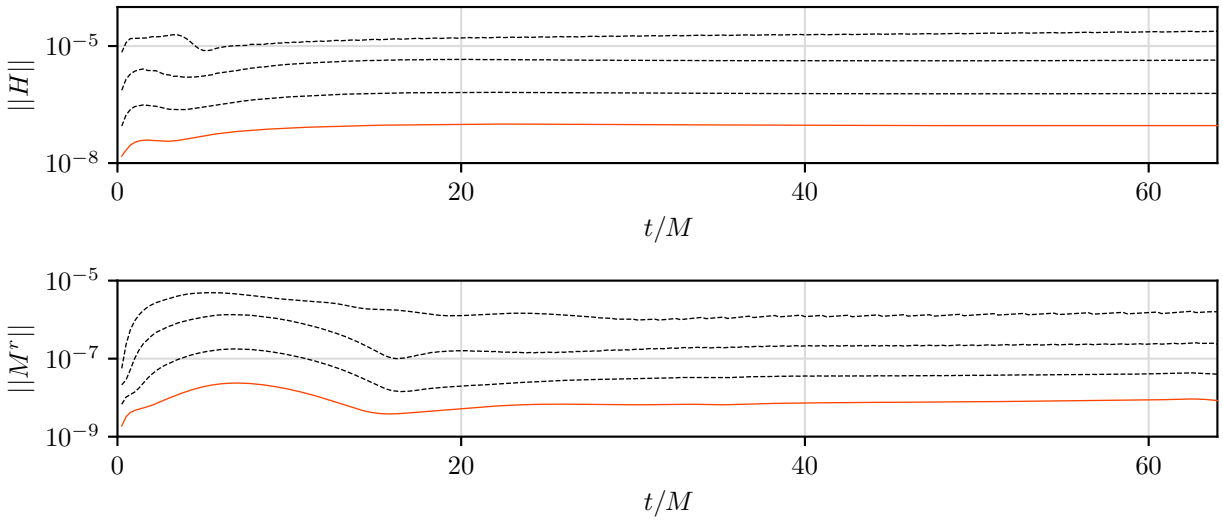

Figure 5.10: l_2 norms of the Hamiltonian and momentum constraint violations for the GBSSN formulation. Each successive line denotes a factor of 2 grid refinement. The solid line denotes the most refined simulation.

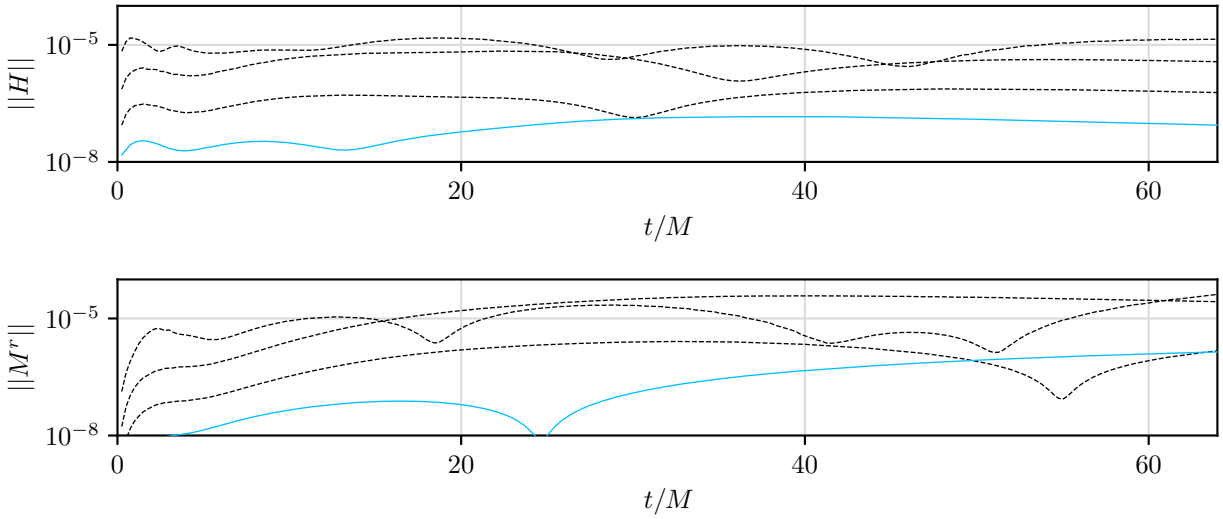

Figure 5.11: l_2 norms of the Hamiltonian and momentum constraint violations for the FCCZ4 formulation. The errors in the momentum constraint appear to be dominated by artifacts that arise at the mesh refinement boundaries. Our GBSSN and RCCZ4 simulations used identical parameters and neither experienced the same sort of issues arising at the mesh refinement boundaries. Rather than attempting to find more optimal parameters which could resolve these issues at the cost of preventing direct comparison with GBSSN and RCCZ4, the simulation is left as-is and we note that it would almost certainly be possible to find better parameters for FCCZ4 which would mitigate these issues.

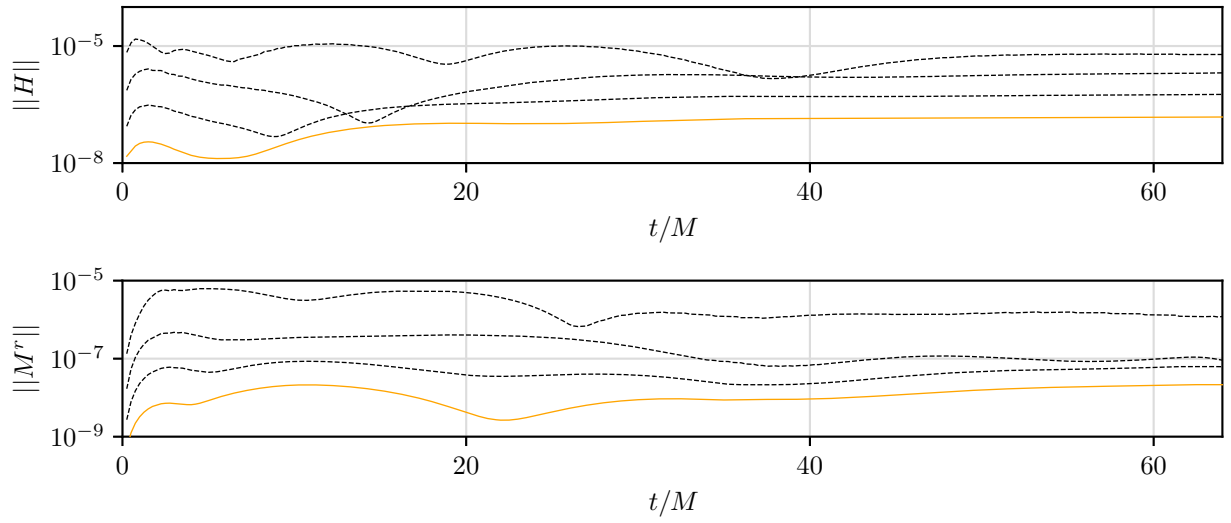

Figure 5.12: l_2 norms of the Hamiltonian and momentum constraint violations for the RCCZ4 formulation. Each successive line denotes a factor of 2 grid refinement. The solid line denotes the most refined simulation.

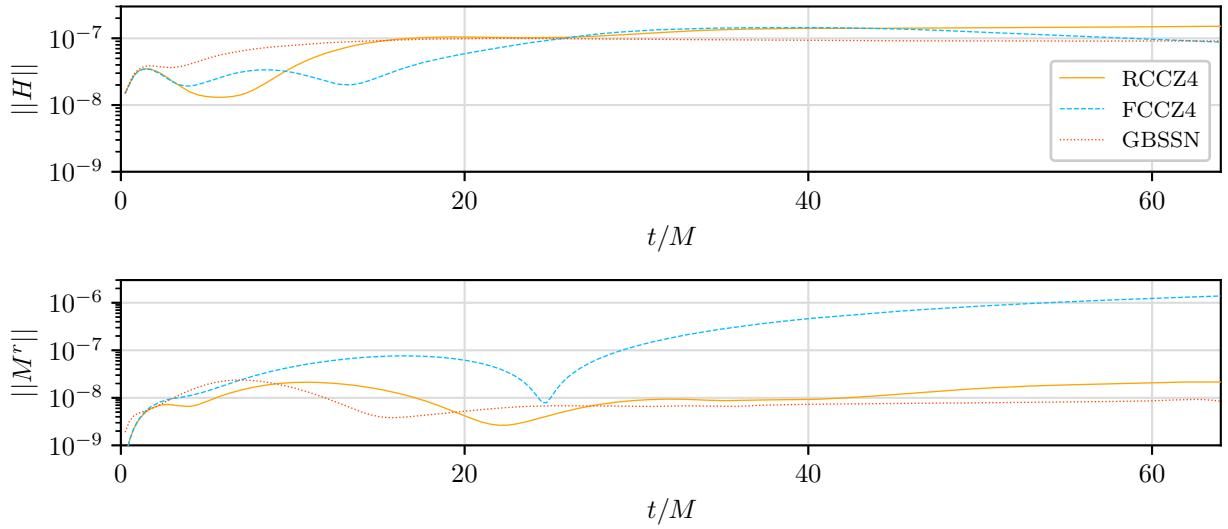

Figure 5.13: l_2 norms of the Hamiltonian constraint and momentum constraint violation for the $h_r = h_r^3$ run of each of the RCCZ4, FCCZ4 and GBSSN formulations. Here we can observe key differences in the constraint violating behaviours of each formulation. As the GBSSN simulation does not couple the Hamiltonian constraint to a propagating degree of freedom, errors within the horizon and at refinement boundaries are unable to propagate. Due to the fact that the black hole is not moving and the simulation quickly approaches a nearly stationary state, this lack of time dependence is advantageous. As shown in Section 5.4.1, the opposite is true when the simulation is highly dynamic. In those cases, both RCCZ4 and FCCZ4 provide orders of magnitude better constraint conservation.

errors become dominated by issues arising from grid refinement boundaries), the performance of each method is roughly equivalent.

5.4.3 Critical Collapse

Critical collapse represents the extreme strong field regime of general relativity and is therefore an excellent test case to determine the capabilities of a numerical formulation. Here we compare the RCCZ4, FCCZ4 and GBSSN formalisms, without constraint damping, in a test that studies each formalism's capacity to resolve the threshold of black hole formation using gauges which are natural extensions of the 1+log slicing, (5.71–5.73), with zero shift. For additional information concerning critical collapse, see [43] for the original study concerning the massless scalar field in spherical symmetry and [56, 58] for more general reviews.

For each of GBSSN, FCCZ4 and RCCZ4, we perform AMR simulations of massless scalar field collapse with a relative, per-step truncation error tolerance of 10^{-4}. We tune the amplitude of our initial data to the threshold of black hole formation with a relative tolerance of $\sim 10^{-12}$.

Figures 5.14–5.15 plot the central value of the lapse and the scalar field, respectively, against proper time at the approximate accumulation point (the spacetime point at which a naked singularity would form in the limit of infinite tuning) for the subcritical simulation closest to criticality in each formalism. Figures. 5.16–5.18 plot the magnitudes of constraint violations from these calculations. For these simulations we expect all dimensionful quantities to grow exponentially in $-\ln(\tau^\star - \tau)$ due to the discretely self-similar nature of the critical solution. To facilitate analysis of the overall growth rate of constraint violations, we plot the cumulative maximum, $\mathrm{cummax}(f(t), t)$, of each quantity. This function returns the largest magnitude encountered on the domain of the simulation up until that point in time (e.g. $\mathrm{cummax}(R, t_0)$ would return the largest value of R encountered during the simulation for $t = [0, t_0]$).

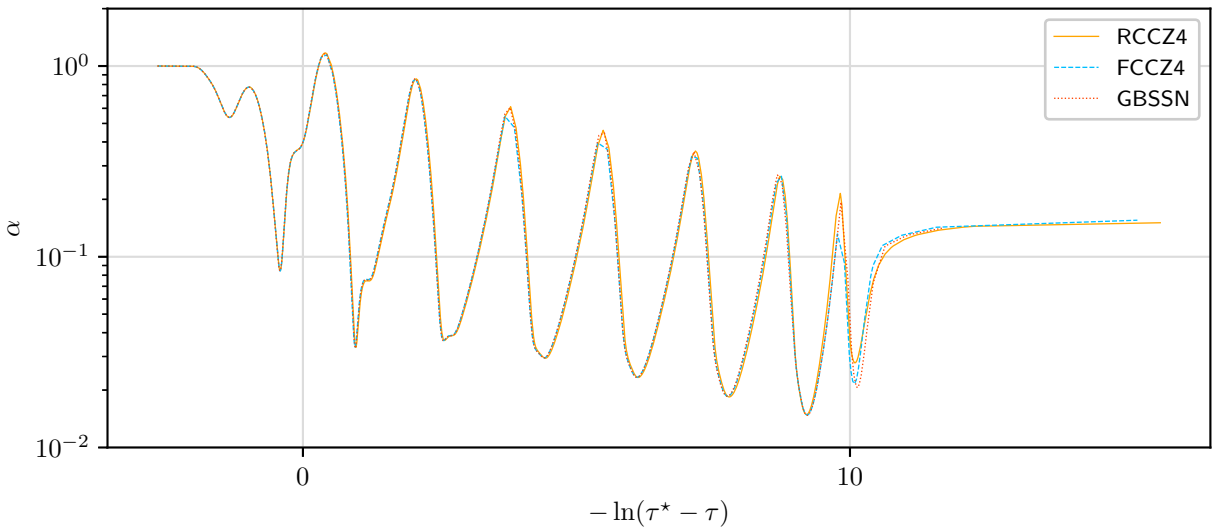

Figure 5.14: Lapse, α, at the accumulation point as a function of $-\ln(\tau^\star - \tau)$ with $\tau^\star$ an approximate accumulation time which is different for each set of simulations. Each of GBSSN, FCCZ4 and RCCZ4 are well suited to performing the critical evolutions. The observed discrepancies in α are primarily due to our output of data with insufficient frequency to resolve the peaks adequately. As expected, we are able to resolve approximately 3 echos at a relative search tolerance of 10^{-12}.

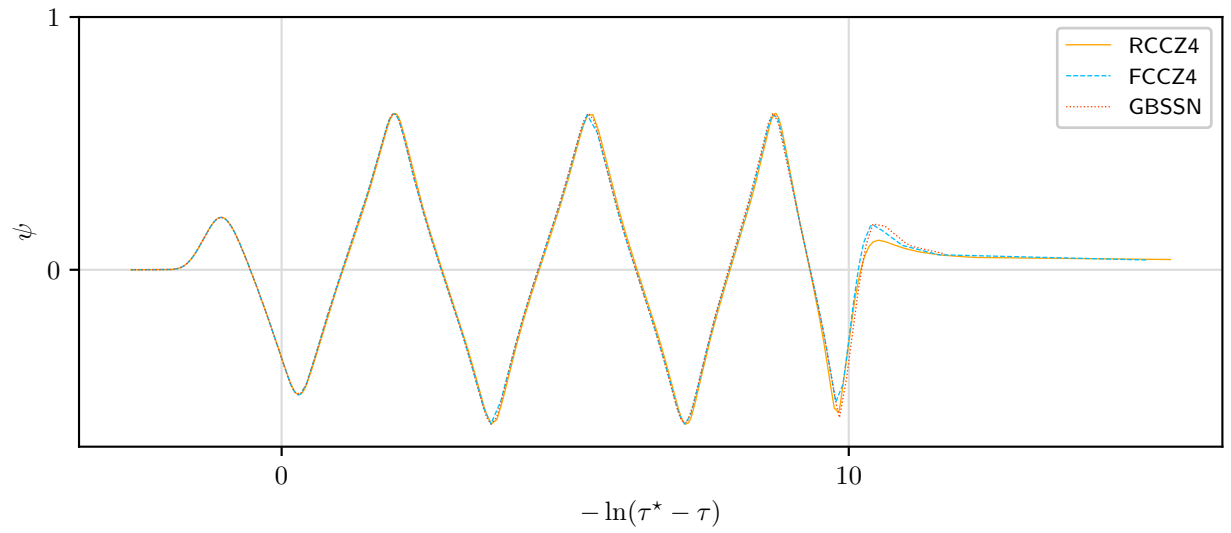

Figure 5.15: Scalar field, ψ, at the accumulation point as a function of $-\ln(\tau^\star - \tau)$. The discrete self similarity (DSS) is evident. Tuning the amplitude of our initial data to the threshold of black hole formation with a relative tolerance of $\sim 10^{-12}$ allows us to resolve approximately three echos.

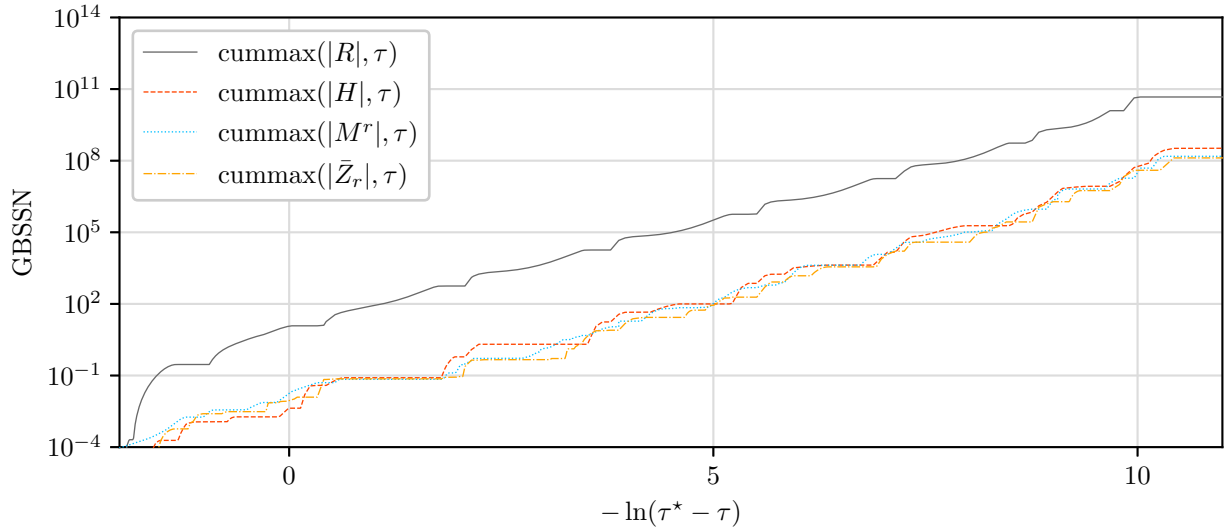

Figure 5.16: Cumulative maximal values of R, $\bar{Z}_r$, the Hamiltonian constraint and momentum constraint violations for critical collapse of the scalar field in the GBSSN formulation. For clarity, we have not shown the behaviour of the Hamiltonian constraint post-dispersal, where it is dominated by a large non propagating remnant similar to that seen in Fig. 5.1.

As seen in Figs. 5.16–5.18, when evolved using identical error tolerances and parameters, we find that GBSSN does the best at maintaining a constant level of relative constraint violation throughout the simulation. We find that with a per-step error tolerance of 10^{-4}, GBSSN maintains a constant error ratio of about 10^{-3} relative to the magnitude of the Ricci scalar. For FCCZ4, this is reduced to 10^{-2} while RCCZ4 performs similarly to FCCZ4 for the first echo or so and then

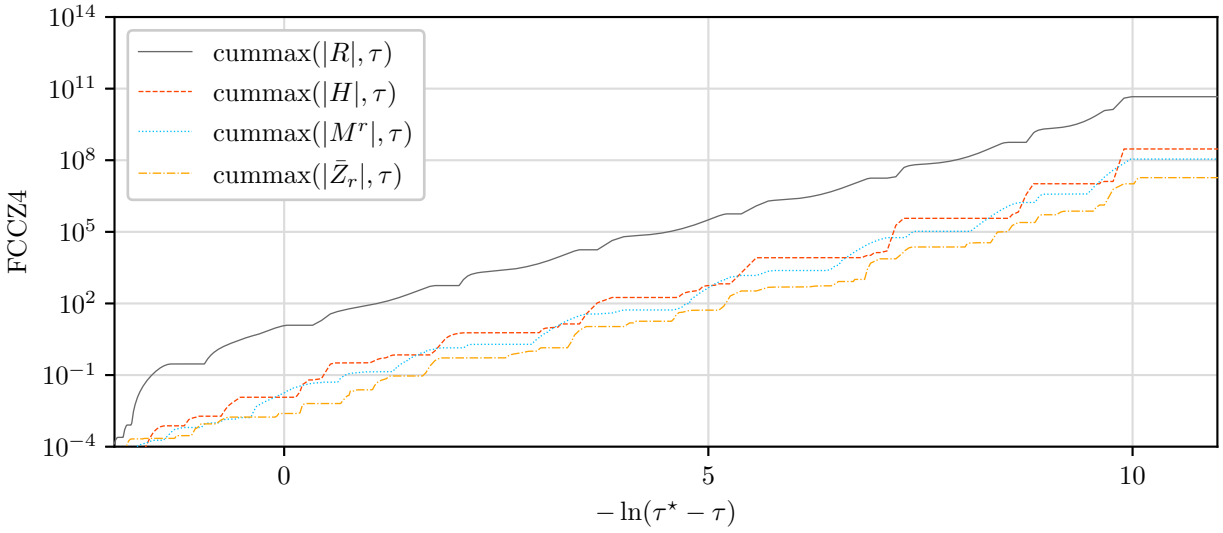

Figure 5.17: Cumulative maximal values of R, $\bar{Z}_r$, the Hamiltonian constraint and momentum constraint violations for critical collapse of the scalar field in the FCCZ4 formulation. For subcritical simulations close to criticality, the post dispersal constraint violating remnant is much smaller than that of GBSSN but is still too large to continue the simulation for long periods of time.

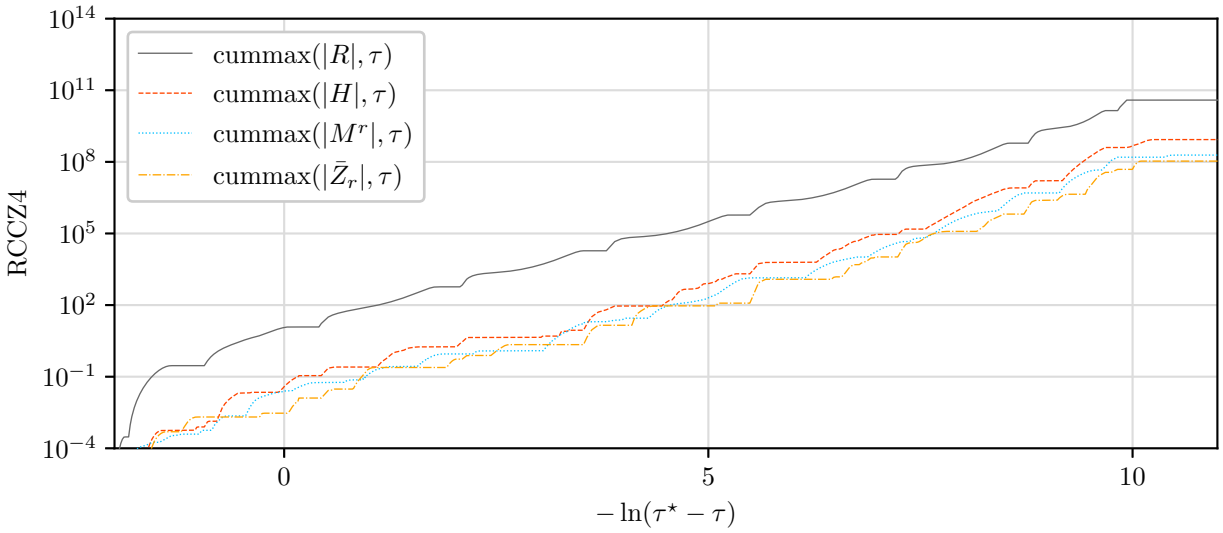

Figure 5.18: Cumulative maximal values of R, $\bar{Z}_r$, the Hamiltonian constraint and momentum constraint violations for critical collapse of the scalar field in the RCCZ4 formulation. For subcritical simulations close to criticality, the post dispersal constraint violating remnant is much smaller than that of GBSSN but is still too large to continue the simulation for long periods of time. Close to criticality, the constraint violations grow noticeably faster than either GBSSN or FCCZ4 (while still providing adequate resolution to investigate criticality).

gradually accumulates more error, performing worse than either GBSSN or FCCZ4 at late times.

At this point, the cause of this dip in performance for RCCZ4 is unclear to us. However, it is entirely possible that it is due to a suboptimal regridding strategy. Alternatively, it could very well be that the variant of the 1+log slicing condition used, Eqn. (5.73), is not ideal for controlling the Hamiltonian constraint. We tried several variations of the form $\partial_t \alpha = -2\alpha(K - 2f(\alpha)\widetilde{\Theta})$, which, for the most part, resulted in similar performance and stability properties. When we compare the suboptimal performance of RCCZ4 in the critical collapse of the scalar field to the performance in both the subcritical convergence tests and black hole evolution, we are lead to believe that RCCZ4 may perform best when coupled with a Lambda driver shift condition.

5.5 Hyperbolicity of RCCZ4

We now turn to an analysis of the hyperbolicity of RCCZ4. We demonstrate that, relative to GBSSN, RCCZ4 has one fewer zero-velocity modes, which roughly corresponds to the fact that in Z4 derived formulations the equivalent of the Hamiltonian constraint is dynamical [25, 47, 63]. As outlined in [6, 39, 89], and in the context of numerical relativity, these zero-velocity modes often correspond to constraint violations and are thought to contribute to instabilities. Consequently, formulations that minimize these modes are generally favoured.

Here we derive the conditions under which RCCZ4 is hyperbolic, performing a pseudodifferential reduction [57, 90] following the procedure of Cao and Wu [39] who have previously applied the method to a study of the hyperbolicity of BSSN in $f(R)$ gravity. We consider the RCCZ4 equations of motion (5.32)–(5.38) in the vacuum and choose a generalization of the Bona-Masso family of lapses [5, 30] together with generalized Lambda drivers for the shift. Specifically, defining

$$\partial_0 = \partial_t - \beta^i \partial_i \tag{5.79}$$

the equation for the lapse is

$$\partial_0 \alpha = -\alpha^2 h\left(\alpha, \chi, x^\mu\right)\left(K - K_0 - \frac{m\left(\alpha, \chi, x^\mu\right)}{\alpha}\widetilde{\Theta}\right). \tag{5.80}$$

Our generalized Lambda driver takes the form

$$\partial_0 \beta^i = \alpha^2 G\left(\alpha, \chi, x^\mu\right) B^i, \tag{5.81}$$

where the auxiliary vector B^i satifies

$$\partial_0 B^i = e^{-4\chi} H\left(\alpha, \chi, x^\mu\right) \partial_0 \widetilde{\Lambda}^i - \eta\left(B^i, \alpha, x^\mu\right), \tag{5.82}$$

and G and H are some specified functions.

We wish to determine the conditions under which the RCCZ4 system is strongly hyperbolic. This essentially amounts to verifying that the system admits a well defined Cauchy problem; i.e. that there exist no high frequency modes with growth rates which cannot be bounded by some exponential function of time [90]. We can thus study strong hyperbolicity by linearizing the equations about some generic solution and examining the resulting system in the high frequency regime where it takes the form

$$\partial_0 u = \mathbf{M}^i \partial_i u + \mathbf{S} u. \tag{5.83}$$

Here, u is a vector of n solution fields, $\mathbf{M}^i$ are n-by-n characteristic matrices and $\mathbf{S}u$ is a source vector that may depend on the fundamental variables u but not on their derivatives. Fourier

transforming the solution u via

$$\hat{u}\left(\omega\right) = \int e^{i(\omega_k x^k)} u\left(x\right) \mathrm{d}^3 x, \tag{5.84}$$

we can write (5.83) as

$$\partial_0 \hat{u} = i\omega_i \mathbf{M}^i \hat{u} + \mathbf{S}\hat{u}. \tag{5.85}$$

From this, we define the principal symbol of the system as $\mathbf{P}_1 = i\left|\omega\right|\mathbf{P} = i\omega_i \mathbf{M}^i$. The hyperbolicity of the system can then be discerned from the properties of $\mathbf{P}$:

- If $\mathbf{P}$ has imaginary eigenvalues, the system is not hyperbolic and cannot be formulated as a well-posed Cauchy problem.
- If $\mathbf{P}$ has only real eigenvalues but does not possess a complete set of eigenvectors, the system is weakly hyperbolic and may have issues with ill-posedness.
- If $\mathbf{P}$ has both real eigenvalues and a complete set of eigenvectors, the system is strongly hyperbolic and the Cauchy problem is well-posed.

Returning to the specific case of the RCCZ4 formulation in vacuum, we freeze the coefficients in (5.52)–(5.56). Upon applying a Fourier transformation to the linear constant coefficient problem that arises, we obtain:

$$\partial_0 \hat{\chi} = -\frac{1}{6}\alpha \hat{K} + \frac{1}{6}\left(i\omega_k\right)\hat{\beta}^k, \tag{5.86}$$

$$\partial_0 \hat{K} = \alpha \hat{R} + \omega_l \omega_m \gamma^{lm} \hat{\alpha} + 2\alpha\gamma^{lm}\left(i\omega_l \hat{Z}_m\right), \tag{5.87}$$

$$\partial_0 \hat{\tilde{\Theta}} = \frac{1}{2}\alpha^2\left(\hat{R} + 2\left(i\omega_i\right)\hat{Z}_j\gamma^{ij}\right), \tag{5.88}$$

$$\partial_0 \hat{\tilde{\gamma}}_{ij} = -2\alpha\hat{\tilde{A}}_{ij} - \frac{2}{3}\tilde{\gamma}_{ij}\left(i\omega_m\right)\hat{\beta}^m + \tilde{\gamma}_{im}\left(i\omega_j\right)\hat{\beta}^m + \tilde{\gamma}_{mj}\left(i\omega_i\right)\hat{\beta}^m, \tag{5.89}$$

$$\partial_0 \hat{\tilde{A}}_{ij} = e^{-4\chi}\left[\omega_i\omega_j\gamma^{ij}\hat{\alpha} + \alpha\hat{R}_{ij} + 2\alpha\left(i\omega_{(i}\hat{Z}_{j)}\right)\right]^{\mathrm{TF}}, \tag{5.90}$$

$$\partial_0 \hat{\tilde{\Lambda}}^i = \tilde{\gamma}^{mn}\left(-\omega_m\omega_n\right)\hat{\beta}^i + \frac{1}{3}\tilde{\gamma}^{ik}\left(-\omega_k\omega_n\right)\hat{\beta}^n - \frac{4}{3}\alpha\tilde{\gamma}^{ij}\left(i\omega_j\right)\hat{K} + 2\tilde{\gamma}^{ik}\left(i\omega_k\right)\hat{\tilde{\Theta}}, \tag{5.91}$$

$$\partial_0 \hat{Z}_i = \alpha\left[\left(i\omega_j\right)\hat{\tilde{A}}_{ki}\tilde{\gamma}^{jk} - \frac{2}{3}\left(i\omega_i\right)\hat{K}\right] + \left(i\omega_j\right)\hat{\tilde{\Theta}}, \tag{5.92}$$

$$\partial_0 \hat{\alpha} = -\alpha^2 h\hat{K} + \alpha h m'\hat{\tilde{\Theta}}, \tag{5.93}$$

$$\partial_0 \hat{\beta}^i = \alpha^2 G\hat{B}^i, \tag{5.94}$$

$$\partial_0 \hat{B}^i = 2H\gamma^{im}\partial_0\hat{Z}_m + H\left(i\omega^n\right)\tilde{\gamma}^{mi}\partial_0\hat{\tilde{\gamma}}_{mn}. \tag{5.95}$$

Here, since we are interested in the high frequency regime, we have kept only the highest order derivative terms. In these equations $\hat{R}_{ij}$ may either be considered as a function of $\tilde{\Lambda}^i$ (as would be the case for GBSSN):

$$\hat{R}_{ij} = \frac{1}{2}\tilde{\gamma}^{lm}\left(\omega_l\omega_m\right)\hat{\tilde{\gamma}}_{ij} + \frac{1}{2}\tilde{\gamma}_{mi}\left(i\omega_j\right)\hat{\tilde{\Lambda}}^m + \frac{1}{2}\tilde{\gamma}_{mj}\left(i\omega_i\right)\hat{\tilde{\Lambda}}^m + 2\left(\omega_i\omega_j\right)\hat{\chi} + 2\gamma_{ij}\gamma^{lm}\left(\omega_l\omega_m\right)\hat{\chi}, \tag{5.96}$$

or as a function of $\tilde{\Delta}^i$ (as derived in Sec. 5.2):

$$\hat{R}_{ij} = \frac{1}{2}\tilde{\gamma}^{lm}\left(\omega_l\omega_m\right)\hat{\tilde{\gamma}}_{ij} + \frac{1}{2}\tilde{\gamma}_{mi}\left(i\omega_j\right)\hat{\tilde{\Delta}}^m + \frac{1}{2}\tilde{\gamma}_{mj}\left(i\omega_i\right)\hat{\tilde{\Delta}}^m + 2\left(\omega_i\omega_j\right)\hat{\chi} + 2\gamma_{ij}\gamma^{lm}\left(\omega_l\omega_m\right)\hat{\chi}. \tag{5.97}$$

In what follows, $\epsilon = 1$ corresponds to the use of $\widetilde{\Delta}^i$ while $\epsilon = 2$ corresponds to the definition in terms of $\widetilde{\Lambda}^i$. Roughly following [39], we introduce the variables:

$$\omega_i = |\omega|\,\widetilde{\omega}_i, \tag{5.98}$$

$$|\omega|^2 = \gamma^{ij}\omega_i\omega_j, \tag{5.99}$$

$$\hat{\alpha} = \frac{-i\alpha}{|\omega|}\hat{a}, \tag{5.100}$$

$$\hat{\chi} = \frac{-i}{|\omega|}\hat{X}, \tag{5.101}$$

$$\hat{\tilde{\Theta}} = \alpha\hat{\Omega}, \tag{5.102}$$

$$\hat{\tilde{\Lambda}}^i = \tilde{\gamma}^{ij}\hat{\tilde{\Lambda}}_j, \tag{5.103}$$

$$\hat{\beta}^i = \frac{-i\alpha}{|\omega|}\gamma^{ij}\hat{b}_j, \tag{5.104}$$

$$\hat{B}^i = \gamma^{ij}\hat{B}_j, \tag{5.105}$$

$$\hat{\tilde{\gamma}}_{ij} = \frac{-ie^{-4\chi}}{|\omega|}\hat{l}_{ij}, \tag{5.106}$$

$$\hat{\tilde{A}}_{ij} = e^{-4\chi}\hat{L}_{ij}, \tag{5.107}$$

which permits us to write (5.86)–(5.95) as a first order pseudodifferential system of the form

$$\partial_0\hat{u} = i\,|\omega|\,\alpha\mathbf{P}\hat{u}, \tag{5.108}$$

where

$$\hat{u} = \begin{bmatrix}\hat{a} & \hat{\chi} & \hat{\Omega} & \hat{K} & \hat{b}_i & \hat{B}_i & \hat{\tilde{\Lambda}}_i & \hat{l}_{ij} & \hat{L}_{ij}\end{bmatrix}^{\mathrm{T}}. \tag{5.109}$$

Provided that $\mathbf{P}$ is diagonalizable with purely real eigenvalues, the system will be strongly hyperbolic [39, 89, 90]. Then, following the methodology of Nagy et al. [39, 90], we decompose the eigenvalue equation

$$\mathbf{P}\hat{u} = \lambda\hat{u}, \tag{5.110}$$

by projecting $\hat{u}$ into longitudinal and transverse components with respect to $\widetilde{\omega}_i$ via application of the projection operator

$$q_{ij} = \gamma_{ij} - \widetilde{\omega}_i\widetilde{\omega}_j. \tag{5.111}$$

Explicitly, we split all rank-1 and 2 covariant tensors into their components in and orthogonal to q_{ij}. In such a decomposition, symmetric rank-2 tensors on the 3D hypersurface with metric γ_{ij} may be represented as:

$$\hat{X}_{ij} = \widetilde{\omega}_i\widetilde{\omega}_j\hat{X} + \frac{1}{2}q_{ij}\hat{X}' + 2\widetilde{\omega}_{(i}\hat{X}'_{j)} + \hat{X}'_{\langle ij\rangle}, \tag{5.112}$$

with

$$\hat{X} = \widetilde{\omega}^i\widetilde{\omega}^j\hat{X}_{ij}, \tag{5.113}$$

$$\hat{X}' = q^{ij}\hat{X}_{ij}, \tag{5.114}$$

$$\hat{X}'_i = q_i{}^j\widetilde{\omega}^k\hat{X}_{jk}, \tag{5.115}$$

$$\hat{X}'_{\langle ij\rangle} = q_i{}^l q_j{}^m\left(\hat{X}_{lm} - \frac{1}{2}\hat{X}'q_{lm}\right), \tag{5.116}$$

and where angle brackets denote a tensorial quantity which is trace free with respect to q_{ij}. Similarly, covectors may be split according to

$$\hat{Y}_i = \omega_i \hat{Y} + \hat{Y}_i^{'}, \tag{5.117}$$

with

$$\hat{Y} = \tilde{\omega}^i \hat{Y}_i, \tag{5.118}$$

$$\hat{Y}_i^{'} = q_j{}^l \hat{Y}_j. \tag{5.119}$$

Upon application of these tensor and vector decompositions to (5.108), we find that $\mathbf{P}$ can be written in block diagonal form:

$$\mathbf{P} = \begin{bmatrix} \mathbf{P}^{\mathrm{S}} & 0 & 0 \\ 0 & \mathbf{P}^{\mathrm{V}} & 0 \\ 0 & 0 & \mathbf{P}^{\mathrm{T}} \end{bmatrix}, \tag{5.120}$$

with $\mathbf{P}^{\mathrm{S}}$, $\mathbf{P}^{\mathrm{V}}$ and $\mathbf{P}^{\mathrm{T}}$ denoting scalar, vector and tensor components. Following a lengthy calculation, we find the following results for (1) the scalar components:

$$\partial_0 \hat{a} = i\,|\omega|\,\alpha \left[-h\hat{K} + hm\hat{\Omega} \right], \tag{5.121}$$

$$\partial_0 \hat{b} = i\,|\omega|\,\alpha \left[G\hat{B} \right], \tag{5.122}$$

$$\partial_0 \hat{B} = i\,|\omega|\,\alpha \left[\frac{4H}{3}\hat{b} - \frac{4H}{3}\hat{K} + 2H\hat{\Omega} \right], \tag{5.123}$$

$$\partial_0 \hat{X} = i\,|\omega|\,\alpha \left[\frac{1}{6}\hat{b} - \frac{1}{6}\hat{K} \right], \tag{5.124}$$

$$\partial_0 \hat{l} = i\,|\omega|\,\alpha \left[\frac{4}{3}\hat{b} - 2\hat{L} \right], \tag{5.125}$$

$$\partial_0 \hat{l}^{'} = i\,|\omega|\,\alpha \left[-\frac{4}{3}\hat{b} + 2\hat{L} \right], \tag{5.126}$$

$$\partial_0 \hat{K} = i\,|\omega|\,\alpha \left[-\hat{a} - 8\hat{X} + \frac{1}{2}\hat{l} - \frac{1}{2}\hat{l}^{'} + 2\epsilon\hat{Z} \right], \tag{5.127}$$

$$\partial_0 \hat{\Omega} = i\,|\omega|\,\alpha \left[-4\hat{X} + \frac{1}{4}\hat{l} - \frac{1}{4}\hat{l}^{'} + \epsilon\hat{Z} \right], \tag{5.128}$$

$$\partial_0 \hat{L} = i\,|\omega|\,\alpha \left[-\frac{2}{3}\hat{a} - \frac{4}{3}\hat{X} + \frac{1}{3}\hat{l} + \frac{1}{6}\hat{l}^{'} + \frac{4\epsilon}{3}\hat{Z} \right], \tag{5.129}$$

$$\partial_0 \hat{Z} = i\,|\omega|\,\alpha \left[\hat{L} - \frac{2}{3}\hat{K} + \hat{\Omega} \right], \tag{5.130}$$

(2) the vector components:

$$\partial_0 \hat{b}_i^{'} = i\,|\omega|\,\alpha \left[G\hat{B}_i^{'} \right], \tag{5.131}$$

$$\partial_0 \hat{B}_i^{'} = i\,|\omega|\,\alpha \left[H\hat{b}_i^{'} \right], \tag{5.132}$$

$$\partial_0 \hat{l}_i^{'} = i\,|\omega|\,\alpha \left[\hat{b}_i^{'} - 2\hat{L}_i^{'} \right], \tag{5.133}$$

$$\partial_0 \hat{L}_i^{'} = i\,|\omega|\,\alpha \left[\epsilon\hat{Z}_i^{'} \right], \tag{5.134}$$

$$\partial_0 \hat{Z}_i^{'} = i\,|\omega|\,\alpha \left[\hat{L}_i^{'} \right], \tag{5.135}$$

and (3) tensor components:

$$\partial_0 \hat{l}'_{\langle ij \rangle} = i\,|\omega|\,\alpha\left[-2\hat{L}'_{\langle ij \rangle}\right], \tag{5.136}$$

$$\partial_0 \hat{L}'_{\langle ij \rangle} = i\,|\omega|\,\alpha\left[-\frac{1}{2}\hat{l}'_{\langle ij \rangle}\right]. \tag{5.137}$$

Note that since $\hat{A}_{ij}$ is trace-free we have $\hat{L}' = -\hat{L}$, which is why no evolution equation for $\hat{L}'$ appears. Expressing these systems of equations as matrix equations of the form (5.110) and (5.120), the eigenvalues of $\mathbf{P}^{\mathrm{S}}$ are:

$$\lambda = 0,\ 0,\ \pm 1,\ \pm\sqrt{\epsilon},\ \pm\sqrt{h},\ \pm\sqrt{\frac{4}{3}GH}. \tag{5.138}$$

Comparing with the results of [25, 39] (which consider various BSSN-type systems), we observe that RCCZ4 has one fewer zero velocity eigenvalue than GBSSN. It is this eigenvalue which corresponds to the Hamiltonian constraint advection and it is largely responsible for the superior performance of FCCZ4 relative to GBSSN [25, 47, 63]. Treating $\widetilde{R}_{ij}$ as a function of $\widetilde{\Lambda}^i$ versus $\widetilde{\Delta}^i$ ($\epsilon = 2$ versus $\epsilon = 1$) has the effect of increasing the speed of propagation of several modes, but otherwise has no effect on hyperbolicity. In fact, we see that RCCZ4 appears to be well defined for a fairly wide range of ϵ which roughly corresponds to modified equations of motion in which the Ricci tensor is supplemented by additional terms of the form $\widetilde{D}_{(i}\bar{Z}_{j)}$.

In the case of the vector components, the eigenvalues of the matrix $\mathbf{P}^{\mathrm{V}}$ each have multiplicity 2 (rather than 3) due to the projection constraints of the form $\tilde{\omega}^i \hat{X}_i = 0$. The eigenvalues are:

$$\lambda = 0,\ \pm\sqrt{\epsilon},\ \pm\sqrt{GH}. \tag{5.139}$$

Finally, for the tensor components, the eigenvalues of $\mathbf{P}^{\mathrm{T}}$ have multiplicity 2 (rather than 6) due to the three projection constraints of the form $\tilde{\omega}^i \hat{X}'_{ij} = 0$ and the trace-free condition $\hat{X}'_{\langle ij \rangle}\gamma^{ij} = 0$. The eigenvalues are the same as we would find for BSSN and ADM [25, 39, 90]:

$$\lambda = \pm 1. \tag{5.140}$$

In order to guarantee weak hyperbolicity, all of these eigenvalues must be real, so we must have

$$GH > 0,\ h > 0,\ \epsilon > 0. \tag{5.141}$$

Strong hyperbolicity additionally requires that each of $\mathbf{P}^S$, $\mathbf{P}^V$ and $\mathbf{P}^T$ are diagonalizable. For this to be the case, all of the following conditions must hold:

$$h \neq \epsilon,\ HG \neq \frac{3}{4},\ HG \neq \frac{3}{4}h,\ HG \neq \frac{3}{4}\epsilon, \tag{5.142}$$

so that $\mathbf{P}$ has a complete set of eigenvectors. If we perform the same sort of pseudodifferential decomposition for FCCZ4 (using a slightly modified gauge), we find that RCCZ4 and FCCZ4 share the same principal part and we thus conclude that the two methods have identical stability characteristics in the high frequency limit.

5.6 Summary and Conclusions

In this paper, we have introduced our novel RCCZ4 formulation of numerical relativity. We have demonstrated that it is possible to achieve roughly equivalent performance to GBSSN and FCCZ4

through a modification of Z4 wherein constraint violations are coupled to a reference metric completely independently of the physical metric. We have shown that this approach works in the presence of black holes and holds up robustly in a variety of 1D simulations including the critical collapse of a scalar field. In addition to stably evolving spherically symmetric simulations in the strong field, we have demonstrated that our formulation is strongly hyperbolic through the use of a pseudodifferential first order reduction.

Our formulation of RCCZ4 chose the simplest possible reference metric, but we can easily imagine formulations in which the components of $\mathring{g}_{\mu\nu}$ are chosen or evolved in such a way so as to provide additional beneficial properties aside from the vanishing of the Ricci tensor. We suspect that it will be in modifications to the choice of $\mathring{g}_{\mu\nu}$ in which the full utility of RCCZ4-like formulations is realized.

The core idea behind RCCZ4—coupling the constraint equations to a metric different from the physical metric—could potentially be used to derive methods with greater stability and superior error characteristics than either GBSSN or FCCZ4. In our opinion, the main takeaway should not be that RCCZ4, as it stands, is a complete formulation with performance approaching or exceeding FCCZ4 and GBSSN. Rather, the main lesson should be that the Z4 formulation of general relativity can be modified such that the constraints are coupled to a metric other then the physical one, and that such a modification may be useful in tailoring the properties of the system as they pertain to constraint advection and damping.

5.7 Acknowledgements

This research was supported by the Natural Sciences and Engineering Research Council of Canada (NSERC).

Chapter 6

Universality in the Critical Collapse of the Einstein-Maxwell System

We report on critical phenomena in the gravitational collapse of the electromagnetic field in axisymmetry using cylindrical coordinates. We perform detailed numerical simulations of four families of dipole and quadrupole initial data fine-tuned to the onset of black hole formation. It has been previously observed that families which bifurcate into two on-axis critical solutions exhibit distinct growth characteristics from those which collapse at the center of symmetry. In contrast, our results indicate similar growth characteristics and periodicity across all families of initial data, including those examined in earlier works. More precisely, for all families investigated, we observe power-law scaling for the maximum of the electromagnetic field invariant ($\max|F_{\mu\nu}F^{\mu\nu}| \sim |p - p^\star|^{-2\gamma}$) with $\gamma \approx 0.149(9)$. We find evidence of approximate discrete self-similarity in near-critical time evolutions with a log-scale echoing period of $\Delta \approx 0.62(8)$ across all families of initial data. Our methodology, while reproducing the results of prior studies up to a point, provides new insights into the later stages of critical searches and we propose a mechanism to explain the observed differences between our work and the previous calculations.

6.1 Introduction

In this paper we report results from an investigation of critical collapse in the Einstein-Maxwell (EM) system, a model where the electromagnetic field is coupled to the general relativistic gravitational field. We start with a brief review of black hole critical phenomena in gravitational collapse, and direct those unfamiliar with the subject to the comprehensive review articles [56] and [58].

When studying the critical collapse of a gravitational system, we consider the evolution of a single parameter family of initial data with the parameter p chosen such that when p is sufficiently small, the gravitational interaction is weak. As the magnitude of p is increased, the gravitational interaction becomes strong and for sufficiently large p, the time evolution of the system eventually results in a spacetime containing a black hole. By carefully tuning p, we find a critical parameter $p^\star$ representing the threshold of black hole formation for that particular family of initial data. The behaviour of solutions arising in the near critical regime, $p \to p^\star$, is complex and varied; its study comprises the core of what is referred to as critical phenomena in gravitational collapse.

Depending on the particulars of the model, we may find behaviour such as the existence of universality in the critical solutions, the scaling of physical quantities as functions of $|p - p^\star|$, or symmetries of the critical solution beyond those imposed by the initial data or model. Here, we are exclusively interested in type II critical phenomena which was first studied in the context of the collapse of a massless scalar field in spherical symmetry [43].

Type II critical phenomena are typically seen in systems with massless or highly relativistic matter fields. For these systems, the critical point $p^\star$ partitions the phase space of solutions in two such that for $p < p^\star$ we have complete dispersal while for $p > p^\star$ the final state of the system contains a black hole: the critical solution, which is transient and represents neither dispersal nor

black hole formation, sits at the interface of these two regions. Most studies of type II critical phenomena have been performed in the context of spherical symmetry, and until stated otherwise we will restrict attention to the spherically symmetric case.

A fundamental property of all type II critical solutions which have been determined to date is that they are self similar. Depending on the specific matter content of the system under consideration, the critical solution may be either continuously self similar (CSS) or discretely self similar (DSS). For a CSS spacetime in coordinates adapted to the symmetry, the metric coefficients take the form [58]:

$$g_{ab}\left(\tau, x^i\right) = e^{-2\tau}\widetilde{g}_{ab}\left(x^i\right), \tag{6.1}$$

where τ is the negative logarithm of a spacetime scale and x^i are generalized dimensionless angles about the critical point. For DSS spacetimes in adapted coordinates we have instead [58]:

$$g_{ab}\left(\tau, x^i\right) = e^{-2\tau}\widetilde{g}_{ab}\left(\tau, x^i\right), \tag{6.2}$$

$$\widetilde{g}_{ab}\left(\tau, x^i\right) = \widetilde{g}_{ab}\left(\tau + \Delta, x^i\right), \tag{6.3}$$

where $\widetilde{g}_{ab}$ is function of τ and x^i which is periodic in τ with period Δ. Therefore, in the vicinity of $p^\star$, a DSS critical solution exhibits periodic scale invariance in length and time. In almost all cases which have been studied in spherical symmetry the critical solutions which have been found (for both types of self-similarity) are universal, by which we mean that they do not depend on the specifics of the initial data families that are used to generate them [55, 58, 70, 81]. The echoing period, Δ, when it exists, is similarly universal.

For systems with a CSS critical solution, invariant dimensionful quantities, such as the mass of the resulting black hole in the supercritical regime, scale according to

$$\ln\left(M\right) = \gamma \ln\left|p - p^\star\right| + c_{\mathrm{M}}, \tag{6.4}$$

where γ is a universal exponent and c_M is some family-dependent constant. When the critical solution is DSS, a universal periodic function, f_M, with period Δ is superimposed on this basic power law [58]:

$$\ln\left(M\right) = \gamma \ln\left|p - p^\star\right| + f_{\mathrm{M}}\left(\gamma \ln\left|p - p^\star\right|\right) + c_{\mathrm{M}}\,. \tag{6.5}$$

Other dimensionful quantities scale in a corresponding manner. For example, if we were to look at the maximum energy density, $\rho_{\max}$, encountered during a given subcritical simulation (performed in coordinates adapted to the self similarity) we would have

$$\ln\left(\rho_{\max}\right) = -2\gamma \ln\left|p - p^\star\right| + f_\rho\left(\gamma \ln\left|p - p^\star\right|\right) + c_\rho, \tag{6.6}$$

where f_ρ is another universal periodic function and c_ρ is another family-dependent constant. Although type II critical solutions are generically unstable, they tend to be minimally so: they typically have a single unstable mode in perturbation theory and, in the above scaling laws, γ turns out to be the inverse of the Lyapunov exponent of this unstable mode.

Since the original spherically-symmetric scalar field work, many other models have been thoroughly investigated. Going beyond spherical symmetry, among the most important studies are those of the critical collapse of axisymmetric vacuum gravitational waves, originally examined by Abrahams and Evans [1, 2]. The study of vacuum critical collapse provides a means of achieving arbitrarily large space-time curvatures outside of a black hole through purely gravitational processes. In the critical limit this culminates in the formation of a naked singularity, which continues

to be an object of great theoretical interest. Fundamentally, although the critical features are not unique to the vacuum case, the vacuum provides the most natural gravitational context and is therefore most likely to provide information relevant to the studies of quantum gravity and cosmic censorship.

Simulations of vacuum critical collapse have proven to be difficult and replication (or otherwise) of early results has been challenging. It has only been in the past few years that work in this context has seen significant progress [19, 21, 49, 62, 64, 68, 74]. In particular, advances in formalisms and in the choices of gauge has enabled groups to expand upon the original work of Abrahams and Evans. In general, investigations into the collapse of non-spherically symmetric systems have yielded far more complicated pictures than their spherically symmetric counterparts, with family-dependent scaling and splitting of the critical solution into distinct loci of collapse appearing in a number of models [1, 2, 19–21, 44, 58, 74, 85].

Turning now to the EM system, we note that, as in the case of the pure Einstein vacuum, the model has no dynamical freedom in spherical symmetry and must therefore exhibit non-spherical critical behaviour. Recently, Baumgarte et al. [20], and Mendoza and Baumgarte [85] investigated the critical collapse of the EM model in axisymmetry. Using a covariant version of the formalism of Baumgarte, Shapiro, Shibata and Nakamura (BSSN) in spherical polar coordinates, they found evidence for family-dependent critical solutions for dipole and quadrupole initial data. Specifically, for each type of initial data, distinct values of γ and Δ were found.

In this paper, we present the results of our own investigation into the critical collapse of the EM system, also in axisymmetry, but using cylindrical coordinates. We incorporate an investigation of the critical behaviour in the well-studied massless scalar field model to test and calibrate our code, as well as to verify the validity of our analysis procedures which are then applied to the more complicated EM system.

We investigate a total of five families of initial data for the EM model, three of which are new, and the other two which are chosen in an attempt to replicate the experiments of Mendoza and Baumgarte [20, 85]. In contrast to the prior work, which yielded distinct scaling exponents for the quadrupolar computations relative to the dipolar ones, we find evidence of universality in γ and Δ across all families. We do not, however, observe evidence for universality in the periodic functions f_i as defined in (6.5)–(6.6).

For dipolar-type initial data we find that the collapse occurs at the center of symmetry (in this case the coordinate origin) and that the EM fields maintain a roughly dipolar character throughout the collapse process. Conversely, for quadrupolar initial data, we observe that the system eventually splits into two well separated, on-axis, centers of collapse. That is, after the initial data is evolved for some period of time, the matter splits into two distributions of equal magnitude, each centered on the $\rho = 0$ axis, with one distribution centered at positive z and the other at a corresponding location below the $z = 0$ plane. After this bifurcation occurs, the matter continues the process of collapse. In the limit that $p \to p^\star$, the matter collapses at the points $(z, \rho) = (z_c, 0)$ and $(z, \rho) = (-z_c, 0)$; these are the points at which a naked singularity would form in the critical limit and we refer to them as accumulation points. Although the evolution of quadrupole initial data prior to the bifurcation is initially consistent with [85], subsequent collapse at the mirrored centers appears to become dominated by a critical solution which exhibits similar properties to the dipole cases.

6.2 Background

Our investigation is restricted to the case of axial symmetry. In terms of Cartesian coordinates (x, y, z) we adopt the usual cylindrical coordinates, (z, ρ, ϕ):

$$z = z, \tag{6.7}$$
$$\rho = \sqrt{x^2 + y^2}, \tag{6.8}$$
$$\phi = \arctan\left(\frac{y}{x}\right). \tag{6.9}$$

For both the generation of initial data and its eventual evolution, we limit our investigation to the case of zero angular momentum and adopt the line element,

$$\begin{aligned} ds^2 = &\left(-\alpha^2 + \rho^2\beta_\rho\beta^\rho + \beta_z\beta^z\right)dt^2 + \left(2\beta_z dz + 2\rho\beta_\rho d\rho\right)dt \\ &+ \left(G_a dz^2 + G_b d\rho^2 + \rho^2 G_c d\phi^2 + 2\rho G_d dz d\rho\right), \end{aligned} \tag{6.10}$$

with corresponding metric,

$$\begin{aligned} g_{\mu\nu} &= \begin{pmatrix} -\alpha^2 + \beta_l\beta^l & \beta_j \\ \beta_i & \gamma_{ij} \end{pmatrix}, \\ &= \begin{pmatrix} -\alpha^2 + \rho^2\beta_\rho\beta^p + \beta_z\beta^z & \beta_z & \rho\beta_\rho & 0 \\ \beta_z & G_a & \rho G_d & 0 \\ \rho\beta_\rho & \rho G_d & G_b & 0 \\ 0 & 0 & 0 & \rho^2 G_c \end{pmatrix}. \end{aligned} \tag{6.11}$$

Here and below, all spacetime functions, g, have coordinate dependence $g(t, z, \rho)$. For convenience in our numerical calculations and derivations, we have chosen the form of the metric components in (6.11) so that all of the basic dynamic variables satisfy

$$\lim_{\rho\to 0} g(t, z, \rho) = g_0(t, z) + \rho^2 g_2(t, z) + \dots \tag{6.12}$$

Thus, all of the dynamical variables have even character about $\rho = 0$. Using standard definitions of the spatial stress tensor S_{ij} (with spatial trace S), momentum, j^i, and energy density ρ_E, we have

$$S_{ij} = \gamma^\alpha{}_i\gamma^\beta{}_j T_{\alpha\beta}, \tag{6.13}$$
$$S = \gamma^{ij} S_{ij}, \tag{6.14}$$
$$j^i = -\gamma^{ij}\gamma^\mu{}_j n^\nu T_{\mu\nu}, \tag{6.15}$$
$$\rho_E = n^\mu n^\nu T_{\mu\nu}\,. \tag{6.16}$$

We adopt the generalized BSSN (GBSSN) decomposition of Brown [9, 22, 37, 47, 116] and take the so-called Lagrangian choice for the evolution of the determinant of the conformal metric,

$$\partial_t\hat{\gamma} = 0, \tag{6.17}$$

such that the equations of motion are given by

$$\mathcal{L}_m = (\partial_t - \mathcal{L}_\beta)\,, \tag{6.18}$$

$$\mathcal{L}_{m\chi} = -\frac{1}{6}\alpha K + \frac{1}{6}\hat{D}_m\beta^m, \tag{6.19}$$

$$\mathcal{L}_m K = -D^2\alpha + \alpha\left(\hat{A}_{ij}\hat{A}^{ij} + \frac{1}{3}K^2\right) + 4\pi\alpha\left(\rho_E + S\right), \tag{6.20}$$

$$\mathcal{L}_m\hat{\gamma}_{ij} = -2\alpha\hat{A}_{ij} - \frac{2}{3}\hat{\gamma}_{ij}\hat{D}_m\beta^m, \tag{6.21}$$

$$\mathcal{L}_m\hat{A}_{ij} = e^{-4\chi}\left[-D_iD_j\alpha + \alpha R_{ij} - 8\pi\alpha S_{ij}\right]^{\mathrm{TF}} - \frac{2}{3}\hat{A}_{ij}\hat{D}_m\beta^m + \alpha\left(K\hat{A}_{ij} - 2\hat{A}_{ik}\hat{A}^k{}_j\right), \tag{6.22}$$

$$\begin{aligned}\mathcal{L}_m\hat{\Lambda}^i = {}& \hat{\gamma}^{mn}\mathring{D}_m\mathring{D}_n\beta^i - 2\hat{A}^{im}\hat{D}_m\alpha + 2\alpha\left(6\hat{A}^{ij}\hat{D}_j\chi - \frac{2}{3}\hat{\gamma}^{ij}\hat{D}_jK - 8\pi\hat{j}^i\right)\\ & + \frac{1}{3}\left[\hat{D}^i\left(\hat{D}_n\beta^n\right) + 2\hat{\Lambda}^i\hat{D}_n\beta^n\right] + 2\alpha\hat{A}^{mn}\hat{\Delta}^i{}_{mn}.\end{aligned} \tag{6.23}$$

These equations introduce two additional metrics: the conformal metric $\hat{\gamma}_{ij}$,

$$\hat{\gamma}_{ij} = e^{-4\chi}\gamma_{ij} = \begin{pmatrix} g_a & \rho g_d & 0\\ \rho g_d & g_b & 0\\ 0 & 0 & \rho^2 g_c\end{pmatrix}, \tag{6.24}$$

and a flat reference metric $\mathring{\gamma}_{ij}$,

$$\mathring{\gamma}_{ij} = \begin{pmatrix} 1 & 0 & 0\\ 0 & 1 & 0\\ 0 & 0 & \rho^2\end{pmatrix}, \tag{6.25}$$

which shares the same divergence characteristics as $\hat{\gamma}_{ij}$ and serves to regularize several quantities related to the contracted Christoffel symbols. In (6.19)–(6.23), hats denote quantities raised with $\hat{\gamma}^{ij}$ while $\hat{D}$ and $\mathring{D}$ denote covariant differentiation with respect to the conformal metric and flat reference metric, respectively.

In (6.22), the Ricci tensor is split into conformal and scale components via

$$R_{ij} = \hat{R}_{ij} + R^\chi_{ij}, \tag{6.26}$$

$$\hat{R}_{ij} = -\frac{1}{2}\hat{\gamma}^{mn}\mathring{D}_m\mathring{D}_n\hat{\gamma}_{ij} + \hat{\gamma}_{m(i}\mathring{D}_{j)}\hat{\Lambda}^m + \hat{\Lambda}^m\hat{\Delta}_{(ij)m} + 2\hat{\Delta}^{mn}{}_{(i}\hat{\Delta}_{j)mn} + \hat{\Delta}^{mn}{}_i\hat{\Delta}_{mnj}, \tag{6.27}$$

$$R^\chi_{ij} = -2\hat{D}_i\hat{D}_j\chi - 2\hat{\gamma}_{ij}\hat{D}^k\hat{D}_k\chi + 4\hat{D}_i\chi\hat{D}_j\chi - 4\hat{\gamma}_{ij}\hat{D}^k\chi\hat{D}_k\chi\,. \tag{6.28}$$

We note that in an appropriate gauge, the GBSSN variables have no unstable growing modes associated with constraint violation [39, 89]. The Hamiltonian, momentum and contracted Christoffel constraints take the form

$$H = \frac{1}{2}\left(R + \frac{2}{3}K^2 - \hat{A}_{ij}\hat{A}^{ij}\right) - 8\pi\rho, \tag{6.29}$$

$$M^i = e^{-4\chi}\left(\hat{D}_j\hat{A}^{ij} - \frac{2}{3}\hat{\gamma}^{ij}\hat{D}_jK + 6\hat{A}^{ij}\hat{D}_j\chi - 8\pi\hat{j}^i\right) = \left(M^z, \rho M^\rho, 0\right), \tag{6.30}$$

$$Z^i = \hat{\Lambda}^i - \hat{\Delta}^i = \left(Z^z, \rho Z^\rho, 0\right). \tag{6.31}$$

It is worth noting that in (6.19)–(6.23) we have not included the usual dimensionful constraint damping parameters. The critical solutions we investigate have no single length scale and our code must be able to deal with solutions spanning many orders of magnitude in scale. By choosing a set of damping parameters which worked well at a given scale, we might have introduced inconsistent and difficult to debug behaviours at other scales. These might include:

- Improved constraint conservation in the long wavelength regime at the expense of the short wavelength regime.
- Unexpected interactions with Kreiss-Oliger dissipation [72].
- Scale dependent issues arising at grid boundaries due to suboptimally chosen adaptive mesh refinement (AMR) parameters.

In order to avoid these possibilities and to ensure our that code had no preferential length scale, we omitted the damping parameters in our simulations.

In summary, the complete set of geometric variables is given by the lapse, α, shift, β^i,

$$n^\mu = \left(\frac{1}{\alpha}, -\frac{\beta^i}{\alpha}\right), \tag{6.32}$$

$$\beta^i = (\beta^z, \rho\beta^\rho, 0), \tag{6.33}$$

conformal factor, χ, conformal metric, $\hat{\gamma}_{ij}$,

$$\hat{\gamma}_{ij} = e^{-4\chi}\gamma_{ij} = \begin{pmatrix} g_a & \rho g_d & 0 \\ \rho g_d & g_b & 0 \\ 0 & 0 & \rho^2 g_c \end{pmatrix}, \tag{6.34}$$

trace of the extrinsic curvature, K, conformal trace-free extrinsic curvature, $\hat{A}_{ij}$,

$$\hat{A}_{ij} = e^{-4\chi}\left(K_{ij} - \frac{1}{3}\gamma_{ij}K\right), \tag{6.35}$$

$$= \begin{pmatrix} A_a & \rho A_d & 0 \\ \rho A_d & A_b & 0 \\ 0 & 0 & \rho^2 A_c \end{pmatrix}, \tag{6.36}$$

the quantities Δ^i representing the difference between the contracted Christoffel symbols of the conformal metric ($\hat{\Gamma}^i{}_{jk}$) and flat reference metric ($\mathring{\Gamma}^i{}_{jk}$),

$$\hat{\Delta}^i{}_{ij} = \hat{\Gamma}^i{}_{jk} - \mathring{\Gamma}^i_{jk}, \tag{6.37}$$

$$\hat{\Delta}^i = \hat{\Gamma}^i - \mathring{\Gamma}^i{}_{jk}\hat{\gamma}^{jk}, \tag{6.38}$$

$$\hat{\Delta}^i = \left(\hat{\Delta}^z, \rho\hat{\Delta}^\rho, 0\right), \tag{6.39}$$

and finally, the quantities Λ^i, representing the quantities Δ^i promoted to independent dynamical degrees of freedom rather than being viewed as functions of $\hat{\gamma}_{ij}$ and $\mathring{\gamma}_{ij}$,

$$\hat{\Lambda}^i = \left(\hat{\Lambda}^z, \rho\hat{\Lambda}^\rho, 0\right). \tag{6.40}$$

Here, as is the case for the spacetime 4-metric, all of the GBSSN functions are taken to have even character about $\rho = 0$. For a more in-depth review of the GBSSN formulation we refer the reader to the works of Brown [37] and Alcubierre et al. [9].

In our investigations of critical behaviour we consider both the massless scalar field and the Maxwell field. In the first instance, we have the Einstein equations and stress tensor,

$$G_{\mu\nu} = 8\pi T^{\mathrm{S}}_{\mu\nu}, \tag{6.41}$$

$$T^{\mathrm{S}}_{\alpha\beta} = \nabla_\alpha \mu \nabla_\beta \mu - \frac{1}{2} g_{\alpha\beta} \nabla_\gamma \mu \nabla^\gamma \mu, \tag{6.42}$$

and a matter equation of motion,

$$\nabla^\alpha \nabla_\alpha \mu = 0\,. \tag{6.43}$$

For the Einstein-Maxwell system we have

$$G_{\mu\nu} = 8\pi T^{\mathrm{EM}}_{\mu\nu}, \tag{6.44}$$

$$T^{\mathrm{EM}}_{\mu\nu} = F_\mu{}^\alpha F_{\nu\alpha} - \frac{1}{4} g_{\mu\nu} F_{\alpha\beta} F^{\alpha\beta}, \tag{6.45}$$

and matter equations of motion,

$$\nabla_\mu F^{\nu\mu} = 0, \tag{6.46}$$

$$\nabla_\mu {}^\star F^{\nu\mu} = 0. \tag{6.47}$$

Here,

$${}^\star F^{\mu\nu} = \frac{1}{2} \tilde{\epsilon}^{\mu\nu\gamma\delta} F_{\gamma\delta}, \tag{6.48}$$

with

$$\tilde{\epsilon}^{\alpha\beta\gamma\delta} = \frac{(-1)^s}{\sqrt{|g|}} \epsilon^{\alpha\beta\gamma\delta}, \tag{6.49}$$

where $s = 1$ is the metric signature and $\epsilon^{\alpha\beta\gamma\delta}$ is the 4D Levi-Civita symbol.

Rather than use (6.46)–(6.47) and a vector potential decomposition of $F_{\mu\nu}$, we incorporate the source-free Maxwell equations into a larger system, similarly to how the GBSSN and FCCZ4 formalisms embed general relativity within variations of the Z4 system [9, 47]. In the case of general relativity, this embedding enables the Hamiltonian and momentum constraints to be expressed through propagating degrees of freedom. Analogously, for the Maxwell fields, the divergence conditions become tied to propagating degrees of freedom [71, 95]:

$$-\sigma n^\nu \Psi_E = \nabla_\mu \left(F^{\nu\mu} + g^{\nu\mu} \Psi_E \right), \tag{6.50}$$

$$-\sigma n^\nu \Psi_B = \nabla_\mu \left({}^\star F^{\nu\mu} + g^{\nu\mu} \Psi_B \right). \tag{6.51}$$

Here, σ is a dimensionful damping parameter and Ψ_E and Ψ_B are constraint fields which couple to the violation of the divergence conditions for the electric and magnetic fields, respectively. By promoting the constraints to propagating degrees of freedom, our solutions gain additional stability and exhibit advection and damping of constraint violations which would otherwise accumulate.

Finally, we take the following definitions of the electric fields, E^α, magnetic fields, B^α, and Maxwell tensors, $F^{\alpha\beta}$ and ${}^\star F^{\alpha\beta}$,

$$E^\alpha = F^{\alpha\beta} n_\beta, \tag{6.52}$$
$$B^\alpha = {}^\star F^{\beta\alpha} n_\beta, \tag{6.53}$$
$$F^{\alpha\beta} = n^\alpha E^\beta - n^\beta E^\alpha + \tilde{\epsilon}^{\gamma\delta\alpha\beta} n_\gamma B_\delta \tag{6.54}$$
$${}^\star F^{\alpha\beta} = n^\beta B^\alpha - n^\alpha B^\beta + \tilde{\epsilon}^{\gamma\delta\alpha\beta} n_\gamma E_\delta \tag{6.55}$$

The evolution equations for the electric and magnetic fields, and the constraint variables, now take the form:

$$\mathcal{L}_m E^i = \tilde{\epsilon}^{ijk} D_j \left(\alpha B_k\right) + \alpha K E^i + \alpha \gamma^{ij} D_j \Psi_E, \tag{6.56}$$
$$\mathcal{L}_m B^i = -\tilde{\epsilon}^{ijk} D_j \left(\alpha E_k\right) + \alpha K B^i - \alpha \gamma^{ij} D_j \Psi_B, \tag{6.57}$$
$$\mathcal{L}_m \Psi_E = \alpha D_i E^i, \tag{6.58}$$
$$\mathcal{L}_m \Psi_B = -\alpha D_i B^i, \tag{6.59}$$

where we have once again set dimensionful damping parameters to zero to avoid setting a preferential length scale. Under the restriction to axisymmetry, the electric, magnetic, and associated fields simplify as

$$E^i = \left(0, 0, E^\phi\right), \tag{6.60}$$
$$B^i = \left(B^z, \rho B^\rho, 0\right), \tag{6.61}$$
$$\Psi_E = 0, \tag{6.62}$$
$${}^\star F_{\mu\nu} F^{\mu\nu} = -F_{\mu\nu} F^{\mu\nu}. \tag{6.63}$$

Similarly to the GBSSN functions, all of B^z, B^ρ, E^ϕ, Ψ_B and $F_{\mu\nu}F^{\mu\nu}$ are constructed to be even about the $\rho = 0$ axis. As is the case for the Hamiltonian, momentum and contracted Christoffel constraints of GBSSN, Ψ_B and Ψ_E evolve stably and vanish in the continuum limit provided the initial data obeys the relevant constraints.

6.3 Initial Data

We assume time symmetry on the initial slice such that $K_{ij} = j^i = 0$ with the momentum constraints automatically satisfied. Thus, our initial data represents a superposition of ingoing and outgoing solutions of equal magnitude and implies the existence of a family of privileged, on-axis, inertial observers who are likewise stationary at the initial time. Through careful construction, the geodesics these observers follow enable us to extract information concerning the evolution of our critical systems in a way that is completely independent of gauge.

Under the York-Lichnerowicz conformal decomposition and given time symmetry, the $t = 0$ Hamiltonian constraint takes the form

$$2H = 8\hat{D}_i \hat{D}^i e^\chi - \hat{R} e^\chi + 16\pi e^{5\chi} \rho = 0. \tag{6.64}$$

We choose the initial conformal 3-metric to be flat and isotropic and define the electric and magnetic fields as $E^i = e^{-9\chi/2}\tilde{E}^i$, $B^i = e^{-9\chi/2}\tilde{B}^i$ with $\tilde{E}^i$ and $\tilde{B}^i$ specified according to some initial

profiles. These choices greatly simplify (6.64), and upon defining

$$\kappa = e^{\chi}, \tag{6.65}$$

$$\mathring{D}^2\kappa = \left(\partial_{\rho\rho}\kappa + \frac{\partial_\rho\kappa}{\rho} + \partial_{zz}\kappa\right), \tag{6.66}$$

the elliptic equation for the Einstein-Maxwell system takes the form

$$\mathring{D}^2\kappa = -\pi\left(\rho^2\tilde{B}^{\rho^2} + \tilde{B}^{z^2} + \rho^2\tilde{E}^{\phi^2}\right), \tag{6.67}$$

while the corresponding equation for the scalar field is

$$\mathring{D}^2\kappa = -\pi\kappa\left((\partial_z\mu)^2 + (\partial_\rho\mu)^2\right). \tag{6.68}$$

In the case of the massless scalar field or pure electric field we are free to simply specify μ or $\tilde{E}^\phi$. For the case of a pure magnetic field we must additionally satisfy $D_iB^i = 0$. Under the transform $\bar{B}^i = e^{-6\chi}B^i = e^{-3/2\cdot\chi}\tilde{B}^i$, B may be trivially derived from a vector potential via $\bar{B} = -\mathring{\nabla}\times A$. Taking $A^z = 0$ and $A^\rho = 0$ results in families which satisfy the relevant constraints. Initially stationary magnetic type data is then specified via

$$A^i = \left(0, 0, A^\phi\right), \tag{6.69}$$

$$\bar{B}^z = -\partial_\rho A^\phi - \frac{A^\phi}{\rho}, \tag{6.70}$$

$$\bar{B}^\rho = \frac{1}{\rho}\partial_z A^\phi. \tag{6.71}$$

The initial data for the collapse of the massless scalar field is given in Table 6.1. We make use of the function

$$g\left(z, \rho, \rho_0, \lambda\right) = \exp\left(-\frac{z^2 + (\rho+\rho_0)^2}{\lambda^2}\right), \tag{6.72}$$

and present all initial data in a manner which is manifestly scale invariant with respect to the parameter λ: under a rescaling $\lambda \to \lambda/\lambda'$ all dimensionless quantities $f(t, z, \rho)$ transform as $f(t, z, \rho) \to f(t/\lambda', z/\lambda', \rho/\lambda')$.

Family	Initial Data	$p^\star$
$W_{l=0}$	$\mu = p\cdot\left(g\left(z,\rho,\rho_0,\lambda\right) + g\left(z,\rho,-\rho_0,\lambda\right)\right)$	~ 0.152
$W_{l=1}$	$\mu = p\cdot\frac{z}{\lambda}\left(g\left(z,\rho,\rho_0,\lambda\right) + g\left(z,\rho,-\rho_0,\lambda\right)\right)$	~ 0.297

Table 6.1: Families of initial data for the massless scalar field. The form of the initial data is scale invariant with respect to λ and we adopt $\lambda = 1$, $\rho_0 = 0$ for all simulations. We refer to family $W_{l=0}$ as monopole type initial data and family $W_{l=1}$ as dipole type. The final column gives the approximate value of the critical parameter $p^\star$ for each family.

For the Einstein-Maxwell system we investigate the families of initial data presented in Tables 6.2 and 6.3. The families given in Table 6.2 are new to this work while those given in Table 6.3 correspond to the dipole and quadrupole families of [85]. The families of Table 6.2 were chosen in

Family	Initial Data	$p^\star$
$E_{l=1}$	$\tilde{E}^\phi = p \cdot \frac{1}{\lambda^2}\left(g\left(z,\rho,\rho_0,\lambda\right) + g\left(z,\rho,-\rho_0,\lambda\right)\right)$	~ 0.644
$M_{l=1}$	$A^\phi = p \cdot \frac{\rho}{\lambda}\left(g\left(z,\rho,\rho_0,\lambda\right) + g\left(z,\rho,-\rho_0,\lambda\right)\right)$	~ 0.377
$M_{l=2}$	$A^\phi = p \cdot \frac{z\rho}{\lambda^2}\left(g\left(z,\rho,\rho_0,\lambda\right) + g\left(z,\rho,-\rho_0,\lambda\right)\right)$	~ 0.896

Table 6.2: Families of initial data for the Einstein-Maxwell system. The form of the initial data is scale invariant with respect to λ and we refer to family $E_{l=1}$ as the electric dipole type, $M_{l=1}$ as the magnetic dipole type and $M_{l=2}$ as the magnetic quadrupole type. $\tilde{B}^i$ is determined from A^ϕ via (6.69)–(6.71). All of our investigations adopt $\lambda = 1$ and $\rho_0 = 0$. We note that although $\tilde{E}^i$ and A^i are pure multipoles, the initial spacetime is far from flat and, in fact, the evolution is initially in the strong-field regime.

the hope that that similarities and differences in the underlying behaviors of dipole ($l = 1$) and quadrupole ($l = 2$) solutions would reveal information concerning the universality of the critical solutions. The two families of dipole initial data ($E_{l=1}$ and $M_{l=1}$) correspond to electric and magnetic dipoles, respectively, and are initially quite dissimilar.

As stated, the families of Table 6.3 correspond to those in [85] where the initial data was presented in an orthonormal coordinate basis. Here we present it in terms of the tensor quantities $\bar{E}^i = e^{-6\chi}E^i$. Notably, we do not find the same critical points for the data in Table 6.3 as was found in [85]. Instead of $p^\star_{\rm dipole} \approx 0.913$ and $p^\star_{\rm quad} \approx 3.53$, we find $p^\star_{\rm dipole} \approx 0.258$ and $p^\star_{\rm quad} \approx 0.997$. In light of the results of Sec. 6.5.3 and since the ratios among the two family parameters are essentially identical, we suspect that either our initial data or that of [85] was simply scaled by some unaccounted for factor.

Family	Initial Data	$p^\star$
$E_{\rm dipole}$	$\bar{E}^\phi = p \cdot \frac{8}{\lambda^2}\exp\left(-\frac{z^2+\rho^2}{\lambda^2}\right)$	~ 0.258
$E_{\rm quad}$	$\bar{E}^\phi = p \cdot \frac{16z}{3\lambda^3}\exp\left(-\frac{z^2+\rho^2}{\lambda^2}\right)$	~ 0.997

Table 6.3: Families of initial data specified in [85]. Here, we have expressed the initial data in standard tensor notation, rather than in an orthonormal basis as in [85], so that p is a dimensionless strength parameter.

6.4 Numerics and Validation

We calculate the initial data using (6.67) and (6.68) with a multigrid method on a spatially compactified grid,

$$z = \tan\left(\frac{Z\pi}{2}\right), \quad -1 \leq Z \leq 1\,, \tag{6.73}$$

$$\rho = \tan\left(\frac{R\pi}{2}\right), \quad 0 \leq R \leq 1\,, \tag{6.74}$$

which renders the outer boundary conditions trivial. A consequence of this transform is that the eigenvalues of the finite difference approximations of (6.67) and (6.68) become highly anisotropic:

for a number of grid points that provides adequate accuracy, the characteristic magnitude of the action of the differential operator on the grid function κ may be as much as $1 \cdot 10^7$ times larger near the edge of the grid as it is at the origin. To account for the resulting large eigenvalue anisotropy, line relaxation is employed to increase convergence rates.

An unfortunate side effect of using a global line relaxation technique is that at our chosen resolution, and for a tuning precision $|p^\star - p|/\, p^\star \lesssim 1 \cdot 10^{-9}$, we lose the ability to discriminate between sets of initial data. That is, the price we pay for global relaxation of the highly anisotropic problem is a loss of precision. We resolve this issue by calculating three reference solutions corresponding to parameters p_1, p_2 and p_3 near the critical point, $p^\star$, such that $|p^\star - p_i|/\, p^\star \approx 1 \cdot 10^{-6}$ and $|p_j - p_i|/\, p^\star \approx 1 \cdot 10^{-6}$ for $i \neq j$. For simulations with $|p^\star - p|/\, p^\star \lesssim 1 \cdot 10^{-6}$, initial data is then calculated via third order point-wise spatial interpolation of grid functions using the three reference solutions. The error thereby introduced is orders of magnitude below that of the numerical truncation error in the subsequent evolution and may be safely ignored.

Our evolution code is built on a slightly modified version of PAMR [102] and AMRD [101]. We use a second order in space and time integrator with Kreiss-Oliger dissipation terms to damp high-frequency solution components. Additional resolution is allocated as required through the use of AMR based on local truncation error estimates.

Close to criticality, these simulations made heavy use of AMR. A run for family $M_{l=1}$, for example, would have a base resolution of $[129, 129]$ with four levels of 2:1 refinement at $t = 0$. At the closest approach to criticality ($|p^\star - p|\, /p^\star \approx 1 \cdot 10^{-13}$), the simulation would have ~ 20 levels of refinement representing an increase in resolution on order of 10,000.

The code was originally based on a fourth order in space and time method. During the course of our investigations we found that, without great care, spatial differentiation in the vicinity of grid boundaries could easily become pathological for higher order integration schemes and this was particularly true when we used explicit time integration. Without careful consideration, these sometimes subtle effects could completely negate any advantages gained from the use of a higher order scheme. As a result, the decision was made to employ a much easier to debug second order accurate method. Specifically, we opted to use a second order Runge-Kutta integrator with second order accurate centered spatial differencing and fourth order Kreiss-Oliger dissipation [72]. In order to reduce the effect of spurious reflection from AMR boundaries, we employ a technique very similar to that of Mongwane [88].

6.4.1 Choice of Gauge

Our evolution code accommodates a wide variety of hyperbolic gauges with most of our investigations focusing on versions of the standard Delta driver and 1+log families of shift and slicing conditions [7, 8, 23, 38]. We found that there were no significant issues associated with using various Delta driver shifts for evolutions moderately close to criticality ($|p - p^\star|/p^\star < 1 \cdot 10^{-3}$), but that their use tended to significantly increase the grid resolution, and therefore computational cost, required to resolve the solutions. As such, the results presented in Secs. 6.4.4 and 6.5 are based on the following choice of gauge:

$$\mathcal{L}_m \alpha = -2\alpha K, \tag{6.75}$$

$$\beta^r = 0, \tag{6.76}$$

$$\beta^z = 0. \tag{6.77}$$

6.4.2 Classification of Spacetimes

We characterize spacetimes as either subcritical or supercritical based on two primary indicators: the dispersal of fields and the collapse of the lapse. While the more definitive approach to flagging a spacetime containing a black hole would be to identify an apparent horizon, we opt for monitoring the lapse collapse due to its simplicity and practicality. One drawback of this approach is the potential ambiguity in the final stages of the last echo in each family. Specifically, it is unclear whether the behaviour that is observed for putatively marginally supercritical collapse represents a genuine physical singularity or merely a coordinate artifact. However, by closely observing the growth trends of invariant quantities and confirming the dispersion of sub-critical solutions, we are confident that our results, up to the final portion of the last echo, depict the genuine approach to criticality. Given the inherent challenges in precisely determining $p^\star$, we have chosen to exclude the simulations closest to criticality when computing values for γ and Δ across all families of initial data.

6.4.3 GBSSN Considerations

Aside from the standard convergence and independent residual convergence tests (Section 6.4.4), it is important to quantify the behaviour we expect from a code based on the GBSSN formalism when in the critical regime. First and foremost, in their most general forms (without enforcing elliptic constraints) GBSSN evolution schemes are unconstrained. We should therefore expect constraint violations to grow with time while remaining bounded and convergent for well resolved initial data sufficiently far from criticality.

Another potentially overlooked factor concerning the GBSSN formulation is that GBSSN is not only over-determined (e.g. the evolution equations for $\hat{\Lambda}^i$ are implicit in the evolution of the other variables and the maintenance of the constraints), but GBSSN is effectively an embedding of general relativity within a larger Z4 type system under the assumption that the Hamiltonian constraint holds [9, 47]. In practice, this means that a well resolved and convergent solution in GBSSN may cease being a valid solution within the context of general relativity at some point during the evolution. This is perhaps best illustrated by considering the near critical evolution of the Einstein-Maxwell system depicted in Fig. 6.3. Although the Hamiltonian and momentum constraints are well maintained throughout the evolutions, the final "dispersal" state is not a valid solution in the context of general relativity. In this case, the constraint violations of the overdetermined system have made it so that the geometry that remains as the electromagnetic pulse disperses to infinity is a constraint-violating remnant rather than flat spacetime.

The overall effect is that our solutions cannot be trusted for particularly long periods of time after they make their closest approach to criticality. This in turn presents obvious difficulties in determining the mass of any black holes in the supercritical regime where it may take significant coordinate time for the size of the apparent horizon to approach that of the event horizon. For this reason we restrict our analysis to the subcritical regime.

To verify that we remain "close" to a physically meaningful general relativistic solution, we monitor the magnitude of the constraint violations relative to quantities with the same dimension. We also monitor independent residuals for the fundamental dynamical variables. We consider a solution using AMR to be reasonably accurately resolved when:

- The independent residuals and constraints violations of an AMR solution in the strong field (nonlinear) regime are maintained at levels comparable to those determined from convergence tests using uniform grids.
- The independent residuals are kept at acceptable levels relative to the magnitude of the fields.

- The constraint violations are kept small relative to the magnitude of their constituent fields. (e.g. $|H| \ll |R|$).

For a dispersal solution close to the critical point, the second and third of these conditions are guaranteed to fail some period of time after the solution makes its closest approach to criticality. Thankfully, in practice we have found that with adequately strict truncation error requirements (relative truncation errors below $1{\cdot}10^{-3}$ seems sufficient and we maintain $5{\cdot}10^{-5}$ for all simulations), the conditions remain satisfied throughout the collapse process.

6.4.4 Convergence

The parameters for our convergence test simulations are given in Table 6.4. Note that these simulations and those given in Section 6.5 are performed on semi-compactified grids with

$$z = \sinh Z', \quad 0 \leq Z' \leq 12\,, \tag{6.78}$$
$$\rho = \sinh P', \quad 0 \leq P' \leq 12\,. \tag{6.79}$$

For all of the calculations discussed in this paper, appropriate boundary conditions are set at $z = 0$ to mirror or reflect the GBSSN and matter variables, depending on whether the given field has even or odd character about the $z = 0$ plane. This simplification allows us to reduce the required compute time by a factor of two and alleviates issues which occasionally arise from asymmetric placement of AMR boundaries. For these and all subsequent results, initial data was calculated on a fully compactified grid as described in the introduction to this section.

Family	Level	p	$P_{\min}$	$P_{\max}$	N_P	$Z_{\min}$	$Z_{\max}$	N_Z
$M_{l=1}$	1	0.33	0	12	513	0	12	513
$M_{l=1}$	2	0.33	0	12	1025	0	12	1025
$M_{l=1}$	3	0.33	0	12	2049	0	12	2049
$M_{l=1}$	4	0.33	0	12	4097	0	12	4097

Table 6.4: Parameters for magnetic dipole (family $M_{l=1}$) convergence tests. These simulations are well within the nonlinear regime with the critical point given by $p^\star \approx 0.377$. Similar convergence tests were performed for all families listed in Tables 6.1–6.3.

Figs. 6.1–6.2 demonstrate the convergence of the constraints for strong field dispersal solutions of the EM system. These figures additionally plot constraint violations for AMR simulations with a relative error tolerance of $5 \cdot 10^{-5}$, demonstrating that the AMR simulations remain well within the convergent regime. The AMR simulations had an associated compute cost approximately 4 times larger than the lowest resolution unigrid simulations.

Beyond monitoring the various constraints, we computed independent residuals of the various GBSSN quantities. The independent residuals were based on a second order in time and space stencil with three time levels and spatial derivatives evaluated at only the most advanced time. These residuals converged at second order as expected for all our tests.

Fig. 6.3 demonstrates the magnitude of various error metrics relative to the magnitude of the underlying fields. Throughout the collapse process, the solution is well resolved, but during dispersal ($t > 6$), the solution becomes dominated by a non propagating Hamiltonian constraint violation. Again, this is the expected behaviour for GBSSN type simulations where the Hamiltonian constraint is not tied to a dynamical variable or explicitly damped. In the limit of infinite resolution, we expect $R(t, 0, 0)$ and $H(t, 0, 0)$ to approach 0 at late times.

We also note that, in addition to the GBSSN approach, we experimented with implementations of formulations derived from the Z4 formalism. In practice, we found that the use of Z4 formulations (without damping) resulted in significantly better constraint conservation post dispersal while exhibiting degraded Hamiltonian constraint conservation during collapse. As we were predominantly interested in maintaining high accuracy during collapse, we opted to use GBSSN rather than, for example, fully covariant and conformal Z4 (FCCZ4).

Results similar to Figs. 6.1–6.3 hold for all constraints and independent residual evaluators for each of the families $E_{l=1}$, $M_{l=1}$, $M_{l=2}$, $W_{l=1}$ and $W_{l=2}$. In all cases convergence was second order as expected.

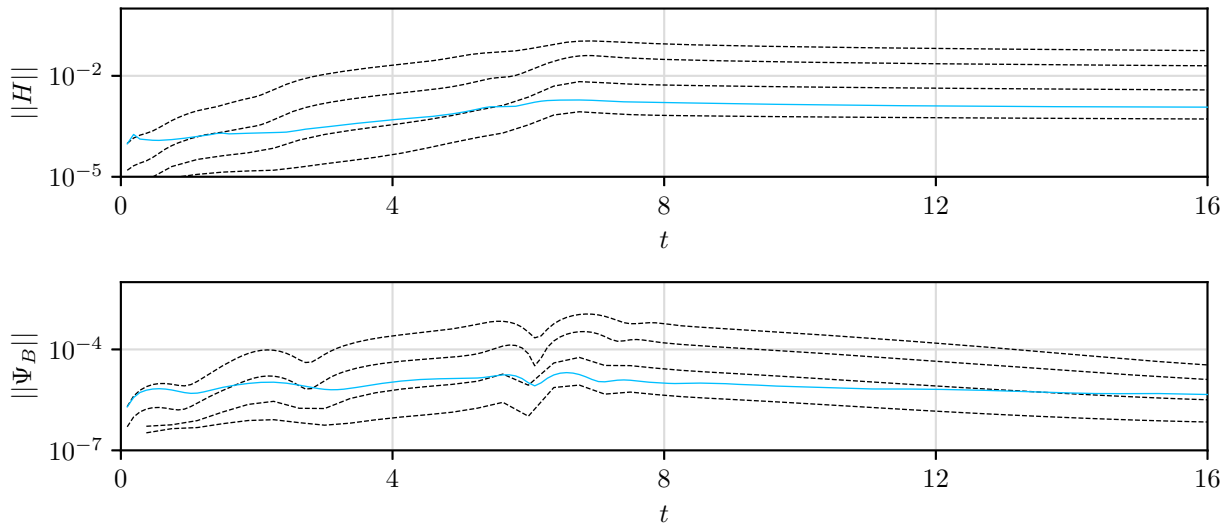

Figure 6.1: Convergence of l_2 norms of Ψ_B and Hamiltonian constraint violations for strong field initial data given by Table 6.4. The plotted norms of the residuals for each run are evaluated by interpolating the results to a uniform grid which has sufficient resolution to resolve the details of the simulation. This enables us to directly compare the convergence properties at the various resolutions. Each of the dashed lines represents a successive refinement (by a factor of 2) of the initial data while the solid line represents an AMR run with a relative error tolerance of $5 \cdot 10^{-5}$. The grid parameters for the various unigrid runs are given in Table 6.4.

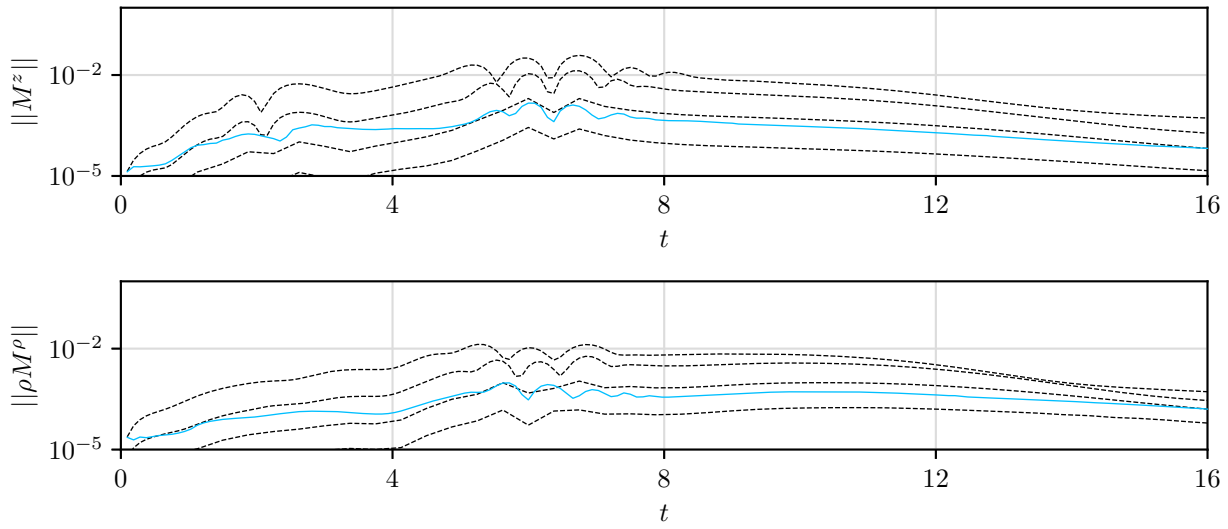

Figure 6.2: As Fig. 6.1 but for the convergence of the momentum constraints. Each of the dashed lines represents a successive refinement of the initial data while the solid line represents an AMR run with a relative error tolerance of $5 \cdot 10^{-5}$.

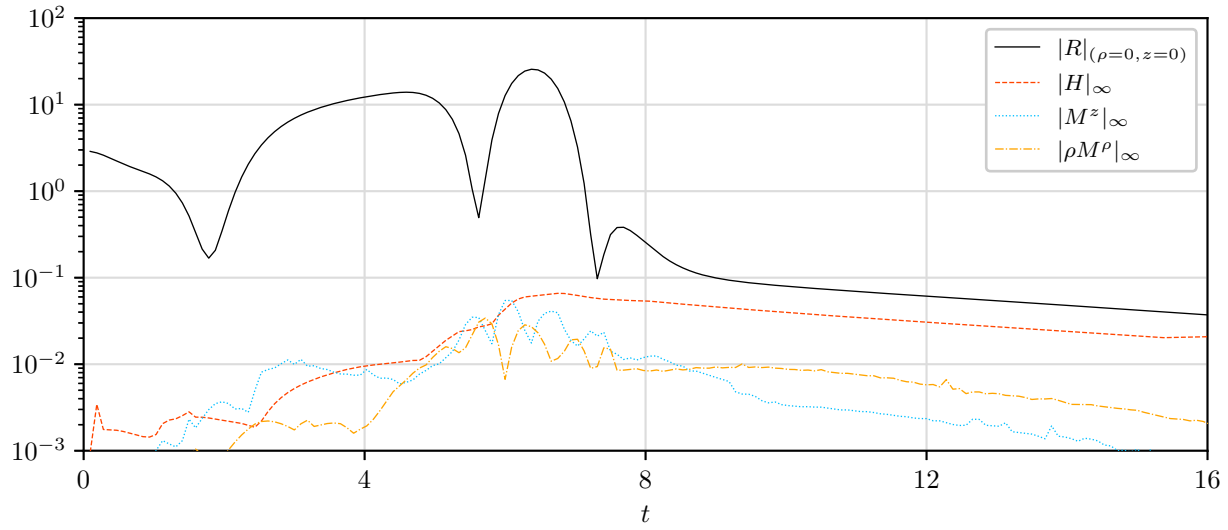

Figure 6.3: Magnitude of the 3D Ricci scalar, R, evaluated at $(0, 0)$ and the l_∞ norms of the Hamiltonian and momentum constraint violations for the AMR runs shown in Figs. 6.1 and 6.2. Post-dispersal, the solution becomes dominated by a non dispersing Hamiltonian constraint violation. Our critical search AMR simulations maintain constraint violations to about 1 part in 500 relative to the magnitude of the relevant fields throughout collapse.

6.5 Results

6.5.1 Massless Scalar Field

We choose to include simulations of massless scalar field collapse in order to test the accuracy of our simulations and to verify the utility of our analysis methods. Extremely high accuracy numerical analysis of the echoing period, Δ, have determined that, for the case of spherically symmetric critical collapse, $\Delta \approx 3.4454524022278213500$ [81, 111] while $\gamma \approx 0.37$ is known from simulations [43]. In this section, we verify that our simulations and analysis are of sufficient accuracy to reproduce these results.

As specified in Table 6.1, family $W_{l=0}$ is given by initially spherically symmetric initial data while family $W_{l=1}$ is initially a dipole. With family $W_{l=0}$, we demonstrate that our code is capable of resolving the spherically symmetric critical solution. By following the evolution of family $W_{l=1}$ we show that our code is capable of resolving situations where the initial data bifurcates into multiple on-axis centers of collapse. Since the results of Mendoza and Baumgarte demonstrated that quadrupole initial data was subject to such a bifurcation, we felt that it was important to validate our code in a similar regime. We have tuned these simulations to near the limits of double precision with $|p^\star - p|/p^\star \approx 1 \cdot 10^{-15}$ for family $W_{l=0}$ and $|p^\star - p|/p^\star \approx 1 \cdot 10^{-14}$ for family $W_{l=1}$.

Consider the proper time, τ, of an inertial observer located at the accumulation point such that the observer would see the formation of a naked singularity at $\tau = \tau^\star$. The echoing period, Δ, is then calculated using three somewhat independent methods. First, Δ_1 is computed by taking the mean and standard deviation of the period between successive echoes at the center of collapse when viewed as a function of $-\ln(\tau^\star - \tau)$. Second, Δ_2 comes from Fourier analysis of the dominant mode at the center of collapse in a similar frame. Third, Δ_3 is calculated via the scaling relation (6.5), which results in an observer independent method given by

$$\Delta_3 \approx \frac{\gamma}{N} \left(\ln |p_1 - p^\star| - \ln |p_2 - p^\star| \right) . \tag{6.80}$$

Here, N is the number of echoing periods observed between simulations with family parameters p_1 and p_2, respectively. Table 6.5 summarizes the results using all three methods.

Plots of the lapse, α, and the scalar field, μ, as a function of logarithmic proper time evaluated at the approximate accumulation points are shown in Figs. 6.4 and 6.5 for families $W_{l=0}$ and $W_{l=1}$, respectively. Here, approximate accumulation points are defined as coordinate locations, (z, ρ), of maximal scalar curvature encountered during the course of a subcritical simulation. These plots enable both direct and indirect calculation of Δ via the DSS time scaling relationship (6.3) and (6.80), respectively.

Unlike the $W_{l=0}$ case, we find that for the family $W_{l=1}$, the solution bifurcates into two centers of collapse. This in turn makes the determination of the world line of the privileged observer non-trivial. As we are starting from time symmetric initial data, the ideal solution would be to integrate the world lines of a family of initially stationary observers and choose the one which was nearest the accumulation point at the closest approach to criticality. Unfortunately, our code is not currently set up to perform such an integration.

As a quick and potentially poor approximation, we choose the world line of an observer who remains at the approximate accumulation point throughout the evolution. This approximation is potentially error-prone because of its gauge dependence and the fact that the observer is generically non-inertial. However, for the case of the $W_{l=1}$ simulations, the solutions very quickly approaches two on-axis copies of the monopole solution so relatively little error appears to have been introduced by this choice.

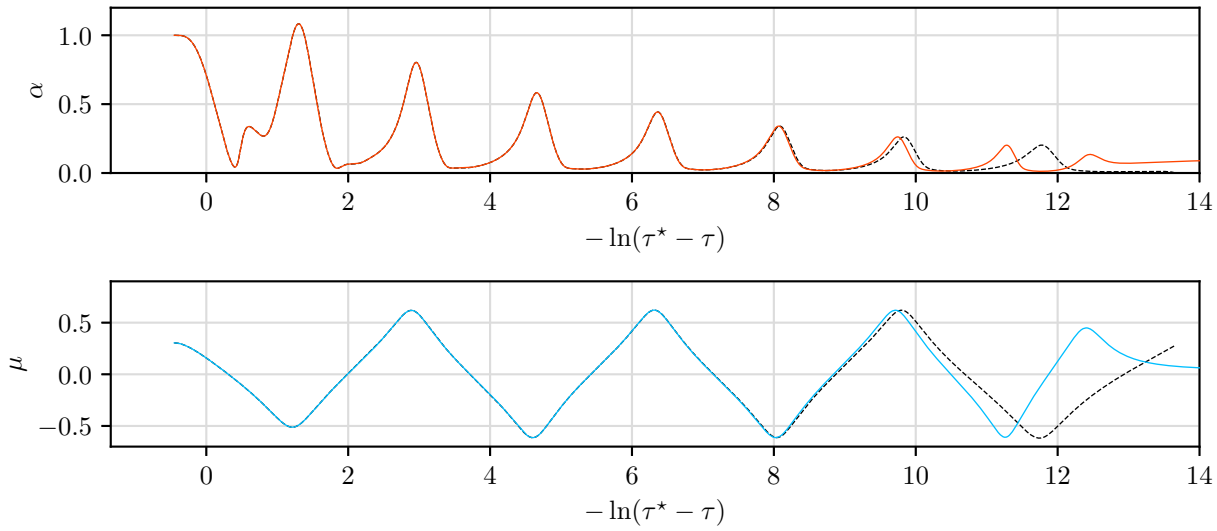

Figure 6.4: Lapse, α, and value of the scalar field, μ, as a function of $-\ln(\tau^\star - \tau)$ at the center of collapse (in this case the origin). Here, family $W_{l=0}$ data is used and both marginally subcritical (solid line) and supercritical (dashed line) solutions with $|p^\star - p|/p^\star \approx 1 \cdot 10^{-15}$ are shown. Since the scalar field quickly approaches the critical solution with an associated strong-field scale that significantly decreases with each echo, we are able to accurately determine $\tau^\star$ to $\approx 1 \cdot 10^{-6}$. Direct measurement of Δ from μ gives $\Delta_1 = 3.43(3)$, $\Delta_2 = 3.5(4)$ and $\Delta_3 = 3.6(4)$.

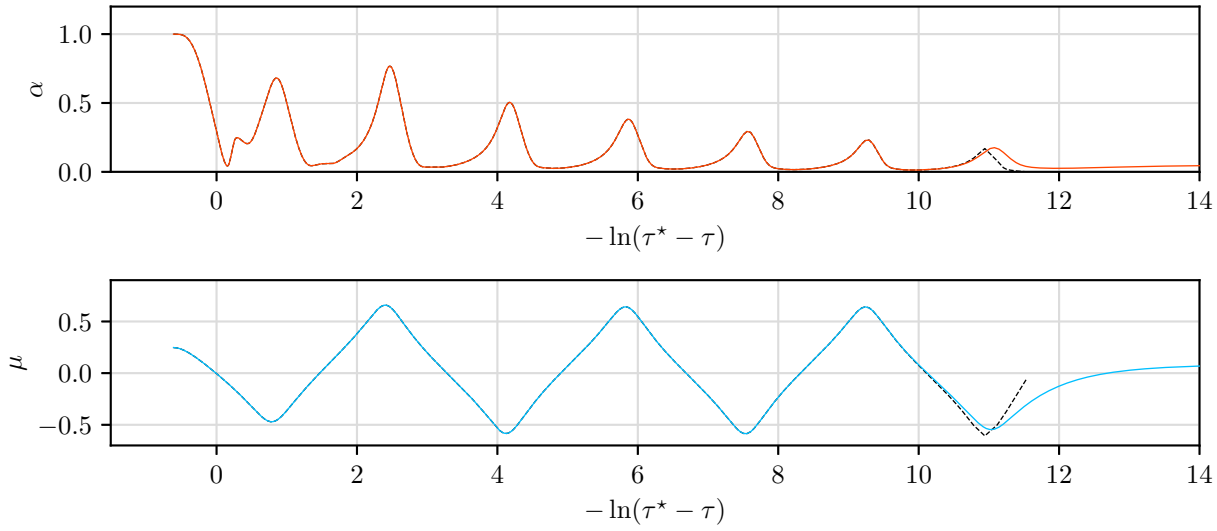

Figure 6.5: Lapse, α, and value of the scalar field, μ, as a function of $-\ln(\tau^\star - \tau)$ at the center of collapse (in this case $z \approx 0.594$). In this case family $W_{l=1}$ data is used and the marginally subcritical (solid line) and supercritical (dashed line) solutions have been determined to an overall accuracy of $|p^\star - p|/p^\star \approx 1 \cdot 10^{-14}$. Here, $\tau^\star$ is computed to $\approx 1 \cdot 10^{-5}$. Direct measurement of Δ from μ gives $\Delta_1 = 3.44(4)$, $\Delta_2 = 3.4(3)$ and $\Delta_3 = 3.2(4)$

The inverse Lyapunov exponent, γ, is calculated by fitting scaling laws of the form (6.6) for

the maximal energy density, $\rho_{\max}$, and 3D Ricci scalar, $R_{\max}$, encountered during the course of a subcritical simulation. In these fits, we make the assumption that the dominant contribution to the putative universal periodic function is sinusoidal. As the specific region in parameter space where the scaling relationship is expected to hold is unknown (the uncertainty in $p^\star$ contaminates the values close to criticality, while radiation of dispersal modes contaminates the data far from criticality), we average a number of fits to reasonable subsets of the available data.

Ideally, we would calculate γ via the maximal scale of some invariant quantity such as the 4D Ricci scalar (equivalently $\nabla_\lambda \mu \nabla^\lambda \mu$) or the Weyl scalar. However, calculations using frame dependent proxies such as the energy density, ρ_E, seem to be common in the literature and we have adopted this approach. In the case of collapse at the center of symmetry we note that ρ_E is linearly related to the invariant T. Figs. 6.6 and 6.7 demonstrate the determination of γ from ρ_E and R for families $W_{l=0}$ and $W_{l=1}$. Again, our results for γ along with those for Δ_1, Δ_2 and Δ_3 in the case of the scalar field are presented in Table 6.5.

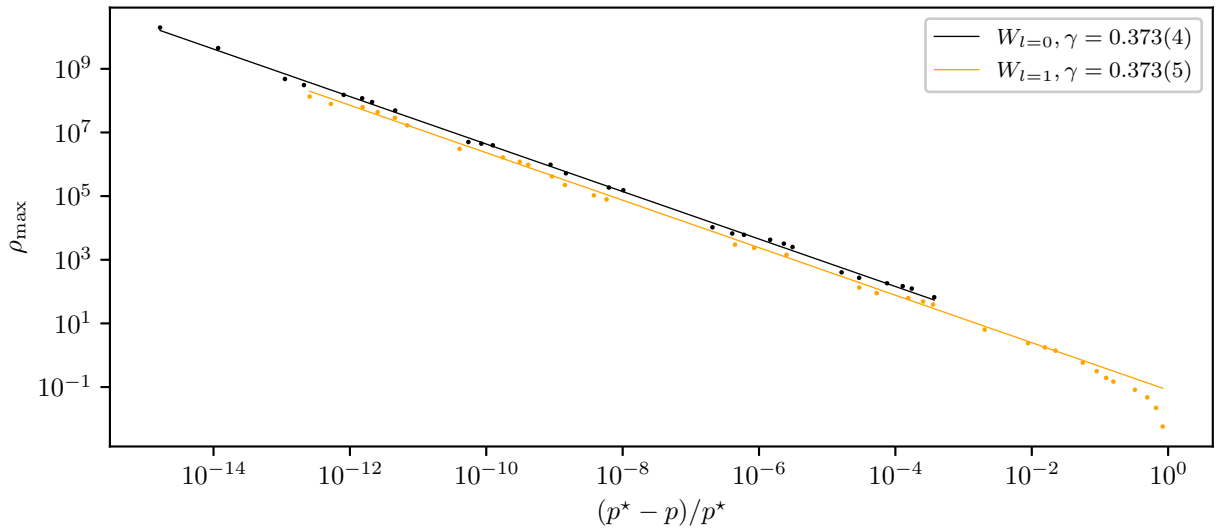

Figure 6.6: Inverse Lyapunov exponent, γ, determined via the scaling of the energy density ρ_E. Plotted here are the maximum values of ρ_E obtained in each subcritical run as a function of $|p^\star - p|/p^\star$. The energy density has dimensions M^{-2} and therefore scales according to $|p^\star - p|^{-2\gamma}$. Superior accuracy would be obtained by fitting to the maximum value of the 4D Ricci scalar or another invariant quantity. The lines represent an averaged fit to the underlying data.

Family	Δ_1	Δ_2	Δ_3	γ
$W_{l=0}$	3.43(3)	3.5(4)	3.6(4)	0.373(4)
$W_{l=1}$	3.44(4)	3.4(3)	3.2(4)	0.373(5)

Table 6.5: Estimated scaling exponents for axisymmetric scalar field collapse. The results summarized here agree with previous investigations to within the estimated error of our calculations. Although Δ_3 is far less precisely determined than Δ_1, it can be found in the absence of knowledge concerning a privileged inertial observer.

The excellent agreement between our computed values for the scaling exponents and previously established results for the massless scalar field demonstrate the accuracy of our simulations and the validity of our analysis. For AMR simulations, where it is impossible or impractical to establish

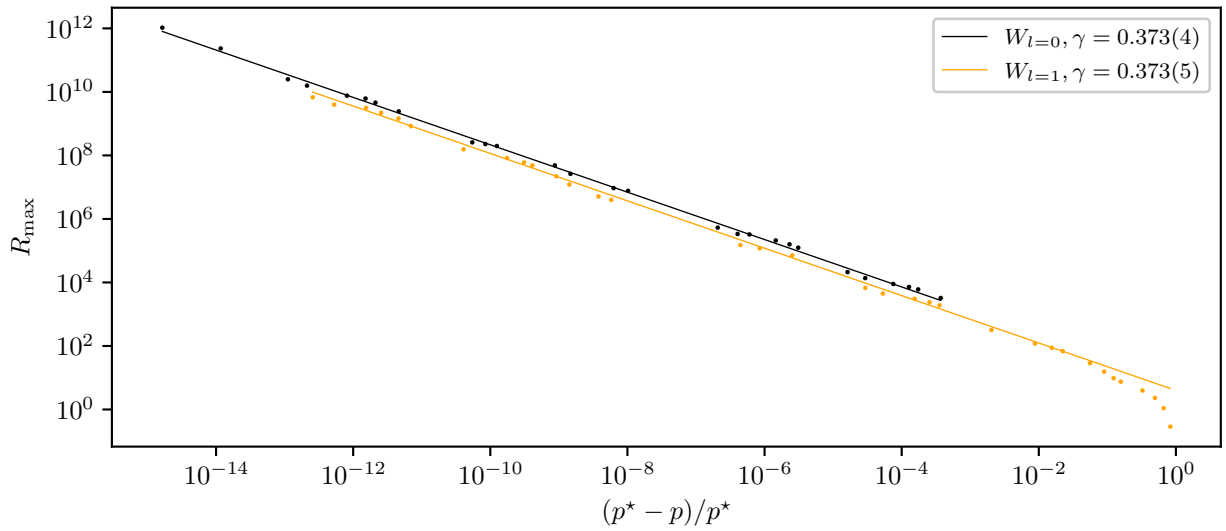

Figure 6.7: Inverse Lyapunov exponent, γ, determined via the scaling of the 3D Ricci scalar R. Plotted here are the maximum values of R obtained in each subcritical run as a function of $|p^\star - p|/p^\star$. The Ricci scalar density has dimensions of M^{-2} and therefore scales according to $|p^\star - p|^{-2\gamma}$. As in Fig. 6.6, the lines represent an averaged fit to the underlying data.

the existence of convergence close to criticality, this process serves as an important verification and validation stage before the presentation of new results. It is worth noting that some previous studies [18, 44, 58] have presented evidence for a non-spherical unstable mode near criticality in scalar field collapse. We see no evidence for such a mode for either our $W_{l=0}$ or $W_{l=1}$ calculations, but have not examined this point in much detail.

6.5.2 Einstein-Maxwell System

With our methodology established and verified via investigation of the massless scalar field, the analysis of the critical collapse of the Einstein-Maxwell system proceeds in parallel fashion. We first consider the previously unstudied families $E_{l=1}$, $M_{l=1}$ and $M_{l=2}$ defined in Table 6.2. Once the behaviour of these solutions has been described, we turn our attention to the families of Table 6.3 which were originally studied by Baumgarte et al. [20], and Mendoza and Baumgarte [85]. In what follows, we define the approximate accumulation points as the coordinate locations of maximal $|F_{\mu\nu}F^{\mu\nu}|$ encountered during a subcritical run.

No bifurcations about the origin were observed for the dipole families $M_{l=1}$ and $E_{l=1}$: both families underwent collapse at the center of symmetry. Unfortunately, a gauge pathology prevented family $E_{l=1}$ from being investigated beyond $|p^\star - p|/p^\star \approx 5 \cdot 10^{-9}$. This shortcoming seems to bear some resemblance to the sort of gauge problems encountered in evolving Brill waves towards criticality [74] and may be able to be resolved through the use of the shock avoiding gauge suggested by Alcubierre in [4] and successfully employed in [19, 21]. Fortunately, the pathology occurs sufficiently late in the evolution to enable the extraction of meaningful information concerning Δ and γ for the family.

Figs. 6.8–6.9 plot α and $|F_{\mu\nu}F^{\mu\nu}|$ at the accumulation point (in this case the origin) versus $-\ln(\tau^\star - \tau)$ for near-critical evolutions of families $M_{l=1}$ and $E_{l=1}$. Since the collapse occurs at the center of symmetry, there is only a single accumulation point and the observers at the origin are

privileged and inertial. As mentioned previously, this enables Δ to be accurately determined via statistical and Fourier analysis.

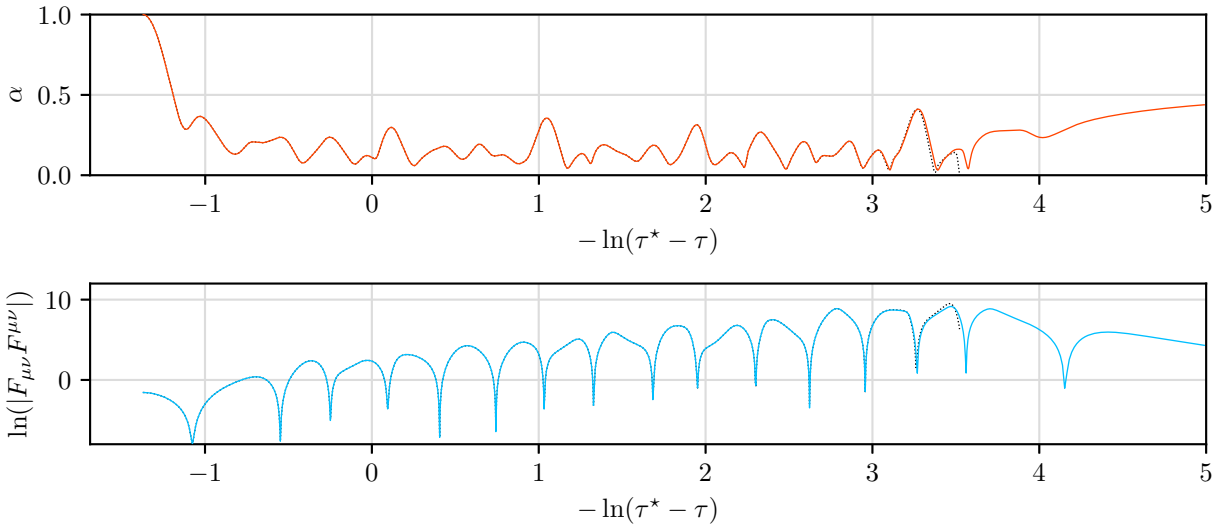

Figure 6.8: Lapse, α, and invariant scalar, $|F_{\mu\nu}F^{\mu\nu}|$, at the center of collapse for family $M_{l=1}$ as a function of $-\ln(\tau^\star - \tau)$ for marginally subcritical (solid line) and supercritical (dashed line) solutions with $|p^\star - p|/p^\star \approx 1 \cdot 10^{-13}$. Unlike the case of the scalar field, the strong-field scale of the critical solution only slowly decreases (i.e. Δ is small compared to the scalar case) and $\tau^\star$ can only be determined to a relative tolerance of about 10^{-4}. Direct measurement of Δ from $F_{\mu\nu}F^{\mu\nu}$ gives $\Delta_1 = 0.64(2)$ via statistical analysis, $\Delta_2 = 0.63(3)$ via Fourier analysis and $\Delta_3 = 0.59(6)$ from (6.80).

The analysis of family $M_{l=2}$ is both more interesting and more involved than that of families $M_{l=1}$ and $E_{l=1}$. In this case, and similarly to what is observed in the case of the massless scalar dipole, as the critical parameter is approached, the solution bifurcates into two on-axis centers of collapse. After this bifurcation the character of the critical solution changes markedly. Specifically, following this transition period, the growth and echoing period of the separated collapsing regions come to resemble those of two separated copies of the $M_{l=1}$ or $E_{l=1}$ critical solutions. This change in character is somewhat obscured in time series plots by the fact that we use the proper time of an accelerated observer at the accumulation point rather than that of a privileged inertial observer. Despite this, the change is evident in the growth rate, γ, when calculated via the scaling relationship

$$\ln\left(|F_{\mu\nu}F^{\mu\nu}|_{\max}\right) = -2\gamma \ln|p - p^\star| + f_F\left(\gamma \ln|p - p^\star|\right) + c_F, \tag{6.81}$$

as well as when Δ is calculated via (6.80). Overall, the two distinct phases of collapse can be seen in Figs. 6.10 and 6.11.

Figure 6.11 shows the results of calculating γ via the scalar invariant $F_{\mu\nu}F^{\mu\nu}$ which should scale as $|p^\star - p|^{-2\gamma}$ as in (6.81). Again, family $M_{l=2}$ appears to exhibit two distinct growth rates separated by a transition region in $\ln|p^\star - p|$. The early behaviour may be due to a slower growing quadrupole mode or perhaps simple radiation of initial data before the critical solution is approached. In total, the behaviour we observe appears to be consistent with the interpretation that, after the bifurcation occurs, the critical solution becomes dominated by the same mode as for families $M_{l=1}$ and $E_{l=1}$. A summary of our estimated values of Δ and γ for the families defined in Table 6.2 is compiled in Table 6.6.

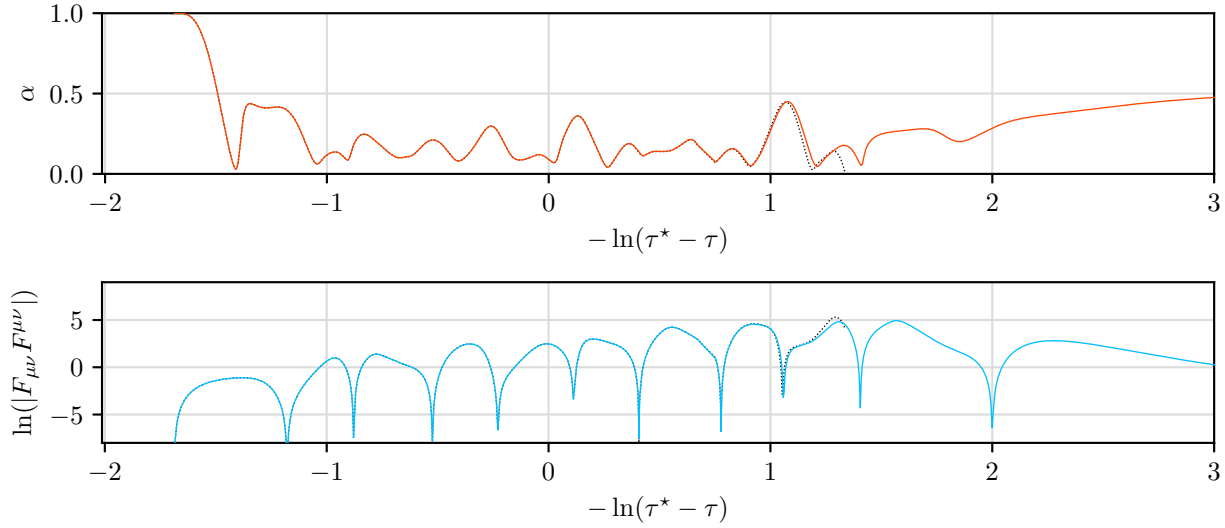

Figure 6.9: Lapse, α, and invariant scalar, $|F_{\mu\nu}F^{\mu\nu}|$, at the center of collapse for family $E_{l=1}$ as a function of $-\ln(\tau^\star - \tau)$ for marginally subcritical (solid line) and supercritical (dashed line) solutions with $|p^\star - p|/p^\star \approx 1 \cdot 10^{-9}$. As with family $M_{l=1}$, the strong-field scale of the critical solution slowly decreases and $\tau^\star$ can only be determined to a relative tolerance of about 10^{-3}. Direct measurement of Δ from $F_{\mu\nu}F^{\mu\nu}$ gives $\Delta_1 = 0.65(3)$ via statistical analysis, $\Delta_2 = 0.65(4)$ via Fourier analysis, and $\Delta_3 = 0.67(8)$ from (6.80).

Family	Δ_1	Δ_2	Δ_3	γ
$E_{l=1}$	0.65(3)	0.65(4)	0.67(8)	0.147(5)
$M_{l=1}$	0.64(2)	0.63(3)	0.59(6)	0.152(3)
$M_{l=2}$	**0.30(2)**	**0.31(3)**	0.19(4)	0.073(10)
$M_{l=2}$	**0.56(3)**	**0.63(6)**	0.64(9)	0.145(6)
E_{quad}	**0.30(5)**	**0.33(2)**	0.61(11)	0.164(19)
E_{quad}	**0.59(4)**	**0.57(4)**	0.59(10)	0.152(20)

Table 6.6: Summary of computed scaling exponents in critical collapse of the EM field for the families presented in Tables 6.2 and 6.3. The analysis of E_{quad} is presented in Section 6.5.3. Here, the two separate rows for $M_{l=2}$ and E_{quad} denote fits to the distinct behavioral regions of the quadrupole solutions; the first row is for p fairly distant from $p^\star$ while the second is for $p \to p^\star$. Results in bold indicate that the measurements were made using the world line of an accelerated observer and are unlikely to be accurate.

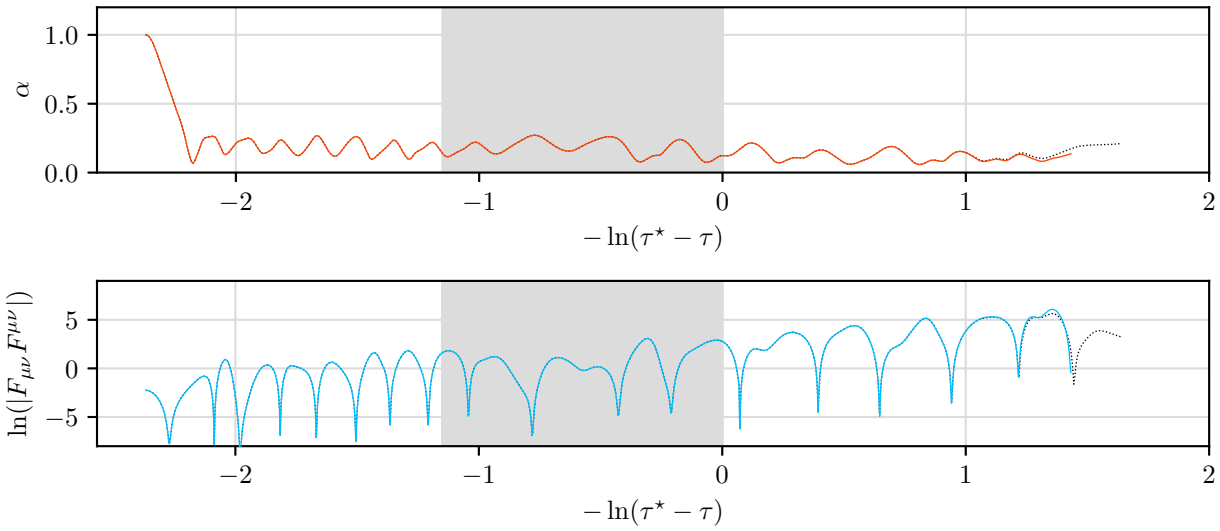

Figure 6.10: Lapse, α, and invariant scalar, $|F_{\mu\nu}F^{\mu\nu}|$, at the center of collapse for family $M_{l=2}$ as a function of $-\ln(\tau^\star - \tau)$ with $|p^\star - p|/p^\star \approx 5 \cdot 10^{-13}$. We use the proper time of a gauge dependent accelerated observer located at $z \approx 0.440$ as our independent variable, τ, making the interpretation of length and time scales potentially problematic. It appears that the critical solution is divided into two separate regions (transition region shown in gray) with differing Δ and γ. A naive measurement of Δ under the assumption that our observer is approximately inertial gives $\Delta_1 = 0.30(2)$ and $\Delta_2 = 0.31(3)$ for the first region and $\Delta_1 = 0.56(3)$, $\Delta_2 = 0.63(6)$ for the second region. Application of (6.80) (which is valid irrespective of the status of the observer) gives $\Delta_3 = 0.19(4)$ for the first region and $\Delta_3 = 0.64(9)$ for the second The values of Δ_2 and Δ_3 measured in the second region as $p \to p^\star$ appear to be consistent with those found for families $E_{l=1}$ and $M_{l=1}$.

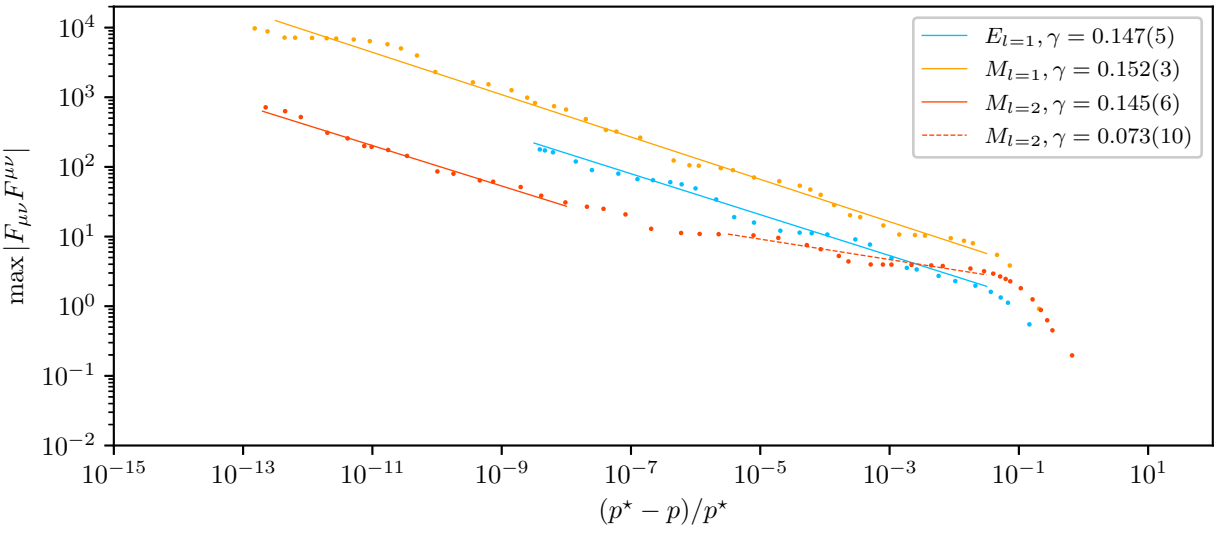

Figure 6.11: Inverse Lyapunov exponent, γ, determined via the scaling of the invariant scalar $|F_{\mu\nu}F^{\mu\nu}|$ which should scale as $|p^\star - p|^{-2\gamma}$. Plotted here are the maximum values of the invariant obtained in each subcritical run as a function of $|p^\star - p|/p^\star$. The lines shown are averaged fits of the underlying data and the quoted values of γ are the slopes of those fits. As described in the text, fits to two distinct regions of family $M_{l=2}$ have been made.

6.5.3 Direct Comparison to Previous Work.

When we compare our dipole and quadrupole results to those of Mendoza and Baumgarte [85] and Baumgarte et al. [20], the results are broadly consistent but do not fully agree to within our approximately determined errors. Although our work and the previous studies both indicate a single unstable mode with $\gamma_{l=1} \approx 0.15$ and $\Delta_{l=1} \approx 0.6$ for dipole type initial data, our investigation into an alternative family of quadrupole type initial data is consistent with a universal (rather than family dependent) growth rate and echoing period. In order to more conclusively determine the consistency of our work with that of [85] and [20], we attempt to replicate the previous computations by performing critical searches for the families listed in Table 6.3.

We perform evolutions of E_{quad} to a tolerance of $\lesssim 4{\cdot}10^{-15}$ so as to resolve the critical solution as accurately as possible. Previously, this family was resolved to a relative tolerance of approximately $1 \cdot 10^{-12}$ [85]. The evolutions for E_{dipole} were performed to a relative tolerance of only $\approx 1 \cdot 10^{-4}$ and for the sole purpose of verifying that we had initial data consistent with [85].

Figure 6.12 directly compares our simulations to those of [85] using both our data and data provided by Mendoza and Baumgarte [17]. This figure plots the minimum value of α on each spatial slice for family E_{quad} for marginally subcritical simulations. Comparing our data, we observe a significant divergence at $\tau \approx 18$; earlier than would be expected based on the relative precision of our searches. Similarly, the scaling of Fig. 6.14 agrees with Fig. 2 of Mendoza and Baumgarte [85] until $|p - p^\star|/p^\star \approx 1 \cdot 10^{-10}$. Past this point, the growth we observed increases relative to what was observed in [85].

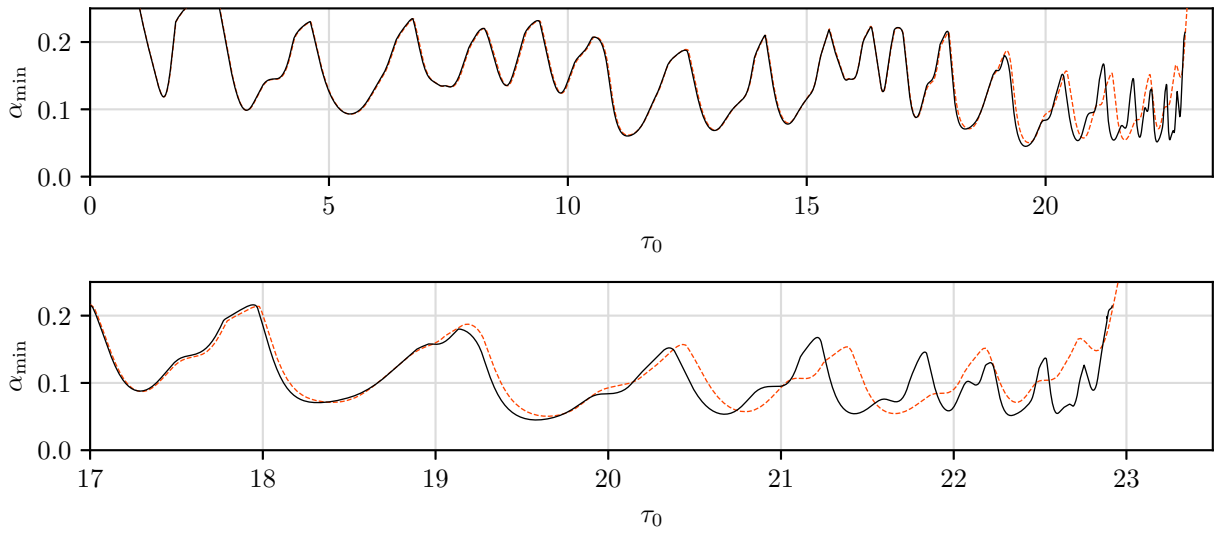

Figure 6.12: Minimum value of α on each spatial slice for family E_{quad} vs the proper time at the origin, τ_0. The data plotted here represents the subcritical simulations closest to criticality for both our investigation (solid black line) and that of Mendoza and Baumgarte [17, 85] (dashed red line). The lower plot highlights the difference in behaviour at late times. Note that we have scaled τ_0 for the data of Mendoza and Baumgarte by a factor of ≈ 1.003 to better align the early minima and maxima of α_0 with our own data. This degree of rescaling should be understood within the context of our simulations being only second order accurate and is performed to eliminate the dominant source of variation in our results far from the critical point. The simulations begin to differ markedly at $\tau \approx 18$, earlier than would be expected based on the relative precision of our searches.

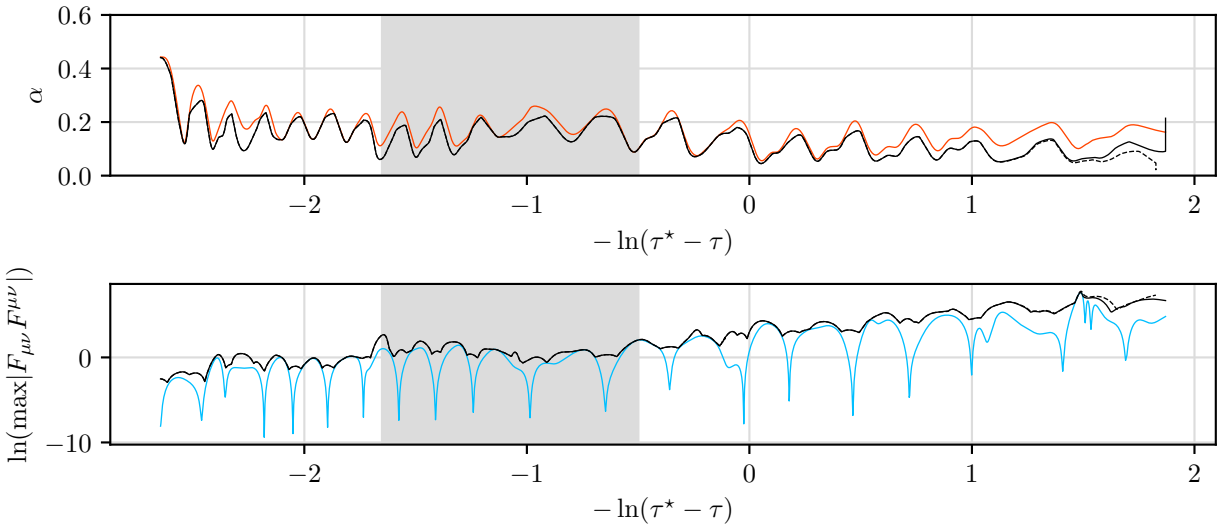

Figure 6.13: Lapse, α, and invariant scalar, $|F_{\mu\nu}F^{\mu\nu}|$, at the center of collapse for family E_{quad} as a function of $-\ln(\tau^\star - \tau)$ for marginally subcritical (solid black line) and supercritical (dashed black line) solutions with $|p^\star - p|/p^\star \approx 4 \cdot 10^{-15}$. Here, the black lines show the extremal values obtained on a spatial slice while the colored lines show the values at the center of collapse as determined by the coordinate location with largest value of $|F_{\mu\nu}F^{\mu\nu}|$ in the subcritical simulation closest to criticality.

Assuming that family E_{quad}, like family $E_{l=2}$, is best described by dividing the near-critical evolution into early and late time behaviour, a naive measurement of Δ under the assumption that our observer at fixed coordinate location is approximately inertial, gives $\Delta_1 = 0.30(5)$, $\Delta_2 = 0.33(2)$ for the first region and $\Delta_1 = 0.59(4)$, $\Delta_2 = 0.57(4)$ for the second region. Application of (6.80) gives $\Delta_3 = 0.61(11)$ for the first region and $\Delta_3 = 0.59(10)$ for the second. The large discrepancy between the values of Δ computed in the first region likely indicates that the solution does not show DSS behaviour far from criticality.

Fig. 6.14 plots $|F_{\mu\nu}F^{\mu\nu}|$ as a function of $|p^\star - p|/p^\star$ and is used to determine $\gamma_{\text{quad}} = 0.152(20)$. This in turn is consistent with the values of γ determined for all other families. It is clear that the early behaviour of family E_{quad} is very different from that of family $M_{l=2}$, which indicates that the early scaling behaviour observed for both families may simply be the result of radiation of features of the initial data on the path to criticality. Again we note that we list the complete set of Δ and γ for family E_{quad} as well as for the families defined in Table 6.2 in Table 6.6 of the previous section.

It is apparent that, close to criticality, the growth rates and echoing periods we observe for family E_{quad} differ markedly from those observed in [85]. Assuming that our results are correct, we hypothesise that the use of spherical polar coordinates with limited resolution in θ [85] may have had the inadvertent effect of leaving insufficient resolution to resolve dipole collapse away from the center of symmetry. If this is the case, then it is plausible that the growth of the dipole mode was suppressed in a manner similar to what is apparently observed.

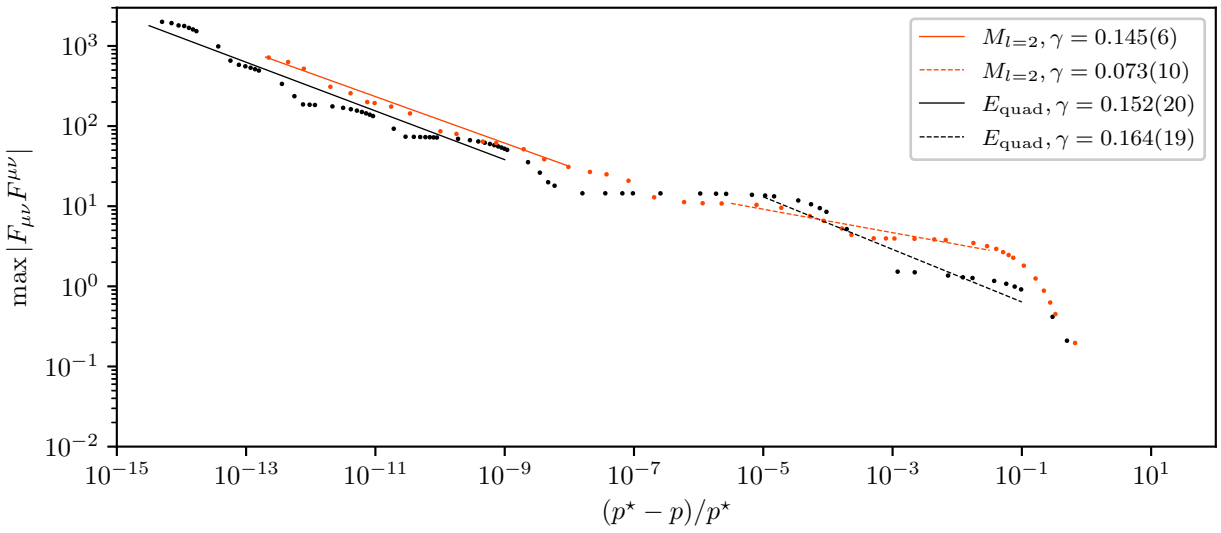

Figure 6.14: γ determined via the scaling of the invariant scalar $|F_{\mu\nu}F^{\mu\nu}|$ which should scale as $|p^\star - p|^{-2\gamma}$. Plotted here are the maximum values of $|F_{\mu\nu}F^{\mu\nu}|$ obtained in each subcritical run as a function of $|p^\star - p|/p^\star$. It is apparent that although both quadrupole solutions exhibit scaling with similar γ close to criticality the initial behaviour is highly family dependent.

6.6 Summary and Conclusions

We have investigated the critical collapse of both the massless scalar field and the Maxwell field in axisymmetry using the GBSSN formulation of general relativity. Our study of the scalar field was largely motivated by the need to calibrate our numerical methods—including AMR—and to develop analysis procedures. Nonetheless we are able to reproduce previous results on massless scalar collapse to the estimated accuracy of our calculations. Moreover, in contrast to some other earlier work [18, 44, 58], we find no evidence of non-spherical unstable modes at criticality. However, as we have not examined this issue very closely we feel that it is well worth further study.

With regard to the Einstein-Maxwell system, we observe that for generic initial data a dipole mode with $\gamma_{l=1} \approx 0.149(9)$ and $\Delta_{l=1} \approx 0.62(8)$ seems to be dominant. If there is an unstable quadrupolar mode, variations between the families $M_{l=2}$ and E_{quad} of Tables 6.2 and 6.3 suggest that it is not universal.

We observe significant differences in the behaviour of family E_{quad} close to criticality relative to the results reported in [85], although our findings appear largely similar until $|p^\star - p|/p^\star \approx 1 \cdot 10^{-10}$. We hypothesize that these differences may be due to the inability of spherical coordinates to fully resolve off-center collapse when limited angular resolution is employed.

The observed consistency between γ and Δ for each of the families in conjunction with the observed variance in the form of $f(x)$ (seen in Figs. 6.11 and 6.14) and absence of perfect DSS (seen in Figs. 6.8–6.10 and Fig. 6.13) is puzzling and requires additional study. Conservatively, it could be that given the slow growth rate of the dipolar critical solution, our simulations have simply not radiated away all traces of their initial data and this manifests in the apparent inconsistency of $f(x)$.

6.7 Acknowledgements

This research was supported by the Natural Sciences and Engineering Research Council of Canada (NSERC). We would additionally like to thank Maria Perez Mendoza and Thomas Baumgarte for generously providing their data, which was instrumental in our comparative analysis (see Sec. 6.5.3 and Fig. 6.12).

Bibliography

[1] Andrew M Abrahams and Charles R Evans. Critical behavior and scaling in vacuum axisymmetric gravitational collapse. *Physical review letters*, 70(20):2980, 1993.

[2] Andrew M Abrahams and Charles R Evans. Universality in axisymmetric vacuum collapse. *Physical Review D*, 49(8):3998, 1994.

[3] Arman Akbarian. *FD: finite difference toolkit*, 2016.

[4] Miguel Alcubierre. Appearance of coordinate shocks in hyperbolic formalisms of general relativity. *Physical Review D*, 55(10):5981, 1997.

[5] Miguel Alcubierre. *Introduction to 3+1 numerical relativity*, volume 140. OUP Oxford, 2008.

[6] Miguel Alcubierre, Gabrielle Allen, Bernd Brügmann, Edward Seidel, and Wai-Mo Suen. Towards an understanding of the stability properties of the 3+1 evolution equations in general relativity. *Physical Review D*, 62(12):124011, 2000.

[7] Miguel Alcubierre, Bernd Brügmann, Peter Diener, Michael Koppitz, Denis Pollney, Edward Seidel, and Ryoji Takahashi. Gauge conditions for long-term numerical black hole evolutions without excision. *Physical Review D*, 67(8):084023, 2003.

[8] Miguel Alcubierre, Bernd Brügmann, Thomas Dramlitsch, José A Font, Philippos Papadopoulos, Edward Seidel, Nikolaos Stergioulas, and Ryoji Takahashi. Towards a stable numerical evolution of strongly gravitating systems in general relativity: The conformal treatments. *Physical Review D*, 62(4):044034, 2000.

[9] Miguel Alcubierre and Martha D Mendez. Formulations of the 3+1 evolution equations in curvilinear coordinates. *General Relativity and Gravitation*, 43(10):2769–2806, 2011.

[10] Daniela Alic, Carles Bona-Casas, Carles Bona, Luciano Rezzolla, and Carlos Palenzuela. Conformal and covariant formulation of the z4 system with constraint-violation damping. *Physical Review D*, 85(6):064040, 2012.

[11] Daniela Alic, Wolfgang Kastaun, and Luciano Rezzolla. Constraint damping of the conformal and covariant formulation of the z4 system in simulations of binary neutron stars. *Physical Review D*, 88(6):064049, 2013.

[12] Pau Amaro-Seoane, Juan Barranco, Argelia Bernal, and Luciano Rezzolla. Constraining scalar fields with stellar kinematics and collisional dark matter. *Journal of Cosmology and Astroparticle Physics*, 2010(11):002, 2010.

[13] Peter Anninos, Joan Massó, Edward Seidel, Wai-Mo Suen, and John Towns. Three-dimensional numerical relativity: The evolution of black holes. *Physical Review D*, 52(4):2059, 1995.

[14] Richard Arnowitt, Stanley Deser, and Charles W Misner. Republication of: The dynamics of general relativity. *General Relativity and Gravitation*, 40:1997–2027, 2008.

[15] J Barranco and A Bernal. Constraining scalar field properties with boson stars as black hole mimickers. *AIP Conference Proceedings*, 1396(1):171–175, 2011.

[16] Manuel Barriola and Alexander Vilenkin. Gravitational field of a global monopole. *Physical Review Letters*, 63(4):341, 1989.

[17] Thomas Baumgarte. personal communication.

[18] Thomas W Baumgarte. Aspherical deformations of the choptuik spacetime. *Physical Review D*, 98(8):084012, 2018.

[19] Thomas W Baumgarte, Bernd Brügmann, Daniela Cors, Carsten Gundlach, David Hilditch, Anton Khirnov, Tomáš Ledvinka, Sarah Renkhoff, and Isabel Suárez Fernández. Critical phenomena in the collapse of gravitational waves, 2023.

[20] Thomas W Baumgarte, Carsten Gundlach, and David Hilditch. Critical phenomena in the gravitational collapse of electromagnetic waves. *Physical Review Letters*, 123(17):171103, 2019.

[21] Thomas W Baumgarte, Carsten Gundlach, and David Hilditch. Critical phenomena in the collapse of quadrupolar and hexadecapolar gravitational waves. *Physical Review D*, 107(8):084012, 2023.

[22] Thomas W Baumgarte, Pedro J Montero, Isabel Cordero-Carrión, and Ewald Müller. Numerical relativity in spherical polar coordinates: Evolution calculations with the bssn formulation. *Physical Review D*, 87(4):044026, 2013.

[23] Thomas W Baumgarte and Stuart L Shapiro. Numerical integration of Einstein's field equations. *Physical Review D*, 59(2):024007, 1998.

[24] Marsha J Berger and Joseph Oliger. Adaptive mesh refinement for hyperbolic partial differential equations. *Journal of computational Physics*, 53(3):484–512, 1984.

[25] Sebastiano Bernuzzi and David Hilditch. Constraint violation in free evolution schemes: Comparing the bssnok formulation with a conformal decomposition of the z4 formulation. *Physical Review D*, 81(8):084003, 2010.

[26] Carles Bona, Tomáš Ledvinka, Carlos Palenzuela, and M Žáček. General-covariant evolution formalism for numerical relativity. *Physical Review D*, 67(10):104005, 2003.

[27] Carles Bona and J Massó. Numerical relativity: Evolving spacetime. *International Journal of Modern Physics C*, 4(04):883–907, 1993.

[28] Carles Bona and Joan Massó. Einstein's evolution equations as a system of balance laws. *Physical review D*, 40(4):1022, 1989.

[29] Carles Bona and Joan Massó. Hyperbolic evolution system for numerical relativity. *Physical Review Letters*, 68(8):1097, 1992.

[30] Carles Bona, Joan Masso, Edward Seidel, and Joan Stela. New formalism for numerical relativity. *Physical Review Letters*, 75(4):600, 1995.

[31] Carles Bona, Joan Massó, Edward Seidel, and Joan Stela. First order hyperbolic formalism for numerical relativity. *Physical Review D*, 56(6):3405, 1997.

[32] Patrick R Brady and Mike J Cai. Critical phenomena in gravitational collapse. *arXiv preprint gr-qc/9812071*, 1998.

[33] Steven Brandt and Bernd Brügmann. A simple construction of initial data for multiple black holes. *Physical Review Letters*, 78(19):3606, 1997.

[34] William L Briggs, Van Emden Henson, and Steve F McCormick. *A multigrid tutorial*. SIAM, 2000.

[35] Y. Brihaye and Y. Verbin. Spherical structures in conformal gravity and its scalar-tensor extension. *Physical Review D*, 80:124048, Dec 2009.

[36] J David Brown. BSSN in spherical symmetry. *Classical and Quantum Gravity*, 25(20):205004, 2008.

[37] J David Brown. Covariant formulations of Baumgarte, Shapiro, Shibata, and Nakamura and the standard gauge. *Physical Review D*, 79(10):104029, 2009.

[38] Manuela Campanelli, Carlos O Lousto, Pedro Marronetti, and Yosef Zlochower. Accurate evolutions of orbiting black-hole binaries without excision. *Physical Review Letters*, 96(11):111101, 2006.

[39] Li-Ming Cao and Liang-Bi Wu. Note on the strong hyperbolicity of f(R) gravity with dynamical shifts. *Physical Review D*, 105(12):124062, 2022.

[40] JR Cash and F Mazzia. A new mesh selection algorithm, based on conditioning, for two-point boundary value codes. *Journal of Computational and Applied Mathematics*, 184(2):362–381, 2005.

[41] Matthew Choptuik. personal communication.

[42] Matthew Choptuik. Lectures for vii Mexican school on gravitation and mathematical physics relativistic astrophysics and numerical relativity. http://laplace.physics.ubc.ca/People/matt/Teaching/06Mexico/mexico06.pdf, 2006.

[43] Matthew W Choptuik. Universality and scaling in gravitational collapse of a massless scalar field. *Physical Review Letters*, 70(1):9, 1993.

[44] Matthew W Choptuik, Eric W Hirschmann, Steven L Liebling, and Frans Pretorius. Critical collapse of the massless scalar field in axisymmetry. *Physical Review D*, 68(4):044007, 2003.

[45] Matthew W Choptuik, Luis Lehner, and Frans Pretorius. Probing strong field gravity through numerical simulations. *arXiv preprint arXiv:1502.06853*, 2015.

[46] Monica Colpi, Stuart L Shapiro, and Ira Wasserman. Boson stars: Gravitational equilibria of self-interacting scalar fields. *Physical review letters*, 57(20):2485, 1986.

[47] David Daverio, Yves Dirian, and Ermis Mitsou. Apples with apples comparison of 3+1 conformal numerical relativity schemes. *arXiv preprint arXiv:1810.12346*, 2018.

[48] Arnaud de Lavallaz and Malcolm Fairbairn. Neutron stars as dark matter probes. *Physical Review D*, 81(12):123521, 2010.

[49] Isabel Suárez Fernández, Sarah Renkhoff, Daniela Cors Agulló, Bernd Brügmann, and David Hilditch. Evolution of brill waves with an adaptive pseudospectral method. *Physical Review D*, 106(2):024036, 2022.

[50] Vladimir Fock. *The theory of space, time and gravitation*. Elsevier, 2015.

[51] Yvonne Foures-Bruhat. Théorème d'existence pour certains systèmes d'équations aux dérivées partielles non linéaires. 1952.

[52] Yvonne Foures-Bruhat. Sur l'intégration des équations de la relativité générale. *Journal of rational mechanics and analysis*, 5(6):951–966, 1956.

[53] Marcelo Gleiser and Richard Watkins. Gravitational stability of scalar matter. *Nuclear Physics B*, 319(3):733–746, 1989.

[54] Eric Gourgoulhon. *3+1 formalism in general relativity: bases of numerical relativity*, volume 846. Springer Science & Business Media, 2012.

[55] Carsten Gundlach. Understanding critical collapse of a scalar field. *Physical Review D*, 55(2):695, 1997.

[56] Carsten Gundlach. Critical phenomena in gravitational collapse. *Living Reviews in Relativity*, 2(1), 1999.

[57] Carsten Gundlach and Jose M Martin-Garcia. Hyperbolicity of second order in space systems of evolution equations. *Classical and Quantum Gravity*, 23(16):S387, 2006.

[58] Carsten Gundlach and Jose M Martin-Garcia. Critical phenomena in gravitational collapse. *Living Reviews in Relativity*, 10(1):1–57, 2007.

[59] Mark Hannam, Sascha Husa, Frank Ohme, Bernd Brügmann, and Niall O Murchadha. Wormholes and trumpets: Schwarzschild spacetime for the moving-puncture generation. *Physical Review D*, 78(6):064020, 2008.

[60] Diego Harari and Carlos Lousto. Repulsive gravitational effects of global monopoles. *Physical Review D*, 42(8):2626, 1990.

[61] Stephen William Hawking and Roger Penrose. The singularities of gravitational collapse and cosmology. *Proceedings of the Royal Society of London. A. Mathematical and Physical Sciences*, 314(1519):529–548, 1970.

[62] David Hilditch, Thomas W Baumgarte, Andreas Weyhausen, Tim Dietrich, Bernd Brügmann, Pedro J Montero, and Ewald Müller. Collapse of nonlinear gravitational waves in moving-puncture coordinates. *Physical Review D*, 88(10):103009, 2013.

[63] David Hilditch, Sebastiano Bernuzzi, Marcus Thierfelder, Zhoujian Cao, Wolfgang Tichy, and Bernd Brügmann. Compact binary evolutions with the z4c formulation. *Physical Review D*, 88(8):084057, 2013.

[64] David Hilditch, Andreas Weyhausen, and Bernd Brügmann. Evolutions of centered brill waves with a pseudospectral method. *Physical Review D*, 96(10):104051, 2017.

[65] Phillippe Jetzer. Boson stars. *Physics Reports*, 220(4):163–227, 1992.

[66] David J Kaup. Klein–Gordon geon. *Physical Review*, 172(5):1331, 1968.

[67] Roy P Kerr. Gravitational field of a spinning mass as an example of algebraically special metrics. *Physical review letters*, 11(5):237, 1963.

[68] Anton Khirnov and Tomáš Ledvinka. Slicing conditions for axisymmetric gravitational collapse of Brill waves. *Classical and Quantum Gravity*, 35(21):215003, 2018.

[69] Burkhard Kleihaus, Jutta Kunz, and Stefanie Schneider. Stable phases of boson stars. *Physical Review D*, 85(2):024045, 2012.

[70] Tatsuhiko Koike, Takashi Hara, and Satoshi Adachi. Critical behavior in gravitational collapse of radiation fluid: A renormalization group (linear perturbation) analysis. *Physical Review Letters*, 74(26):5170, 1995.

[71] Serguei S Komissarov. Multidimensional numerical scheme for resistive relativistic magnetohydrodynamics. *Monthly Notices of the Royal Astronomical Society*, 382(3):995–1004, 2007.

[72] H. Kreiss and J. Oliger. *Methods for the Approximate Solution of Time Dependent Problems*. GARP publications series. International Council of Scientific Unions, World Meteorological Organization, 1973.

[73] Fjodor V Kusmartsev, Eckehard W Mielke, and Franz E Schunck. Gravitational stability of boson stars. *Physical Review D*, 43(12):3895, 1991.

[74] Tomáš Ledvinka and Anton Khirnov. Universality of curvature invariants in critical vacuum gravitational collapse. *Physical Review Letters*, 127(1):011104, 2021.

[75] TD Lee and Yang Pang. Stability of mini-boson stars. *Nuclear Physics B*, 315(2):477–516, 1989.

[76] Luis Lehner, Steven L Liebling, and Oscar Reula. Amr, stability and higher accuracy. *Classical and Quantum Gravity*, 23(16):S421, 2006.

[77] Randall J LeVeque. *Finite difference methods for ordinary and partial differential equations: steady-state and time-dependent problems*. SIAM, 2007.

[78] Xin-zhou Li and Xiang-hua Zhai. Fermion stars with a global monopole. *Physics Letters B*, 364(4):212–215, 1995.

[79] Xin-zhou Li, Xiang-hua Zhai, and Guang Chen. Boson d-stars. *Astroparticle Physics*, 13(2):245–252, 2000.

[80] Steven L Liebling and Carlos Palenzuela. Dynamical boson stars. *Living Reviews in Relativity*, 26(1):1, 2023.

[81] Jose M Martin-Garcia and Carsten Gundlach. Global structure of Choptuik's critical solution in scalar field collapse. *Physical Review D*, 68(2):024011, 2003.

[82] Anja Marunovic. personal communication.

[83] Anja Marunović and Miljenko Murković. A novel black hole mimicker: a boson star and a global monopole nonminimally coupled to gravity. *Classical and Quantum Gravity*, 31(4):045010, 2014.

[84] Francesca Mazzia, Jeff R Cash, and Karline Soetaert. Solving boundary value problems in the open source software R: package bvpSolve. *Opuscula mathematica*, 34(2):387–403, 2014.

[85] Maria F Perez Mendoza and Thomas W Baumgarte. Critical phenomena in the gravitational collapse of electromagnetic dipole and quadrupole waves. *Physical Review D*, 103(12):124048, 2021.

[86] Eckehard W Mielke and Franz E Schunck. Boson stars: Early history and recent prospects. In *Recent Developments in Theoretical and Experimental General Relativity, Gravitation, and Relativistic Field Theories*, volume 1, page 1607. World Scientific Publishing Company, 1999.

[87] Charles W Misner, Kip S Thorne, and John Archibald Wheeler. *Gravitation*. Macmillan, 1973.

[88] Bishop Mongwane. Toward a consistent framework for high order mesh refinement schemes in numerical relativity. *General Relativity and Gravitation*, 47:1–21, 2015.

[89] Bishop Mongwane. On the hyperbolicity and stability of 3+1 formulations of metric f(R) gravity. *General Relativity and Gravitation*, 48:1–25, 2016.

[90] Gabriel Nagy, Omar E Ortiz, and Oscar A Reula. Strongly hyperbolic second order Einstein's evolution equations. *Physical Review D*, 70(4):044012, 2004.

[91] Ulises Nucamendi, Marcelo Salgado, and Daniel Sudarsky. Nonminimal global monopoles and bound orbits. *Physical Review Letters*, 84(14):3037, 2000.

[92] Ulises Nucamendi, Marcelo Salgado, and Daniel Sudarsky. Alternative approach to the galactic dark matter problem. *Physical Review D*, 63(12):125016, 2001.

[93] Ulises Nucamendi and Daniel Sudarsky. Quasi-asymptotically flat spacetimes and their ADM mass. *Classical and Quantum Gravity*, 14(5):1309, 1997.

[94] Carlos Palenzuela, L Lehner, and Steven L Liebling. Orbital dynamics of binary boson star systems. *Physical Review D*, 77(4):044036, 2008.

[95] Carlos Palenzuela, Luis Lehner, and Shin Yoshida. Understanding possible electromagnetic counterparts to loud gravitational wave events: Binary black hole effects on electromagnetic fields. *Physical Review D*, 81(8):084007, 2010.

[96] Carlos Palenzuela, I Olabarrieta, L Lehner, and Steven L Liebling. Head-on collisions of boson stars. *Physical Review D*, 75(6):064005, 2007.

[97] Roger Penrose. Gravitational collapse and space-time singularities. *Physical Review Letters*, 14(3):57, 1965.

[98] Felix AE Pirani. Invariant formulation of gravitational radiation theory. *Physical Review*, 105(3):1089, 1957.

[99] Tomasz Plewa, Timur Linde, V Gregory Weirs, et al. Adaptive mesh refinement-theory and applications. 2005.

[100] William H Press, Brian P Flannery, Saul A Teukolsky, and William T Vetterling. Numerical recipes, 1990.

[101] Frans Pretorius. *AMRD V2 Reference Manual*. Princeton University, 2002.

[102] Frans Pretorius. *PAMR Reference Manual*. Princeton University, 2002.

[103] Frans Pretorius. Evolution of binary black-hole spacetimes. *Physical review letters*, 95(12):121101, 2005.

[104] Frans Pretorius. Numerical relativity using a generalized harmonic decomposition. *Classical and Quantum Gravity*, 22(2):425, 2005.

[105] Frans Pretorius. Simulation of binary black hole spacetimes with a harmonic evolution scheme. *Classical and Quantum Gravity*, 23(16):S529, 2006.

[106] Suvrat Raju. Lessons from the information paradox. *Physics Reports*, 943:1–80, 2022.

[107] Gray Reid and Matthew W Choptuik. Nonminimally coupled topological-defect boson stars: Static solutions. *Physical Review D*, 93(4):044022, 2016.

[108] Gray D. Reid and Matthew W. Choptuik. Rccz4: A reference metric approach to z4, 2023.

[109] Gray D. Reid and Matthew W. Choptuik. Stability of non-minimally coupled topological-defect boson stars, 2023.

[110] Gray D. Reid and Matthew W. Choptuik. Universality in the critical collapse of the einstein-maxwell system, 2023.

[111] Michael Reiterer and Eugene Trubowitz. Choptuik's critical spacetime exists. *Communications in Mathematical Physics*, 368:143–186, 2019.

[112] Lewis Fry Richardson. Ix. the approximate arithmetical solution by finite differences of physical problems involving differential equations, with an application to the stresses in a masonry dam. *Philosophical Transactions of the Royal Society of London. Series A, Containing Papers of a Mathematical or Physical Character*, 210(459-470):307–357, 1911.

[113] Tanja Rindler-Daller and Paul R Shapiro. Angular momentum and vortex formation in Bose–Einstein-condensed cold dark matter haloes. *Monthly Notices of the Royal Astronomical Society*, 422(1):135–161, 2012.

[114] Carlo Rovelli. Loop quantum gravity. *Living reviews in relativity*, 11:1–69, 2008.

[115] Remo Ruffini and Silvano Bonazzola. Systems of self-gravitating particles in general relativity and the concept of an equation of state. *Physical Review*, 187(5):1767, 1969.

[116] Nicolas Sanchis-Gual, Pedro J Montero, Jose A Font, Ewald Müller, and Thomas W Baumgarte. Fully covariant and conformal formulation of the Z4 system in a reference-metric approach: comparison with the BSSN formulation in spherical symmetry. *Physical Review D*, 89(10):104033, 2014.

[117] Franz E Schunck and Eckehard W Mielke. General relativistic boson stars. *Classical and Quantum Gravity*, 20(20):R301, 2003.

[118] Franz E Schunck and Diego F Torres. Boson stars with generic self-interactions. *International Journal of Modern Physics D*, 9(05):601–618, 2000.

[119] Xin Shi and Xinzhou Li. The gravitational field of a global monopole. *Classical and Quantum Gravity*, 8(4):761, 1991.

[120] Masaru Shibata and Takashi Nakamura. Evolution of three-dimensional gravitational waves: Harmonic slicing case. *Physical Review D*, 52(10):5428, 1995.

[121] Marcus Thierfelder, Sebastiano Bernuzzi, David Hilditch, Bernd Brügmann, and Luciano Rezzolla. Trumpet solution from spherical gravitational collapse with puncture gauges. *Physical Review D*, 83(6):064022, 2011.

[122] Diego F Torres, S Capozziello, and G Lambiase. Supermassive boson star at the galactic center? *Physical Review D*, 62(10):104012, 2000.

[123] John A Trangenstein. *Numerical solution of hyperbolic partial differential equations*. Cambridge University Press, 2009.

[124] L Arturo Urena-Lopez and Argelia Bernal. Bosonic gas as a galactic dark matter halo. *Physical Review D*, 82(12):123535, 2010.

[125] Jochum J Van der Bij and Marcelo Gleiser. Stars of bosons with non-minimal energy-momentum tensor. *Physical Letters B*, 194(4):482–486, 1987.

[126] Alexander Vilenkin and E Paul S Shellard. *Cosmic strings and other topological defects*. Cambridge University Press, 2000.

[127] Robert M Wald. *General relativity*. University of Chicago press, 2010.

[128] John Archibald Wheeler. Geons. *Physical Review*, 97(2):511, 1955.

[129] Clifford M Will. The confrontation between general relativity and experiment. *Living reviews in relativity*, 17:1–117, 2014.

[130] Andrew Wilson. *Complete Documentation of the RNPL Distribution*. University of British Columbia, 2006.

[131] James W York Jr. Conformally invariant orthogonal decomposition of symmetric tensors on riemannian manifolds and the initial-value problem of general relativity. *Journal of Mathematical Physics*, 14(4):456–464, 1973.

[132] Ye-Fei Yuan, Ramesh Narayan, and Martin J Rees. Constraining alternate models of black holes: Type I x-ray bursts on accreting fermion-fermion and boson-fermion stars. *The Astrophysical Journal*, 606(2):1112, 2004.

[133] Barton Zwiebach. *A first course in string theory*. Cambridge university press, 2004.

Appendix A

Multiple Precision Shooting Method

A.1 Summary

In this Appendix we briefly review the shooting method for boundary value problems and our novel extension to it—multiple precision shooting—which was used extensively to find approximate solutions for the topological-defect boson stars of Chapter 3.

A.2 Shooting Method for BVPs

Given a set of ODEs, $\mathrm{L}\mathbf{u}(\mathrm{x}) = 0$ and boundary conditions $\mathrm{G}\mathbf{u}(\mathrm{x}) = 0$, where L and G are differential operators and $\mathbf{u}(x)$ is the solution vector, we can formulate a solution as an initial value problem at $x = x_0$ where the initial conditions are given by the guess $\mathbf{u}_0(x_0)$.

Setting $i = 0$, and integrating the problem to the boundary regions, we find the residual $\mathbf{res}_i = \mathrm{G}\mathbf{u}_i$ and then update the initial guess using $\mathbf{u}_{i+1}(x_0) = \mathbf{u}_i(x_0) - \mathrm{J}^{-1}\mathbf{res}_i$, where $\mathrm{J} = \partial \mathrm{G}/\partial \mathbf{u}_i(x_0)$ is the Jacobian of the boundary conditions. Upon repeated iteration $i = 1, 2, 3, \ldots$, the solution is expected to converge quadratically provided $\mathbf{u}_i(x_0)$ is sufficiently close to $\mathbf{u}(x_0)$. Even if the problem is not well defined on the entire domain (i.e. there exist choices of $\mathbf{u}_i(x_0)$ for which the function exhibits discontinuities on the domain), we can sometimes use a modified version of this method.

In the case of the mini-boson star, the only free parameters at the origin are $\omega/\alpha(0)$ and the central amplitude $\psi(0)$. Fixing $\psi(0)$, we find that for $\omega/\alpha(0) < \Omega_i$, where Ω_i is an eigenvalue of the problem, the solution diverges to positive infinity. Conversely, for for $\omega/\alpha(0) > \Omega_i$, the solution diverges to negative infinity. We may therefore use a binary search to find Ω_i precisely enough to integrate to the asymptotic regime of the boson star, where we fit an exponential tail to the star. The algorithms below summarize this process for the boson star (Algorithm 4) and global monopoles (Algorithm 5) respectively,

Algorithm 4 Boson Star Shooting

1: **hold** $\phi(x)$ fixed
2: **initialize** $\psi(0)$
3: **set** bounding values of ω, ω_{high} and ω_{low}
4: **set** $\omega = \frac{1}{2}(\omega_{\text{high}} + \omega_{\text{low}})$
5: **perform** binary search on ω, integrating $\psi(x)$ and
    metric functions as far as possible
6: **find** $r_{\max}$ such that bounding solutions differ by $\sim \epsilon$
7: **fit** tail to $\psi(r)$ for $r > r_{\max}$
8: **integrate** metric functions to asymptotic regime

Algorithm 5 Global Monopole Shooting

hold $\psi(x)$ fixed
initialize $\phi(0) = 0$
set bounding values of $\partial\phi/\partial r$, $\partial\phi/\partial r_{\text{high}}$ and $\partial\phi/\partial r_{\text{low}}$
set $\partial\phi/\partial r = \frac{1}{2}(\partial\phi/\partial r_{\text{high}} + \partial\phi/\partial r_{\text{low}})$
perform binary search on $\partial\phi/\partial r$, integrating
$\phi(x)$ and metric functions as far as possible
find r_{max} such that bounding solutions differ by $\sim \epsilon$
fit tail to $\phi(r)$ for $r > r_{\text{max}}$
integrate metric functions to asymptotic regime

A.3 Multiple Precision Shooting Method

It might be asked why it is not possible to use simple functions (such as gaussians) as initial guesses for the BVP solver rather than needing to craft nearly exact solutions with the shooting method. In practice, we found that for an arbitrary initial guess the solution is more likely to converge to one of the infinitely many excited boson star states [80] than to the ground state. In addition, since we are dealing with a numeric problem on a finite domain, there are "pseudo solutions" which satisfy the boundary conditions to within tolerance where imposed, but fail to converge to any solution when tighter tolerances or higher resolutions are imposed. For these reasons it can be challenging to find good initial guesses even in the absence of a global monopole.

Additionally, once the global monopole field is introduced, the ground state solutions include shells of bosonic matter far from the origin which contain much of the star's mass. Since these solutions are characterized by the appearance of matter shells, an initial guess which does not have the shells in at least approximately the correct positions is unlikely to converge.

In practice, when we supply the BVP solver with simpler initial guesses the solutions either fail to converge or else converge to a pseudo solution for large error tolerances, then fail to converge when subjected to more rigorous error tests. For this reason it is important to supply a very good initial guess to the BVP solver.

Complicating the shooting process is the fact that in many cases double precision (8-byte floating point) is insufficient to tune ω such that the boson star achieves its asymptotic behavior. Fig. A.1 displays an illustrative example, showing the result of shooting in ω with double precision and how it fails to capture the true solution. From experience, certain branches (typically those with many shells) have necessitated finding ω to better than 10^{-150} to integrate the problem to the asymptotic regime. As double precision has a relative error of about 10^{-16}, this is problematic.

Finding a parameter to within 10^{-150} demands the use of extended precision libraries and integrating with such a small error tolerance would be a prohibitively expensive prospect for extensive parameter space surveys. Fortunately, we do not need to actually solve the problem to these tolerances. In practice, maintaining a relative error of 10^{-12} or so is more than sufficient to provide a good initial guess to the BVP solver. As such, we do not have to find ω to within 10^{-150} of the *true value* , we simply have to find ω to within 10^{-150} of a value which results in an *asymptotically well behaved solution* with respect to our given step size and error tolerance.

Thus, we arrive at the following paradigm: use extended precision to differentiate between solutions (characterized by minute differences in ω) while maintaining an error tolerance of $\epsilon \approx 10^{-12}$. In other words, our shooting solutions maintain extremely high precision but only standard accuracy.

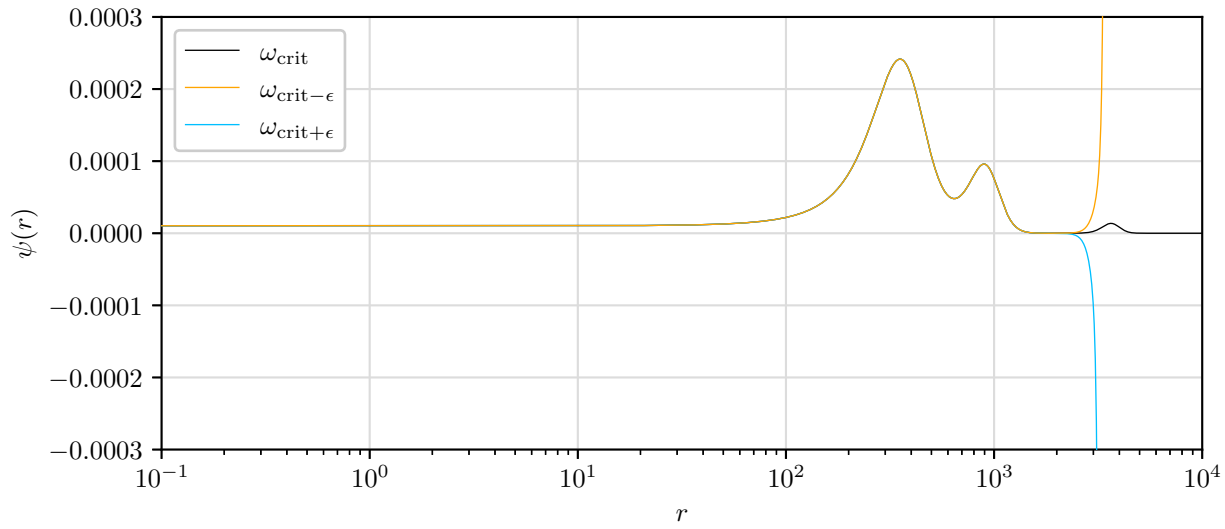

Figure A.1: Profile of the boson star profile for a solution from family b (See Table 3.1). It can be seen that the double precision shooting method ($\epsilon \approx 10^{-16}$) does not localize ω sufficiently to integrate the solution to the asymptotic regime. Here we compare the true solution (black) to the bounding solutions generated via the shooting method and observe that the integration with double precision fails before all relevant features are resolved.

Unfortunately, computations that use extended precision libraries are extremely slow compared to hardware implemented single or double precision operations and performing all operations to accuracy better than 10^{-150} while maintaining an overall integration error of $\epsilon \approx 10^{-12}$ seems wasteful (particularly when the required precision is not known ahead of time and may possibly require accuracy well beyond 10^{-150}). For this particular class of problem it turns out that it is possible to do better.

Using quad precision (16-byte floating point), it is possible to integrate the equations and find ω to a precision of about 10^{-34}. Maintaining an absolute error $\epsilon \approx 10^{-16}$ and relative error of at least $\epsilon \approx 10^{-12}$, we find the radial location, $r_{\rm max}$ where the high and low bounding solutions differ by some value greater than this tolerance (typically 10^{-12} for absolute error and 10^{-8} for relative error) and stop the integration at this point.

We then initialize a new shooting problem at $r = r_{\rm max}$ with the initial conditions being the result of the previous integration and once again integrate outwards, shooting for ω. This process is repeated until the boson star profile is in the asymptotic regime. The overall process is summarized in the algorithm below,

We typically perform about 7 of these iterations (the equivalent of about 200 digits precision in ω, allowing us to integrate out about 7 times as far as quad precision), at which point it is found that the final value of ω differs from the first by about 10^{-10}. This is acceptable considering our desired accuracy. In practice we have found this method to be tens of times faster than integrating with extended precision libraries while having the benefit that we do not have to know the required precision for a given problem in advance.

Algorithm 6 Multiple Precision Shooting Method

hold $\phi(x)$ fixed
initialize $\psi(0)$
while not in asymptotic regime **do**
    set bounding values of ω, ω_{high} and ω_{low}
    set $\omega = \frac{1}{2}(\omega_{\text{high}} + \omega_{\text{low}})$
    perform binary search on ω, integrating
        $\psi(x)$ and metric functions as far as possible
    find r_{max} such that bounding solutions differ by ϵ
    initialize $\psi(r_{\text{max}})$ with bounding solution at r_{max}
end while
integrate metric functions to asymptotic regime

A.4 Generalization to Arbitrary Shooting Problems

This technique works well beyond what is described here and can be easily applied to any problem in which the solution diverges in a predictable manner. Simply put, if we have a true solution, $\phi_0(x)$, a parameter on which the shooting is applied, γ, and the error between the true solution and numerical solution $\phi(x)$ grows faster than $(\gamma - \gamma_0)\, x^n, n > 1$, it will always be possible to find a region in which $\phi(x) - \phi_0(x)$ is small but large compared to $\gamma - \gamma_0$. We can then re-initialise the shooting at this point while introducing errors well below the desired tolerances. Effectively, we are adding a perturbative error to "kick" the numerical solution back towards the critical solution.

Algorithm 7 Generalized Multiple Precision Shooting Method

initialize $\phi(0)$
while not in asymptotic regime **do**
    set bounding values of γ, γ_{high} and γ_{low}
    set $\gamma = \frac{1}{2}(\gamma_{\text{high}} + \gamma_{\text{low}})$
    perform binary search on γ, integrating
        $\phi(x)$ as far as possible
    find x_{max} such that bounding solutions differ by ϵ
    initialize $\phi(x_{max})$ with bounding solution at x_{max}
end while

Note that this method works for problems where we are shooting on the initial value or derivative at $x = 0$ as well. In this case, when we restart the integration, it is restarted with a small perturbation on $\phi(x_0)$ or one of its derivatives and it is the magnitude of this parameter upon which the additional shooting is performed. Additionally, there is no reason why this method should be constrained to the realm of quad precision. Using double precision integration will speed it up astronomically at the cost of lower overall accuracy. If we are using this method to find an initial guess for a generic BVP solver, rather than in a solution in its own right, even single precision integrators maintaining a relative error of $\sim 10^{-3}$ may prove acceptable.

Appendix B

Linear Perturbation Equations for Minimally Coupled d-Stars

B.1 Equations of Motion

We start with the 3+1 equations in polar-areal coordinates and take $T_{\mu\nu}$ to be the combination $T_{\mu\nu} = T^B_{\mu\nu} + T^G_{\mu\nu}$ as defined in (4.4)–(4.5). In this gauge, the evolution of the metric function, a, is governed by

$$\partial_t a = \frac{T_{tr} a r}{2}, \tag{B.1}$$

the Hamiltonian constraint is

$$\frac{2r\partial_r a}{a} = 1 - a^2 + \frac{a^2 r^2 T_{tt}}{\alpha^2}, \tag{B.2}$$

and the slicing condition takes the form

$$2r\partial_r \alpha = \frac{2r\alpha\partial_r a}{a} + \left(\alpha T_{rr} - \frac{a^2 T_{tt}}{\alpha}\right) r^2 + 2\alpha\left(a^2 - 1\right). \tag{B.3}$$

Note that (B.1) is redundant but provides a useful non-trivial consistency test for the system. In both the evolutionary and stationary cases, the Hamiltonian constraint and polar-areal slicing condition may be arranged to give explicit expressions for $\partial_r a$ and $\partial_r \alpha$, respectively. In this form, the Hamiltonian constraint is completely independent of α, and the constraints may be independently integrated. Moreover, since the constraints are first order in r, no boundary value solver is needed.

To simplify the resulting equations, we define the following quantities:

$$\zeta = \frac{1}{1 + \xi_B \phi_R^2 + \xi_B \phi_I^2 + \xi_G \Delta^2 \phi_M^2}, \tag{B.4}$$

$$\Lambda_r = \left(\phi_R \Phi_R + \phi_I \Phi_I\right) \xi_B + \xi_G \Delta^2 \phi_M \Phi_M, \tag{B.5}$$

$$\Lambda_t = \left(\phi_R \Pi_R + \phi_I \Pi_I\right) \xi_B + \xi_G \Delta^2 \phi_M \Pi_M, \tag{B.6}$$

$$\delta = 2 + 2\Lambda_r r \zeta. \tag{B.7}$$

Upon substitution of (B.4)–(B.7) into (B.1)–(B.3), we find the following equations for a and α:

$$\begin{aligned} \partial_t a = {} & \frac{2\xi_G \Delta^2 \zeta r \alpha \left(\phi_M \partial_r \Pi_M + \Pi_M \Phi_M\right)}{\delta} + \frac{2\xi_B \zeta r \alpha \left(\Pi_R \Phi_R + \Pi_I \Phi_I + \phi_R \partial_r \Pi_R + \phi_I \partial_r \Pi_I\right)}{\delta} \\ & - \frac{2\zeta r \alpha \left(\xi_G \Delta^2 \phi_M \Pi_M + \xi_B \left(\phi_R \Pi_R + \phi_I \Pi_I\right)\right) \partial_r a}{\delta a} \\ & + \frac{\zeta r \alpha \left(\Pi_R \Phi_R + \Pi_I \Phi_I + \Delta^2 \Pi_M \Phi_M + \Pi_P \Phi_P\right)}{\delta}, \end{aligned} \tag{B.8}$$

$$\frac{4\partial_r a}{ra^3} = -\frac{2}{r^2} + \frac{2}{r^2a^2} - \Bigg[-2V - \frac{2\Delta^2{\phi_M}^2}{r^2} + \frac{1}{a^2}\Bigg(- \left(\Phi_R^2 + \Phi_I^2 + \Pi_R^2 + \Pi_I^2 + \Phi_P^2 + \Pi_P^2 \right. \\ \left. + \Delta^2\left[\Phi_M^2 + \Pi_M^2\right]\right) - 4\left(\phi_R\partial_r\Phi_R + \phi_I\partial_r\Phi_I + \Phi_R^2 + \Phi_I^2\right)\xi_B - 4\left(\phi_M\partial_r\Phi_M + \Phi_M^2\right)\Delta^2\xi_G \\ - \frac{8\Lambda_r}{r} + \frac{4\Lambda_t\partial_t a}{\alpha} + \frac{4\Lambda_r\partial_r a}{a^3}\Bigg)\Bigg]\zeta, \tag{B.9}$$

$$\frac{\partial_r\alpha}{a^2r} = \frac{\alpha\partial_r a}{a^3r} + \frac{\alpha}{r^2} - \frac{\alpha}{a^2r^2} + \Bigg[- \alpha V - \frac{\alpha\Delta^2\phi_M^2}{r^2} + \frac{\left(\phi_R\partial_t\Pi_R + \phi_I\partial_t\Pi_I\right)\xi_B + \Delta^2\xi_G\phi_M\partial_t\Pi_M}{a} \\ + \frac{\alpha\xi_B\left(-\phi_R\partial_r\Phi_R + \Pi_R^2 - \Phi_R^2\right)}{a^2} + \frac{\alpha\xi_B\left(-\phi_I\partial_r\Phi_I + \Pi_I^2 - \Phi_I^2\right)}{a^2} \\ + \frac{\alpha\xi_G\Delta^2\left(-\phi_M\partial_r\Phi_M + \Pi_M^2 - \Phi_M^2\right)}{a^2} - \frac{4\Lambda_r\alpha}{a^2r} - \frac{\Lambda_r}{a}\partial_r\left(\frac{\alpha}{a}\right)\Bigg]\zeta. \tag{B.10}$$

B.2 Linear Perturbation Theory Equations

Following the decomposition of Section 4.6, we write the boson star field, Ψ, as

$$\Psi = e^{-i\omega t}\left(\psi_R + i\psi_I\right) = \phi_R + i\phi_I, \tag{B.11}$$

$$\phi_R(r,t) = \cos\left(\omega t\right)\psi_R(r,t) + \sin\left(\omega t\right)\psi_I(r,t), \tag{B.12}$$

$$\phi_I(r,t) = \cos\left(\omega t\right)\psi_I(r,t) - \sin\left(\omega t\right)\psi_R(r,t), \tag{B.13}$$

and perturb about the stationary solutions $\mu_0(r)$, $\nu_0(r)$, $\psi_0(r)$ and $\phi_0(r)$:

$$\mu(r,t) = \mu_0(r) + \epsilon\delta\mu(r)e^{i\beta t}, \tag{B.14}$$

$$\nu(r,t) = \nu_0(r) + \epsilon\delta\nu(r)e^{i\beta t}, \tag{B.15}$$

$$\psi_R(r,t) = \psi_0(r) + \epsilon\delta\psi_R(r)e^{i\beta t}, \tag{B.16}$$

$$\psi_I(r,t) = \frac{\epsilon}{i\beta}\delta\psi_I(r)e^{i\beta t}, \tag{B.17}$$

$$\phi_M(r,t) = \phi_0(r) + \epsilon\delta\phi(r)e^{i\beta t}. \tag{B.18}$$

Expanding the equations of motion to first order in ϵ, we find a complicated set of equations for linearized non-minimally coupled perturbations. To reduce the complexity of these equations, we restrict ourselves to the minimally coupled case ($\xi_{\mathrm{B}} = \xi_G = 0$) whereby the stationary solutions satisfy:

$$\partial_r\mu_0 = \Bigg(\Bigg(\frac{\lambda_B\psi_0^4}{4} + \left(\frac{m^2}{2} + \frac{\omega^2}{2e^{\nu_0}}\right)\psi_0^2 + \frac{\lambda_G\Delta^4\left(\phi_0^2 - 1\right)^2}{4}\Bigg)e^{\mu_0} + \frac{\Delta^2\left(\partial_r\phi_0\right)^2}{2} \\ + \frac{\left(\partial_r\psi_0\right)^2}{2}\Bigg)r + \frac{1 + \left(\Delta^2\phi_0^2 - 1\right)e^{\mu_0}}{r}, \tag{B.19}$$

$$\partial_r\nu_0 = \Bigg(\Bigg(\frac{-\lambda_B\psi_0^4}{4} - \left(\frac{m^2}{2} - \frac{\omega^2}{2e^{\nu_0}}\right)\psi_0^2 - \frac{\lambda_G\Delta^4\left(\phi_0^2 - 1\right)^2}{4}\Bigg)e^{\mu_0} + \frac{\Delta^2\left(\partial_r\phi_0\right)^2}{2} \\ + \frac{\left(\partial_r\psi_0\right)^2}{2}\Bigg)r - \frac{1 + \left(\Delta^2\phi_0^2 - 1\right)e^{\mu_0}}{r}, \tag{B.20}$$

$$\partial_r^2\psi_0 = \left(\lambda_B\psi_0^3 + \left(m^2 - \frac{\omega^2}{e^{\nu_0}}\right)\psi_0\right)e^{\mu_0} + \left(\frac{\partial_r\mu_0}{2} - \frac{\partial_r\nu_0}{2} - \frac{2}{r}\right)\partial_r\psi_0, \tag{B.21}$$

$$\partial_r^2\phi_0 = \lambda_G\Delta^2\left(\phi_0^3 - \phi_0\right)e^{\mu_0} + \frac{2\phi_0 e^{\mu_0}}{r^2} + \left(\frac{\partial_r\mu_0}{2} - \frac{\partial_r\nu_0}{2} - \frac{2}{r}\right)\partial_r\phi_0, \tag{B.22}$$

and the equations for the perturbed quantities reduce to the following:

$$\partial_r\delta N = r^2 e^{\frac{1}{2}(\mu_0-\nu_0)}\left(\frac{(\delta\mu - \delta\nu)\,\omega\psi_0^2}{4} + \left(\omega\delta\psi_R - \frac{\delta\psi_I}{2}\right)\psi_0\right). \tag{B.23}$$

$$\begin{aligned}\partial_r\delta\mu = \Bigg(\Bigg(\lambda_G\Delta^4\left(\phi_0^3 - \phi_0\right) + \frac{2\Delta^2\phi_0}{r^2}\Bigg)\delta\phi + \Bigg(\frac{\lambda_B\psi_0^4}{4} + \left(\frac{m^2}{2} + \frac{\omega^2}{2e^{\nu_0}}\right)\psi_0^2 + \frac{\Delta^2\phi_0^2 - 1}{r^2} \\ + \frac{\lambda_G\Delta^4\left(\phi_0^2-1\right)^2}{4}\Bigg)\delta\mu + \lambda_B\psi_0^3\delta\psi_R - \frac{\omega^2\psi_0^2\delta\nu}{2e^{\nu_0}} + \Bigg(\left(m^2 + \frac{\omega^2}{e^{\nu_0}}\right)\delta\psi_R \\ - \frac{\omega\delta\psi_I}{e^{\nu_0}}\Bigg)\psi_0\Bigg)e^{\mu_0}r + r\Delta^2\left(\partial_r\phi_0\right)\left(\partial_r\delta\phi\right) + r\left(\partial_r\psi_0\right)\left(\partial_r\delta\psi_R\right),\end{aligned} \tag{B.24}$$

$$\begin{aligned}\partial_r\delta\nu = \Bigg(\Bigg(2\lambda_G\Delta^4\left(\phi_0 - \phi_0^3\right) - \frac{4\Delta^2\phi_0}{r^2}\Bigg)\delta\phi - \frac{1}{2}\Bigg(\lambda_G\Delta^4\left(\phi_0^2-1\right)^2 + \frac{4\left(\Delta^2\phi_0^2 - 1\right)}{r^2} \\ + 2m^2\psi_0^2 + \lambda_B\psi_0^4\Bigg)\delta\mu - 2\left(\lambda_B\psi_0^3 + m^2\psi_0\right)\delta\psi_R\Bigg)e^{\mu_0}r + \partial_r\delta\mu,\end{aligned} \tag{B.25}$$

$$\begin{aligned}\partial_r^2\delta\psi_R = \frac{1}{2}\left(\partial_r\mu_0 - \partial_r\nu_0 - \frac{4}{r}\right)\partial_r\delta\psi_R + \frac{\left(\partial_r\delta\mu - \partial_r\delta\nu\right)\partial_r\psi_0}{2} + \Bigg(\frac{\left(\delta\nu - \delta\mu\right)\omega^2\psi_0}{e^{\nu_0}} \\ + \left(m^2 + 3\lambda_B\psi_0^2\right)\delta\psi_R + \left(m^2\psi_0 + \lambda_B\psi_0^3\right)\delta\mu + \frac{2\omega\delta\psi_I - \left(\omega^2 + \beta^2\right)\delta\psi_R}{e^{\nu_0}}\Bigg)e^{\mu_0},\end{aligned} \tag{B.26}$$

$$\begin{aligned}\partial_r^2\delta\psi_I = \frac{1}{2}\left(\partial_r\mu_0 - \partial_r\nu_0 - \frac{4}{r}\right)\partial_r\delta\psi_I + \Bigg(\Bigg(m^2 + \lambda_B\psi_0^2 - \frac{\left(\omega^2+\beta^2\right)}{e^{\nu_0}}\Bigg)\delta\psi_I \\ + \frac{\omega\beta^2\left(\delta\mu - \delta\nu\right)\psi_0}{2e^{\nu_0}} + \frac{2\omega\beta^2\delta\psi_R}{e^{\nu_0}}\Bigg)e^{\mu_0},\end{aligned} \tag{B.27}$$

$$\begin{aligned}\partial_r^2\delta\phi = \frac{1}{2}\left(\partial_r\mu_0 - \partial_r\nu_0 - \frac{4}{r}\right)\partial_r\delta\phi + \Bigg(\Bigg(\lambda_G\Delta^2\left(3\phi_0^2 - 1\right) + \frac{2}{r^2}\Bigg)\delta\phi \\ + \left(\lambda_G\Delta^2\left(\phi_0^3 - \phi_0\right) + \frac{2\phi_0}{r^2}\right)\delta\mu - \frac{\beta^2\delta\phi}{e^{\nu_0}}\Bigg)e^{\mu_0} + \frac{\left(\partial_r\mu_1 - \partial_r\nu_1\right)\partial_r\phi_0}{2},\end{aligned} \tag{B.28}$$

Given that the deviations from the stationary solutions given by (B.23–B.28) involve perturbations of three dynamic fields (with the metric perturbations having no dynamic freedom of their own), it is not immediately obvious that the perturbations should be purely exponential or oscillatory in time. For example, one could imagine perturbations involving under or over damped oscillations corresponding to complex β^2. Here, we follow the work of Jetzer [65], and demonstrate that a set of equations equivalent to (B.23–B.28) may be written in the following form,

$$\mathrm{L}_{ij}\mathbf{f}_j = -\beta^2 e^{\mu_0-\nu_0}\mathrm{G}_{ij}\mathbf{f}_j, \tag{B.29}$$

where L_{ij} is a Hermitian differential operator, $\mathbf{f_j}$ is the solution vector and G_{ij} is a diagonal matrix. It then follows that the eigenvalues of the above pulsation equation (for β^2) are purely real. As before we expand our fields about the stationary solutions, but do not yet enforce exponential time

dependence:

$$\mu(t,r) = \mu_0(r) + \epsilon\delta\mu(t,r), \tag{B.30}$$
$$\nu(t,r) = \nu_0(r) + \epsilon\delta\nu(t,r), \tag{B.31}$$
$$\psi_R(t,r) = \psi_0(r) + \epsilon\delta\psi_R(t,r), \tag{B.32}$$
$$\psi_I(t,r) = \epsilon\psi_0(r)\delta\psi_I(t,r), \tag{B.33}$$
$$\phi(t,r) = \phi_0(r) + \epsilon\delta\phi(t,r). \tag{B.34}$$

Substituting these expressions into the equations of motion for the fields and metric and truncating to linear order in the perturbation, we find a coupled system of perturbation equations. In particular, the equation $G_{rt} = T_{rt}$ produces the following simple expression for $\delta\mu$:

$$\partial_t\delta\mu = r\left(\Delta^2\left(\partial_t\delta\phi\right)\left(\partial_r\phi_0\right) - \left(\partial_r\delta\psi_I\right)\psi_0^2\omega + \left(\partial_r\psi_0\right)\left(\partial_t\psi_R\right)\right). \tag{B.35}$$

With the substitution

$$\delta\psi_I = \partial_t\delta\tilde{\psi}_I, \tag{B.36}$$

(B.35) becomes a total derivative with respect to time and may be integrated to give,

$$\delta\mu = r\left(\Delta^2\left(\delta\phi\right)\left(\partial_r\phi_0\right) + \left(\delta\psi_R\right)\left(\partial_r\psi_0\right) - \left(\omega\psi_0^2\right)\partial_r\delta\tilde{\psi}_I\right). \tag{B.37}$$

We may also obtain an expression for $\delta\nu$ by solving the perturbed $G_{tt} = T_{tt}$ equation for $\delta\nu$ and substituting the relevant expressions for $\delta\psi_I$, $\delta\mu$, $\partial_r^2\psi_0$, $\partial_r^2\phi_0$, $\partial_r\mu_0$, and $\partial_r\nu_0$:

$$\begin{aligned}\delta\nu = &-\frac{re^{\nu_0}\lambda_G\Delta^4\left(\phi_0^2-1\right)^2\partial_r\delta\tilde{\psi}_I}{2\omega} - \frac{2\partial_t^2\delta\tilde{\psi}_I}{\omega} + \Delta^2\left(\delta\phi\left(\partial_r\phi_0\right)r - \frac{2\phi_0^2e^{\nu_0}\left(\partial_r\delta\tilde{\psi}_I\right)}{r\omega}\right) \\ &+ e^{\nu_0}\left(\frac{2}{r\omega} - \frac{\left(\lambda_B\psi_0^4 + 2m^2\psi_0^2\right)r}{2\omega}\right)\partial_r\delta\tilde{\psi}_I - r\omega\psi_0^2\left(\partial_r\delta\tilde{\psi}_I\right) + \left(r\partial_r\psi_0 + \frac{4}{\psi_0}\right)\delta\psi_R \\ &+ 2\left(\left(\frac{2\partial_r\psi_0}{\psi_0} + \frac{1}{r}\right)\partial_r\delta\tilde{\psi}_I + \partial_r^2\delta\tilde{\psi}_I\right)\frac{e^{\nu_0}}{\omega e^{\mu_0}}.\end{aligned} \tag{B.38}$$

With the perturbed metric functions now defined solely in terms of the stationary solution and perturbed matter fields, we find expressions for $\partial_r^2\delta\psi_R$, $\partial_r^3\delta\tilde{\psi}_I$ and $\partial_r^2\delta\phi$ through substitution. At this stage, the perturbation equations consist of three second order expression in $\mathbf{f}_j = (\delta\psi_R, \partial_r\delta\tilde{\psi}_I, \delta\phi)$ with all time derivatives appearing as second order expressions. Substituting:

$$\delta\tilde{\psi}_I(r,t) = \delta\tilde{\psi}_I(r)e^{i\beta t}, \tag{B.39}$$
$$\delta\psi_R(r,t) = \delta\psi_R(r)e^{i\beta t}, \tag{B.40}$$
$$\delta\phi(r,t) = \delta\phi(r)e^{i\beta t}, \tag{B.41}$$

we may write our coupled perturbation expressions as,

$$\tilde{\mathrm{L}}_{ij}\mathbf{f}_j = -\beta^2e^{\mu_0-\nu_0}\mathbf{f}_j, \tag{B.42}$$

where $\tilde{\mathrm{L}}_{ij}$ is a second order, non-Hermitian operator of the following form:

$$\begin{bmatrix} \frac{\partial^2}{\partial r^2} + a_1\frac{\partial}{\partial r} + b_1 & c_1\frac{\partial}{\partial r} + d_1 & e_1 \\ c_2\frac{\partial}{\partial r} + d_2 & \frac{\partial^2}{\partial r^2} + a_2\frac{\partial}{\partial r} + b_2 & h_2 \\ e_3 & h_3 & \frac{\partial^2}{\partial r^2} + a_3\frac{\partial}{\partial r} + b_3 \end{bmatrix}. \tag{B.43}$$

Here, all subscripted quantities should be understood to be functions of r. The goal is now to find a diagonal matrix, M_{ij}, such that $\mathrm{L}_{ij} = \mathrm{M}_{ik}\tilde{\mathrm{L}}_{kj}$ is a Hermitian operator of the form

$$\begin{bmatrix} \frac{\partial}{\partial r}M_1\frac{\partial}{\partial r} + B_1 & -\frac{\partial}{\partial r}C_1 + D_1 & E_1 \\ C_1\frac{\partial}{\partial r} + D_1 & \frac{\partial}{\partial r}M_2\frac{\partial}{\partial r} + B_2 & H_1 \\ E_1 & H_1 & \frac{\partial}{\partial r}M_3\frac{\partial}{\partial r} + B_3 \end{bmatrix}, \tag{B.44}$$

and

$$\mathrm{M}_{ij} = \begin{bmatrix} M_1 & 0 & 0 \\ 0 & M_2 & 0 \\ 0 & 0 & M_3 \end{bmatrix}. \tag{B.45}$$

Fortunately, this turns out to be a well defined problem and the M_i's and C_1 take the form:

$$M_1 = r^2 e^{\frac{1}{2}(\nu_0 - \mu_0)}, \tag{B.46}$$

$$M_2 = r^2 e^{\frac{3}{2}(\nu_0 - \mu_0)}\psi_0^2, \tag{B.47}$$

$$M_3 = r^2\Delta^2 e^{\frac{1}{2}(\nu_0 - \mu_0)}, \tag{B.48}$$

$$C_1 = 2\omega r^2 \psi_0 e^{\frac{1}{2}(\nu_0 - \mu_0)}, \tag{B.49}$$

while the remaining terms are sufficiently cumbersome that it is not particularly enlightening to write them out explicitly. One could, of course, use the equations just derived to solve the perturbation problem rather than (B.23–B.28). Unfortunately, as is often the case with such matters, by the time we verified that the equations permitted only real eigenvalues, the previous formalism had already been adopted and investigated. Due to the significant reduction in complexity these equations represent, we would highly recommend future work to follow this approach rather than the more direct method we adopted.

Appendix C

Derivation of the GBSSN Formulation

Heuristically speaking, BSSN type formulations are particularly useful as they re-express the ADM equations in strongly hyperbolic forms conducive to stable numerical evolution. The original BSSN reformulation of the Einstein equations is accomplished by factoring out a scale factor, χ, from the 3-metric, decomposing the extrinsic curvature into trace and trace-free components and promoting the contracted Christoffel symbols to evolutionary variables. As tensor equations, the form of the ADM equations is invariant under a coordinate change. However, in their standard form, the BSSN equations are derived on a flat cartesian background which simplifies the derivation but breaks the explicit covariance of the ADM equations. We note that the Bona–Masso [27–31] and NOR formulations of Nagy et. al [90] achieve hyperbolicity in a similar manner. However, neither of these approaches adopts a conformal decomposition.

GBSSN (Generalized BSSN), differs from the standard form of the BSSN equations through the introduction of an arbitrary (but typically flat) background metric [9, 37]. This permits us to write evolution equations for the difference between the two sets of contracted Christoffel symbols (a tensorial quantity). In doing so, we maintain explicit covariance of the EOM while canceling the divergences in the Christoffel symbols which frequently appear in non-Cartesian coordinate systems.

In this appendix we rederive the GBSSN formulation of Brown [9, 37]. This rederivation was done in part to verify the EOM, but primarily as practice in preparation for the derivation of our RCCZ4 formulation detailed in App. E.

C.1 Conventions

The GBSSN formulation of Brown [9, 37] starts by foliating 4D spacetime into a sequence of spacelike hypersurfaces, Σ_t, with each hypersurface having a 3-metric γ_{ij}. The standard ADM equations decompose the 4-metric as

$$ds^2 = -\alpha^2 dt^2 + \gamma_{ij}\left(dx^i + \beta^i dt\right)\left(dx^j + \beta^j dt\right). \tag{C.1}$$

Explicitly, the 4-metric and its inverse are

$$g_{\mu\nu} = \begin{pmatrix} g_{00} & g_{0j} \\ g_{i0} & g_{ij} \end{pmatrix} = \begin{pmatrix} -\alpha^2 + \beta^k\beta_k & \beta_j \\ \beta_i & \gamma_{ij} \end{pmatrix}, \tag{C.2}$$

$$g^{\mu\nu} = \begin{pmatrix} g^{00} & g^{0j} \\ g^{i0} & g^{ij} \end{pmatrix} = \begin{pmatrix} -\frac{1}{\alpha^2} & \frac{\beta^j}{\alpha^2} \\ \frac{\beta^i}{\alpha^2} & \gamma^{ij} - \frac{\beta^i\beta^j}{\alpha^2} \end{pmatrix}, \tag{C.3}$$

while the unit normal to the foliation, n^μ, and projection tensor, $\gamma^\mu{}_\nu$, may be written as:

$$n_\mu = (-\alpha, 0_i), \tag{C.4}$$

$$n^\mu = \left(\frac{1}{\alpha}, -\frac{\beta^i}{\alpha}\right), \tag{C.5}$$

$$\gamma^{\mu}{}_{\nu} = g^{\mu}{}_{\nu} + n^{\mu}n_{\nu}, \tag{C.6}$$

$$\gamma_{\mu\nu} = \begin{pmatrix} \beta^k\beta_k & \beta_j \\ \beta_i & \gamma_{ij} \end{pmatrix}, \tag{C.7}$$

with α the lapse and β^i the shift. Adopting the convention that $\mathcal{L}_m$ is the Lie derivative along αn^{μ}:

$$\mathcal{L}_m = \partial_t - \mathcal{L}_\beta, \tag{C.8}$$

the ADM equations of motion are:

$$\mathcal{L}_m\gamma_{ij} = -2\alpha K_{ij}, \tag{C.9}$$

$$\mathcal{L}_m K_{ij} = -D_iD_j\alpha + \alpha\left(R_{ij} + KK_{ij} - 2K_{ik}K^k{}_j\right) + 4\pi\alpha\left(\gamma_{ij}\left(S-\rho\right) - 2S_{ij}\right), \tag{C.10}$$

and the Hamiltonian and Momentum constraints are, respectively:

$$H = \frac{1}{2}\left(R + K^2 - K_{ij}K^{ij}\right) - 8\pi\rho = 0, \tag{C.11}$$

$$M^i = D_jK^{ij} - \gamma^{ij}D_jK - 8\pi j^i = 0. \tag{C.12}$$

In the above equations, the extrinsic curvature, K_{ij}, and 3D Ricci tensor, R_{ij}, are:

$$K_{ij} = -\frac{1}{2\alpha}\left(\partial_t\gamma_{ij} - \mathcal{L}_\beta\gamma_{ij}\right), \tag{C.13}$$

$$R_{ij} = 2\Gamma^k{}_{i[j,k]} + 2\Gamma^k{}_{l[k}\Gamma^l{}_{j]i}, \tag{C.14}$$

and the spatial stress tensor, S_{ij}, stress, S, momentum density, j^i and energy density, ρ, take their usual forms:

$$S_{ij} = \gamma^{\alpha}{}_i\gamma^{\beta}{}_jT_{\alpha\beta}, \tag{C.15}$$

$$S = \gamma^{ij}S_{ij}, \tag{C.16}$$

$$j^i = -\gamma^{ij}\gamma^{\mu}{}_jn^{\nu}T_{\mu\nu}, \tag{C.17}$$

$$\rho = n^{\mu}n^{\nu}T_{\mu\nu}. \tag{C.18}$$

In all of the equations above, we have denoted the connection of the induced 3-metric as D while the connection of the 4-metric is ∇. Specific connections are denoted with accents. In particular, $\hat{D}$, $\mathring{D}$ and $\widetilde{D}$ are connections with respect to conformal, flat and placeholder 3-metrics[6]. In what follows, we make extensive use of the following relation between the D and the ∇ connections

$$D_\gamma T^{\alpha_1\cdots\alpha_p}{}_{\beta_1\cdots\beta_q} = \gamma^{\alpha_1}{}_{\mu_1}\cdots\gamma^{\alpha_p}{}_{\mu_p}\gamma^{\nu_1}{}_{\beta_1}\cdots\gamma^{\nu_q}{}_{\beta_q}\gamma^{\delta}{}_{\gamma}\nabla_\delta T^{\mu_1\cdots\mu_p}{}_{\nu_1\cdots\nu_q}, \tag{C.19}$$

where $T^{\mu_1\cdots\mu_p}{}_{\nu_1\cdots\nu_q}$ is an arbitrary tensor in Σ. We also make extensive use of the following relationships linking two connections on the same manifold:

$$C^{\gamma}{}_{\alpha\beta} = \Gamma^{\gamma}{}_{\alpha\beta} - \widetilde{\Gamma}^{\gamma}{}_{\alpha\beta}, \tag{C.20}$$

$$\nabla_\gamma T^{\alpha_1\cdots\alpha_n}{}_{\beta_1\cdots\beta_m} = \widetilde{\nabla}_\gamma T^{\alpha_1\cdots\alpha_n}{}_{\beta_1\cdots\beta_m} + \sum_{r=1}^{n} C^{\alpha_r}{}_{\gamma\delta}T^{\alpha_1\cdots\delta\cdots\alpha_n}{}_{\beta_1\cdots\beta_m} \tag{C.21}$$

$$- \sum_{r=1}^{m} C^{\delta}{}_{\gamma\beta_r}T^{\alpha_1\cdots\alpha_n}{}_{\beta_1\cdots\delta\cdots\beta_n}.$$

[6]In Chapter 5 we use $\widetilde{D}$ to denote the conformal connection instead of $\hat{D}$. In these sections, hats are reserved to denote the frequency space representations of various quantities.

C.2 Derivation Overview

We begin by defining the conformal 3-metric, $\hat{\gamma}_{ij}$, and conformal factor, χ, as

$$\hat{\gamma}_{ij} = e^{-4\chi}\gamma_{ij}, \tag{C.22}$$

with an associated trace, $\hat{\gamma}$, given by

$$\hat{\gamma} = e^{-12\chi}\gamma. \tag{C.23}$$

In the original BSSN system, the conformal metric is taken to have unit determinant. However, as χ encodes an arbitrary rescaling of the 3-metric, we are free to choose an evolution equation for $\hat{\gamma}$. Of all the possible choices, there are two particularly natural ones:

$$\partial_t \hat{\gamma} = 0, \tag{C.24}$$

$$\partial_t \hat{\gamma} - \mathcal{L}_\beta \hat{\gamma} = 0. \tag{C.25}$$

The first of these, (C.24), is designated the "Lagrangian" choice as it follows (and is adapted to) the coordinates, while the second, (C.25), is referred to as the "Eulerian" choice. As the Eulerian choice does not lead to a reduction to the standard BSSN equations in Cartesian coordinates, we stick to the Lagrangian choice for the remainder of the derivation. Note that since $\hat{\gamma}$ is not a true scalar, but rather a scalar density of weight 2, its Lie derivative is

$$\mathcal{L}_\beta \hat{\gamma} = \beta^i \partial_i \hat{\gamma} + 2\hat{\gamma}\partial_i \beta^i, \tag{C.26}$$

where we have used

$$\mathcal{L}_\beta \left(f\gamma^{n/2} \right) = \gamma^{n/2}\beta^i \partial_i f + f\beta^i \partial_i \gamma^{n/2} + n\gamma^{n/2}\partial_i \beta^i. \tag{C.27}$$

Now, from the definition of $\hat{\gamma}$, we have

$$\chi = \frac{1}{12} \ln \left(\frac{\gamma}{\hat{\gamma}} \right), \tag{C.28}$$

and using Eqns. (C.28) and (C.9) we find:

$$\partial_t \chi = \frac{1}{12} \left(\frac{\partial_t \gamma}{\gamma} - \frac{\partial_t \hat{\gamma}}{\hat{\gamma}} \right), \tag{C.29}$$

$$\mathcal{L}_m \chi = -\frac{1}{6}\alpha K + \frac{1}{6}\hat{D}_m \beta^m. \tag{C.30}$$

Next, we define the trace-free extrinsic curvature, $\hat{A}_{ij}$

$$\hat{A}_{ij} = e^{-4\chi} \left(K_{ij} - \frac{1}{3}\gamma_{ij} K \right), \tag{C.31}$$

as well as the contracted Christoffel symbols, $\hat{\Gamma}^i$, and the dynamic variables $\hat{\Delta}^i$ (sometimes referred to as the conformal connection functions in analogy with BSSN):

$$\hat{\Gamma}^i = \hat{\Gamma}^i{}_{jk}\hat{\gamma}^{jk}, \tag{C.32}$$

$$\hat{\Delta}^i{}_{ij} = \hat{\Gamma}^i{}_{jk} - \mathring{\Gamma}^i_{jk}, \tag{C.33}$$

$$\hat{\Delta}^i = \hat{\Gamma}^i - \mathring{\Gamma}^i{}_{jk}\hat{\gamma}^{jk}. \tag{C.34}$$

Although neither $\hat{\Gamma}^i{}_{jk}$ or $\mathring{\Gamma}^i{}_{jk}$ are tensors, the difference between the two, $\hat{\Delta}^i{}_{ij}$, is a proper tensor. This fact may be verified by considering the action of an arbitrary coordinate transformation on the difference. As such, $\hat{\Delta}^i$, is a true vector and an evolution equation for the quantity may be written in fully covariant form. After a significant amount of manipulation, the EOM take the final form:

$$\mathcal{L}_m\chi = -\frac{1}{6}\alpha K + \frac{1}{6}\hat{D}_m\beta^m, \tag{C.35}$$

$$\mathcal{L}_m\hat{\gamma}_{ij} = -2\alpha\hat{A}_{ij} - \frac{2}{3}\hat{\gamma}_{ij}\hat{D}_m\beta^m, \tag{C.36}$$

$$\mathcal{L}_m\hat{A}_{ij} = e^{-4\chi}\left[-D_iD_j\alpha + \alpha R_{ij} - 8\pi\alpha S_{ij}\right]^{\mathrm{TF}} - \frac{2}{3}\hat{A}_{ij}\hat{D}_m\beta^m + \alpha\left(K\hat{A}_{ij} - 2\hat{A}_{ik}\hat{A}^k{}_j\right), \tag{C.37}$$

$$\mathcal{L}_mK = -D^2\alpha + \alpha\left(\hat{A}_{ij}\hat{A}^{ij} + \frac{1}{3}K^2\right) + 4\pi\alpha\left(\rho + S\right), \tag{C.38}$$

$$\mathcal{L}_m\hat{\Delta}^i = \hat{\gamma}^{mn}\mathring{D}_m\mathring{D}_n\beta^i - 2\hat{D}_m\left(\alpha\hat{A}^{im}\right) + 2\alpha\hat{A}^{mn}\hat{\Delta}^i{}_{mn} + \frac{1}{3}\left[\hat{D}^i\left(\hat{D}_n\beta^i\right) + 2\hat{\Delta}^i\hat{D}_n\beta^n\right], \tag{C.39}$$

while the Hamiltonian and momentum constraints become:

$$H = \frac{1}{2}\left(R + \frac{2}{3}K^2 - \hat{A}_{ij}\hat{A}^{ij}\right) - 8\pi\rho = 0, \tag{C.40}$$

$$M^i = e^{-4\chi}\left(\hat{D}_j\hat{A}^{ij} - \frac{2}{3}\hat{\gamma}^{ij}\hat{D}_jK + 6\hat{A}^{ij}\hat{D}_j\chi - 8\pi\hat{j}^i\right) = 0. \tag{C.41}$$

In the above equations, all "hatted" quantities are raised and lowered with the conformal metric. "TF" denotes "trace free" with respect to the 3-metric γ_{ij} and not $\hat{\gamma}_{ij}$. Finally, the Ricci tensor may be split into scale-factor and conformal components as:

$$R_{ij} = \hat{R}_{ij} + R^{\chi}_{ij}, \tag{C.42}$$

$$\hat{R}_{ij} = -\frac{1}{2}\hat{\gamma}^{mn}\mathring{D}_m\mathring{D}_n\hat{\gamma}_{ij} + \hat{\gamma}_{m(i}\mathring{D}_{j)}\hat{\Delta}^m + \hat{\Delta}^m\hat{\Delta}_{(ij)m} + 2\hat{\Delta}^{mn}{}_{(i}\hat{\Delta}_{j)mn} + \hat{\Delta}^{mn}{}_i\hat{\Delta}_{mnj}, \tag{C.43}$$

$$R^{\chi}_{ij} = -2\hat{D}_i\hat{D}_j\chi - 2\hat{\gamma}_{ij}\hat{D}^k\hat{D}_k\chi + 4\hat{D}_i\chi\hat{D}_j\chi - 4\hat{\gamma}_{ij}\hat{D}^k\chi\hat{D}_k\chi. \tag{C.44}$$

It transpires that, with the evolution equation given for $\hat{\Delta}^i$ above, the GBSSN formulation is only weakly hyperbolic. By rearranging the momentum constraint (C.41) into an expression for $\hat{D}_j\hat{A}^{ij}$

$$\hat{D}_j\hat{A}^{ij} = \frac{2}{3}\hat{\gamma}^{ij}\hat{D}_jK - 6\hat{A}^{ij}\hat{D}_j\chi + 8\pi\hat{j}^i, \tag{C.45}$$

and substituting this into (C.39), the evolution equation for $\hat{\Delta}^i$, we recover a strongly hyperbolic formulation:

$$\begin{aligned}\mathcal{L}_m\hat{\Delta}^i = {}& \hat{\gamma}^{mn}\mathring{D}_m\mathring{D}_n\beta^i - 2\hat{A}^{im}\hat{D}_m\alpha + 2\alpha\hat{A}^{mn}\hat{\Delta}^i{}_{mn} + \frac{1}{3}\left[\hat{D}^i\left(\hat{D}_n\beta^n\right) + 2\hat{\Delta}^i\hat{D}_n\beta^n\right] \\ & + 2\alpha\left(6\hat{A}^{ij}\hat{D}_j\chi - \frac{2}{3}\hat{\gamma}^{ij}\hat{D}_jK - 8\pi\hat{j}^i\right).\end{aligned} \tag{C.46}$$

C.3 Hamiltonian and Momentum Constraints

Substituting the GBSSN variables into (C.40), the definition of the Hamiltonian constraint, we find:

$$H = \frac{1}{2}\left(R + \frac{2}{3}K^2 - \hat{A}_{ij}\hat{A}^{ij}\right) - 8\pi\rho = 0. \tag{C.47}$$

Similarly, (C.41), the momentum constraint, becomes:

$$M^i = e^{-4\chi}\left(\hat{D}_j\hat{A}^{ij} - \frac{2}{3}\hat{\gamma}^{ij}\hat{D}_j K + 6\hat{A}^{ij}\hat{D}_j\chi - 8\pi\hat{j}^i\right) = 0. \tag{C.48}$$

C.4 Evolution of $\hat{\gamma}_{ij}$

Although essentially trivial, we include the following simple derivations for completeness. Starting from the ADM equation for the evolution of the 3-metric

$$\mathcal{L}_m\gamma_{ij} = -2\alpha K_{ij}, \tag{C.49}$$

we substitute the definition of the 3-metric (C.22), in terms of the conformal metric and conformal factor, into (C.49):

$$\begin{aligned}
\mathcal{L}_m\left(\hat{\gamma}_{ij}e^{4\chi}\right) &= -2\alpha K_{ij}, &\text{(C.50)}\\
\mathcal{L}_m\hat{\gamma}_{ij} &= -4\hat{\gamma}_{ij}\mathcal{L}_m\chi - 2\alpha e^{-4\chi}K_{ij}, &\text{(C.51)}\\
&= \hat{\gamma}_{ij}\left(\frac{2}{3}\alpha K - \frac{2}{3}\hat{D}_m\beta^m\right) - 2\alpha e^{-4\chi}K_{ij}.
\end{aligned}$$

Expressing K_{ij} in terms of $\hat{A}_{ij}$, χ and K via (C.31), we find the GBSSN equation for the evolution of $\hat{\gamma}_{ij}$:

$$\mathcal{L}_m\hat{\gamma}_{ij} = -2\alpha\hat{A}_{ij} - \frac{2}{3}\hat{\gamma}_{ij}\hat{D}_m\beta^m.$$

C.5 Evolution of K

Beginning with, (C.10), the ADM equation for the evolution of the extrinsic curvature, we contract with the 3-metric:

$$\begin{aligned}
\mathcal{L}_m K_{ij} &= -D_iD_j\alpha + \alpha\left(R_{ij} + KK_{ij} - 2K_{ik}K^k{}_j\right) + 4\pi\alpha\left[\gamma_{ij}\left(S-\rho\right) - 2S_{ij}\right], &\text{(C.52)}\\
\gamma^{ij}\mathcal{L}_m K_{ij} &= -D_iD^i\alpha + \alpha\left(R + K^2 - 2K_{ij}K^{ij}\right) + 4\pi\alpha\left(S - 3\rho\right). &\text{(C.53)}
\end{aligned}$$

Next, we express the evolution of the extrinsic curvature trace in terms of (C.53) and (C.49):

$$\begin{aligned}
\mathcal{L}_m K &= \mathcal{L}_m\left(\gamma^{ij}K_{ij}\right), &\text{(C.54)}\\
&= \gamma^{ij}\mathcal{L}_m K_{ij} + 2\alpha K_{ij}K^{ij},\\
&= -D^2\alpha + \alpha\left(R + K^2\right) + 4\pi\alpha\left(S - 3\rho\right).
\end{aligned}$$

We rearrange the Hamiltonian constraint, (C.41), as an expression for R and substitute it into (C.54), yielding (C.38), the GBSSN evolution equation for K:

$$\mathcal{L}_m K = -D^2\alpha + \alpha\left(\hat{A}_{ij}\hat{A}^{ij} + \frac{1}{3}K^2\right) + 4\pi\alpha\left(S + \rho\right). \tag{C.55}$$

C.6 Evolution of $\hat{A}_{ij}$

Starting with (C.10), the ADM equation for the evolution of the extrinsic curvature, we re-express the right hand side of the equation in terms of the GBSSN quantities:

$$\begin{aligned}\mathcal{L}_m K_{ij} &= -D_i D_j \alpha + \alpha\left(R_{ij} + K K_{ij} - 2K_{ik}K^k{}_j\right) + 4\pi\alpha\left[\gamma_{ij}\left(S-\rho\right) - 2S_{ij}\right], \\ &= -D_i D_j \alpha + \alpha\left[R_{ij} + K\left(\hat{A}_{ij}e^{4\chi} + \frac{1}{3}\hat{\gamma}_{ij}e^{4\chi}K\right)\right] + 4\pi\alpha\left[\gamma_{ij}\left(S-\rho\right) - 2S_{ij}\right] \\ &\quad - 2\hat{\gamma}^{km}\alpha e^{-4\chi}\left(\hat{A}_{ik}e^{4\chi} + \frac{1}{3}\hat{\gamma}_{ik}e^{4\chi}K\right)\left(\hat{A}_{mj}e^{4\chi} + \frac{1}{3}\hat{\gamma}_{mj}e^{4\chi}K\right), \\ &= -D_i D_j \alpha + \alpha\left[R_{ij} + e^{4\chi}\left(\frac{1}{3}K\hat{A}_{ij} + \frac{1}{9}K^2\hat{\gamma}_{ij} - 2\hat{A}_{ik}\hat{A}^k{}_j\right)\right] + 4\pi\alpha\left[\gamma_{ij}\left(S-\rho\right) - 2S_{ij}\right].\end{aligned} \tag{C.56}$$

Next, we express the left hand side in terms of the GBSSN quantities and substitute the evolution equations for K, χ and $\hat{\gamma}_{ij}$ respectively:

$$\begin{aligned}\mathcal{L}_m K_{ij} &= \mathcal{L}_m\left(\hat{A}_{ij}e^{4\chi} + \frac{1}{3}\hat{\gamma}_{ij}e^{4\chi}K\right), \\ &= e^{4\chi}\left[\mathcal{L}_m\hat{A}_{ij} + \frac{1}{3}\hat{\gamma}_{ij}\mathcal{L}_m K + \frac{1}{3}K\mathcal{L}_m\hat{\gamma}_{ij} + \mathcal{L}_m\chi\left(4\widetilde{A}_{ij} + \frac{4}{3}\hat{\gamma}_{ij}K\right)\right].\end{aligned} \tag{C.57}$$

Combining the above and solving for $\mathcal{L}_m\hat{A}_{ij}$, we find:

$$\begin{aligned}\mathcal{L}_m\hat{A}_{ij} = e^{-4\chi}\Big[&- D_i D_j\alpha + R_{ij} + 4\pi\alpha\left(\gamma_{ij}[S-\rho] - 2S_{ij}\right) \\ &- \frac{1}{3}\gamma_{ij}\left(-D^2\alpha + \alpha\left[\hat{A}_{ij}\hat{A}^{ij} + \frac{1}{3}K^2 + 4\pi\left(S+\rho\right) - K^2\right]\right)\Big] \\ &+ \alpha\left[K\hat{A}_{ij} - 2\hat{A}_{ik}\hat{A}^k{}_j\right] - \frac{2}{3}\hat{A}_{ij}\hat{D}_m\beta^m.\end{aligned} \tag{C.58}$$

Defining the trace free component of a rank 2 tensor B_{ij} as

$$B^{\mathrm{TF}}_{ij} = B_{ij} - \frac{1}{3}\gamma_{ij}B, \tag{C.59}$$

we substitute the Hamiltonian constraint for R to find:

$$R_{ij} = R^{\mathrm{TF}}_{ij} + \frac{1}{3}\gamma_{ij}\left(16\pi\rho - \frac{2}{3}K^2 + \hat{A}_{ij}\hat{A}^{ij}\right). \tag{C.60}$$

Substituting (C.60) into (C.58) and simplifying using the definition of a trace-free rank 2 tensor we arrive at:

$$\mathcal{L}_m\hat{A}_{ij} = e^{-4\chi}\left[-D_iD_j\alpha + \alpha R_{ij} - 8\pi\alpha S_{ij}\right]^{\mathrm{TF}} - \frac{2}{3}\hat{A}_{ij}\hat{D}_m\beta^m + \alpha\left(K\hat{A}_{ij} - 2\hat{A}_{ik}\hat{A}^k{}_j\right). \tag{C.61}$$

C.7 Covariant Decomposition of the Ricci Tensor

In what follows, recall the following identities valid for a general metric $\widetilde{\gamma}_{ij}$:

$$\widetilde{\Gamma}^i{}_{ij} = \frac{1}{2}\partial_j \ln\widetilde{\gamma}, \tag{C.62}$$

$$\widetilde{\Gamma}^i = \frac{-1}{\sqrt{|\widetilde{\gamma}|}}\partial_j\left(\sqrt{|\widetilde{\gamma}|}\widetilde{\gamma}^{ij}\right), \tag{C.63}$$

and the relation linking the covariant derivatives associated with different metrics, derived from the metric compatibility of each connection with its respective metric:

$$\widetilde{D}_i\gamma_{jk} = 2C_{(jk)i}, \tag{C.64}$$

$$\widetilde{D}_i\gamma^{jk} = -2C^{(jk)}{}_i. \tag{C.65}$$

We want to express the Ricci tensor R_{ij} in terms of the Ricci tensor $\widetilde{R}_{ij}$. Working towards this, we start by expressing the difference between the Riemann tensors associated with γ_{ij} and $\widetilde{\gamma}_{ij}$:

$$R^i{}_{jkl} - \widetilde{R}^i{}_{jkl} = 2\partial_{[k}\Gamma^i{}_{l]j} + 2\Gamma^i{}_{m[k}\Gamma^m{}_{l]j} - 2\partial_{[k}\widetilde{\Gamma}^i{}_{l]j} - 2\widetilde{\Gamma}^i{}_{m[k}\widetilde{\Gamma}^m{}_{l]j}. \tag{C.66}$$

Making use of the following identities:

$$\widetilde{\nabla}_{[k}C^i{}_{l]j} = \partial_{[k}C^i{}_{l]j} - \widetilde{\Gamma}^i{}_{m[k}C^m{}_{l]j}, \tag{C.67}$$

$$\begin{aligned} C^i{}_{m[k}C^m{}_{l]j} &= \Gamma^i{}_{m[k}C^m{}_{lj]} - \widetilde{\Gamma}^i{}_{m[k}C^m{}_{lj]}, \\ &= \Gamma^i{}_{m[k}\Gamma^m{}_{lj]} - \widetilde{\Gamma}^i{}_{m[k}\widetilde{\Gamma}^m{}_{lj]}, \end{aligned} \tag{C.68}$$

our expression for the Riemann tensor becomes:

$$R^i{}_{jkl} = \widetilde{R}^i_{jkl} + 2\widetilde{\nabla}_{[k}C^i{}_{l]j} + 2C^i{}_{m[k}C^m{}_{l]j}\,. \tag{C.69}$$

Expanding (C.66), lowering with γ_{ij} and simplifying our expression becomes:

$$R_{ijkl} = \gamma_{in}\widetilde{R}^n{}_{jkl} + \gamma_{in}\left(\widetilde{\nabla}_k C^n{}_{lj} - \widetilde{\nabla}_l C^n{}_{kj}\right) + C_{imk}C^m{}_{lj} - C_{iml}C^m{}_{kj}\,. \tag{C.70}$$

Now, making use of the following expressions:

$$C^i{}_{jk} = \frac{1}{2}\gamma^{im}\left(\widetilde{\nabla}_j\gamma_{km} + \widetilde{\nabla}_k\gamma_{jm} - \widetilde{\nabla}_m\gamma_{jk}\right), \tag{C.71}$$

$$\widetilde{\nabla}_k C^i{}_{lj} = \frac{1}{2}\gamma^{im}\left(\widetilde{\nabla}_k\widetilde{\nabla}_l\gamma_{jm} + \widetilde{\nabla}_k\widetilde{\nabla}_j\gamma_{lm} - \widetilde{\nabla}_k\widetilde{\nabla}_m\gamma_{lj}\right) - 2C^{(im)}{}_k C_{mlj}, \tag{C.72}$$

$$\widetilde{\nabla}_l\widetilde{\nabla}_k\gamma_{ij} - \widetilde{\nabla}_k\widetilde{\nabla}_l\gamma_{ij} = \widetilde{R}^m{}_{ilk}\gamma_{mj} + \widetilde{R}^m{}_{jlk}\gamma_{mi}, \tag{C.73}$$

equation, (C.70), our expression for the Riemann tensor, can be written as:

$$R_{ijkl} = \frac{1}{2}\left(\gamma_{im}\widetilde{R}^m{}_{jkl} - \gamma_{jm}\widetilde{R}^m{}_{ikl} + 2\widetilde{\nabla}_k\widetilde{\nabla}_{[j}\gamma_{i]l} + 2\widetilde{\nabla}_l\widetilde{\nabla}_{[i}\gamma_{j]k}\right) + 2C_{mi[l}C^m{}_{k]j}\,. \tag{C.74}$$

Contracting on the second and fourth indices, we begin the process of finding an expression for the Ricci tensor

$$\begin{aligned} R_{ij} = {} & \frac{1}{2}\left(\gamma^{mn}\gamma_{il}\widetilde{R}^l{}_{mjn} - \widetilde{R}^l{}_{ijl}\right) + \frac{1}{2}\gamma^{mn}\widetilde{\nabla}_j\widetilde{\nabla}_m\gamma_{in} + C_{mni}C^{mn}{}_j - C_{mij}C^m \\ & - \frac{1}{2}\gamma^{mn}\left(\widetilde{\nabla}_n\widetilde{\nabla}_m\gamma_{ij} + \widetilde{\nabla}_j\widetilde{\nabla}_i\gamma_{mn} - \widetilde{\nabla}_m\widetilde{\nabla}_i\gamma_{jn}\right)\,. \end{aligned} \tag{C.75}$$

Making use of the expression for the commutator of covariant derivatives of γ_{ij}, (C.73), this expression simplifies considerably to

$$\begin{aligned} R_{ij} = {} & -\gamma^{mn}\widetilde{R}^k{}_{mn(i}\gamma_{j)k} - \frac{1}{2}\gamma^{mn}\left(\widetilde{\nabla}_m\widetilde{\nabla}_n\gamma_{ij} + \widetilde{\nabla}_i\widetilde{\nabla}_j\gamma_{mn} - \widetilde{\nabla}_i\widetilde{\nabla}_m\gamma_{jn} - \widetilde{\nabla}_j\widetilde{\nabla}_m\gamma_{in}\right) \\ & + C_{mni}C^{mn}{}_j - C_{mij}C^m\,. \end{aligned} \tag{C.76}$$

Finally, using the easily verified identities:

$$\tilde{\nabla}_i C^l{}_{jl} - \tilde{\nabla}_j C^l{}_{il} = 0, \tag{C.77}$$

$$\gamma_{mi}\tilde{\nabla}_j C^m = \tilde{\nabla}_j C_i - C^m C_{mij} - C^m C_{imj}, \tag{C.78}$$

our expression for the Ricci tensor takes the following form:

$$\begin{aligned} R_{ij} &= -\frac{1}{2}\gamma^{mn}\tilde{\nabla}_m\tilde{\nabla}_n\gamma_{ij} + \tilde{\nabla}_{(i}C_{j)} + 2C^{mn}{}_{(i}C_{j)mn} + C_{mni}C^{mn}{}_j \\ &\quad - C_{mij}C^m - \gamma^{mn}\tilde{R}^k{}_{mn(i}\gamma_{j)k}, \\ &= -\frac{1}{2}\gamma^{mn}\tilde{\nabla}_m\tilde{\nabla}_n\gamma_{ij} + \gamma_{m(i}\tilde{\nabla}_{j)}C^m + C^m C_{(ij)m} + 2C^{mn}{}_{(i}C_{j)mn} \\ &\quad + C^{mn}{}_i C_{mnj} - \gamma^{mn}\tilde{R}^k{}_{mn(i}\gamma_{j)k}. \end{aligned} \tag{C.79}$$

C.8 Conformal Covariant Ricci Tensor

We wish to express the 3-Ricci tensor in terms of explicitly covariant components and divide it into a conformal component, $\hat{R}_{ij}$ and scale component R^χ_{ij}. We begin by expressing the Ricci tensor in coordinates adapted to the foliation. For an arbitrary vector v^j, the contraction $R_{ij}v^j$ is given by:

$$\begin{aligned} R_{ij}v^j &= D_j D_i v^j - D_i D_j v^j, \\ &= \hat{R}_{ij}v^j + v^j\hat{D}_k\hat{\Delta}^k{}_{ij} - v^j\hat{D}_i\hat{\Delta}^k{}_{jk} + \hat{\Delta}^l{}_{lk}\hat{\Delta}^k{}_{ij}v^j - \hat{\Delta}^k{}_{li}\hat{\Delta}^l{}_{kj}v^j. \end{aligned} \tag{C.80}$$

Substituting the definition of the conformal metric and simplifying, we find:

$$\hat{\Delta}^k{}_{ij} = 2\left(\delta^k{}_i\hat{D}_j\chi + \delta^k{}_j\hat{D}_i\chi - \hat{\gamma}_{ij}\hat{D}^k\chi\right), \tag{C.81}$$

$$\hat{\Delta}^i{}_{ij} = 6\hat{D}_j\chi, \tag{C.82}$$

$$\hat{D}_i\hat{\Delta}^k{}_{kj} = 6\hat{D}_i\hat{D}_j\chi, \tag{C.83}$$

$$\hat{D}_k\hat{\Delta}^k{}_{ij} = 4\hat{D}_i\hat{D}_j\chi - 2\hat{\gamma}_{ij}\hat{D}^2\chi, \tag{C.84}$$

which allows us to write R_{ij} as:

$$R_{ij} = \hat{R}_{ij} + R^\chi_{ij}, \tag{C.85}$$

$$R^\chi_{ij} = -2\hat{D}_i\hat{D}_j\chi - 2\hat{\gamma}_{ij}\hat{D}_k\hat{D}^k\chi + 4\hat{D}_i\chi\hat{D}_j\chi - 4\hat{\gamma}_{ij}\hat{D}_k\chi\hat{D}^k\chi. \tag{C.86}$$

Finally, we wish to express $\hat{R}_{ij}$ in a concise, explicitly covariant form. After a fair amount of manipulation (as shown in Section C.7), the following covariant expression for the Ricci tensor can be derived:

$$\begin{aligned} \hat{R}_{ij} &= -\frac{1}{2}\gamma^{mn}\mathring{D}_m\mathring{D}_n\hat{\gamma}_{ij} + \hat{\gamma}_{m(i}\mathring{D}_{j)}\hat{\Delta}^m + \hat{\Delta}^m\hat{\Delta}_{(ij)m} + 2\hat{\Delta}^{mn}{}_{(i}\hat{\Delta}_{j)mn} + \hat{\Delta}^{mn}{}_i\hat{\Delta}_{mnj} \\ &\quad - \gamma^{mn}\mathring{R}^k{}_{mn(i}\hat{\gamma}_{j)k}. \end{aligned} \tag{C.87}$$

As our background metric, $\mathring{\gamma}$, is flat, our final expression for the conformal Ricci tensor becomes

$$\hat{R}_{ij} = -\frac{1}{2}\hat{\gamma}^{mn}\mathring{D}_m\mathring{D}_n\hat{\gamma}_{ij} + \hat{\gamma}_{m(i}\mathring{D}_{j)}\hat{\Delta}^m + \hat{\Delta}^m\hat{\Delta}_{(ij)m} + 2\hat{\Delta}^{mn}{}_{(i}\hat{\Delta}_{j)mn} + \hat{\Delta}^{mn}{}_i\hat{\Delta}_{mnj}. \tag{C.88}$$

C.9 Evolution of $\hat{\Delta}^i$

We begin by expressing $\hat{\Delta}^i$ in terms of covariant derivatives on the flat metric:

$$\begin{aligned}\mathring{D}_j\hat{\gamma}^{ij} &= \partial_j\hat{\gamma}^{ij} + \left(\mathring{\Gamma}^i{}_{jk} - \hat{\Gamma}^i{}_{jk}\right)\hat{\gamma}^{kj} + \left(\mathring{\Gamma}^j{}_{jk} - \hat{\Gamma}^j{}_{jk}\right)\hat{\gamma}^{ik} + \hat{\Gamma}^i{}_{jk}\hat{\gamma}^{kj} + \hat{\Gamma}^j{}_{jk}\hat{\gamma}^{ik}, \\ &= \hat{\nabla}\hat{\gamma}^{ij} - \hat{\Delta}^i + \frac{1}{2}\left(\partial_k \ln\mathring{\gamma} - \partial_k\ln\hat{\gamma}\right)\hat{\gamma}^{ik}, \\ &= -\hat{\Delta}^i - \frac{1}{2}\hat{\nabla}_k \ln\left(\frac{\hat{\gamma}}{\mathring{\gamma}}\right)\hat{\gamma}^{ik}.\end{aligned} \tag{C.89}$$

We assume the Lagrangian perspective ($\partial_t\hat{\gamma} = 0$) and constrain the determinants of the flat and conformal metrics to be equal on the initial time slice. Under these assumptions

$$\hat{\Delta}^i = -\mathring{D}_j\hat{\gamma}^{ij}. \tag{C.90}$$

Next, we express the evolution of $\hat{\gamma}^{ij}$ in terms of Lie derivatives on an arbitrary metric $\widetilde{\gamma}$. Noting that $\mathcal{L}_t = \partial_t$ in coordinates adapted to the foliation, we have:

$$\mathcal{L}_m\hat{\gamma}^{ij} = 2\alpha\hat{A}^{ij} + \frac{2}{3}\hat{\gamma}^{ij}\hat{D}_m\beta^m, \tag{C.91}$$

$$\begin{aligned}\mathcal{L}_t\hat{\gamma}^{ij} &= 2\alpha\hat{A}^{ij} + \frac{2}{3}\hat{\gamma}^{ij}\hat{D}_m\beta^m + \mathcal{L}_\beta\hat{\gamma}^{ij}, \\ &= 2\alpha\hat{A}^{ij} + \frac{2}{3}\hat{\gamma}^{ij}\hat{D}_m\beta^m + \beta^k\widetilde{D}_k\hat{\gamma}^{ij} - \hat{\gamma}^{kj}\widetilde{D}_k\beta^i - \hat{\gamma}^{ik}\widetilde{D}_k\beta^j.\end{aligned} \tag{C.92}$$

Taking the flat space divergence of $\mathcal{L}_t\hat{\gamma}^{ij}$ we find (noting that ∂_t commutes with $\mathring{\gamma}_i$ provided $\mathring{\gamma}_{ij}$ is stationary):

$$\mathcal{L}_t\left(\mathring{D}_j\hat{\gamma}^{ij}\right) = \mathring{D}_j\mathcal{L}_\beta\hat{\gamma}^{ij} + 2\mathring{D}_j\left(\alpha\hat{A}_{ij}\right) + \frac{2}{3}\mathring{D}_j\hat{\gamma}^{ij}\hat{D}_m\beta^m + \frac{2}{3}\hat{\gamma}^{ij}\mathring{D}_j\left(\hat{D}_m\beta^m\right). \tag{C.93}$$

Simplifying the flat space covariant derivative of $\mathcal{L}_\beta\hat{\gamma}^{ij}$:

$$\begin{aligned}\mathring{D}_j\mathcal{L}_\beta\hat{\gamma}^{ij} &= \mathring{D}_j\left(\beta^k\widetilde{D}_k\hat{\gamma}^{ij} - \hat{\gamma}^{kj}\widetilde{D}_k\beta^i - \hat{\gamma}^{ik}\widetilde{D}_k\beta^j\right), \\ &= \beta^m\left(\mathring{D}_j\widetilde{D}_m\hat{\gamma}^{ij}\right) + \mathring{D}_j\beta^m\widetilde{D}_m\hat{\gamma}^{ij} - \mathring{D}_j\hat{\gamma}^{mj}\widetilde{D}_m\beta^i - \hat{\gamma}^{mj}\mathring{D}_j\widetilde{D}_m\beta^i - \mathring{D}_j\hat{\gamma}^{im}\widetilde{D}_m\beta^j \\ &\quad - \hat{\gamma}^{im}\mathring{D}_j\widetilde{D}_m\beta^j.\end{aligned} \tag{C.94}$$

Fixing $\widetilde{\gamma}_{ij} = \mathring{\gamma}_{ij}$, and simplifying, we find:

$$\mathring{D}_j\mathcal{L}_\beta\hat{\gamma}^{ij} = \mathcal{L}_\beta\left(\mathring{D}_j\hat{\gamma}^{ij}\right) - \hat{\gamma}^{mn}\mathring{D}_m\mathring{D}_n\beta^i - \hat{\gamma}^{mi}\mathring{D}_m\mathring{D}_n\beta^n. \tag{C.95}$$

Upon substituting this last result into our evolution equation for $\mathcal{L}_t\left(\mathring{D}_j\hat{\gamma}^{ij}\right)$ and substituting (C.90), we find:

$$\mathcal{L}_m\hat{\Delta}^i = \hat{\gamma}^{mn}\mathring{D}_m\mathring{D}_n\beta^i - 2\mathring{D}_j\left(\alpha\hat{A}^{ij}\right) + \frac{1}{3}\hat{\gamma}^{mi}\mathring{D}_m\mathring{D}_n\beta^n + \frac{2}{3}\hat{\Delta}^i\mathring{D}_m\beta^m. \tag{C.96}$$

Taking advantage of the fact that $\mathring{D}_n\beta^n = \hat{D}_n\beta^n$ if $\mathring{\gamma} = \hat{\gamma}$ and that

$$\hat{D}_m\left(\alpha\hat{A}^{im}\right) = \mathring{D}_m\left(\alpha\hat{A}^{im}\right) + \alpha\hat{A}^{mn}\hat{\Delta}^i{}_{mn}, \tag{C.97}$$

we may express the evolution equation for $\hat{\Delta}^i$ in the following concise form:

$$\mathcal{L}_m \hat{\Delta}^i = \hat{\gamma}^{mn} \mathring{D}_m \mathring{D}_n \beta^i - 2\hat{D}_j \left(\alpha \hat{A}^{ij} \right) + 2\alpha \hat{A}^{mn} \hat{\Delta}^i{}_{mn} + \frac{1}{3} \hat{\gamma}^{mi} \hat{D}_m \hat{D}_n \beta^n + \frac{2}{3} \hat{\Delta}^i \hat{D}_n \beta^n. \tag{C.98}$$

Unfortunately, according to [9] the GBSSN equations with this choice for the evolution of $\hat{\Delta}^i$ are only weakly hyperbolic. The equations may be made strongly hyperbolic by expressing the momentum constraint as an expression for the divergence of $\hat{A}^{ij}$

$$\hat{D}_j \hat{A}^{ij} = \frac{2}{3} \hat{\gamma}^{ij} \hat{D}_j K - 6\hat{A}^{ij} \hat{D}_j \chi + 8\pi \hat{j}^i, \tag{C.99}$$

and substituting this expression into (C.98):

$$\begin{aligned} \mathcal{L}_m \hat{\Delta}^i &= \hat{\gamma}^{mn} \mathring{D}_m \mathring{D}_n \beta^i + \alpha \left(\frac{4}{3} \hat{\gamma}^{ij} \hat{D}_j K - 12\hat{A}^{ij} \hat{D}_j \chi + 16\pi \hat{j}^i \right) - 2\hat{A}^{ij} \hat{D}_j \alpha + 2\alpha \hat{A}^{mn} \hat{\Delta}^i{}_{mn} && \text{(C.100)} \\ &\quad + \frac{1}{3} \hat{\gamma}^{mi} \hat{D}_m \hat{D}_n \beta^n + \frac{2}{3} \hat{\Delta}^i \hat{D}_n \beta^n, \\ &= \hat{\gamma}^{mn} \mathring{D}_m \mathring{D}_n \beta^i - 2\hat{A}^{im} \hat{D}_m \alpha + 2\alpha \hat{A}^{mn} \hat{\Delta}^i{}_{mn} + 2\alpha \left(6\hat{A}^{ij} \hat{D}_j \chi - \frac{2}{3} \hat{\gamma}^{ij} \hat{D}_j K - 8\pi \hat{j}^i \right) && \text{(C.101)} \\ &\quad + \frac{1}{3} \left[\hat{D}^i \left(\hat{D}_n \beta^n \right) + 2\hat{\Delta}^i \hat{D}_n \beta^n \right]. \end{aligned}$$

Note that Alcubierre et. al [9] present slightly different equations in which the Eulerian/Lagrangian choice is not specified and the precise multiple of the momentum constraint added to C.98 is left freely specifiable.

Appendix D

Derivation of the FCCZ4 Formulation

One might wonder if something similar to GBSSN can be derived by embedding the Einstein equations within a larger system such that the constraint equations are naturally promoted to propagating degrees of freedom. The answer is a resounding yes, and brings us naturally to the Z4 and FCCZ4 (fully Covariant Conformal Z4) formulations of the Einstein equations [9, 26, 47, 116].

The Z4 formulation takes its name from the introduction of a four vector, Z_μ, to the Einstein equations:

$$R_{\mu\nu} - \frac{1}{2}g_{\mu\nu}R + 2\nabla_{(\mu}Z_{\nu)} - g_{\mu\nu}\nabla_\sigma Z^\sigma - 2\kappa_1 n_{(\mu}Z_{\nu)} - \kappa_1\kappa_2 g_{\mu\nu}n_\sigma Z^\sigma - 8\pi T_{\mu\nu} = 0, \tag{D.1}$$

where κ_1 and κ_2 are damping parameters. Equivalently, the trace reversed form is:

$$R_{\mu\nu} + 2\nabla_{(\mu}Z_{\nu)} - \kappa_1\left(2n_{(\mu}Z_{\nu)} - (1+\kappa_2)\,g_{\mu\nu}n^\sigma Z_\sigma\right) - 8\pi\left(T_{\mu\nu} - \frac{1}{2}g_{\mu\nu}T\right) = 0, \tag{D.2}$$

and the trace (with respect to $g^{\mu\nu}$) is:

$$R + 2\nabla_\sigma Z^\sigma + 2\kappa_1 n_\sigma Z^\sigma + 4\kappa_1(1+\kappa_2)\,n_\sigma Z^\sigma + 8\pi T = 0. \tag{D.3}$$

For judiciously chosen values of the damping parameters, violations of the Hamiltonian and momentum constraints are advected and/or damped under evolution of the modified field equations. In the limit $Z_\mu \to 0$, one recovers general relativity.

If we examine formulations such as NOR [90] and GBSSN [37] in detail, we find that they are essentially minor variations on Z4-derived formulations in which the temporal component of Z_u is not evolved and where substitutions or additions of the Hamiltonian and momentum constraints have been made [9, 47, 116].

As with Appendix C which rederived GBSSN, our purpose in this appendix is both to verify the equations of Sanchis-Gaul et al. [116] and to familiarise ourselves with the formalism in preparation for the derivation of RCCZ4 (Appendix E). As detailed below, our derivation differs from that of [116] in what was likely a simple typo on the part of the authors.

D.1 Derivation Overview

Our derivation begins by defining the quantities Θ and $\bar{Z}^i$ through the projection of Z_μ onto and orthogonal to our foliation Σ_t:

$$\Theta = -n_\mu Z^\mu, \tag{D.4}$$

$$\bar{Z}_i = \gamma^\mu{}_i Z_\mu, \tag{D.5}$$

$$\bar{Z}^i = \gamma^{ij} Z_j. \tag{D.6}$$

Having done so, we project (D.1)–(D.3) onto and orthogonal to our foliation Σ_t to find the Z4 equivalent of the ADM equations:

$$\mathcal{L}_m \gamma_{ij} = -2\alpha K_{ij}, \tag{D.7}$$

$$\begin{aligned}\mathcal{L}_m K_{ij} = &-D_i D_j \alpha + \alpha \left(R_{ij} + 2D_{(i}\bar{Z}_{j)} - 2K_{ik}K^k{}_j + (K - 2\Theta) K_{ij} \right) \\ &+ 4\pi\alpha \left(\gamma_{ij} (S - \rho) - 2S_{ij} \right) - \alpha\kappa_1 (1 + \kappa_2) \gamma_{ij}\Theta,\end{aligned} \tag{D.8}$$

$$\mathcal{L}_m \Theta = \frac{\alpha}{2} \left(R + K^2 - K_{ij}K^{ij} - 16\pi\rho - 2\Theta K + 2D_i\bar{Z}^i - 2\bar{Z}^i D_i \ln\alpha \right) - \alpha\kappa_1 (2 + \kappa_2)\Theta, \tag{D.9}$$

$$\mathcal{L}_m \bar{Z}_i = \alpha \left(D_j K^j{}_i - D_i K - 8\pi j_i + D_i\Theta - 2\bar{Z}_j K^j{}_i - \Theta D_i \ln\alpha - \kappa_1 \bar{Z}_i \right). \tag{D.10}$$

In order to cast (D.7)–(D.10) in a form better suited to evolving black hole spacetimes, we perform the same covariant and conformal decomposition that we would for GBSSN (see Appendix C). We rewrite the 3-metric, γ_{ij} and extrinsic curvature, K_{ij} in terms of the conformal factor, χ, the conformal metric, $\hat{\gamma}_{ij}$, the trace of the extrinsic curvature, K, and the conformal trace free extrinsic curvature, $\hat{A}_{ij}$:

$$\gamma_{ij} = e^{4\chi}\hat{\gamma}_{ij} \tag{D.11}$$

$$K_{ij} = e^{4\chi} \left(\hat{A}_{ij} - \frac{1}{3}\hat{\gamma}_{ij} K \right). \tag{D.12}$$

As with GBSSN, we define the quantities $\hat{\Delta}^i{}_{jk}$ and $\hat{\Delta}^i$ in terms of the difference between the Christoffel symbols of the conformal metric $\hat{\gamma}_{ij}$ and those of a flat background metric $\mathring{\gamma}_{ij}$:

$$\hat{\Gamma}^i = \hat{\Gamma}^i{}_{jk}\hat{\gamma}^{jk}, \tag{D.13}$$

$$\hat{\Delta}^i{}_{ij} = \hat{\Gamma}^i{}_{jk} - \mathring{\Gamma}^i_{jk}, \tag{D.14}$$

$$\hat{\Delta}^i = \hat{\Gamma}^i - \mathring{\Gamma}^i{}_{jk}\hat{\gamma}^{jk}. \tag{D.15}$$

Unlike in GBSSN where $\hat{\Lambda}^i$ is defined to be the dynamical version of $\hat{\Delta}^i$, in FCCZ4, we define it in terms of $\hat{\Delta}^i$ (calculated from $\hat{\gamma}_{ij}$) and the spatial projection of Z_μ:

$$\hat{\Lambda}^i = \hat{\Delta}^i + 2\hat{\gamma}^{ij}\bar{Z}_j. \tag{D.16}$$

After a significant amount of manipulation, we can rewrite (D.7)–(D.10) in terms of $\hat{\gamma}_{ij}$, $\hat{A}_{ij}$, χ, K, Θ, $\bar{Z}_i$ and $\hat{\Lambda}^i$ and recover the FCCZ4 equations of Sanchis-Gual et al. [116]:

$$\mathcal{L}_m \hat{\gamma}_{ij} = -2\alpha\hat{A}_{ij} - \frac{2}{3}\hat{\gamma}_{ij}\hat{D}_m\beta^m, \tag{D.17}$$

$$\begin{aligned}\mathcal{L}_m \hat{A}_{ij} = &e^{-4\chi} \left[+4\hat{D}_{(i}\chi\hat{D}_{j)}\alpha - \hat{D}_i\hat{D}_j\alpha + \alpha \left(\hat{R}_{ij} + \overset{\chi}{R}_{ij} + 2D_{(i}\bar{Z}_{j)} - 8\pi S_{ij} \right) \right]^{\mathrm{TF}} \\ &- \frac{2}{3}\hat{A}_{ij}\hat{D}_m\beta^m - 2\alpha\hat{A}_{ik}\hat{A}^k{}_j + \alpha\hat{A}_{ij}(K - 2\Theta),\end{aligned} \tag{D.18}$$

$$\mathcal{L}_m \chi = -\frac{1}{6}\alpha K + \frac{1}{6}\hat{D}_m\beta^m, \tag{D.19}$$

$$\mathcal{L}_m K = -D^2\alpha + \alpha R + \alpha \left(K^2 - 2\Theta K \right) + 2\alpha D_i\bar{Z}^i + 4\pi\alpha (S - 3\rho) - 3\alpha\kappa_1 (1 + \kappa_2)\Theta, \tag{D.20}$$

$$\mathcal{L}_m \Theta = \frac{\alpha}{2} \left(R - \hat{A}_{ij}\hat{A}^{ij} + \frac{2}{3}K^2 - 2\Theta K + 2D_i\bar{Z}^i - 2\bar{Z}^i D_i \ln\alpha - 16\pi\rho \right) - \alpha\kappa_1 (2 + \kappa_2)\Theta, \tag{D.21}$$

$$\begin{aligned}\mathcal{L}_m \hat{\Lambda}^i = &\hat{\gamma}^{mn}\mathring{D}_m\mathring{D}_n\beta^i + \frac{2}{3}\hat{\Lambda}^i\hat{D}_n\beta^n + \frac{1}{3}\hat{D}^i\hat{D}_n\beta^n - 2\hat{A}^{ik}\left(\hat{D}_k\alpha - 6\alpha\hat{D}_k\chi \right) + 2\alpha\hat{A}^{jk}\hat{\Delta}^i{}_{jk} \\ &- \frac{4}{3}\alpha\hat{D}^i K + 2\hat{\gamma}^{ik}\left(\alpha\hat{D}_k\Theta - \Theta\hat{D}_k\alpha - \frac{2}{3}\alpha K\bar{Z}_k \right) - 16\pi\alpha\hat{\gamma}^{ij}j_j - 2\alpha\kappa_1\hat{\gamma}^{ij}\bar{Z}_j.\end{aligned} \tag{D.22}$$

D.2 Spatial projection

We begin by finding the evolution equation for the extrinsic curvature by projecting all free indices of (D.2) onto Σ. The terms present in the usual Einstein equations follow the ordinary ADM derivation, so here we concentrate on the terms containing Z^μ,

$$\begin{aligned}
\gamma^\mu{}_l\gamma^\nu{}_m\nabla_\mu Z_\nu &= \gamma^\mu{}_l\gamma^\nu{}_m\nabla_\mu\left(\gamma^\lambda{}_\nu Z_\lambda + \Theta n_\nu\right), && \text{(D.23)}\\
&= D_l\bar{Z}_m + \gamma^\mu{}_l\gamma^\nu{}_m\nabla_\mu\left(\Theta n_\nu\right),\\
&= D_l\bar{Z}_m + \gamma^\mu{}_l\gamma^\nu{}_m\Theta\left(-K_{\mu\nu} - D_\nu\ln\left(\alpha\right)n_\mu\right),\\
&= D_l\bar{Z}_m - \Theta K_{lm},\\
\gamma^\mu{}_l\gamma^\nu{}_m n_\mu Z_\nu &= 0 && \text{(D.24)}\\
\gamma^\mu{}_l\gamma^\nu{}_m g_{\mu\nu}n_\sigma Z^\sigma &= \gamma^\mu{}_l\gamma^\nu{}_m\left(\gamma_{\mu\nu} - n_\mu n_\nu\right)\left(-\Theta\right) && \text{(D.25)}\\
&= \gamma^\mu{}_l\gamma^\nu{}_m\gamma_{\mu\nu}\left(-\Theta\right)\\
&= -\gamma_{lm}\Theta
\end{aligned}$$

Adding these to (C.10), the ADM equation of the extrinsic curvature, we recover (D.8).

D.3 Temporal Projection

Next, we modify the Hamiltonian constraint by taking the full projection of (D.1) onto $n^\mu n^\nu$. Again, we consider only those terms that have been added to the usual Einstein equations.

$$\begin{aligned}
n^\mu n^\nu n_\mu Z_\nu &= -n^\nu Z_\nu && \text{(D.26)}\\
&= \Theta,\\
n^\mu n^\nu g_{\mu\nu}n_\sigma Z^\sigma &= -n_\sigma Z^\sigma && \text{(D.27)}\\
&= \Theta,\\
n^\mu n^\nu\nabla_\mu Z_\nu &= n^\mu\nabla_\mu\left(n^\nu Z_\nu\right) - n^\mu Z_\nu\nabla_\mu n^\nu, && \text{(D.28)}\\
&= -n^\mu\nabla_\mu\Theta + n^\mu Z_\nu\left[K^\nu{}_\mu + D^\nu\ln\left(\alpha\right)n_\mu\right],\\
&= -\frac{1}{\alpha}\mathcal{L}_m\Theta - \bar{Z}^i D_i\ln\left(\alpha\right),\\
n^\mu n^\nu g_{\mu\nu}\nabla_\sigma Z^\sigma &= -\nabla_\sigma Z^\sigma, && \text{(D.29)}\\
&= -\nabla_\sigma\left(Z^\sigma + n^\sigma\Theta\right),\\
&= -\nabla_\sigma Z^\sigma + \Theta K - \frac{1}{\alpha}\mathcal{L}_m\Theta,\\
&= -\frac{1}{\sqrt{-g}}\partial_i\left(\sqrt{-g}\bar{Z}^i\right) + \Theta K - \frac{1}{\alpha}\mathcal{L}_m\Theta,\\
&= -D_i\bar{Z}^i - \bar{Z}^i D_i\ln\left(\alpha\right) + \Theta K - \frac{1}{\alpha}\mathcal{L}_m\Theta.
\end{aligned}$$

Upon adding these to (C.11), the ADM Hamiltonian constraint, we find (D.9).

D.4 Mixed Projection

Finally, in order to find our evolution equation for Z_μ, we project the components of (D.1) which contain factors of Z_μ onto $\gamma^\mu{}_a n^\nu$:

$$\begin{aligned}\gamma^\mu{}_i n^\nu g_{\mu\nu}\nabla_\sigma Z^\sigma &= \gamma^\mu{}_i n^\nu \left(\gamma_{\mu\nu} - n_\mu n_\nu\right)\nabla_\sigma Z^\sigma, \\ &= 0,\end{aligned} \tag{D.30}$$

$$\gamma^\mu{}_i n^\nu n_\mu Z_\nu = 0 \tag{D.31}$$

$$\gamma^\mu{}_i n^\nu n_\nu Z_\mu = -\bar{Z}_i \tag{D.32}$$

and,

$$\begin{aligned}\gamma^\mu{}_i n^\nu \nabla_\mu Z_\nu &= \gamma^\mu{}_i \nabla_\mu \left(n^\nu Z_\nu\right) - \gamma^\mu{}_i \left(\nabla_\mu n^\nu\right) Z_\nu, \\ &= -\gamma^\mu{}_i \nabla_\mu \Theta + K^\nu{}_i \bar{Z}_\nu, \\ &= -\left(\delta^\mu{}_i + n^\mu n_i\right)\nabla_\mu \Theta + \bar{Z}_\nu K^\nu{}_i, \\ &= -\partial_i \Theta - n_i n^\mu \nabla_\mu \Theta + \bar{Z}_\nu K^\nu{}_i, \\ &= -\partial_i \Theta - \frac{1}{\alpha} n_i \mathcal{L}_m \Theta + \bar{Z}_\nu K^\nu{}_i, \\ &= -D_i \Theta + \bar{Z}_j K^j{}_i,\end{aligned} \tag{D.33}$$

where in the last step we have restricted ourselves to spatial indices. Projecting the final component,

$$\begin{aligned}\gamma^\mu{}_i n^\nu \nabla_\nu Z_\mu &= n^\nu \nabla_\nu \left(\gamma^\mu{}_i Z_\mu\right) - Z_\mu n^\nu \nabla_\nu \gamma^\mu{}_i, \\ &= n^\nu \nabla_\nu \bar{Z}_i - Z_\mu n^\nu \nabla_\nu \left(\delta^\mu{}_i + n^\mu n_i\right), \\ &= n^\nu \nabla_\nu \bar{Z}_i - Z_\mu n^\nu n^\mu \left(\nabla_\nu n_i\right) - Z_\mu n^\nu n_i \left(\nabla_\nu n^\mu\right), \\ &= n^\nu \nabla_\nu \bar{Z}_i + \Theta n^\nu \left(-K_{i\nu} - D_i \ln\left(\alpha\right) n_\nu\right) + Z_\mu n^\nu n_i D^\mu \ln\left(\alpha\right) n_\nu, \\ &= n^\nu \nabla_\nu \bar{Z}_i - \bar{Z}_\mu n_i D^\mu \ln\left(\alpha\right) + \Theta D_i \ln\left(\alpha\right),\end{aligned} \tag{D.34}$$

and using,

$$\begin{aligned}\frac{1}{\alpha}\mathcal{L}_m \bar{Z}_\beta &= n^\alpha \nabla_\alpha \bar{Z}_\beta + \bar{Z}_\alpha \nabla_\beta n^\alpha + \frac{1}{\alpha} n^\alpha \bar{Z}_\alpha \nabla_\beta \alpha, \\ &= n^\alpha \nabla_\alpha \bar{Z}_\beta - \bar{Z}_\alpha K^\alpha{}_\beta - D^\alpha \ln\left(\alpha\right) n_\beta \bar{Z}_\alpha,\end{aligned} \tag{D.35}$$

the above becomes,

$$\gamma^\mu{}_i n^\nu \nabla_\nu Z_\mu = \frac{1}{\alpha}\mathcal{L}_m \bar{Z}_i + \bar{Z}_j K^j{}_i + \Theta D_i \ln\left(\alpha\right). \tag{D.36}$$

Restricting to spatial indices, the sum total of the $Z4$ terms becomes,

$$\begin{aligned}&\gamma^\mu{}_i n^\nu \left(2\nabla_{(\mu} Z_{\nu)} - g_{\mu\nu}\nabla_\sigma Z^\sigma - 2\kappa_1 n_{(\mu} Z_{\nu)} - \kappa_1 \kappa_2 g_{\mu\nu} n_\sigma Z^\sigma\right) = \frac{1}{\alpha}\mathcal{L}_m \bar{Z}_i + 2\bar{Z}_j K^j{}_i \\ &\quad - D_i \Theta + \Theta D_i \ln\alpha + \kappa_1 \bar{Z}_i.\end{aligned} \tag{D.37}$$

Upon addition of these quantities to (C.12), the ADM momentum constraint, we recover (D.10).

D.5 FCCZ4 Form of the Equations

In this section, we try to refrain from redundant derivation by focusing primarily on the differences between the GBSSN and FCCZ4 equations. In that context, we first note that the equations for $\hat{\gamma}_{ij}$ and χ are identical in both cases.

D.5.1 Evolution of K

Beginning with the Lie derivative of K along m:

$$\mathcal{L}_m K = \gamma^{ij}\mathcal{L}_m K_{ij} + K_{ij}\mathcal{L}_m\gamma^{ij}, \tag{D.38}$$

and the Z4 form of the evolution of the extrinsic curvature:

$$\begin{aligned}\mathcal{L}_m K_{ij} = &-D_iD_j\alpha + \alpha\left(R_{ij} + 2D_{(i}\bar{Z}_{j)} - 2K_{ik}K^k{}_j + (K-2\Theta)K_{ij}\right)\\ &+ 4\pi\alpha\left(\gamma_{ij}(S-\rho) - 2S_{ij}\right) - \alpha\kappa_1(1+\kappa_2)\gamma_{ij}\Theta,\end{aligned} \tag{D.39}$$

we substitute (D.7) for $\mathcal{L}_m\gamma^{ij}$, to find (D.20):

$$\begin{aligned}\mathcal{L}_m K &= -D_iD^i\alpha + \alpha\left(R + 2D_i\bar{Z}^i - 2K^{lm}K_{lm} + (K-2\Theta)K\right) - 8\pi\alpha\left(S - \frac{3}{2}(S-\rho)\right)\\ &\quad - 3\alpha\kappa_1(1+\kappa_2)\Theta + 2\alpha K_{ij}K^{ij},\\ &= -D_iD^i\alpha + \alpha\left(R + 2D_i\bar{Z}^i + K^2 - 2\Theta K + 4\pi(S-3\rho)\right) - 3\alpha\kappa_1(1+\kappa_2)\Theta,\\ &= -D_iD^i\alpha + \alpha R + \alpha\left(K^2 - 2\Theta K\right) + 2\alpha D_i\bar{Z}^i + 4\pi\alpha(S-3\rho) - 3\alpha\kappa_1(1+\kappa_2)\Theta.\end{aligned} \tag{D.40}$$

D.5.2 Evolution of $\hat{A}_{ij}$

Recall the ADM equation for the evolution of the extrinsic curvature:

$$\mathcal{L}_m K_{ij} = -D_iD_j\alpha + \alpha\left(R_{ij} + KK_{ij} - 2K_{ik}K^k{}_j\right) + 4\pi\alpha\left[\gamma_{ij}(S-\rho) - 2S_{ij}\right], \tag{D.41}$$

and compare it with the equivalent Z4 equation,

$$\begin{aligned}\mathcal{L}_m K_{ij} = &-D_iD_j\alpha + \alpha\left(R_{ij} + 2D_{(i}\bar{Z}_{j)} - 2K_{ik}K^k{}_j + (K-2\Theta)K_{ij}\right)\\ &+ 4\pi\alpha\left(\gamma_{ij}(S-\rho) - 2S_{ij}\right) - \alpha\kappa_1(1+\kappa_2)\gamma_{ij}\Theta\,.\end{aligned} \tag{D.42}$$

If we define

$$\bar{R}_{ij} = R_{ij} + 2D_{(i}\bar{Z}_{j)} - 2\Theta K_{ij}, \tag{D.43}$$

and note that this new pseudo-curvature has the same symmetries as a true curvature, we may follow the GBSSN derivation of $\mathcal{L}_m\hat{A}_{ij}$ exactly (see Sec. C.6) and substitute the definition of this new quantity as a final step. Doing so yields (D.18)

$$\begin{aligned}\mathcal{L}_m\hat{A}_{ij} &= e^{-4\chi}\left[-D_iD_j\alpha + \alpha\widetilde{R}_{ij} - 8\pi\alpha S_{ij}\right]^{\mathrm{TF}} - \frac{2}{3}\hat{A}_{ij}\hat{D}_m\beta^m + \alpha\left(K\hat{A}_{ij} - 2\hat{A}_{ik}\hat{A}^k{}_j\right),\\ &= -\frac{2}{3}\hat{A}_{ij}\hat{D}_m\beta^m - 2\alpha\hat{A}_{ik}\hat{A}^k{}_j + \alpha\hat{A}_{ij}(K-2\Theta)\\ &\quad + e^{-4\chi}\left[-D_iD_j\alpha + \alpha\left(\hat{R}_{ij} + \overset{\chi}{R}_{ij} + 2D_{(i}\bar{Z}_{j)} - 8\pi S_{ij}\right)\right]^{\mathrm{TF}},\\ &= -\frac{2}{3}\hat{A}_{ij}\hat{D}_m\beta^m - 2\alpha\hat{A}_{ik}\hat{A}^k{}_j + \alpha\hat{A}_{ij}(K-2\Theta)\\ &\quad + e^{-4\chi}\left[+4\hat{D}_{(i}\chi\hat{D}_{j)}\alpha - \hat{D}_i\hat{D}_j\alpha + \alpha\left(\hat{R}_{ij} + \overset{\chi}{R}_{ij} + 2D_{(i}\bar{Z}_{j)} - 8\pi S_{ij}\right)\right]^{\mathrm{TF}},\end{aligned} \tag{D.44}$$

D.5.3 Evolution of Θ

Essentially trivial substitution of the conformal variables into (D.9), the augmented Hamiltonian constraint, gives (D.21):

$$\begin{aligned}\mathcal{L}_m\Theta &= \frac{\alpha}{2}\left(R + K^2 - K_{ij}K^{ij} - 16\pi\rho - 2\Theta K - 2D_i\bar{Z}^i - 2\bar{Z}^i D_i \ln\alpha\right) - \alpha\kappa_1\left(2+\kappa_2\right)\Theta, \\ &= \frac{\alpha}{2}\left(R - \hat{A}_{ij}\hat{A}^{ij} + \frac{2}{3}K^2 - 2\Theta K + 2D_i\bar{Z}^i - 2\bar{Z}^i D_i \ln\alpha - 16\pi\rho\right) - \alpha\kappa_1\left(2+\kappa_2\right)\Theta.\end{aligned} \tag{D.45}$$

D.5.4 Evolution of $\hat{\Lambda}^i$

Starting from (D.10), the Z4 analog of the momentum constraint:

$$\mathcal{L}_m\bar{Z}_i = \alpha\left(D_j K^j{}_i - D_i K - 8\pi j_i + D_i\Theta - 2\bar{Z}_j K^j{}_i - \Theta D_i \ln\alpha - \kappa_1\bar{Z}_i\right), \tag{D.46}$$

we raise $\bar{Z}_i$ with the 3-metric, substitute the conformal variables and substitute (D.17) and (D.19) for the evolution of $\hat{\gamma}_{ij}$ and χ respectively:

$$\begin{aligned}\mathcal{L}_m\bar{Z}^i &= \gamma^{ij}\mathcal{L}_m\bar{Z}_i + \bar{Z}_i\mathcal{L}_m\gamma^{ij}, \\ &= \hat{\gamma}^{ij}e^{-4\chi}\mathcal{L}_m\bar{Z}_i + \bar{Z}_i\mathcal{L}_m\left(\gamma^{ij}e^{-4\chi}\right) \\ &= \alpha\left(e^{-4\chi}D_l\hat{A}^{li} + \hat{A}^{li}D_l e^{-4\chi} - \frac{2}{3}D^i K - 8\pi j^i + D^i\Theta - \Theta D^i\ln\left(\alpha\right) - \kappa_1\gamma^{ij}\bar{Z}_j\right).\end{aligned} \tag{D.47}$$

Replacing the covariant derivatives on the 3-metric with those on the conformal 3-metric yields

$$\mathcal{L}_m\bar{Z}^i = \alpha e^{-4\chi}\left(\hat{D}_l\hat{A}^{li} + 6\hat{A}^{li}\hat{D}_l\chi - \frac{2}{3}\hat{D}^i K - 8\pi\hat{j}^i + \hat{D}^i\Theta - \Theta D^i\ln\left(\alpha\right) - \kappa_1\hat{\gamma}^{ij}\bar{Z}_j\right). \tag{D.48}$$

The evolution of $\hat{\Lambda}^i$ is then given by:

$$\begin{aligned}\mathcal{L}_m\hat{\Lambda}^i &= \mathcal{L}_m\hat{\Delta}^i + 2\mathcal{L}_m\left(\hat{\gamma}^{ij}\bar{Z}_j\right), \\ &= \mathcal{L}_m\hat{\Delta}^i + 8e^{4\chi}\bar{Z}^i\mathcal{L}_m\chi + 2e^{4\chi}\mathcal{L}_m\bar{Z}^i.\end{aligned} \tag{D.49}$$

Into this, we can substitute (D.48) for $\mathcal{L}_m\bar{Z}^i$, (D.19) for $\mathcal{L}_m\chi$ and C.98 for $\mathcal{L}_m\hat{\Delta}^i$

$$\begin{aligned}\mathcal{L}_m\hat{\Lambda}^i = \hat{\gamma}^{mn}\mathring{D}_m\mathring{D}_n\beta^i + \frac{2}{3}\hat{\Lambda}^i\hat{D}_n\beta^n + \frac{1}{3}\hat{D}^i\hat{D}_n\beta^n - 2\hat{A}^{ik}\left(\hat{D}_k\alpha - 6\alpha\hat{D}_k\chi\right) + 2\alpha\hat{A}^{jk}\hat{\Delta}^i{}_{jk} \\ - \frac{4}{3}\alpha\hat{D}^i K + 2\hat{\gamma}^{ik}\left(\alpha\hat{D}_k\Theta - \Theta\hat{D}_k\alpha - \frac{2}{3}\alpha K\bar{Z}_k\right) - 16\pi\alpha\hat{\gamma}^{ij}j_j - 2\alpha\kappa_1\hat{\gamma}^{ij}\bar{Z}_j,\end{aligned} \tag{D.50}$$

resulting in (D.22).

Here it should be noted that the original derivation of these equations performed by Sanchis-Gauls et al. [116] had an additional factor of $\frac{4}{3}\hat{D}_l\beta^l e^{4\chi}\bar{Z}^i$. This appears to corresponds to a minor typo in the equations where those authors accidentally used $\frac{2}{3}\hat{\Delta}^i\hat{D}_n\beta^n$ in place of $\frac{2}{3}\hat{\Lambda}^i\hat{D}_n\beta^n$.

Appendix E

Derivation of the RCCZ4 Formulation

E.1 3+1 Form of RZ4

The RZ4 equations in canonical and trace-reversed form with damping are given by (5.10) and (5.11). As we have been predominantly interested in investigating scale invariant problems, we set the damping parameters κ_1 and κ_2 to zero, yielding the simpler set of equations:

$$R_{\mu\nu} - \frac{1}{2}g_{\mu\nu}R + 2\mathring{\nabla}_{(\mu}Z_{\nu)} - g_{\mu\nu}\mathring{\nabla}_{(\alpha}Z_{\beta)}g^{\alpha\beta} - 8\pi T_{\mu\nu} = 0, \tag{E.1}$$

$$R_{\mu\nu} + 2\mathring{\nabla}_{(\mu}Z_{\nu)} - 8\pi\left(T_{\mu\nu} - \frac{1}{2}g_{\mu\nu}T\right) = 0, \tag{E.2}$$

$$R + 2\mathring{\nabla}_{(\mu}Z_{\nu)}g^{\mu\nu} + 8\pi T = 0. \tag{E.3}$$

Here, (E.1) is RZ4 written in canonical form, (E.2) is written in trace-reversed form and (E.3) is the trace of (E.2) taken with respect to the physical metric $g^{\mu\nu}$.

To derive the ADM equivalent of the RZ4 equations we roughly follow the ADM derivations of [5, 54] and take projections of (E.1)–(E.3) onto and orthogonal to the spatial hypersurfaces which foliate four dimensional spacetime in a standard 3+1 decomposition. In what follows, we consider only the simplest case where $\mathring{g}_{\mu\nu}$ is a time-invariant, curvature-free Lorentzian metric with $\mathring{g}_{tt} = -1, \mathring{g}_{tj} = 0$.

E.1.1 Spatial projection

We begin by finding the evolution equation for the extrinsic curvature by projecting both indices of (E.2) onto Σ. The terms present in the Einstein equations follow the ordinary ADM derivation so we concentrate on the terms containing Z^μ:

$$\gamma^\mu{}_\lambda\gamma^\nu{}_\sigma\mathring{\nabla}_\mu Z_\nu = \gamma^\mu{}_\lambda\gamma^\nu{}_\sigma\left(\partial_\mu\bar{Z}_\nu + \Theta\partial_\mu n_\nu - \mathring{\Gamma}^\rho{}_{\mu\nu}\left(\bar{Z}_\rho + n_\rho\Theta\right)\right). \tag{E.4}$$

We now note that, since $n_i = 0$, when restricting to spatial indices we have:

$$\begin{aligned}\gamma^\mu{}_l\gamma^\nu{}_m\partial_\mu n_\nu &= \left(\delta^\mu{}_l + n^\mu n_l\right)\left(\delta^\nu{}_m + n^\nu n_m\right)\partial_\mu n_\nu, \\ &= \left(\delta^\mu{}_l\delta^\nu{}_m + \delta^\mu{}_l n^\nu n_m + \delta^\nu{}_m n^\mu n_l + n^\mu n_l n^\nu n_m\right)\partial_\mu n_\nu, \\ &= \left(\partial_l n_m + n^\nu n_m\partial_l n_\nu + n^\mu n_l\partial_\mu n_m + n^\mu n_l n^\nu n_m\partial_\mu n_\nu\right), \\ &= 0,\end{aligned} \tag{E.5}$$

and therefore

$$\begin{aligned}2\gamma^\mu{}_i\gamma^\nu{}_j\mathring{\nabla}_{(\mu}Z_{\nu)} &= 2\gamma^\mu{}_i\gamma^\nu{}_j\left(\partial_{(\mu}\bar{Z}_{\nu)} + \Theta\partial_{(\mu}n_{\nu)} - \mathring{\Gamma}^\rho{}_{\mu\nu}\left(\bar{Z}_\rho + n_\rho\Theta\right)\right), \\ &= 2\gamma^\mu{}_i\gamma^\nu{}_j\left(\partial_{(\mu}\bar{Z}_{\nu)} - \mathring{\Gamma}^\rho{}_{\mu\nu}\left(\bar{Z}_\rho + n_\rho\Theta\right)\right).\end{aligned} \tag{E.6}$$

Assuming $\mathring{g}_{\mu\nu} = \delta_{tt} + \mathring{\gamma}_{ij}$ with $\mathring{R}_{ij} = \mathring{\Gamma}^{t}{}_{ij} = 0$ (e.g. we take the simplest possible flat background 3-metric), this simplifies further to,

$$\begin{aligned} 2\gamma^{\mu}{}_{i}\gamma^{\nu}{}_{j}\mathring{\nabla}_{(\mu}Z_{\nu)} =& 2\gamma^{\mu}{}_{i}\gamma^{\nu}{}_{j}\left(\partial_{(\mu}\bar{Z}_{\nu)} - \mathring{\Gamma}^{k}{}_{\mu\nu}\bar{Z}_{k}\right), \\ =& 2\left(\delta^{\mu}{}_{i}\delta^{\nu}{}_{j} + \delta^{\mu}{}_{i}n^{\nu}n_{j} + \delta^{\nu}{}_{j}n^{\nu}n_{i} + n^{\mu}n_{i}n^{\nu}n_{j}\right)\left(\partial_{(\mu}\bar{Z}_{\nu)} - \mathring{\Gamma}^{k}{}_{\mu\nu}\bar{Z}_{k}\right), \\ =& 2\partial_{(i}\bar{Z}_{j)} - 2\mathring{\Gamma}^{k}{}_{ij}\bar{Z}_{k}, \\ =& 2\mathring{D}_{(i}\bar{Z}_{j)}\,. \end{aligned} \tag{E.7}$$

Here, we have made use of the fact that, with the connection given above, the Christoffel symbols for the spatial component of the background metric are identical to those of its four dimensional counterpart. Adding (E.7) to the evolution equation for the extrinsic curvature,

$$\mathcal{L}_{m}K_{ij} = -D_{i}D_{j}\alpha + \alpha\left(R_{ij} + KK_{ij} - 2K_{ik}K^{k}{}_{j}\right) + 4\pi\alpha\left(\gamma_{ij}\left(S-\rho\right) - 2S_{ij}\right), \tag{E.8}$$

we recover (5.17).

E.1.2 Temporal Projection

Next, we modify the Hamiltonian constraint by considering the full projection of (E.1) onto $n^{\mu}n^{\nu}$. Focusing on the terms that have been added to the original Einstein equations we have:

$$\begin{aligned} n^{\mu}n^{\nu}\mathring{\nabla}_{\mu}Z_{\nu} &= n^{\mu}\mathring{\nabla}_{\mu}\left(n^{\nu}Z_{\nu}\right) - n^{\mu}Z_{\nu}\mathring{\nabla}_{\mu}n^{\nu}, \\ &= -n^{\mu}\mathring{\nabla}_{\mu}\Theta - n^{\mu}Z_{\nu}\mathring{\nabla}_{\mu}n^{\nu}, \\ &= -\frac{1}{\alpha}\mathcal{L}_{m}\Theta - n^{\mu}Z_{\nu}\mathring{\nabla}_{\mu}n^{\nu}, \end{aligned} \tag{E.9}$$

$$\begin{aligned} n^{\mu}n^{\nu}g_{\mu\nu}\left(\mathring{\nabla}_{\lambda}Z_{\sigma}\right)g^{\lambda\sigma} &= -\left(\mathring{\nabla}_{\lambda}Z_{\sigma}\right)g^{\lambda\sigma}, \\ &= -g^{\lambda\sigma}\mathring{\nabla}_{\lambda}\left(\bar{Z}_{\sigma} + n_{\sigma}\Theta\right), \\ &= -\frac{1}{\alpha}\mathcal{L}_{m}\Theta - g^{\lambda\sigma}\mathring{\nabla}_{\lambda}\bar{Z}_{\sigma} - g^{\lambda\sigma}\Theta\mathring{\nabla}_{\lambda}n_{\sigma}. \end{aligned} \tag{E.10}$$

Thus, we find

$$\begin{aligned} n^{\mu}n^{\nu}\left(2\mathring{\nabla}_{(\mu}Z_{\nu)} - g_{\mu\nu}\mathring{\nabla}_{\lambda}Z_{\sigma}g^{\lambda\sigma}\right) = &-\frac{1}{\alpha}\mathcal{L}_{m}\Theta - 2n^{\mu}\left(\bar{Z}_{\nu} + n_{\nu}\Theta\right)\mathring{\nabla}_{\mu}n^{\nu} \\ &+ g^{\lambda\sigma}\mathring{\nabla}_{\lambda}\bar{Z}_{\sigma} + g^{\lambda\sigma}\Theta\mathring{\nabla}_{\lambda}n_{\sigma}. \end{aligned} \tag{E.11}$$

Now, expressing n^{μ} and $g_{\mu\nu}$ in terms of α, β^{i} and γ_{ij} and simplifying, (E.11) becomes:

$$\begin{aligned} n^{\mu}n^{\nu}\left(2\mathring{\nabla}_{(\mu}Z_{\nu)} - g_{\mu\nu}\mathring{\nabla}_{\lambda}Z_{\sigma}g^{\lambda\sigma}\right) = &-\frac{1}{\alpha}\mathcal{L}_{m}\Theta - \frac{\Theta}{\alpha^{2}}\mathcal{L}_{m}\alpha + \frac{\bar{Z}_{i}}{\alpha^{2}}\left(\mathcal{L}_{m}\beta^{i} - \beta^{j}\mathring{D}_{j}\beta^{i}\right) \\ &+ \gamma^{ij}\mathring{D}_{i}\bar{Z}_{j}. \end{aligned} \tag{E.12}$$

Adding these to the ADM Hamiltonian constraint,

$$H = \frac{1}{2}\left(R + K^{2} - K_{ij}K^{ij}\right) - 8\pi\rho = 0, \tag{E.13}$$

and solving for $\mathcal{L}_{m}\Theta$, we recover (5.18).

E.1.3 Mixed Projection

We find the evolution equation for the momentum constraint propagator by taking the mixed projection onto $\gamma^{\mu}{}_{\lambda}n^{\nu}$ of the terms that have been added to the Einstein equations in (E.1). Upon restricting to spatial indices we find:

$$\begin{aligned}
\gamma^{\mu}{}_{i}n^{\nu}\mathring{\nabla}_{\mu}Z_{\nu} &= -\gamma^{\mu}{}_{i}\mathring{\nabla}_{\mu}\Theta - \gamma^{\mu}{}_{i}Z_{\nu}\mathring{\nabla}_{\mu}n^{\nu}, && \text{(E.14)}\\
&= -\partial_{i}\Theta - n_{i}n^{\mu}\mathring{\nabla}_{\mu}\Theta - \gamma^{\mu}{}_{i}\left(\bar{Z}_{\nu}+\Theta n_{\nu}\right)\mathring{\nabla}_{\mu}n^{\nu},\\
&= -D_{i}\Theta - \gamma^{\mu}{}_{i}\left(\bar{Z}_{\nu}+\Theta n_{\nu}\right)\mathring{\nabla}_{\mu}n^{\nu},\\
\gamma^{\mu}{}_{i}n^{\nu}\mathring{\nabla}_{\nu}Z_{\mu} &= n^{\nu}\mathring{\nabla}_{\nu}\left(\gamma^{\mu}{}_{i}Z_{\mu}\right) - Z_{\mu}n^{\nu}\mathring{\nabla}_{\nu}\gamma^{\mu}{}_{i}, && \text{(E.15)}\\
&= n^{\nu}\mathring{\nabla}_{\nu}\bar{Z}_{i} - Z_{\mu}n^{\nu}\mathring{\nabla}_{\nu}\left(\delta^{\mu}{}_{i}+n^{\mu}n_{i}\right),\\
&= n^{\nu}\mathring{\nabla}_{\nu}\bar{Z}_{i} - n_{i}Z_{\mu}n^{\nu}\mathring{\nabla}_{\nu}n^{\mu} + \Theta n^{\nu}\mathring{\nabla}_{\nu}n_{i},\\
&= n^{\nu}\mathring{\nabla}_{\nu}\bar{Z}_{i} + \Theta n^{\nu}\mathring{\nabla}_{\nu}n_{i},\\
&= \frac{1}{\alpha}\mathcal{L}_{m}\bar{Z}_{i} - \bar{Z}_{\mu}\mathring{\nabla}_{i}n^{\mu},\\
\gamma^{\mu}{}_{i}n^{\nu}\left(g_{\mu\nu}g^{\lambda\sigma}\mathring{\nabla}_{\lambda}Z_{\sigma}\right) &= \gamma^{\mu}{}_{i}n^{\nu}\left(\gamma_{\mu\nu}-n_{\mu}n_{\nu}\right)\left(g^{\lambda\sigma}\mathring{\nabla}_{\lambda}Z_{\sigma}\right), && \text{(E.16)}\\
&= 0.
\end{aligned}$$

Now, expressing n^{μ} and $g_{\mu\nu}$ in terms of the 3+1 variables (α, β^{i} and γ_{ij}) and simplifying the resulting expression, we find:

$$\begin{aligned}
\gamma^{\mu}{}_{a}n^{\nu}\left(2\mathring{\nabla}_{(\mu}Z_{\nu)} - g_{\mu\nu}g^{\lambda\sigma}\mathring{\nabla}_{l}Z_{m}\right) &= \frac{1}{\alpha}\mathcal{L}_{m}\bar{Z}_{i} - \bar{Z}_{\mu}\mathring{\nabla}_{i}n^{\mu} - \mathring{D}_{i}\Theta - \gamma^{\mu}{}_{i}\left(\bar{Z}_{\nu}+\Theta n_{\nu}\right)\mathring{\nabla}_{\mu}n^{\nu}, && \text{(E.17)}\\
&= \frac{1}{\alpha}\mathcal{L}_{m}\bar{Z}_{i} + \frac{2}{\alpha}\bar{Z}_{j}\mathring{D}_{i}\beta^{j} - \mathring{D}_{i}\Theta - \Theta\mathring{D}_{i}\ln\left(\alpha\right).
\end{aligned}$$

Upon substitution of this expression into the ADM momentum constraint,

$$M^{i} = D_{j}K^{ij} - \gamma^{ij}D_{j}K - 8\pi j^{i} = 0, \tag{E.18}$$

and solving for $\mathcal{L}_{m}\bar{Z}_{i}$, we recover (5.19).

E.2 Derivation of RCCZ4

Now that we have the ADM equivalent of the RZ4 equations, the derivation of the RCCZ4 equations proceeds in a fairly straightforward manner. To recap, the ADM equivalents of the RZ4 equations so far derived are:

$$\mathcal{L}_{m}\gamma_{ij} = -2\alpha K_{ij}, \tag{E.19}$$

$$\mathcal{L}_{m}K_{ij} = -D_{i}D_{j}\alpha + \alpha\left(R_{ij} + KK_{ij} - 2K_{ik}K^{k}{}_{j}\right) + 4\pi\alpha\left(\left[S-\rho\right]\gamma_{ij} - 2S_{ij}\right) + 2\alpha\mathring{D}_{(i}\bar{Z}_{j)}, \tag{E.20}$$

$$\mathcal{L}_{m}\Theta = \frac{\alpha}{2}\left(R + K^{2} - K_{ij}K^{ij} - 16\pi\rho\right) + \alpha\gamma^{ij}\mathring{D}_{i}\bar{Z}_{j} - \frac{\Theta}{\alpha}\mathcal{L}_{m}\alpha + \frac{\bar{Z}_{i}}{\alpha}\left(\mathcal{L}_{m}\beta^{i} - \beta^{j}\mathring{D}_{j}\beta^{i}\right), \tag{E.21}$$

$$\mathcal{L}_{m}\bar{Z}_{i} = \alpha\left(D_{j}K^{j}{}_{i} - D_{i}K - 8\pi j_{i}\right) - 2\bar{Z}_{j}\mathring{D}_{i}\beta^{j} + \Theta\mathring{D}_{i}\alpha + \alpha\mathring{D}_{i}\Theta, \tag{E.22}$$

and the process of determining the RCCZ4 equations essentially boils down to substituting for the conformal variables in a manner exactly analogous to FCCZ4 [116].

We observe that (E.19), the evolution equation for γ_{ij}, is unchanged from the ADM case and therefore the evolution equations for χ and $\hat{\gamma}_{ij}$ are the same as in FCCZ4 and GBSSN [37, 116]:

$$\mathcal{L}_m\chi = -\frac{1}{6}\alpha K + \frac{1}{6}\widetilde{D}_m\beta^m, \tag{E.23}$$

$$\mathcal{L}_m\widetilde{\gamma}_{ij} = -2\alpha\widetilde{A}_{ij} - \frac{2}{3}\widetilde{\gamma}_{ij}\widetilde{D}_m\beta^m. \tag{E.24}$$

E.2.1 Evolution of the Extrinsic Curvature Trace

Beginning with the Lie derivative of K along m:

$$\mathcal{L}_mK = \gamma^{ij}\mathcal{L}_mK_{ij} + K_{ij}\mathcal{L}_m\gamma^{ij}, \tag{E.25}$$

and (E.20), the RZ4 form of the evolution of the extrinsic curvature, we substitute (E.19) for $\mathcal{L}_m\gamma^{ij}$, to find (5.33):

$$\begin{aligned}\mathcal{L}_mK &= \gamma^{ij}\mathcal{L}_mK_{ij} + K_{ij}\mathcal{L}_m\gamma^{ij} \qquad\qquad (E.26)\\ &= -D^iD_i\alpha + \alpha\left(R + K^2 - 2K_{ij}K^{ij}\right) + 4\pi\alpha\left(3\left[S-\rho\right] - 2S\right) + 2\alpha\gamma^{ij}\mathring{D}_{(i}\bar{Z}_{j)} + 2\alpha K_{ij}K^{ij}\\ &= -D^2\alpha + \alpha\left(R + K^2 + 2\gamma^{ij}\mathring{D}_{(i}\bar{Z}_{j)} + 4\pi\left(S - 3\rho\right)\right).\end{aligned}$$

E.2.2 Evolution of the Trace-Free Extrinsic Curvature

The evolution of $\mathcal{L}_m\widetilde{A}_{ij}$ is given by

$$\begin{aligned}\mathcal{L}_m\widetilde{A}_{ij} &= \mathcal{L}_m\left(e^{-4\chi}\left(K_{ij} - \frac{1}{3}\gamma_{ij}K\right)\right) \qquad\qquad (E.27)\\ &= -4\widetilde{A}_{ij}\mathcal{L}_m\chi + e^{-4\chi}\left(\mathcal{L}_mK_{ij} - \frac{1}{3}K\mathcal{L}_m\gamma_{ij} - \frac{1}{3}\gamma_{ij}\mathcal{L}_mK\right).\end{aligned}$$

If we express this equation in terms of the conformal decomposition and make use of (E.20) and (E.26), the RZ4 evolution equations for K_{ij} and K respectively, we find (5.36):

$$\begin{aligned}\mathcal{L}_m\widetilde{A}_{ij} &= e^{-4\chi}\left[-D_iD_j\alpha + \alpha R_{ij} - 8\pi\alpha S_{ij} + 2\alpha\mathring{D}_{(i}\bar{Z}_{j)}\right]^{\mathrm{TF}} + \alpha\left(K\widetilde{A}_{ij} - 2\widetilde{A}_{ik}\widetilde{A}^k{}_j\right) \qquad (E.28)\\ &\quad - \frac{2}{3}\widetilde{A}_{ij}\widetilde{D}_l\beta^l.\end{aligned}$$

Equivalently, we could start from the GBSSN equation for $\widetilde{A}_{ij}$ [9, 37]:

$$\mathcal{L}_m\widetilde{A}_{ij} = e^{-4\chi}\left[-D_iD_j\alpha + \alpha R_{ij} - 8\pi\alpha S_{ij}\right]^{\mathrm{TF}} + \alpha\left(K\widetilde{A}_{ij} - 2\widetilde{A}_{ik}\widetilde{A}^k{}_j\right) - \frac{2}{3}\widetilde{A}_{ij}\widetilde{D}_l\beta^l, \tag{E.29}$$

and note that (E.20) is, save for the term involving $\mathring{D}_{(i}\bar{Z}_{j)}$, identical to the ADM expression for the evolution for the extrinsic curvature. If we define

$$\bar{R}_{ij} = R_{ij} + 2\mathring{D}_{(i}\bar{Z}_{j)}, \tag{E.30}$$

and note that this new pseudo-curvature has the same symmetries as a true curvature, we may follow the GBSSN derivation of $\mathcal{L}_m\hat{A}_{ij}$ exactly and substitute the definition of this new quantity as a final step. Doing so recovers (5.36) in a much simpler manner.

E.2.3 Evolution of Theta

Essentially trivial substitution of the conformal variables into (E.21), the augmented Hamiltonian constraint, gives:

$$\mathcal{L}_m\Theta = \frac{\alpha}{2}\left(R - \hat{A}_{ij}\hat{A}^{ij} + \frac{2}{3}K^2 - 16\pi\rho\right) + \alpha\gamma^{ij}\mathring{D}_i\bar{Z}_j - \frac{\Theta}{\alpha}\mathcal{L}_m\alpha + \frac{\bar{Z}_i}{\alpha}\left(\mathcal{L}_m\beta^i - \beta^j\mathring{D}_j\beta^i\right). \quad \text{(E.31)}$$

E.2.4 Evolution of Lambda

From (5.28), the definition of $\widetilde{\Lambda}^i$ we find the following expression for the evolution of $\mathcal{L}_m\widetilde{\Lambda}^i$

$$\mathcal{L}_m\widetilde{\Lambda}^i = \mathcal{L}_m\widetilde{\Delta}^i + 2\mathcal{L}_m\big(\tilde{\gamma}^{ij}\bar{Z}_j\big). \quad \text{(E.32)}$$

In this expression, an expression for $\mathcal{L}_m\bar{Z}_i$ may be found through substitution of the conformal variables into (E.22):

$$\mathcal{L}_m\bar{Z}_i = \alpha\left(D_l\hat{A}^l{}_i - \frac{2}{3}D_iK - 8\pi j_i\right) - 2\bar{Z}_j\mathring{D}_i\beta^j + \Theta\mathring{D}_i\alpha + \alpha\mathring{D}_i\Theta. \quad \text{(E.33)}$$

Now, the quantity $\widetilde{\Delta}^i$ can be expressed in terms of the action of the flat space covariant derivative on the conformal metric:

$$\mathring{D}_j\tilde{\gamma}^{ij} = -\widetilde{\Delta}^i - \frac{1}{2}D_k\ln\left(\frac{\tilde{\gamma}}{\mathring{\gamma}}\right)\tilde{\gamma}^{ik}, \quad \text{(E.34)}$$

and, noting that since $\tilde{\gamma} = \mathring{\gamma}$ (we have chosen our conformal and flat space metrics to have the same determinant), $\widetilde{\Delta}^i$ may be expressed as:

$$\widetilde{\Delta}^i = -\mathring{D}_j\tilde{\gamma}^{ij}. \quad \text{(E.35)}$$

We may then find an evolution equation for $\widetilde{\Delta}^i$ entirely in terms of (E.24), the equation of motion for $\tilde{\gamma}_{ij}$, and the definition of $\widetilde{\Delta}^i{}_{jk}$:

$$\mathcal{L}_m\hat{\Delta}^i = \hat{\gamma}^{mn}\mathring{D}_m\mathring{D}_n\beta^i - 2\mathring{D}_j\left(\alpha\hat{A}^{ij}\right) + \frac{1}{3}\hat{\gamma}^{mi}\mathring{D}_m\mathring{D}_n\beta^n + \frac{2}{3}\hat{\Delta}^i\mathring{D}_m\beta^m. \quad \text{(E.36)}$$

Finally, (E.32) may be expressed as:

$$\begin{aligned}\mathcal{L}_m\widetilde{\Lambda}^i &= \mathcal{L}_m\widetilde{\Delta}^i + 2\mathcal{L}_m\big(\tilde{\gamma}^{ij}\bar{Z}_j\big), \quad \text{(E.37)}\\ &= \hat{\gamma}^{mn}\mathring{D}_m\mathring{D}_n\beta^i - 2\hat{A}^{ij}\mathring{D}_j\alpha + \frac{1}{3}\hat{\gamma}^{mi}\mathring{D}_m\mathring{D}_n\beta^n + \frac{2}{3}\widetilde{\Lambda}^i\widetilde{D}_n\beta^n + 4\alpha\bar{Z}_j\widetilde{A}^{ij} + 12\alpha\widetilde{A}^{li}\widetilde{\Delta}_l\chi\\ &\quad - \frac{4}{3}\alpha\widetilde{D}^iK - 16\pi\alpha\widetilde{j}^i + 2\alpha\widetilde{D}^i\Theta + 2\alpha\Theta\widetilde{D}^i\ln\alpha - 4\bar{Z}_l\tilde{\gamma}^{ij}\mathring{D}_j\beta^l.\end{aligned}$$

E.2.5 Simplifying Substitution

Equation (E.31) is not particularly well suited to evolution: when the lapse approaches 0, terms on the right hand side approach infinity. Fortunately, it can be regularized by defining a new evolutionary variable $\widetilde{\Theta}$ in terms of Θ, α, $\bar{Z}$ and β^i:

$$\Theta = \frac{\widetilde{\Theta}}{\alpha} + \frac{\beta^i\bar{Z}_i}{\alpha}. \quad \text{(E.38)}$$

In terms of these variables, we recover the evolution forms for $\mathcal{L}_m\widetilde{\Theta}$, $\mathcal{L}_m\widetilde{\Lambda}^i$ and $\mathcal{L}_m\bar{Z}_i$ expressed in (5.31), (5.37) and (5.38) respectively:

$$\mathcal{L}_m\widetilde{\Theta} = \frac{\alpha^2}{2}\left(R - \widetilde{A}_{ij}\widetilde{A}^{ij} + \frac{2}{3}K^2 - 16\pi\rho + 2\gamma^{ij}\mathring{D}_i\bar{Z}_j\right) - \beta^j\left(\beta^l\mathring{D}_j\bar{Z}_l + \mathring{D}_j\widetilde{\Theta}\right) \tag{E.39}$$
$$- \alpha\beta^j\left(D_l\widetilde{A}^l{}_j - \frac{2}{3}\widetilde{D}_jK - 8\pi j_j\right),$$

$$\mathcal{L}_m\widetilde{\Lambda}^i = \tilde{\gamma}^{mn}\mathring{D}_m\mathring{D}_n\beta^i - 2\widetilde{A}^{im}\widetilde{D}_m\alpha + 2\alpha\widetilde{A}^{mn}\widetilde{\Delta}^i{}_{mn} + \frac{1}{3}\widetilde{D}^i\widetilde{D}_n\beta^n + \frac{2}{3}\widetilde{\Lambda}^i\widetilde{D}_n\beta^n \tag{E.40}$$
$$+ 4\alpha\left(\bar{Z}_j\widetilde{A}^{ij} + 3\widetilde{A}^{li}\widetilde{D}_l\chi - \frac{1}{3}\widetilde{D}^iK - 4\pi\widetilde{j^i}\right) + 2\widetilde{D}^i\widetilde{\Theta} + 2\tilde{\gamma}^{ij}\left(\beta^l\ \mathring{D}_j\bar{Z}_l - \bar{Z}_l\mathring{D}_j\beta^l\right),$$

$$\mathcal{L}_m\bar{Z}_i = \alpha\left[D_l\widetilde{A}^l{}_i - \frac{2}{3}\widetilde{D}_iK - 8\pi j_i\right] - \bar{Z}_l\mathring{D}_i\beta^l + \beta^l\mathring{D}_i\bar{Z}_l + \mathring{D}_i\widetilde{\Theta}. \tag{E.41}$$

Appendix F

Hyperbolicity of FCCZ4 and GBSSN

Here we first provide an explicit calculation demonstrating the application of the technique of pseudodifferential reduction to a non-linear wave equation (Sec. F.1) in order to demonstrate hyperbolicity. In Sec. F.2 we turn our attention to the case of FCCZ4 as presented in Sec. 5.3 and demonstrate that FCCZ4 has the same principal part as RCCZ4. Finally, in Sec. F.3 we demonstrate that GBSSN has one additional zero-velocity mode corresponding to the non-dynamical Hamiltonian constraint. In what follows, we closely follow the work of Cao and Wu [39] on the hyperbolicity of a BSSN type formulation in $f(R)$ gravity.

F.1 Hyperbolicity of the Nonlinear Wave Equation

As a primer for the subsequent sections which demonstrate the conditions under which FCCZ4 and GBSSN may be made hyperbolic, we derive the conditions under which a non-linear wave equation is hyperbolic. Consider the second order PDE:

$$\partial_{tt}\psi = c(t,x^i)^2\partial^i\partial_i\psi - \mu^2\psi - \lambda\psi^3, \tag{F.1}$$

where ψ is a real scalar field, $c(t,x^i)$ is a generalized velocity and μ and λ are quadratic and quartic interaction potentials respectively.

In order for this system to be hyperbolic with characteristics which propagate at speed $\sim |c|$ in the high frequency limit, we must have $c(t,x^i)$ some real function. As an introductory exercise, we wish to verify this condition which essentially amounts to verifying that the given system admits a well defined Cauchy problem; i.e. that there exist no high frequency modes with growth rates which cannot be bounded by some exponential function of time. In brief, we can study strong hyperbolicity by linearizing the system about some generic solution and examining the resulting system in its high frequency regime where it can be written in the form

$$\partial_0 u = \mathbf{M}^i\partial_i u + \mathbf{S}u. \tag{F.2}$$

Here, u is a vector of n solution fields, $\mathbf{M}^i$ are n-by-n characteristic matrices and $\mathbf{S}u$ is a source vector that may depend on the fundamental variables u but not on their derivatives. Fourier transforming the solution u via

$$\hat{u}(\omega) = \int e^{i\omega\cdot x}u(x)\,\mathrm{d}^3x, \tag{F.3}$$

we can write (F.2) as

$$\partial_0\hat{u} = i\omega_i\mathbf{M}^i\hat{u} + \mathbf{S}\hat{u}. \tag{F.4}$$

From this, we define the principal symbol of the system as $\mathbf{P}_1 = i|\omega|\,\mathbf{P} = i\omega_i\mathbf{M}^i$. The nature of hyperbolicity of the system can then be discerned from the properties of $\mathbf{P}$:

- If **P** has imaginary eigenvalues, the system is not hyperbolic and cannot be formulated as a well-posed Cauchy problem.
- If **P** has only real eigenvalues but does not possess a complete set of eigenvectors, the system is weakly hyperbolic and may have issues with ill-posedness.
- If **P** has both real eigenvalues and a complete set of eigenvectors, the system is strongly hyperbolic and the Cauchy problem is well-posed.

We therefore consider the non-linear wave equation (F.1) written in first order in time form:

$$\partial_t \pi = c^2 \partial^i \partial_i \psi - \mu^2 \psi - \lambda^4 \psi^3, \tag{F.5}$$

$$\partial_t \psi = \pi \tag{F.6}$$

where we have suppressed the functional dependence of $c(t, x^i)$. As we are interested in the high frequency regime, we freeze the coefficients and perturb about some solution π_0, ψ_0:

$$\partial_t \left(\pi_0 + \delta\pi\right) = c^2 \partial^i \partial_i \left(\psi_0 + \delta\psi\right) - \mu^2 \left(\psi_0 + \delta\psi\right) - \lambda^4 \left(\psi_0 + \delta\psi\right)^3, \tag{F.7}$$

$$\partial_t \left(\psi_0 + \delta\psi\right) = \left(\pi_0 + \delta\pi\right). \tag{F.8}$$

Expanding and and keeping only terms which are first order in our perturbation, we find:

$$\partial_t \delta\pi = c^2 \partial^i \partial_i \delta\psi - \mu^2 \delta\psi - 3\lambda^4 \psi_0^2 \delta\psi, \tag{F.9}$$

$$\partial_t \delta\psi = \delta\pi. \tag{F.10}$$

Fourier transforming the resulting linear constant coefficient problem (and adopting the convention that hatted quantities represent the Fourier transforms of the perturbation while untransformed quantities are the background solution), we find:

$$\partial_t \hat{\pi} = -c^2 \gamma^{ij} \omega_i \omega_j \hat{\psi} - \mu^2 \hat{\psi} - 3\lambda^4 \psi^2 \hat{\psi}, \tag{F.11}$$

$$\partial_t \hat{\psi} = \hat{\pi}. \tag{F.12}$$

We then introduce the variables:

$$\omega_i = |\omega| \, \widetilde{\omega}_i, \tag{F.13}$$

$$|\omega|^2 = \gamma^{ij} \omega_i \omega_j, \tag{F.14}$$

$$\hat{\psi} = \frac{-i}{|\omega|} \hat{\Phi}, \tag{F.15}$$

which permit us to write (F.52–F.59) as a first order pseudodifferential system of the form

$$\partial_t \hat{u} = i \, |\omega| \, \mathbf{P} \hat{u}. \tag{F.16}$$

Explicitly, to leading order in $|\omega|$:

$$\partial_t \begin{bmatrix} \hat{\pi} \\ \hat{\Phi} \end{bmatrix} = i \, |\omega| \begin{bmatrix} 0 & c^2 \\ 1 & 0 \end{bmatrix} \begin{bmatrix} \hat{\pi} \\ \hat{\Phi} \end{bmatrix}, \tag{F.17}$$

and we find that **P** has eigenvalues $\lambda = \pm\sqrt{c^2}$ with a complete set of eigenvectors provided that $c \neq 0$. Therefore, in order for (F.1) to represent a hyperbolic wave equation, we recover the known result that c must be some non-zero real function.

F.2 Hyperbolicity of FCCZ4

Here, we analyse the FCCZ4 formulation of Sanchis-Gual et al. (5.44)–(5.50) taking Z_i as the evolutionary variable and using natural extensions to the generalized lapse and shift of Sec. 5.5. Defining

$$\partial_0 = \partial_t - \beta^i \partial_i, \tag{F.18}$$

these gauge conditions take the form:

$$\partial_0 \alpha = -\alpha^2 h\left(\alpha, \chi, x^\mu\right)\left(K - K_0 - m'\left(\alpha, \chi, x^\mu\right)\Theta\right), \tag{F.19}$$

$$\partial_0 \beta^i = \alpha^2 G\left(\alpha, \chi, x^\mu\right) B^i, \tag{F.20}$$

$$\partial_0 B^i = e^{-4\chi} H\left(\alpha, \chi, x^\mu\right) \partial_0 \widetilde{\Lambda}^i - \eta\left(B^i, \alpha, x^\mu\right). \tag{F.21}$$

Freezing coefficients in the differential equations and analyzing the linear constant coefficient problem by means of a Fourier transform as in Secs. F.1 and 5.5, the vacuum equations (to leading order) become:

$$\partial_0 \hat{\chi} = -\frac{1}{6}\alpha \hat{K} + \frac{1}{6}\left(i\omega_k\right)\hat{\beta}^k, \tag{F.22}$$

$$\partial_0 \hat{K} = \alpha \hat{R} + \omega_l \omega_m \gamma^{lm} \hat{\alpha} + 2\alpha \gamma^{lm}\left(i\omega_l \hat{Z}_m\right), \tag{F.23}$$

$$\partial_0 \hat{\Theta} = \frac{1}{2}\alpha\left(\hat{R} + 2\left(i\omega_i\right)\hat{Z}_j \gamma^{ij}\right), \tag{F.24}$$

$$\partial_0 \hat{\tilde{\gamma}}_{ij} = -2\alpha \hat{\tilde{A}}_{ij} - \frac{2}{3}\tilde{\gamma}_{ij}\left(i\omega_m\right)\hat{\beta}^m + \tilde{\gamma}_{im}\left(i\omega_j\right)\hat{\beta}^m + \tilde{\gamma}_{mj}\left(i\omega_i\right)\hat{\beta}^m, \tag{F.25}$$

$$\partial_0 \hat{\tilde{A}}_{ij} = e^{-4\chi}\left[\omega_i \omega_j \gamma^{ij}\hat{\alpha} + \alpha \hat{R}_{ij} + 2\alpha\left(i\omega_{(i}\hat{Z}_{j)}\right)\right]^{\mathrm{TF}}, \tag{F.26}$$

$$\partial_0 \hat{Z}_i = \alpha\left[\left(i\omega_j\right)\hat{\tilde{A}}_{ki}\tilde{\gamma}^{jk} - \frac{2}{3}\left(i\omega_i\right)\hat{K} + \left(i\omega_i\right)\hat{\Theta}\right], \tag{F.27}$$

$$\partial_0 \hat{\tilde{\Lambda}}^i = \tilde{\gamma}^{mn}\left(-\omega_m\omega_n\right)\hat{\beta}^i + \frac{1}{3}\tilde{\gamma}^{ik}\left(-\omega_k\omega_n\right)\hat{\beta}^n - \frac{4}{3}\alpha\tilde{\gamma}^{ij}\left(i\omega_j\right)\hat{K} + 2\alpha\tilde{\gamma}^{ik}\left(i\omega_k\right)\hat{\Theta}, \tag{F.28}$$

$$\partial_0 \hat{\alpha} = -\alpha^2 h \hat{K} + \alpha^2 m h \hat{\Theta}, \tag{F.29}$$

$$\partial_0 \hat{\beta}^i = \alpha^2 G \hat{B}^i, \tag{F.30}$$

$$\partial_0 \hat{B}^i = 2H\gamma^{im}\partial_0 \hat{Z}_m + H\left(i\omega^n\right)\tilde{\gamma}^{mi}\partial_0 \hat{\tilde{\gamma}}_{mn}, \tag{F.31}$$

and, as for the case of RCCZ4 in Sec. 5.5, $\widetilde{R}_{ij}$ may may once again be either be considered as a function of $\widetilde{\Lambda}^i$ or as a function of $\widetilde{\Delta}^i$. As with RCCZ4, (F.22)–(F.31) may be expressed by projecting rank-2 tensors and covectors according to (5.112) and (5.117) respectively. For the scalar components (1), we have:

$$\partial_0 \hat{a} = i\left|\omega\right|\alpha\left[-h\hat{K} + hm'\hat{\Theta}\right], \tag{F.32}$$

$$\partial_0 \hat{b} = i\left|\omega\right|\alpha\left[G\hat{B}\right], \tag{F.33}$$

$$\partial_0 \hat{B} = i\left|\omega\right|\alpha\left[\frac{4H}{3}\hat{b} - \frac{4H}{3}\hat{K} + 2H\hat{\Theta}\right], \tag{F.34}$$

$$\partial_0 \hat{X} = i\left|\omega\right|\alpha\left[\frac{1}{6}\hat{b} - \frac{1}{6}\hat{K}\right], \tag{F.35}$$

$$\partial_0 \hat{l} = i\left|\omega\right|\alpha\left[\frac{4}{3}\hat{b} - 2\hat{L}\right], \tag{F.36}$$

$$\partial_0 \hat{l}' = i\,|\omega|\,\alpha\left[-\frac{4}{3}\hat{b} + 2\hat{L}\right], \tag{F.37}$$

$$\partial_0 \hat{K} = i\,|\omega|\,\alpha\left[-\hat{a} - 8\hat{X} + \frac{1}{2}\hat{l} - \frac{1}{2}\hat{l}' + 2\epsilon\hat{Z}\right], \tag{F.38}$$

$$\partial_0 \hat{\Theta} = i\,|\omega|\,\alpha\left[-4\hat{X} + \frac{1}{4}\hat{l} - \frac{1}{4}\hat{l}' + \epsilon\hat{Z}\right], \tag{F.39}$$

$$\partial_0 \hat{L} = i\,|\omega|\,\alpha\left[-\frac{2}{3}\hat{a} - \frac{4}{3}\hat{X} + \frac{1}{3}\hat{l} + \frac{1}{6}\hat{l}' + \frac{4\epsilon}{3}\hat{Z}\right], \tag{F.40}$$

$$\partial_0 \hat{Z} = i\,|\omega|\,\alpha\left[\hat{L} - \frac{2}{3}\hat{K} + \hat{\Theta}\right], \tag{F.41}$$

where, as in the case of RCCZ4, we have $\hat{L}' = -\hat{L}$. In terms of the vector components (2), we find:

$$\partial_0 \hat{b}_i' = i\,|\omega|\,\alpha\left[G\hat{B}_i'\right], \tag{F.42}$$

$$\partial_0 \hat{B}_i' = i\,|\omega|\,\alpha\left[H\hat{b}_i'\right], \tag{F.43}$$

$$\partial_0 \hat{l}_i' = i\,|\omega|\,\alpha\left[\hat{b}_i' - 2\hat{L}_i'\right], \tag{F.44}$$

$$\partial_0 \hat{L}_i' = i\,|\omega|\,\alpha\left[\epsilon\hat{Z}_i'\right], \tag{F.45}$$

$$\partial_0 \hat{Z}_i' = i\,|\omega|\,\alpha\left[\hat{L}_i'\right]. \tag{F.46}$$

Finally, for the tensor components (3) we have:

$$\partial_0 \hat{l}'_{\langle ij\rangle} = i\,|\omega|\,\alpha\left[-2\hat{L}'_{\langle ij\rangle}\right], \tag{F.47}$$

$$\partial_0 \hat{L}'_{\langle ij\rangle} = i\,|\omega|\,\alpha\left[-\frac{1}{2}\hat{l}'_{\langle ij\rangle}\right]. \tag{F.48}$$

Under the substitutions $\hat{\Theta} \to \hat{\Omega}$ and $m' \to m$, (F.32)–(F.48) are the same equations as the pseudodifferential decomposition of RCCZ4 of Sec. 5.5. We conclude that RCCZ4 and FCCZ4 share identical stability characteristics in the high frequency limit and both possess well-posed initial value formulations provided the conditions derived in Sec. 5.5 hold.

F.3 Hyperbolicity of GBSSN

As a point of comparison to RCCZ4 and FCCZ4, we rederive the conditions under which GBSSN is hyperbolic, following the procedure of Cao and Wu [39] who have previously applied this method to studying the hyperbolicity of BSSN in $f(R)$ gravity. In these calculations, we use the GBSSN formulation of Brown [37] as presented in (5.52–5.56). For our gauge, we choose a natural modification of the gauge of Sec. 5.5 as it applies to GBSSN (using the convention that the $\widetilde{\Lambda}^i$ rather than $\widetilde{\Delta}^i$ are the dynamical quantities):

$$\partial_0 \alpha = -\alpha^2 h\left(\alpha, \chi, x^\mu\right)\left(K - K_0\left(x^\mu\right)\right), \tag{F.49}$$

$$\partial_0 \beta^i = \alpha^2 G\left(\alpha, \chi, x^\mu\right) B^i, \tag{F.50}$$

$$\partial_0 B^i = e^{-4\chi} H\left(\alpha, \chi, x^\mu\right) \partial_0 \widetilde{\Lambda}^i - \eta\left(B^i, \alpha, x^\mu\right). \tag{F.51}$$

As with RCCZ4 and FCCZ4, we consider the case of GBSSN in the vacuum. After freezing the coefficients in the differential equations (5.52)–(5.56) and Fourier transforming the resulting linear constant coefficient problem, we find:

$$\partial_0 \hat{\chi} = -\frac{1}{6}\alpha \hat{K} + \frac{1}{6}\left(i\omega_k\right)\hat{\beta}^k, \tag{F.52}$$

$$\partial_0 \hat{K} = \omega_i \omega_j \gamma^{ij} \hat{\alpha}, \tag{F.53}$$

$$\partial_0 \hat{\tilde{\gamma}}_{ij} = -2\alpha \hat{\tilde{A}}_{ij} - \frac{2}{3}\tilde{\gamma}_{ij}\left(i\omega_m\right)\hat{\beta}^m + \tilde{\gamma}_{im}\left(i\omega_j\right)\hat{\beta}^m + \tilde{\gamma}_{mj}\left(i\omega_i\right)\hat{\beta}^m, \tag{F.54}$$

$$\partial_0 \hat{\tilde{A}}_{ij} = e^{-4\chi}\left[\omega_i\omega_j\gamma^{ij}\hat{\alpha} + \alpha\hat{R}_{ij}\right]^{\mathrm{TF}}, \tag{F.55}$$

$$\partial_0 \hat{\tilde{\Lambda}}^i = -\omega_k\omega_l\hat{\gamma}^{kl}\hat{\beta}^i - 2\alpha\tilde{\gamma}^{ik}\tilde{\gamma}^{jl}\left(i\omega_j\hat{\tilde{A}}_{kl}\right) - \frac{4}{3}\alpha\tilde{\gamma}^{ij}\left(i\omega_j\right)\hat{K} - \frac{1}{3}\tilde{\gamma}^{ij}\omega_j\omega_l\hat{\beta}^l, \tag{F.56}$$

$$\partial_0 \hat{\alpha} = -\alpha^2 h \hat{K}, \tag{F.57}$$

$$\partial_0 \hat{\beta}^i = \alpha^2 G \hat{B}^i, \tag{F.58}$$

$$\partial_0 \hat{B}^i = e^{-4\chi} H\left[\partial_0 \hat{\tilde{\Lambda}}^i\right], \tag{F.59}$$

where $\widetilde{R}_{ij}$ is understood to be a function of $\widetilde{\Lambda}^i$. As before, Eqns. (F.52)–(F.59) may be expressed by projecting rank-2 tensors and covectors according to (5.112) and (5.117) respectively. After a somewhat lengthy calculation, we find the following results for (1) the scalar components:

$$\partial_0 \hat{a} = i\left|\omega\right|\alpha\left[-h\hat{K}\right], \tag{F.60}$$

$$\partial_0 \hat{b} = i\left|\omega\right|\alpha\left[G\hat{B}\right], \tag{F.61}$$

$$\partial_0 \hat{B} = i\left|\omega\right|\alpha\left[\frac{4H}{3}\hat{b} - \frac{4H}{3}\hat{K}\right], \tag{F.62}$$

$$\partial_0 \hat{X} = i\left|\omega\right|\alpha\left[\frac{1}{6}\hat{b} - \frac{1}{6}\hat{K}\right], \tag{F.63}$$

$$\partial_0 \hat{l} = i\left|\omega\right|\alpha\left[\frac{4}{3}\hat{b} - 2\hat{L}\right], \tag{F.64}$$

$$\partial_0 \hat{l}' = i\left|\omega\right|\alpha\left[-\frac{4}{3}\hat{b} + 2\hat{L}\right], \tag{F.65}$$

$$\partial_0 \hat{K} = i\left|\omega\right|\alpha\left[-\hat{a}\right], \tag{F.66}$$

$$\partial_0 \hat{L} = i\left|\omega\right|\alpha\left[-\frac{2}{3}\hat{a} - \frac{4}{3}\hat{X} - \frac{1}{3}\hat{l} + \frac{1}{6}\hat{l}' + \frac{2}{3}\hat{\Lambda}\right], \tag{F.67}$$

$$\partial_0 \hat{\Lambda} = i\left|\omega\right|\alpha\left[\frac{4}{3}\hat{b} - \frac{4}{3}\hat{K}\right], \tag{F.68}$$

(2) the vector components:

$$\partial_0 \hat{b}'_i = i\left|\omega\right|\alpha\left[G\hat{B}'_i\right], \tag{F.69}$$

$$\partial_0 \hat{B}'_i = i\left|\omega\right|\alpha\left[H\hat{b}'_i\right], \tag{F.70}$$

$$\partial_0 \hat{l}'_i = i\left|\omega\right|\alpha\left[\hat{b}'_i - 2\hat{L}'_i\right], \tag{F.71}$$

$$\partial_0 \hat{L}'_i = i\,|\omega|\,\alpha\left[\frac{1}{2}\hat{\Lambda}'_i - \frac{1}{2}\hat{l}'_i\right], \tag{F.72}$$

$$\partial_0 \hat{\Lambda}'_i = i\,|\omega|\,\alpha\left[\hat{b}'_i\right], \tag{F.73}$$

and (3) the tensor components:

$$\partial_0 \hat{l}'_{\langle ij\rangle} = i\,|\omega|\,\alpha\left[-2\hat{L}'_{\langle ij\rangle}\right], \tag{F.74}$$

$$\partial_0 \hat{L}'_{\langle ij\rangle} = i\,|\omega|\,\alpha\left[-\frac{1}{2}\hat{l}'_{\langle ij\rangle}\right], \tag{F.75}$$

respectively. Computing the eigenvalues and eigenvectors of $\mathbf{P}^{\mathrm{S}}$ we find:

$$\lambda = 0, 0, 0, \pm 1, \pm\sqrt{\frac{4}{3}GH}, \pm\sqrt{h}. \tag{F.76}$$

Examining these in detail, we observe that GBSSN has one more zero velocity eigenvalue than RCCZ4 and FCCZ4. It is this eigenvalue which corresponds to the Hamiltonian constraint advection and is largely responsible for the superior performance of FCCZ4 relative to GBSSN [47, 63]. In the case of the vector components, the eigenvalues of the matrix $\mathbf{P}^{\mathrm{V}}$ once again have multiplicity 2 and are:

$$\lambda = 0, \pm 1, \pm\sqrt{GH}. \tag{F.77}$$

Finally, for the tensor components, the eigenvalues of $\mathbf{P}^{\mathrm{T}}$ have multiplicity 2 and take the form:

$$\lambda = \pm 1. \tag{F.78}$$

In order to guarantee weak hyperbolicity, these eigenvalues must be real with

$$GH > 0,\ h > 0. \tag{F.79}$$

Strong hyperbolicity requires that the matrix $\mathbf{P}$ is diagonalizable and, in addition to requiring real eigenvalues, demands

$$h \neq \frac{4GH}{3}, \tag{F.80}$$

for the diagonalizability condition to be met.

Appendix G

Derivation of the Embedded Covariant and Conformal Maxwell Equations

Here we derive the equations of motion for the source-free Maxwell fields of Chapter 6.2. We follow a procedure similar to Palenzuela et al. [95] and Komissarov [71] by embedding the Maxwell equations within a larger system. Analogous to the manner in which BSSN type formulations embed general relativity within variations of the Z4 system [9, 47], this embedding allows us to associate the constraint equations with propagating degrees of freedom.

G.1 Maxwell Equations in Curved Space

Consider first the Maxwell equations written in tensor form using units where the speed of light, c, and vacuum magnetic permeability, μ_0, are both unity:

$$\nabla_\mu F^{\nu\mu} = j^\nu, \tag{G.1}$$

$$\nabla_\mu {}^\star F^{\nu\mu} = 0. \tag{G.2}$$

Here $F_{\mu\nu}$ is a completely antisymmetric tensor known as the Maxwell tensor, ${}^\star F_{\mu\nu}$ is the Faraday tensor and j^μ is the 4-vector of electric current. When both the electric and magnetic susceptibility of the medium vanish, the Faraday tensor is the dual of the Maxwell tensor

$${}^\star F^{\mu\nu} = \frac{1}{2}\tilde{\epsilon}^{\mu\nu\gamma\delta} F_{\gamma\delta}. \tag{G.3}$$

In (G.3), $\tilde{\epsilon}^{\mu\nu\gamma\delta}$ is the Levi-Civita tensor which is itself defined in terms of the Levi-Civita symbol and metric determinant $|g|$:

$$\tilde{\epsilon}^{abcd} = \frac{(-1)}{\sqrt{|g|}}\epsilon^{abcd}, \tag{G.4}$$

The Maxwell tensor may be used to construct the electromagnetic stress-energy tensor:

$$T^{\mu\nu} = F^{\mu\alpha}F^{\nu}{}_{\alpha} - \frac{1}{4}g^{\mu\nu}F_{\alpha\beta}F^{\alpha\beta}. \tag{G.5}$$

G.2 Embedded Maxwell Equations

Again, rather than use (G.1)–(G.2) and a vector potential decomposition of $F_{\mu\nu}$, we incorporate the Maxwell equations into a larger system, similarly to how the GBSSN and FCCZ4 formalisms embed general relativity within variations of the Z4 system [9, 47]. In the case of general relativity, this embedding enables the Hamiltonian and momentum constraints to be expressed through

propagating degrees of freedom (see Appendices C–E). Analogously, for the Maxwell fields, we can tie the divergence conditions to propagating degrees of freedom [71, 95]:

$$\nabla_\mu \left(F^{\nu\mu} + g^{\nu\mu}\Psi_E\right) = -\sigma n^\nu \Psi_E + j^\nu, \tag{G.6}$$

$$\nabla_\mu \left({}^\star F^{\nu\mu} + g^{\nu\mu}\Psi_B\right) = -\sigma n^\nu \Psi_B. \tag{G.7}$$

Here, σ is a dimensionful damping parameter and Ψ_E and Ψ_B are constraint fields which couple to the violation of the divergence conditions for the electric and magnetic fields, respectively. By promoting the constraints to propagating degrees of freedom, our solutions gain additional stability and exhibit advection and damping of constraint violations which would otherwise accumulate.

By decomposing the Maxwell and Faraday tensors into electric, E^α, and magnetic, B^α, fields:

$$E^\alpha = F^{\alpha\beta} n_\beta, \tag{G.8}$$

$$B^\alpha = {}^\star F^{\beta\alpha} n_\beta, \tag{G.9}$$

$$F^{\alpha\beta} = n^\alpha E^\beta - n^\beta E^\alpha + \tilde{\epsilon}^{\gamma\delta\alpha\beta} n_\gamma B_\delta, \tag{G.10}$$

$${}^\star F^{\alpha\beta} = n^\beta B^\alpha - n^\alpha B^\beta + \tilde{\epsilon}^{\gamma\delta\alpha\beta} n_\gamma E_\delta, \tag{G.11}$$

and defining the charge density, ρ, and current density, J_i by projecting j^μ onto and orthogonal to our foliation:

$$\rho = -n_\mu j^\mu \tag{G.12}$$

$$J^i = \gamma^i{}_\mu j^\mu \tag{G.13}$$

we can express (G.6) and (G.6) in terms of evolution equations for E^α, B^α, Ψ_E and Ψ_B:

$$\mathcal{L}_m E^i = \tilde{\epsilon}^{ijk} D_j \left(\alpha B_k\right) + \alpha K E^i + \alpha \gamma^{ij} D_j \Psi_E - J^i, \tag{G.14}$$

$$\mathcal{L}_m B^i = -\tilde{\epsilon}^{ijk} D_j \left(\alpha E_k\right) + \alpha K B^i - \alpha \gamma^{ij} D_j \Psi_B, \tag{G.15}$$

$$\mathcal{L}_m \Psi_E = \alpha \left[D_i E^i + \sigma \Psi_E - \rho\right], \tag{G.16}$$

$$\mathcal{L}_m \Psi_B = \alpha \left[-D_i B^i + \sigma \Psi_B\right]. \tag{G.17}$$

Here, as in previous chapters, $\mathcal{L}_m = \partial_t - \mathcal{L}_\beta$ is the Lie derivative along $m^\mu = \alpha n^\mu$.

From the anti-symmetry of F^{ab} and the definition of n_b, it is obvious that E^a and B^a are both purely spatial vectors. As $F^{\mu\nu}$ and ${}^\star F^{\mu\nu}$ are true tensors, their unique contractions $F_{\mu\nu}{}^\star F^{\mu\nu}$ and $F_{\mu\nu}F^{\mu\nu}$ are coordinate invariant scalars which have dimension length^{-2} like the Ricci scalar.

G.3 Evolution Equations for Ψ_E and Ψ_B

We begin our derivation of (G.14)–(G.17) by contracting (G.6) with the unit normal to the hypersurface, n^α

$$n_\alpha \nabla_\beta \left(F^{\alpha\beta} + g^{\alpha\beta}\Psi_E\right) = \sigma \Psi_E - \rho\,. \tag{G.18}$$

Via the definition of the extrinsic curvature

$$\nabla_\nu n_\mu = -K_{\mu\nu} - D_\mu \ln(\alpha) n_\nu \tag{G.19}$$

and (G.10), the definition of $F^{\mu\nu}$ in terms of the electric and magnetic fields, (G.18) becomes:

$$-\nabla_\mu E^\mu + n^\mu \nabla_\mu \Psi_E + E^\mu D_\mu \ln\left(\alpha\right) = \sigma \Psi_E - \rho. \tag{G.20}$$

Employing the identity

$$\begin{aligned}\nabla_\mu E^\mu &= \frac{1}{\alpha\sqrt{\gamma}}\partial_\mu\left(\alpha\sqrt{\gamma}E^\mu\right), \\ &= E^i D_i \ln(\alpha) + D_i E^i,\end{aligned} \tag{G.21}$$

we can express (G.20) as

$$n^\nu \nabla_\nu \Psi_E = D_i E^i + \sigma\Psi_E - \rho. \tag{G.22}$$

Written in terms of the Lie derivative, we recover (G.16):

$$\mathcal{L}_m \Psi_E = \alpha\left[D_i E^i + \sigma\Psi_E - \rho\right]. \tag{G.23}$$

We find (G.17) in an exactly analogous manner by contracting (G.7) with n_α and following the procedure outlined above.

G.4 Evolution Equations for E^a and B^a

Expanding (G.7):

$$\nabla_\nu\left({}^\star F^{\mu\nu} + g^{\mu\nu}\Psi_B\right) = -\sigma n^\mu \Psi_B, \tag{G.24}$$

$$\nabla_\nu\left(-n^\mu B^\nu + n^\nu B^\mu + \tilde{\epsilon}_{\lambda\sigma}{}^{\mu\nu} n^\lambda E^\sigma + g^{\mu\nu}\Psi_B\right) = -\sigma n^\mu \Psi_B, \tag{G.25}$$

and concentrating on the magnetic components we have:

$$\begin{aligned}\nabla_\nu\left(-n^\mu B^\nu + n^\nu B^\mu\right) &= -\nabla_\nu n^\mu B^\nu - n^\mu \nabla_\nu B^\nu + \nabla_\nu n^\nu B^\mu + n^\nu \nabla_\nu B^\mu, \\ &= n^\nu \nabla_\nu B^\mu - B^\nu \nabla_\nu n^\mu - n^\mu \nabla_\nu B^\nu + B^\mu \nabla_\nu n^\nu, \\ &= \mathcal{L}_n B^\mu - n^\mu \nabla_\nu B^\nu + B^\mu \nabla_\nu n^\nu, \\ &= \mathcal{L}_n B^\mu - n^\mu \nabla_\nu B^\nu - K B^\mu,\end{aligned} \tag{G.26}$$

where we have made use of the fact that $B^\mu n_\mu = 0$. Expressing $\mathcal{L}_n B^\mu$ in terms of $\mathcal{L}_m B^\mu$:

$$\begin{aligned}\nabla_\nu\left(-n^\mu B^\nu + n^\nu B^\mu\right) &= \frac{1}{\alpha}\mathcal{L}_m B^\mu + \frac{1}{\alpha} n^\mu B^\nu D_\nu \alpha - n^\mu \nabla_\nu B^\nu - K B^\mu, \\ &= \frac{1}{\alpha}\mathcal{L}_m B^\mu - K B^\mu - \left(\nabla_\nu B^\nu - B^\nu D_\nu \ln\alpha\right) n^\mu \\ &= \frac{1}{\alpha}\mathcal{L}_m B^\mu - n^\mu D_\nu B^\nu - K B^\mu\end{aligned} \tag{G.27}$$

Turning our attention to the electric components, we note that $\nabla_\mu\sqrt{|g|} = 0$ and the electric simplify may be written as:

$$\begin{aligned}\nabla_\nu(\tilde{\epsilon}_{\lambda\sigma}{}^{\mu\nu} n^\lambda E^\sigma) &= \nabla_\nu\left(n_\lambda E_\sigma\right)\tilde{\epsilon}^{\lambda\sigma\mu\nu}, \\ &= -\tilde{\epsilon}^{\lambda\sigma\mu\nu} E_\sigma n_\nu D_\lambda(\ln\alpha) + \tilde{\epsilon}^{\lambda\sigma\mu\nu} n_\lambda \nabla_\nu E_\sigma.\end{aligned} \tag{G.28}$$

Repeatedly inserting the identity $g^\mu{}_\nu = \delta^\mu{}_\nu = \gamma^\mu{}_\nu - n^\mu n_\nu$ into $\tilde{\epsilon}^{\lambda\sigma\mu\nu} n_\lambda \nabla_\nu E_\sigma$, we find:

$$\begin{aligned}\nabla_\nu(\tilde{\epsilon}_{\lambda\sigma}{}^{\mu\nu} n^\lambda E^\sigma) &= -\tilde{\epsilon}^{\lambda\sigma\mu\nu} E_\sigma n_\nu D_\lambda(\ln\alpha) + \tilde{\epsilon}^{\lambda\sigma\mu\nu} n_\lambda D_\nu E_\sigma, \\ &= \frac{1}{\alpha}\tilde{\epsilon}^{\nu\mu\lambda\sigma} D_\lambda\left(\alpha E_\sigma\right) n_\nu.\end{aligned} \tag{G.29}$$

Next, we express $\nabla_\nu g^{\mu\nu}\Psi_B$ in terms of quantities defined on our foliation,

$$\begin{aligned}\nabla_\nu \left(g^{\mu\nu}\Psi_B\right) &= \left(\gamma^{\mu\nu} - n^\mu n^\nu\right)\nabla_\nu \Psi_B \\ &= \gamma^{\mu\nu}\nabla_\nu\Psi_B - n^\mu \mathcal{L}_n \Psi_B \\ &= \gamma^{\mu\nu} D_\nu \Psi_B - n^\mu \left[-D_\nu B^\nu + \sigma\Psi_B\right]\end{aligned} \tag{G.30}$$

Now that we have representations of the magnetic, electric and scalar sectors of (G.25), we can substitute each of (G.27), (G.29) and (G.30) into (G.25) to give:

$$\begin{aligned}&\nabla_\nu\left(-n^\mu B^\nu + n^\nu B^\mu + \tilde{\epsilon}_{\lambda\sigma}{}^{\mu\nu} n^\lambda E^\sigma + g^{\mu\nu}\Psi_B\right) + \sigma n^\mu \Psi_B = 0, \\ &\frac{1}{\alpha}\mathcal{L}_m B^\mu - K B^\mu + \frac{1}{\alpha}\tilde{\epsilon}^{\nu\mu\lambda\sigma} n_\nu D_\lambda\left(\alpha E_\sigma\right) + \gamma^{\mu\nu} D_\nu \Psi_B = 0.\end{aligned} \tag{G.31}$$

Solving for $\mathcal{L}_m B^\mu$ and projecting on Σ_t (recall that $B^\mu n_\nu = E^\mu n_\mu = 0$) recovers (G.15):

$$\mathcal{L}_m B^i = -\tilde{\epsilon}^{ijk} D_j\left(\alpha E_k\right) + \alpha K B^i - \alpha\gamma^{ij} D_j \Psi_B. \tag{G.32}$$

The derivation of (G.14) follows a nearly identical procedure starting from (G.7) as opposed to (G.6) with the only significant departure being the projection of j^μ onto Σ_t.

G.5 Conformal Form of Evolution Equations

Trivial substitution of the conformal variables of Appendices C–E into (G.14)–(G.17) yields:

$$\mathcal{L}_m E^i = \hat{\epsilon}^{ijk}\hat{D}_j\left(\alpha B_k\right)e^{-6\chi} + \alpha K E^i + \alpha\gamma^{ij}\hat{D}_j\Psi_E - J^i, \tag{G.33}$$

$$\mathcal{L}_m B^i = -\hat{\epsilon}^{ijk}\hat{D}_j\left(\alpha E_k\right)e^{-6\chi} + \alpha K B^i - \alpha\gamma^{ij}\hat{D}_j\Psi_B, \tag{G.34}$$

$$\mathcal{L}_m \Psi_E = \alpha\left[e^{-6\chi}\hat{D}_i\left(e^{6\chi}E^i\right) + \sigma\Psi_E - \rho\right], \tag{G.35}$$

$$\mathcal{L}_m \Psi_B = \alpha\left[-e^{-6\chi}\hat{D}_i\left(e^{6\chi}B^i\right) + \sigma\Psi_B\right]. \tag{G.36}$$

These are the embedded covariant and conformal Maxwell Equations.

G.6 Heuristic Proof of Damping Properties

As a quick sanity check, it is worth verifying that these equations do, in fact, result in advection of constraint violations for the simple case of Minkowski spacetime without charge ($j^\mu = 0$). The following calculation shows that, at least in this limited flat space case, the constraints are advected and damped away from the source of the violations as desired.

Let $C_E = \partial_i E^i$ be the constraint violation of the electric field. Differentiating with respect to time and substituting (G.14) for $\partial_t E^i$ gives:

$$\begin{aligned}\partial_t C_E &= \partial_i \partial_t E^i, \\ &= \partial_i\left(\epsilon^{ijk}\partial_j B_k + \gamma^{ij}\partial_j\Psi_E\right), \\ &= \partial_i\partial^i\Psi_E.\end{aligned} \tag{G.37}$$

Differentiating once more in time and substituting (G.16) for $\partial_t \Psi_E$:

$$\begin{aligned} \partial_{tt} C_E &= \partial_i \partial^i \partial_t \Psi_E, \\ &= \partial_i \partial^i \partial_j E^j + \sigma \partial_i \partial^i \Psi_E, \\ &= \partial_i \partial^i C_E + \sigma \partial_i \partial^i \Psi_E, \\ &= \partial_i \partial^i C_E + \sigma \partial_t C_E, \end{aligned} \tag{G.38}$$

yields a damped wave equation for C_E:

$$\Box C_E = +\sigma \partial_t C_E. \tag{G.39}$$

For $\sigma < 0$, therefore, the constraint violations will be both advected away from their sources and damped. For $\sigma = 0$, the constraint violation propagates at the speed of light.

Appendix H

Achieving Smoothness at AMR Boundaries

In our use of adaptive mesh refinement (AMR) during our investigations of critical collapse, we repeatedly encountered issues related to irregularities arising at the grid refinement boundaries. These irregularities were observed to disrupt convergence and frequently resulted in spurious re-gridding and intolerably large constraint violations. In many cases the irregularities became so pathological that the errors thereby introduced would cause the AMR algorithm to attempt to use an essentially unbounded number of refinement levels. This appendix gives an overview of the methods we used to resolve these problems.

These methods were developed organically in response to issues arising from our attempts to resolve critical collapse using AMR as implemented in PAMR/AMRD [101, 102]. At the time of implementation (2017–2018), we were not aware that very similar methods had been previously employed by Mongwane in his 2015 treatment of AMR transition zones [88]. We therefore present our motivation and derivation but acknowledge that much of our method is virtually identical to previously published work. The primary differences appear to be in our motivation (Secs. H.3 and H.4), determination of parameters (Sec. H.6) and implementation of the distance function (Sec. H.7).

H.1 AMR in Brief

The Berger-Oliger approach to AMR, introduced in the 1980's [24] is one of the pioneering, and still most prevalent, approaches to adaptive mesh refinement. At the heart of this method is the idea of using a hierarchy of nested uniform grids to allocate additional resolution (which may be contrasted with other, grid free, approaches to achieve adaptive resolution). In the Berger-Oliger scheme, the computational domain is initially covered by a coarse grid and as the simulation progresses and additional resolution is required, child grids are introduced in regions of interest as depicted in Fig. H.1.

The location of these child grids is typically determined based on features of the solution being computed and may be based upon solution gradients, features of interest or estimates of local truncation error (see Sec 2.4). When new child grids are created at any level, initial data is determined by transfer of values from regions which overlap extant grids at that level, as well as by interpolation from the parent grid as necessary.

In order to ensure accuracy, fine grids are typically evolved using smaller time steps than the coarse grids and the boundaries of the fine grids are set using interpolation from the coarser parent grids. Conversely, when parent and child time levels are aligned, the values computed on the child grid are passed back to the parent grid using a restriction operation.

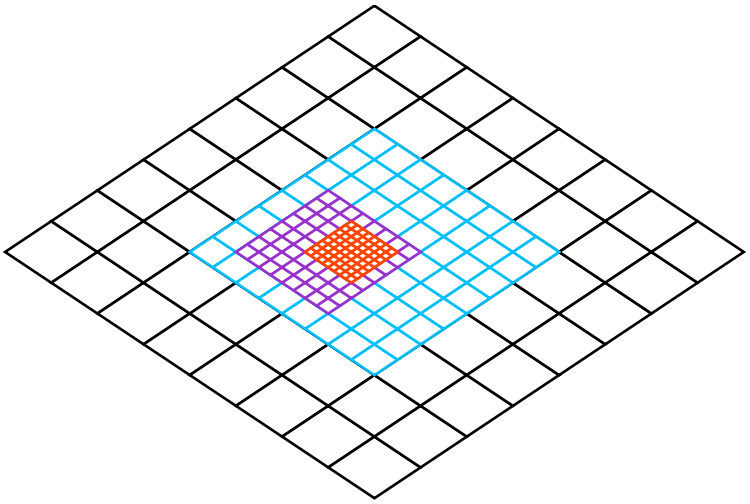

Figure H.1: An AMR grid consisting of 4 levels (displayed in black, blue, purple and red) with a 2:1 refinement ratio. In this example, the grids would be allocated using local truncation error estimates. The grid functions on each grid are evolved separately, but the boundaries of a refinement region are set via interpolation from the coarser parent grid. When time levels are aligned, the fine grid solution is injected onto the coarse level grid as described in [24, 101, 102]

H.2 Introduction and Conventions

In what follows we will assume two spatial dimensions, (x, y), but all techniques generalize readily to higher dimensions. We consider the problem of boundary interpolation in an AMR scheme following Berger and Oliger [24] except, as is the case for PAMR [102] and AMRD [101], we assume that child grids are aligned with the parent grid coordinate system and share common points in both space and time. For a parent grid at level l with coordinates ${}^{(l)}x_i$ and ${}^{(l)}y_j$ and grid spacings ${}^{(l)}h_x$ and ${}^{(l)}h_y$, any child grid will have an integer grid refinement ratio, ρ, relative to its parent. Specifically, the parent and child grid spacings satisfy:

$$ {}^{(l+1)}h_x = {}^{(l)}h_x/\rho, \tag{H.1} $$

$$ {}^{(l+1)}h_y = {}^{(l)}h_y/\rho, \tag{H.2} $$

and we assume that the edges of the child grids are aligned with points on the parent grids.

In what follows, we will assume that we are working with hyperbolic systems of equations such that each of the spatial grid spacings is h (i.e. ${}^{(l)}h_x = {}^{(l)}h_y = {}^{(l)}h$) and the temporal spacing at level l is given by ${}^{(l)}h_t = \lambda {}^{(l)}h$. Here λ is the Courant factor as discussed in Secs. 2.2–2.3. This restriction does not significantly change our analysis, but it does simplify notation. Furthermore, we will restrict our analysis to the case where $\rho = 2$, such that there is a factor of 2 refinement between successive levels in the grid hierarchy. Once again, this does not change the core of the analysis but it implies that if someone wishes to use this method in a code with refinement ratios different than 2, they should rederive the results of Sec. H.6.

We further assume that, for a region where the finest grid is at level l, the solution is well resolved both at level l and level $l-1$. In this case, we can sensibly invoke the Richardson ansatz [112] and calculate a local estimation of the truncation error on the interior of the fine grid. Assuming

that the grids are synchronized at time $t = t_0$ and that the integration is $O(h^p)$, then at time $t = t_0 + \lambda^{(l-1)}h$, the solution, $\tilde{u}$, on the fine ($^{(l)}\tilde{u}$) and coarse ($^{(l-1)}\tilde{u}$) grids within the interior will be:

$$^{(l)}\tilde{u} = u + 2\lambda h(h)^p\tilde{\epsilon}_p + \cdots, \tag{H.3}$$

$$^{(l-1)}\tilde{u} = u + 2\lambda h(2h)^p\tilde{\epsilon}_p + \cdots, \tag{H.4}$$

where $h = {}^{(l)}h = 1/2 \cdot {}^{(l-1)}h$, u is the continuum solution that would be found for initial data prescribed at $t = t_0$ and $\tilde{\epsilon}_p$ is the h-independent leading order error function in the Richardson expansion. From this, we can determine an approximate solution error $^{(l)}\tilde{e} = {}^{(l)}\tilde{u} - {}^{(l-1)}\tilde{u}$, and, if we had another coarse solution, $^{(l-2)}\tilde{u}$, we could calculate the convergence factor $Q(t)$ as in Sec 2.4:

$$Q(t) = \frac{||{}^{(l-2)}\tilde{u} - {}^{(l-1)}\tilde{u}||_x}{||{}^{(l-1)}\tilde{u} - {}^{(l)}\tilde{u}||_x}, \tag{H.5}$$

where $||\cdot||_x$ is some norm. If we are in the convergent regime, then we should find:

$$Q(t) \approx \frac{||4\lambda h(4h)^m - 4\lambda h(2h)^m||_x}{||4\lambda h(2h)^m - 4\lambda h(h)^m||_x} \approx 2^m. \tag{H.6}$$

H.3 Spatial Derivatives and Discontinuities

Returning to the unigrid case, consider a spatial differencing operator, $\mathbf{D}^h$, which is an approximation of some continuum operator $\mathbf{D}$ (see Sec. 2.5):

$$\mathbf{D}^h = \mathbf{D} + h^p\mathbf{D}_p + \cdots, \tag{H.7}$$

where $\mathbf{D}_p$ is some higher-order derivative operator. Let u^h be the solution of $\mathbf{D}^h(u^h) - f^h = 0$ (where f^h are some source functions) with Richardson expansion given by

$$u^h = u + h^p\epsilon_p + h^{p+1}\epsilon_{p+1} + \cdots. \tag{H.8}$$

Here, u is the solution of the continuum equation $D(u) - f = 0$ and, again, ϵ_p, ϵ_{p+1}, etc. are, by assumption, h-independent, smooth error functions. We can apply $\mathbf{D}^h$ to u^h to find:

$$\begin{aligned}\mathbf{D}^h(u^h) &= \left(\mathbf{D} + h^p\mathbf{D}_p + \cdots\right)\left(u + h^p\epsilon_p + \cdots\right), \\ &= \mathbf{D}\left(u + h^p\epsilon_p + \cdots\right) + h^p\mathbf{D}_p\left(u + h^p\epsilon_p + \cdots\right) + \cdots. \\ &= \mathbf{D}(u) + h^p\mathbf{D}(\epsilon_p) + h^p\mathbf{D}_p(u) \\ &= \mathbf{D}(u) + O(h^p).\end{aligned} \tag{H.9}$$

We thus see that the action of $\mathbf{D}^h$ on a solution u^h, which differs from u at p^{th} order, is equal to the action of $\mathbf{D}$ on u to p^{th} order.

It is important to realize that this is only true when u^h has a valid Richardson expansion (i.e. the leading order error terms, ϵ_p, are smooth functions). Instead of (H.8), assume that we had:

$$u^h = u + h^p\epsilon_p + h^{p+1}\epsilon_{p+1} + \cdots, \tag{H.10}$$

on one side of a hyperplane partitioning our solution and

$$u^h = u + h^p\tilde{\epsilon}_p + h^{p+1}\tilde{\epsilon}_{p+1} + \cdots, \tag{H.11}$$

on the other side of the partition. In this case, the action of $\mathbf{D}^h$ on u^h in the vicinity of the hyperplane would *no longer* be p^{th} order. Instead, it would be of order $p-d$, where d is the degree of the operator $\mathbf{D}^h$. This can be understood by recalling that any finite difference operator of order d contains a factor of $1/h^d$. If we apply a finite difference operator across a sudden change, e.g. a step function, the leading order term will be proportional to $1/h^d$. Therefore, application of a finite difference operator across a sudden change suppressed by a factor of h^p yields a leading order term proportional to h^{p-d}.

This is exactly what happens in the case of boundary interpolation in AMR: if the boundaries of grid functions on the fine levels are set with order $m < p + d$ interpolation, then we expect discontinuities to develop at the boundaries. In order to completely avoid this, we must therefore, naively, set grid boundaries using order $m \geq p + d$ temporal interpolation when the fine and coarse grids are not aligned. However, due to the fact that boundaries only account for a small portion of the domain, the condition for global (as opposed to local) convergence is that the boundaries must be set with order $(p + d - 1)$ temporal interpolation [24].

H.4 The Issue With Temporal Boundary Interpolation

By ensuring that the boundaries are set with the correct order interpolation, we can easily evolve all grids to synchronized time levels. Once there (and assuming the grid functions are adequately resolved on the coarse grids in the vicinity of the boundaries), recursive injection of grid functions ensures that all grids are ready to be further evolved.

The only issue is that it is actually quite challenging to set up a Berger & Oliger AMR scheme with order $(p+d-1)$ temporal interpolation. Consider the extremely simple case of a wave equation cast in first order form. First make the definitions:

$$\pi \equiv \partial_t \psi, \tag{H.12}$$

$$\phi \equiv \partial_x \psi. \tag{H.13}$$

Then the wave equation can be written as the system

$$\partial_t \pi = \partial_x \phi, \tag{H.14}$$

$$\partial_t \phi = \partial_x \pi. \tag{H.15}$$

Using a simple 2^{nd} order integration scheme (Crank-Nicolson or RK2 with a 3-point spatial stencil for example), we find $p = 2$, $d = 1$, and we therefore require only 2^{nd} order temporal interpolation and two time levels. If we use the second order form of the wave equation however:

$$\partial_t \psi = \pi. \tag{H.16}$$

$$\partial_t \pi = \partial_{xx} \psi, \tag{H.17}$$

and want to make use of a 4^{th} order evolution scheme, we would find $p = 4$, $d = 2$ and would require 5^{th} order temporal interpolation which in turn would require five time levels. Given that AMR is adaptive, there is no guarantee that the AMR hierarchy would even contain the coarse points necessary to perform the interpolation. In short, this implementation is memory inefficient and significantly complicates maintenance of the AMR hierarchy for $p + d - 1 \gtrsim 3$.

H.5 Getting Around Temporal Boundary Interpolation

All of the issues that we have encountered so far have been caused by the need to set values on the grid boundaries during the fine grid evolution. When time levels are not synchronized, we require $(p+d-1)$ time levels to perform the corresponding temporal interpolation. Conversely, when time levels are synchronized, we could follow the approach of Lehner et al. [76] and perform order $p+1$ interpolation with only a single time level. For hyperbolic FDAs, we can take advantage of the fact that the speed of information is finite and simply throw out the contaminated fine grid evolution in the vicinity of the boundaries. This procedure is highlighted in Algorithm 8.

Algorithm 8 Tapered Boundary Algorithm

considering temporally synchronized grid functions, u,
at levels $l-1$ and l: ${}^{(l-1)}u^n$ and ${}^{(l)}u^{2n}$ respectively
initialize ${}^{(l-1)}u^n, {}^{(l)}u^{2n}$
while ${}^{(l)}t < t_{\max}$ **do**
  evolve ${}^{(l-1)}u^n$ **to** ${}^{(l-1)}u^{n+1}$
  evolve ${}^{(l)}u^{2n}$ **to** ${}^{(l)}u^{2n+1}$
  evolve ${}^{(l)}u^{2n+1}$ **to** ${}^{(l)}u^{2(n+1)}$
  interpolate CFL boundary from ${}^{(l-1)}u^{n+1}$ to ${}^{(l)}u^{2(n+1)}$
  inject grid from ${}^{(l)}u^{2(n+1)}$ to ${}^{(l-1)}u^{n+1}$
  set $n = n+1$
end while

Unfortunately, Algorithm 8 is incomplete and provides, at most, order $p+1$ order interpolation. Thus, after application of a derivative operator in the vicinity of the boundary region, the leading order error term will be $O(h^{p+1-d})$. In order to have convergence away from the boundary, we therefore require $O(h^p) \sim O(h^{p+1-d})$, or $d = 1$: as it stands, this algorithm only truly works for hyperbolic PDEs formulated in first order form. The crux of the issue is, once again, that derivatives taken in the vicinity of the boundary are operating on functions which have discontinuities at order $p+1$. Explicitly, at the edge of the boundary there is an abrupt transition between a function of the form

$$\tilde{u}_i^n \sim u_i^n + \left[{}^{(l-1)}E_i^n\right]\left[{}^{(l-1)}h^{p+1}\right], \tag{H.18}$$

and one of the form

$$\tilde{u}_i^n \sim u_i^n + \left[{}^{(l)}E_i^n\right]\left[{}^{(l)}h^{p+1}\right]. \tag{H.19}$$

Here, ${}^{(l-1)}E_i^n$ and ${}^{(l)}E_i^n$ are not the leading order terms in a Richardson expansion: the boundary interpolation will introduce contamination at a lower order and beyond that, flux correction or stabilization techniques such as Kreiss-Oliger dissipation [72], will generally prevent ${}^{(l-1)}E_i^n$ and ${}^{(l)}E_i^n$ from being the same function.

The key word in the phrase "abrupt transition" is *abrupt*. The discontinuity between the functions can be essentially thought of as a step function of width h. We consider the action of blending the two distinct regions via,

$$\tilde{u}_i^n := (1-b_i)\cdot\left(u_i^n + \left[{}^{(l-1)}E_i^n\right]\left[{}^{(l-1)}h^{p+1}\right]\right) b_i \cdot \left(u_i^n + \left[{}^{(l)}E_i^n\right]\left[{}^{(l)}h^{p+1}\right]\right) \tag{H.20}$$

where b_i is a monotonically increasing function which interpolates between 0 and 1 over the span of N_b grid points. This blending approach was previously and independently considered by Mongwane in [88] although it is motivated in a slightly different manner.

By optimizing these interpolating polynomials to zero successive derivatives at the edges of the refined domain, we help to regularize spatial derivatives in the presence of the boundary regions. Equations (H.21)–(H.25) present the first 5 of these interpolating polynomials and they are plotted in Fig. H.2. Figures H.3–H.5 demonstrate how each successive polynomial helps to regularize one further derivative, helping to smooth out the transition region.

$$b_0(x) = H(x) \tag{H.21}$$
$$b_1(x) = x \tag{H.22}$$
$$b_2(x) = x^2(-2x+3) \tag{H.23}$$
$$b_3(x) = x^3(6x^2 - 15x + 10) \tag{H.24}$$
$$b_4(x) = x^4(-20x^3 + 70x^2 - 84x + 35) \tag{H.25}$$

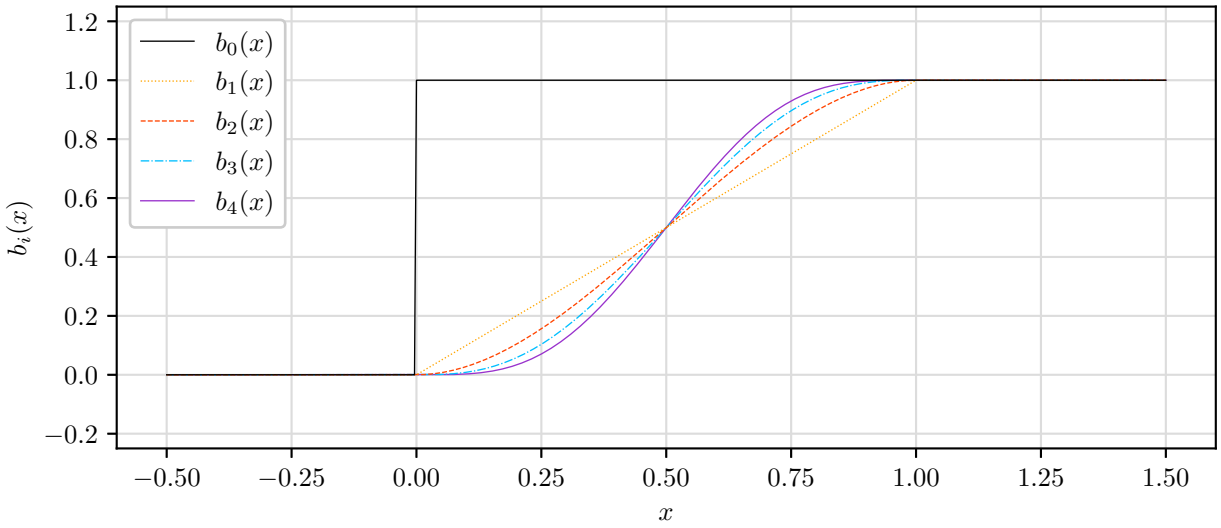

Figure H.2: The first five blending functions with $x = i/(N_\mathrm{b} - 1)$ where i is the number of grid points from the edge of a region and N_b is the width of the blending region. The function $b_1(x)$ is designed to smoothly interpolate between 0 and 1 over the course of N_b grid points. Each successive $b_i(x)$ is derived by requiring that an additional set of derivatives vanishes at the endpoints. E.g. the first derivatives of $b_2(x)$ vanish at $x = 0, 1$ while the first and second derivatives of $b_3(x)$ vanish at $x = 0, 1$. These polynomials are identical to those derived in [88]

Unfortunately this does not truly fix the problem. Reducing the magnitude of the error terms does not effect convergence and the application of a d^th derivative across a boundary with an order $p+1$ discontinuity will still result in a derivative with only order $p+1-d$ accuracy. At this point, though, we should remind ourselves of the core issue we are attempting to fix: preventing spurious regridding of the boundary regions in the wake of refining a region of high truncation error. Achieving perfect convergence is secondary to this goal.

In AMR with a local truncation error tolerance of ϵ_0, grid refinement is performed when some norm of the difference between grid functions on two synchronized levels exceeds ϵ_0. For a hyperbolic

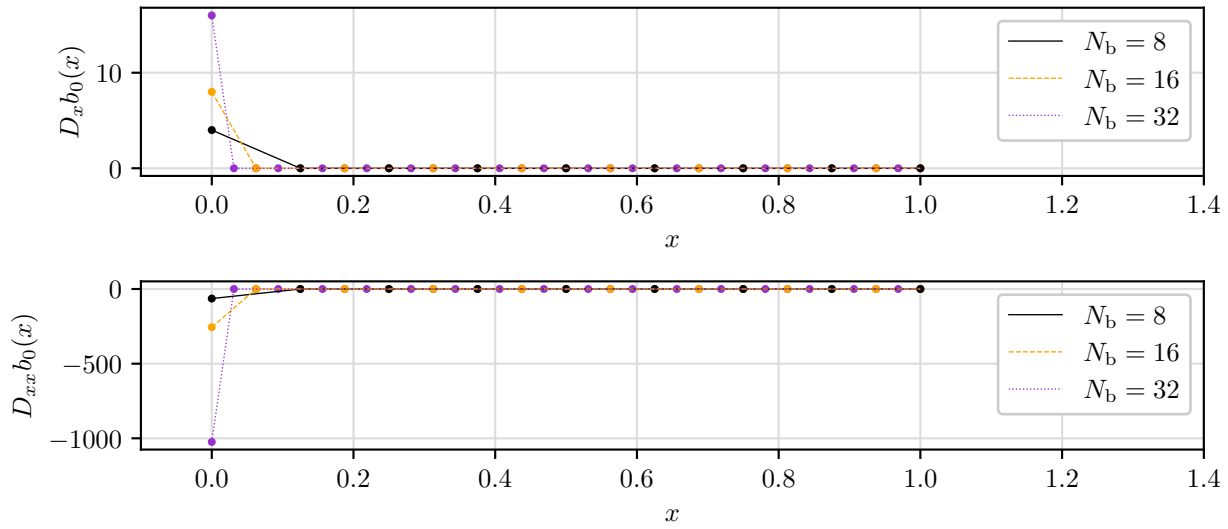

Figure H.3: The effect of applying the second order accurate centered first and second derivative stencils to b_0 for $N_\mathrm{b} = 8, 16, 32$. As resolution increases, the relative error increases dramatically going as $1/N_\mathrm{b}$ for first derivatives and $1/N_\mathrm{b}^2$ for second derivatives. This effect can cause significant numerical error to develop at grid boundaries contributing to spurious regridding.

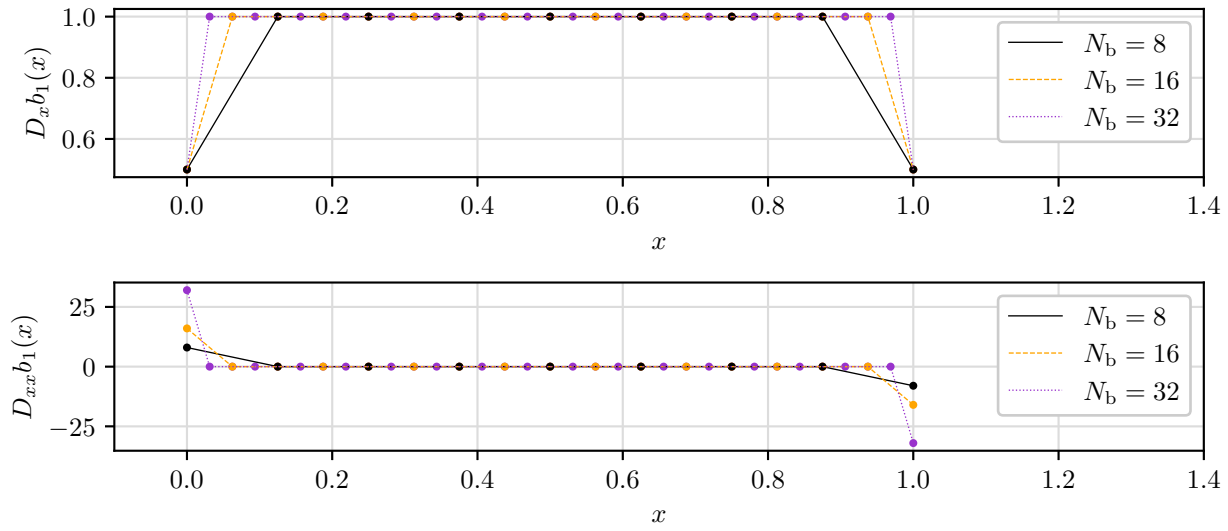

Figure H.4: The effect of applying the second order accurate centered first and second derivative stencils to b_1 for $N_\mathrm{b} = 8, 16, 32$. As resolution increases, $D_x b_1(x)$ converges while $D_x x b_1(x)$ diverges as $1/N_\mathrm{b}$.

PDE of the form

$$\partial_t u = \mathbf{D}_x(u) + f \tag{H.26}$$

with $O(h^p)$ accurate FDA

$$\mathbf{D}_t^h(u^h) = \mathbf{D}_x^h(u^h) + f^h \tag{H.27}$$

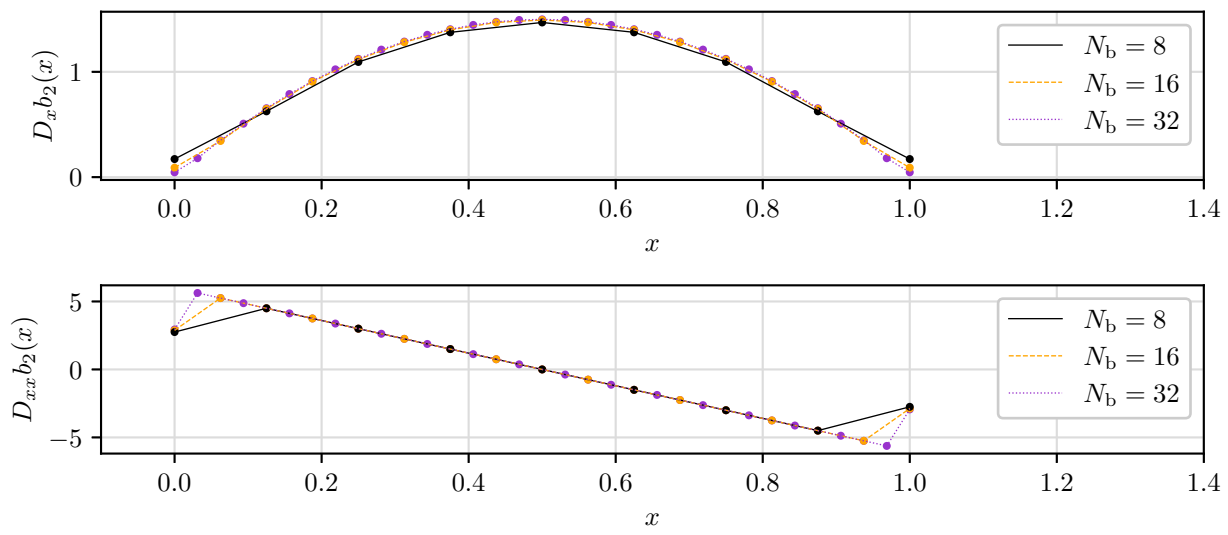

Figure H.5: The effect of applying the second order accurate centered first and second derivative stencils to b_2 for $N_b = 8, 16, 32$. As resolution increases, both $D_x b_1(x)$ and $D_x b_2(x)$ converge.

operating on data with a characteristic magnitude of ~ 1, refinement (in the interior where the Richardson expansion should still hold) occurs when,

$$e \sim 2\lambda \left[{}^{(l)}h\right] \left({}^{(l)}\tilde{u}^{2n+2}\right) - \lambda \left[{}^{(l-1)}h\right] \left({}^{(l-1)}\tilde{u}^{n+1}\right) \geq \epsilon_0, \tag{H.28}$$

$$e \sim 2\lambda \left[{}^{(l)}h\right] \left(\left[{}^{(l)}h^p\right] - \left[2^{(l)}h\right]^p\right) \tilde{\epsilon}_p \geq \epsilon_0. \tag{H.29}$$

Assuming $\tilde{\epsilon}_p \sim 1$, we find that refinement should occur when:

$$e \sim \epsilon_0 \sim \left(2\left[{}^{(l)}h\right]\right)^{p+1} = \left({}^{(l-1)}h\right)^{p+1} \tag{H.30}$$

Consider $h = {}^{(l-1)}h$ and a region requiring refinement with $e \sim h^{p+1} \sim \epsilon_0$ on the interior and $e \sim h^{p+1} < \epsilon_0$ on the exterior. We perform the refinement procedure and evolve the two regions until they are once again synchronized. On the exterior region we will once again find, $e \sim h^{p+1} < \epsilon_0$ while the interior region now has $e \sim (h/2)^{p+1} < \epsilon_0$ (with the addition of the refined grid, level l is now the base grid for the truncation error calculation). If the PDE has d^{th} derivatives, the error on the boundary without blending is then $e \sim (h/2)^{m-d+1}$.

Our goal is then to *prevent spurious regridding in the boundary region*. This is equivalent to asking what conditions on the blending functions are sufficient to ensure the error in this boundary region satisfies $e \lesssim \epsilon_0$. Once we have a blending function which satisfies this condition to our desired tolerance, we can recover full p^{th} order convergence (in the sense of a residual convergence test) by widening the stencil of the blending function by a factor of ρ for each factor of ρ decrease in h. This variant of the Tapered Boundary algorithm is presented in Algorithm 9 and turns out to be essentially identical to the 2015 work of Mongwane [88].

H.6 Determination of Parameters

Determination of the boundary width, N_b, proceeds as follows. Choose the desired per-step error tolerance, ϵ_0, while noting the highest order derivative, d, and associated finite difference stencil.

Algorithm 9 Smooth AMR Algorithm

considering temporally synchronized grid functions, u,
at levels $l-1$ and l: ${}^{(l-1)}u^n$ and ${}^{(l)}u^{2n}$ respectively
initialize ${}^{(l-1)}u^n, {}^{(l)}u^{2n}$
while ${}^{(l)}t < t_{\max}$ **do**
  evolve ${}^{(l-1)}u^n$ **to** ${}^{(l-1)}u^{n+1}$
  evolve ${}^{(l)}u^{2n}$ **to** ${}^{(l)}u^{2n+1}$
  evolve ${}^{(l)}u^{2n+1}$ **to** ${}^{(l)}u^{2(n+1)}$
  interpolate CFL boundary from ${}^{(l-1)}u^{n+1}$ to ${}^{(l)}u^{2(n+1)}$
  blend transition region between ${}^{(l-1)}u^{n+1}$ and ${}^{(l)}u^{2(n+1)}$
  inject grid from ${}^{(l)}u^{2(n+1)}$ to ${}^{(l-1)}u^{n+1}$
  set $n = n+1$
end while

For a given blending function, $b(x)$, d^{th} degree differencing operator D_x^h and blending width, N_{b}, determine,

$$B_{\text{r}} = \max\left(\left|D_x^h b(x)\right|\right) / \max\left(\left|D_x^h b_0(x)\right|\right). \tag{H.31}$$

Then, if $e \sim B_{\text{r}} \cdot (h/2)^{m-d+1} \lesssim \epsilon_0$ is not satisfied, increase N_{b} or choose a different blending function. As a concrete example, consider a fourth order accurate implementation of the wave equation written in second order form (Eqns. (H.16)–(H.17)), with $b(x) = b_0(x)$, $\epsilon_0 = 10^{-5}$ and D_t^h some abstracted fourth order accurate temporal derivative scheme which relies on intermediary time levels (RK4 for example).

$$D_t^h \psi_i^h = \pi_i^h, \tag{H.32}$$

$$D_t^h \pi_i^h = \frac{1}{12h^2}\left(-\psi_{i-2}^h + 16\psi_{i-1}^h - 30\psi_i^h + 16\psi_{i+1}^h - \psi_{i-2}^h\right). \tag{H.33}$$

The maximum of the fourth order accurate second derivative operator acting on $b_0(x)$ is $\sim 1/h^2$ and since $b(x) = b_0(x)$, $B_{\text{r}} = 1$. For data with a characteristic magnitude of 1 (roughly equivalent to using a truncation error estimate normalized to the magnitude of our fields), we have $\epsilon_0 \sim h^{m+1}$, $h \sim 10^{-1}$. The condition for eliminating spurious regridding

$$B_{\text{r}} \cdot (h/2)^{m-d+1} \lesssim \epsilon_0, \tag{H.34}$$

$$1 \cdot \left(10^{-1}/2\right)^{4-2+1} \lesssim 10^{-5}, \tag{H.35}$$

$$0.000125 \lesssim 10^{-5}, \tag{H.36}$$

cannot be satisfied and we conclude that the condition cannot be satisfied with $b(x) = b_0(x)$ without increasing the size of the regridding region well beyond where the error is $\sim \epsilon_0$. For $b(x) = b_1(x)$, $B_r \sim 1/N_{\text{b}}$. The condition for eliminating spurious regridding is:

$$B_{\text{r}} \cdot (h/2)^{m-d+1} \lesssim \epsilon_0, \tag{H.37}$$

$$\frac{1}{N_{\text{b}}} \cdot \left(10^{-1}/2\right)^{4-2+1} \lesssim 10^{-5}, \tag{H.38}$$

$$N_{\text{b}} \gtrsim 16, \tag{H.39}$$

and we expect that the linear blending function with $N_\mathrm{b} \sim 16$ should prevent spurious regridding. For $b(x) = b_2(x)$, $B_r \sim 6/N_\mathrm{b}^2$. The condition for eliminating spurious regridding is therefore:

$$b_\mathrm{r} \cdot (h/2)^{m-d+1} \lesssim \epsilon_0, \tag{H.40}$$

$$\frac{6}{N_\mathrm{b}^2} \cdot \left(10^{-1}/2\right)^{4-2+1} \lesssim 10^{-5}, \tag{H.41}$$

$$N_\mathrm{b} \gtrsim 8. \tag{H.42}$$

It should be noted that the derivations given above are heuristic. In practice there is a complex interplay between the error induced in the boundaries and the size of the regridding region. It is frequently the case that one can satisfy the required error bound by using sufficient dissipation and increasing the size of the regridding region to compensate for the relatively large errors which are introduced by using a low order blending function.

H.7 Implementation

In 1D, the blending function is trivial to implement. For a CFL boundary of width N_cfl and a blending function of width N_b, the minimum grid size is simply $N = N_\mathrm{cfl} + N_\mathrm{b}$ at a physical boundary and $N = 2N_\mathrm{cfl} + 2N_\mathrm{b}$ on the interior. In 2D or higher though, it is necessary to find some distance metric from the boundaries of the refined region which permits smooth interpolation of the blending function near the edges and vertices of the region. In practice, we have found the procedure outlined in Algorithm 10 to be effective.

Algorithm 10 Generate Blending Function

```
for point in region do
    for i in number of dimensions do
        d[2·i] = max(x[i] - (bbox[2·i] + N_cfl·h)/h, 0)
        d[2·i+1] = max((bbox[2·i+1] - N_cfl·h)/h - x[i], 0)
    end for
    inverse_distance = 0
    for i in 2 · number of dimensions do
        if boundary[i] is not a physical boundary then
            inverse_distance += pow(d[i], -m)
        end if
    end for
    distance = pow(inverse_distance, -1/m)
    if distance is infinite or not a number then
        distance = 0
        if all boundaries are physical then
            distance = N_b
        end if
    end if
    relative_distance = min(distance / N_b, 1)
    blend_mask[point] = blend(relative_distance)
end for
```

This algorithm simply calculates the distance from the current point on the grid to the edge of each boundary, and then reduces that distance by N_cfl points. Some power m is chosen, and

the m^{th} inverse of these distances is added together to get a smooth inverse distance. This inverse distance is then raised to the power of $-1/m$ to get a smoothed distance to each boundary. Finally, the distance is divided by N_{b} and clamped between 0 and 1. This clamped relative distance is used to set the value of the smooth interpolating polynomial.

In practice, we find that $m = 4$ has a good blend of smoothness and compactness. For a D dimensional grid, one finds that the minimum grid size is $N = 2N_{\text{cfl}}+2N_{\text{b}}(2D)^{1/m}$ in all dimensions.

H.8 Smooth AMR for the 2D Wave Equation

We implement a minimal example of the blending method in PAMR/AMRD for the 2D wave equation with Dirichlet boundary conditions:

$$\partial_t \psi\left(t,x,y\right) = \pi\left(t,x,y\right), \tag{H.43}$$

$$\partial_t \pi\left(t,x,y\right) = \partial_{xx}\psi\left(t,x,y\right) + \partial_{yy}\psi\left(t,x,y\right), \tag{H.44}$$

$$\psi(t,x_{\min},y) = \psi(t,x_{\max},y) = \psi(t,x,y_{\min}) = \psi(t,x,y_{\max}) = 0, \tag{H.45}$$

$$\pi(t,x_{\min},y) = \pi(t,x_{\max},y) = \pi(t,x,y_{\min}) = \pi(t,x,y_{\max}) = 0, \tag{H.46}$$

using the fourth order discretization given by Eqns. (H.32)–(H.33) with an RK4 integrator and sixth order KO dissipation to curb high frequency instabilities. For initial data we take:

$$\psi\left(0,x,y\right) = e^{-\left((x-x_0)^2+y^2\right)/\sigma^2} + e^{-\left((x+x_0)^2+y^2\right)/\sigma^2}, \tag{H.47}$$

$$\pi\left(0,x,y\right) = 0, \tag{H.48}$$

with parameters

$$x_0 = \frac{3}{2}, \sigma = \frac{1}{4}, N_{\text{b}} = 16, \tag{H.49}$$

$$-x_{\min} = x_{\max} = -y_{\min} = y_{\max} = 3. \tag{H.50}$$

The simulation is evolved until $t = 12$. We use a per-step error tolerance of $\epsilon_0 = 1{\cdot}10^{-5}$ and compare standard AMR using 2^{nd} and 3^{rd} order temporal boundary interpolation to our implementation of smooth AMR with blending functions b_0, b_1 and b_2.

For these settings, we find that the standard AMR with 2^{nd} or 3^{rd} order boundary interpolation develops regridding pathologies. In these runs, boundary errors cause regridding to the finest possible level across the entire domain of the simulation by $t \sim 1$. In order to prevent this, it was necessary to reduce the per-step error tolerance to $\epsilon_0 \sim 1 \cdot 10^{-3}$. Figure H.6 plots the l_2 norm of the residuals between π^h and π (determined by running a unigrid simulation at high resolution) for each of the AMR simulations. Although the difference between b_0 and b_1 or b_2 is marginal for these simulations, we find that the derivatives (Fig. H.7) are much better represented for b_1 and b_2 relative to b_0.

Figures H.9–H.10 demonstrate how the blending technique massively reduces the presence of high frequency noise propagating from grid boundaries. For standard AMR, high frequency "noise" is readily apparent in second derivatives (Figs. H.9–H.8) and absolutely dominates the spectrum by the third or fourth derivative (Figs. H.11–H.10). This sort of high frequency noise may then propagate from the regridding boundaries and can cause a feedback cycle of spurious regridding if insufficiently damped.

Note that in Figs. H.9 and H.11, the regridding regions are set using the b_2 regridding script (e.g. the gridding was not performed based on local truncation error estimation and instead simply

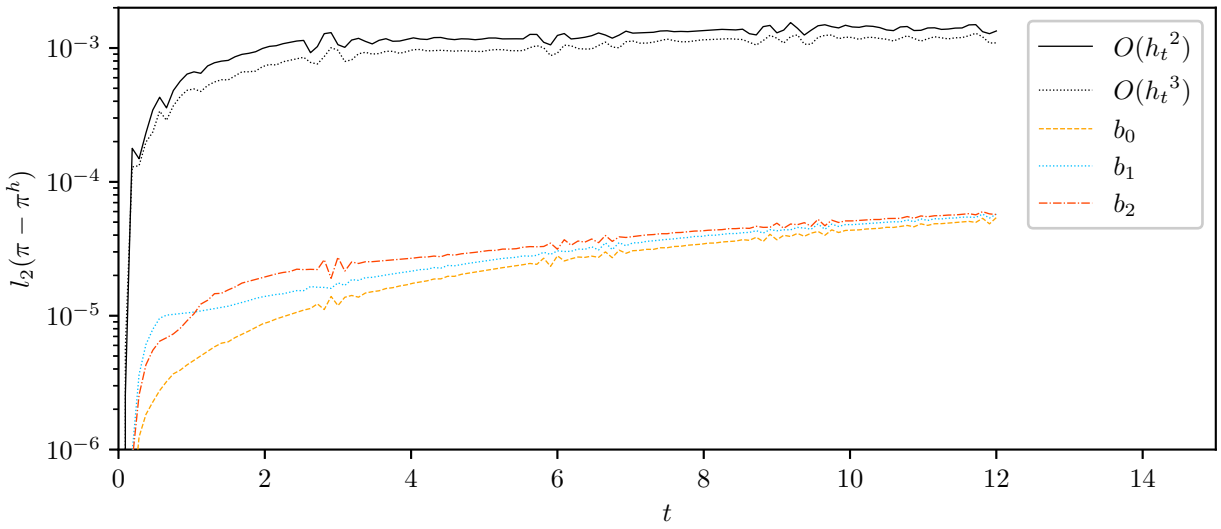

Figure H.6: l_2 norm of the error between the true solution, π, and the computed solutions, π^h, restricted to uniform grids. As AMR with 2nd or 3rd order boundary interpolation develops regridding pathologies for $\epsilon_0 = 1 \cdot 10^{-5}$, these simulations were performed using the b_2 regridding procedure to give a "best case" comparison. The smooth AMR technique seems relatively independent of blending function with the b_0 step function surprisingly outperforming both b_1 and b_2. When we examine the evolution in detail, we see that at the initial time, the b_0 simulation creates larger regridding regions thereby reducing the error. Compare with Fig. H.7 which examines the higher derivative residuals.

copied the regridding procedure of the b_2 simulation). As noted previously, AMR with 2nd or 3rd order boundary interpolation was found to be pathological for $\epsilon_0 = 1 \cdot 10^{-5}$. As such, Figs. H.9 and H.11 and represent idealized, best case scenarios; the actual performance of the method with adaptive truncation error based regridding would be much worse.

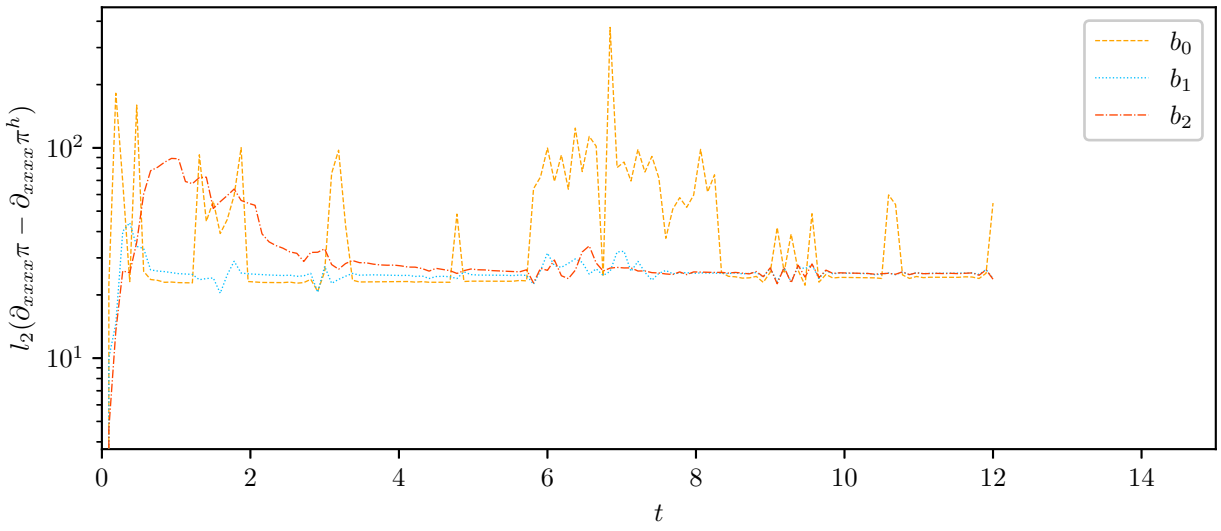

Figure H.7: l_2 norm of the error between $\partial_{xxxx}\pi$ and $\partial_{xxxx}\pi^h$ restricted to uniform grids. Although the presence of the smoothing functions had a minor negative impact on the overall accuracy of the simulation (see Fig. H.6), here we can see its utility. When boundaries are not smoothed, regridding can lead to the formation of high frequency modes (spikes in the above graph) which may then propagate causing additional spurious regridding. In the b_2 and b_1 simulations, regridding is smooth at the level of the fourth derivative, however we see that $N_\mathrm{b} = 16$ is evidently insufficient to derive any improvements from b_2 over b_1. In the case of the wave equation simulation, the boundary errors in the b_0 simulation damp out and are transient. In more complex simulations with frequent regridding and many length scales, those same sorts of errors may become significant and lead to spurious regridding.

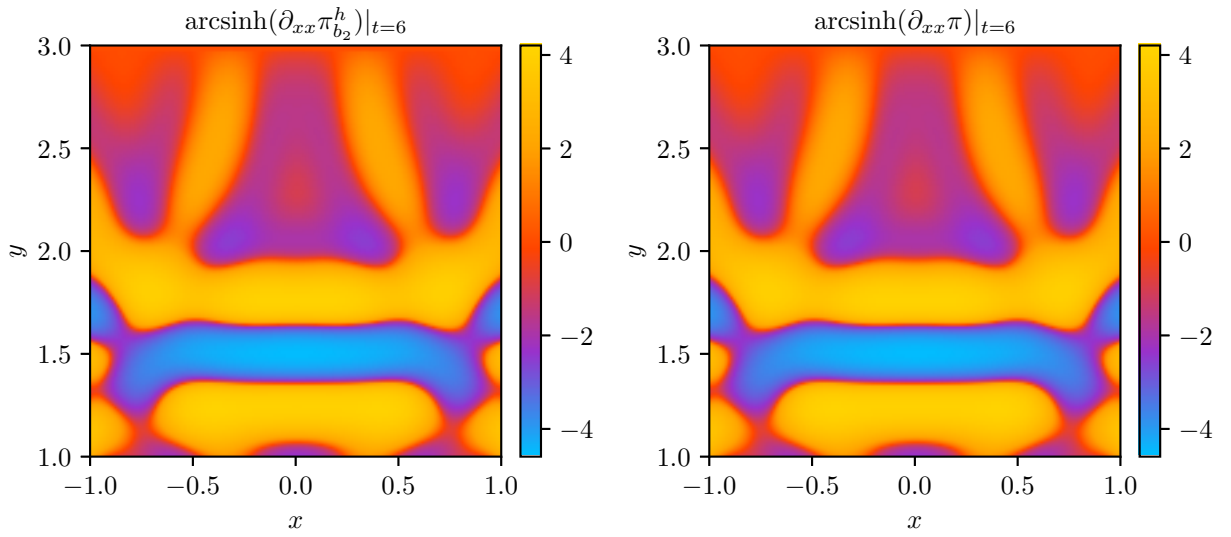

Figure H.8: Second derivative, $\partial_{xx}\pi$ evaluated at $t = 6$ for AMR with blending function b_2 (represented as $\pi^h_{b_2}$) and a high accuracy unigrid simulation (represented as π). Here we have zoomed in on the region $x = [-1, 1]$, $y = [1, 3]$ to better compare with Fig. H.9 which plots the corresponding solution for AMR using second and third order boundary interpolation in time. Note that we are plotting $\text{arcsinh}(\pi^{\text{h}}_{\text{xx}})$ rather than π^h_{xx} and that the AMR simulation appears smooth and essentially indistinguishable from the high-order unigrid solution.

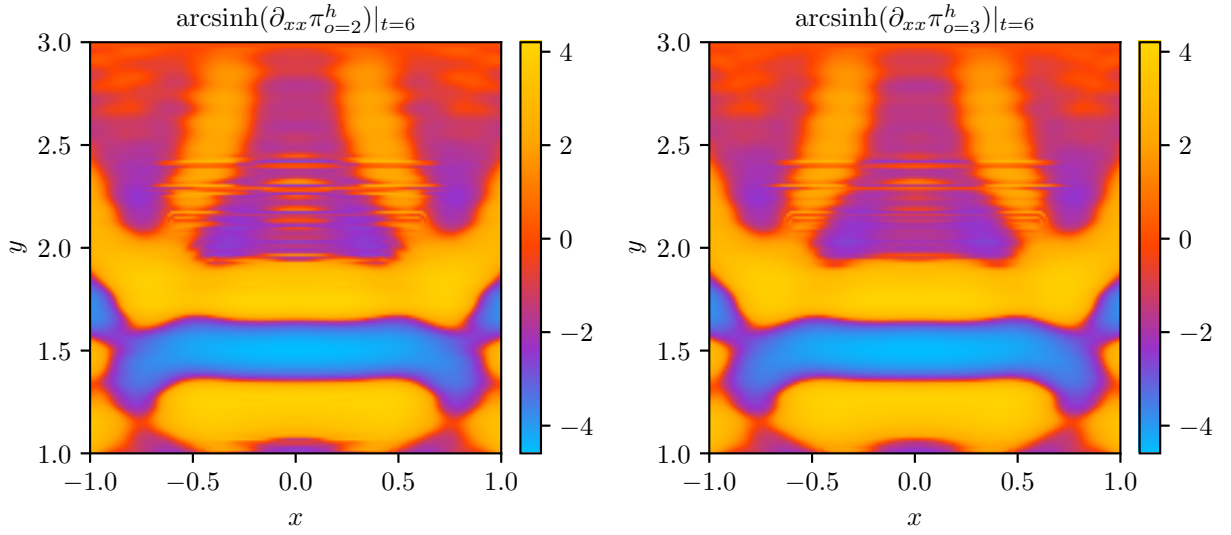

Figure H.9: Second derivative, $\partial_{xx}\pi$ evaluated at $t = 6$ for AMR with second order boundary interpolation (represented as $\pi^h_{o=2}$) and AMR with third order boundary interpolation (represented as $\pi^h_{o=3}$). Here we have zoomed in on the region $x = [-1, 1]$, $y = [1, 3]$ to better highlight propagating high frequency modes which can be seen as narrow striations (compare with Fig. H.8). At an error tolerance of $1 \cdot 10^{-5}$, AMR with second and third order boundary interpolation in time regrids pathologically rendering direct comparisons meaningless. As such, this simulation was performed using the regridding script of the b_2 smooth AMR run. Note that we are plotting $\text{arcsinh}(\psi^{\text{h}}_{\text{xx}})$ rather than ψ^h_{xx} to better highlight the propagating high frequency modes.

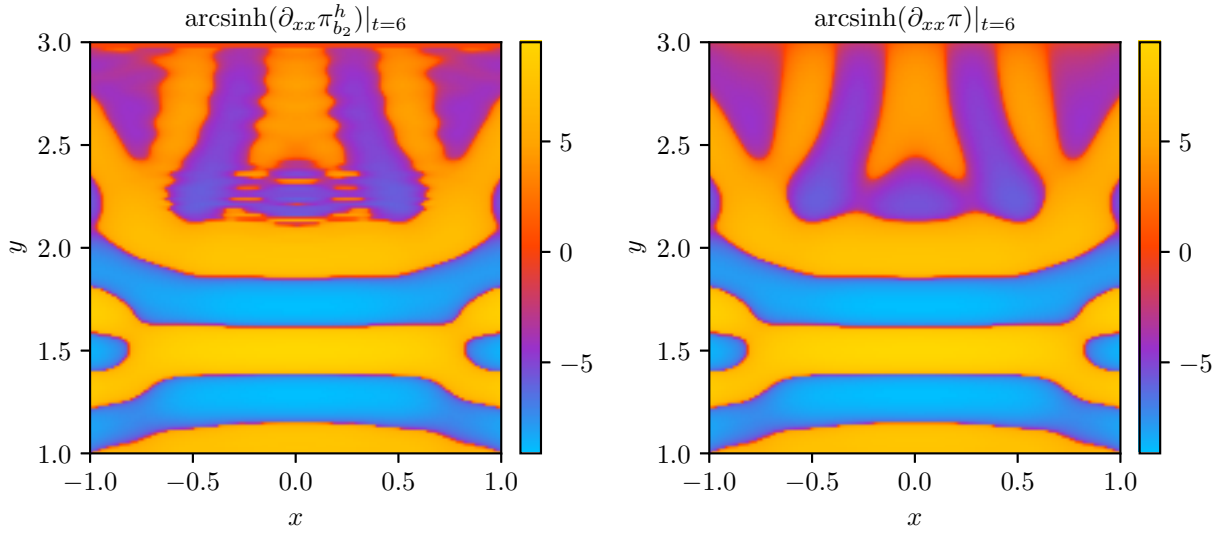

Figure H.10: Fourth derivative, $\partial_{xxxx}\pi$ evaluated at $t = 6$ for AMR with blending function b_2 (represented as $\pi^h_{b_2}$) and a high accuracy unigrid simulation (represented as π). Here we have zoomed in on the region $x = [-1, 1]$, $y = [1, 3]$ to better compare with Fig. H.11 which plots the corresponding solution for AMR using second and third order boundary interpolation in time. Note that we are plotting $\text{arcsinh}(\pi^{\text{h}}_{\text{xxxx}})$ rather than π^h_{xxxx} and although there are clearly departures from the high accuracy unigrid solution, given the overall scale, they are fairly minimal.

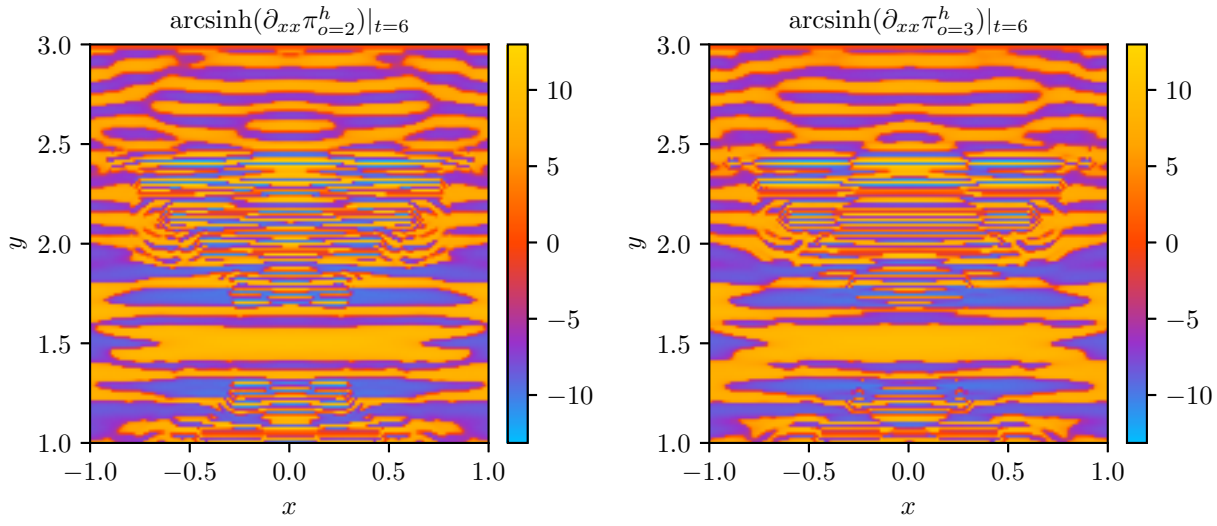

Figure H.11: Fourth derivative, $\partial_{xxxx}\pi$ evaluated at $t = 6$ for AMR with second order boundary interpolation (represented as $\pi^h_{o=2}$) and AMR with third order boundary interpolation (represented as $\pi^h_{o=3}$). Here we have zoomed in on the region $x = [-1, 1]$, $y = [1, 3]$ to better highlight propagating high frequency modes which can be seen to completely dominate the solution (compare with Fig. H.10).